Search for Supersymmetry with Tau Leptons, Muons, Missing Transverse Momentum and Jets with the ATLAS Experiment at the Large Hadron Collider

Dissertation
zur
Erlangung des Doktorgrades (Dr. rer. nat.)
der
Mathematisch-Naturwissenschaftlichen Fakultät
der
Rheinischen Friedrich-Wilhelms-Universität Bonn

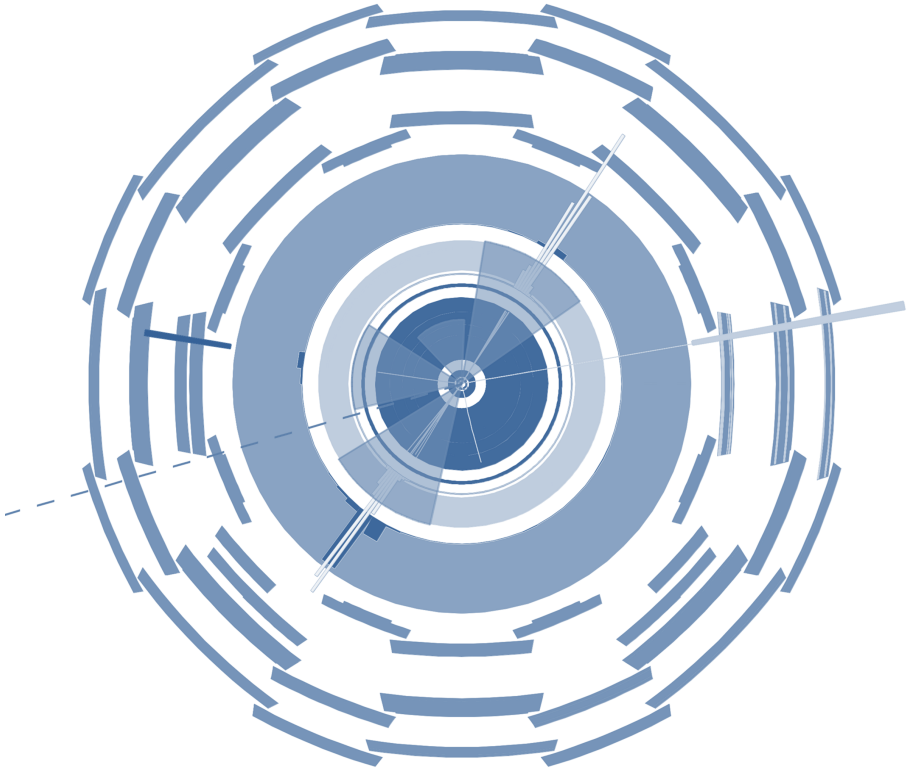

vorgelegt von
Till Nattermann
aus
Greifswald

Bonn 2013

Angefertigt mit Genehmigung der Mathematisch-Naturwissenschaftlichen Fakultät der Rheinischen Friedrich-Wilhelms-Universität Bonn.

1. Gutachter: Prof. Dr. Klaus Desch
2. Gutachter: Prof. Dr. Jochen Dingfelder

Tag der Promotion: 3. September, 2013
Erscheinungsjahr: 2013

Abstract

Beyond the established Standard Model (SM), the search for new physics is among the most important ventures of modern physics. Supersymmetry (SUSY) is a natural candidate for an extension of the SM to account for unexplained phenomena. Therefore, the search for SUSY is an essential part in the physics program of collider experiments. With the ongoing exclusion of SUSY models, the scope of SUSY searches is more and more extended towards models predicting tau lepton final states. Tau leptons might be a unique probe for the existence of SUSY, but these SUSY models could still be veiled by the less striking tau signatures in the detector. This thesis presents a search for SUSY with tau final states at the ATLAS experiment at the LHC. It is among the first published SUSY searches with tau leptons in ATLAS.

The standard tau lepton analyses search for hadronic tau decays and typically suffer from fake tau signatures of various origins. These contributions contaminate the data with unwanted backgrounds. In contrast to hadronically decaying tau leptons, muons have a very characteristic detector appearance. They show up with a clear signature that can be measured with excellent accuracy and high efficiency. The work presented in this thesis extends the searches for pure hadronic tau final states towards final states with muonic tau decays. It is shown that the muon signature helps to reduce background contributions and to probe the identification performance of hadronically decaying taus in the complex experimental environment of the ATLAS detector. In particular, the muon can be used to control fake tau contributions, which is of great benefit for an accurate background prediction.

Based on these studies, SUSY is searched in final states with one muon, at least one hadronically decaying tau lepton, jets and missing transverse energy. The search is performed in proton-proton collisions at $\sqrt{s} = 7\,\text{TeV}$ corresponding to an integrated luminosity of $4.7\,\text{fb}^{-1}$. The considered SUSY model is Gauge Mediated Supersymmetry Breaking (GMSB) with the parameters $N_5 = 3$, $\operatorname{sgn}\mu = +1$, $C_{\tilde{G}} = 1$ and $\langle S \rangle = 250\,\text{TeV}$. Λ and $\tan\beta$ are left as free parameters of the model. The event selection is optimized for maximal sensitivity to GMSB and leaves an expected SM background of $0.80 \pm 0.28^{\text{MC stat.}} \pm 0.275^{\text{syst.}}$ events. The measurement of one event in data agrees well with the SM expectation and the non-observation of any deviation is used to set limits on the possible existence of GMSB models. GMSB models up to $\Lambda = 45\,\text{TeV}$ could be excluded with $95\,\%$ confidence level. The limit is further tightened by the statistical combination with other SUSY searches with tau final states.

Acknowledgements

This thesis was developed over the last years, in which many people contributed to its successful accomplishment. In the first place, I would like to thank *Prof. Dr. Klaus Desch* for the opportunity to work on various topics in the field of high energy physics and his patient and committed support of this work. The grant for creative latitude and close supervision at the same time constituted a prolific scientific environment in which the ideas of this work could develop. I would also like to thank *Philip Bechtle* who assisted the analysis at a detailed and technical level. He always willingly lend an ear for any kind of problem and contributed with many thoughts.

The close and lively collaboration with the ATLAS SUSY with taus team has been among the most fruitful sources of new ideas and helpful comments. In this regard, I am grateful to *Fabrizio Salvatore* for the coordination of this group. He indefatigably reminded the analysts of their responsibilities and thereby consolidated the individual efforts in the tight time schedules of conferences. The exchange of ideas and results with *Trygve Buanes*, *Michel Janus*, *Alex Kastanas*, *Anthony Rose*, *Steffen Schaepe* and *Martin Schultens* helped to confirm and validate results and hence contributed to the reliability of the analysis. Moreover, I would like to thank the *ATLAS collaboration* for the inspiring working atmosphere, the provision of analysis tools and the critical review and approval of results.

The analysis greatly benefits from the *Bonn Analysis Facility*, which provided computing and storage resources for the complex data handling of this analysis. These resources are excellently supported and administrated by *Gizo Nanava*. I would also like to thank the *Bonn Cologne Graduate School* for financial support and a diversity of offered scientific education and training.

Finally, I owe a debt of gratitude to the non-scientific but not less important support by *my parents* and *Michaela Granzow*.

Contents

Chapter 1

Setting the Scene

The Hunt for New Physics

Following its proposal in the early 70's, physicists are searching for any evidence of Supersymmetry (SUSY) as an extension of the Standard Model (SM). The following chapter sketches the general purpose of this work within that effort. The search for SUSY is motivated and the goals of this thesis are settled. In order to preserve the introductory nature of this chapter, its contents are rather generic. More detailed information is given in the subsequent chapters. This introduction merely illustrates the motivation of this work within the actual physics research and outlines the general concepts and structure of the thesis.

1.1 Motivation

The study of the elementary particles and their interactions is one of the fundamental pillars of physics. It comprises the search for the elementary particles, the measurement of their properties and the understanding of their complex interplay in building compound particles, atoms, matter and even large scale structures such as the formation of our galaxy. The aim of this physics domain is the discovery of the fundamental constituents of matter and the development of a theory that describes all their interactions. In a universal theory, the constituents and their interactions should explain all observations in Nature. So far this has not been achieved.

The SM is the best currently known model to describe the elementary particles.[1] It explains the interactions of the known particles by the exchange of gauge particles. While it successfully describes many phenomena, there are still shortcomings within this model. Some experimental observations cannot be explained and require further development of the current model.

Whereas the design of new theories is subject to theoretical physics, these theories have to be confirmed or rejected experimentally. In the current situation, many models might be suited to be a meaningful extension of the SM. Among different proposals, SUSY could be a natural candidate. It solves many shortcomings of the SM, as will explained later. E.g. it gives a natural solution of the hierarchy problem, provides a dark matter candidate and predicts the electroweak mixing angle. But even within a particular theory like SUSY, there is a diversity of different models. It is the responsibility of experimental physics to either find hints for a certain model, or to show that observations are in contradiction to the model's predictions. In the latter case, the model can be rejected. In that sense, this thesis is part of the effort to search for any evidence of SUSY.

[1] Gravity and its theoretical formalism is not included in the SM. At currently accessible energies, this interaction is very weak compared to the others. It is only of interest for large matter systems that are neutral for all the other forces.

1.2 Analysis Concepts

Among many possible approaches to detect SUSY, the direct production and observation of supersymmetric particles is one of the most promising. The Large Hadron Collider (LHC) collides protons with a center-of-mass energy of 7 TeV to 8 TeV and has encouraging potential to create possibly existing SUSY particles. Therefore, the LHC experiments have good prospects to either discover SUSY, or to set limits in the case of no observed new particles. This designates the search for SUSY to be one of the fundamental parts of their physics program. In these searches, the measurement and its interpretation in terms of physics have to be distinguished. E.g. a new SUSY particle might promptly decay and hence only be visible by its decay products. More general, a certain type of physics might appear as a certain signature that can be measured at the experiment.

Since different SUSY models might manifest themselves by very different signatures, the searches for SUSY more or less aim at particular models. Basically, these searches focus on those signatures that have different predictions from SUSY and the SM. Based on the measurement of these signatures, a SUSY model might be discovered or excluded. A discovery can be claimed if significant excess of that signature is seen. If there is exact agreement of the SM prediction and the observation, no hint for new physics is seen. In that case, any SUSY model can be excluded that would give rise to a significant excess. In this sense, SUSY is considered as signal and the SM as background.

The sensitivity of the corresponding analysis heavily depends on the distinctness of the signature in the SM and in SUSY: The more they differ, the stronger the statement, whether a SUSY model can be excluded or not. In the same way, the sensitivity depends on the accuracy of the two predictions: A more precise prediction allows for stronger conclusions from the measurement. However, for a detailed prediction of the SUSY appearance, a specific SUSY model has to be chosen.

In many cases, the demand for maximal significance and a wide sensitivity to many SUSY scenarios are competing aspects of an analysis. On the one hand, a high sensitivity might be achieved by the search for very specific signatures. These could be copiously predicted by a particular SUSY model, but only rarely occur in the SM. On the other hand, a small change in the SUSY model might change its phenomenology, such that the searched signatures are not realized in that slightly different SUSY model. Hence, it would escape detection and the sensitivity is limited to only a certain SUSY model.

In order to guarantee sensitivity over a wide parameter space in potential SUSY models, the search is split up into many analyses, where each looks for certain signatures and hence different models. For some SUSY models, an increased appearance of tau leptons is predicted, which represent a promising signature to look for. Therefore, this thesis concentrates on the search for collisions that produce SUSY particles that decay into tau leptons. Moreover, jets and missing transverse momentum will be shown to be helpful signatures to find SUSY. The final observation will be the number of observed collisions that contain these signatures.

The results of this thesis are among the first findings for SUSY searches with tau leptons published by ATLAS. Since 7 TeV proton collisions mark a new regime of high energy physics, the understanding and validation of contributing backgrounds requires high attention. Particularly, the performance of tau lepton identification in the complex experimental environment of the ATLAS detector is considered. It will be shown to be among the leading challenges in the understanding of SM backgrounds.

1.3 Structure of Thesis

Chapter 2 of this thesis is dedicated to supersymmetric extensions of the SM. The open questions within the SM are introduced and thereby the need for an extension is motivated. It will be shown that possible

SUSY models are already constrained in order to solve these problems. Furthermore, experimental observations and theoretical considerations are given that determine the expected phenomenology at the LHC. This will justify the search signatures of taus, jets and missing transverse momentum. Finally, the chosen SUSY model, the so-called Gauge Mediated Supersymmetry Breaking model (GMSB), is introduced.

In Chapter 3, the details of the experiment are presented. The LHC accelerator chain as well as the detectors of the ATLAS experiment are explained. These detectors will be used to measure the collision products and identify particles thereof. Particularly, the tau and muon identification in the ATLAS detector are crucial for this analysis and hence are described in detail here. In addition, the computer-based simulation of the experiment is outlined. It allows to predict the expected signatures of any kind of physics and is widely used for comparison to the measured data.

The Chapters 2 and 3 provide the theoretical and experimental basis for the final outline in the object selection of the SUSY search. The object selection defines the required particles in the final state and is given in Chapter 4. Since the expected SM backgrounds depend on the required particles, their contributions are investigated as well in this chapter. The methods that are used for background estimates are presented and their results are verified and tested for robustness. Any unexpected difference between simulation and data observation that might not be caused by potential SUSY will be investigated and explained here as well. This will provide a reliable estimate of the SM backgrounds, which is used for the SUSY search.

The final choice of the searched collision signatures is given in Chapter 5. The optimal selection requirements on the SUSY sensitive quantities are derived and the systematic uncertainties for the chosen selection are estimated. Finally, the observed data are shown and the results are interpreted in the context of the considered GMSB scenario. The last Chapter 6 presents a critical review of the analysis. Potential refinements and extensions of the analysis are shown as well as an outlook on future prospects.

Chapter 2

Extending the Standard Model

Supersymmetry and its Phenomenology

The following chapter motivates and introduces the possibility of a supersymmetric extension of the Standard Model (SM). The demands on this new model are deduced from the open questions of the SM and their implications for a possible SUSY appearance at hadron colliders are explained. Finally, the search for collisions with tau leptons is justified and the targeted SUSY model, Gauge Mediated Supersymmetry Breaking (GMSB), is introduced.

2.1 The Standard Model and its Limitations

The SM of particle physics has been successfully verified over a wide range of phenomena and energies. However, there are several issues that can not be explained within this theory. The most important ones are related to ultraviolet corrections to scalar field masses, unification of the fundamental forces and cosmological observations. Focus is put on their conceptual illustration, whereas for more details the text refers to the corresponding literature. Also the answers to these problems, as given in SUSY theories, are stated and their implications for SUSY models are discussed.

2.1.1 Basic Concepts of the Standard Model

The SM of particles physics [1, 2] describes the properties of the known fundamental particles and two of their interactions, the electroweak and the strong interaction. The model has two basic types of particles: Spin-$1/2$ fermions and spin-1 bosons. Whereas fermions are the constituents of matter, their interactions are mediated by bosons. The known particles of the SM and some of their properties are summarized in Figure 2.1.

In the SM, the kinematics of a fermionic particle with the field components Ψ_μ are described by a Lagrangian $\mathcal{L}$ and the Euler- Lagrange equation

$$\frac{\partial \mathcal{L}}{\partial \Psi} - \partial_\mu \frac{\mathcal{L}}{\partial \left(\partial_\mu \Psi\right)} = 0 \,. \tag{2.1}$$

Within the mathematical formalism of the SM, the Lagrangian $\mathcal{L}$ is required to be invariant under local gauge transformations. Depending on the transformation, additional gauge fields have to be introduced to guarantee the invariance. These extra fields couple to the fermiotic fields and can be interpreted as *messengers*, which mediate the interactions between fermions.

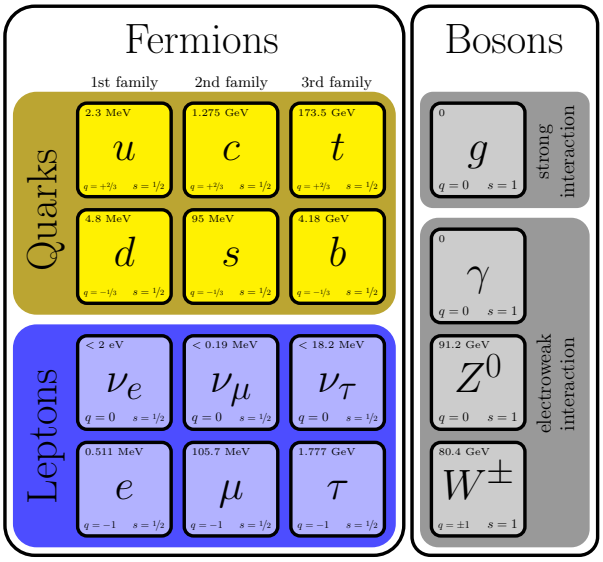

Figure 2.1 The known particles in the Standard Model are grouped into fermions, building matter, and bosons as force carriers. Quarks participate in all interactions, whereas leptons interact only electroweakly. Since neutrinos are electrically neutral, they do not interact electromagnetically. The masses are taken from [3].

The Lagrangian of the electroweak interaction is given by

$$\begin{aligned}\mathcal{L}_{\text{ew}} = &\left(\bar{\nu}_L, \bar{\ell}_L\right) \gamma^\mu \left(i\partial_\mu - g\frac{\vec{\tau}}{2}\cdot\vec{W}_\mu - g'\frac{Y_L}{2}B_\mu\right)\begin{pmatrix}\nu_L\\ \ell_L\end{pmatrix}\\ &+ \bar{\ell}_R\gamma^\mu\left(i\partial_\mu - g'\frac{Y_R}{2}B_\mu\right)\ell_R - \frac{1}{4}\vec{W}_{\mu\nu}\vec{W}^{\mu\nu} - \frac{1}{4}B_{\mu\nu}B^{\mu\nu}\,,\end{aligned} \tag{2.2}$$

with

$$B^{\mu\nu} = \partial^\mu B^\nu - \partial^\nu B^\mu \qquad \text{and} \qquad W_i^{\mu\nu} = \partial^\mu W_i^\nu - \partial^\nu W_i^\mu - g\epsilon^{ijk}W_j^\mu W_k^\nu\,. \tag{2.3}$$

Equation 2.2 is invariant under local transformations of the $\mathrm{SU}(2)_L \times \mathrm{U}(1)_Y$ group, where the subscript L (Y) denotes that the corresponding transformation only applies to the left-chiral (hypercharged) fields. The transformations are given by

$$\begin{pmatrix}\nu_L\\ \ell_L\end{pmatrix} \;\rightarrow\; \underbrace{\exp\left(\frac{i}{2}\vec{\tau}\cdot\vec{\alpha}(x)\right)}_{\mathrm{SU}(2)_L}\underbrace{\exp\left(iY_L\lambda(x)\right)}_{\mathrm{U}(1)_Y}\begin{pmatrix}\nu_L\\ \ell_L\end{pmatrix} \tag{2.4}$$

$$\ell_R \;\rightarrow\; \underbrace{\exp\left(iY_R\lambda(x)\right)}_{\mathrm{U}(1)_Y}\ell_R\,. \tag{2.5}$$

Here, the right-chiral fields only undergo the transformations of the $\mathrm{U}(1)_Y$ group since they have no weak isospin and do not participate in weak interactions. The left-chiral fields are also subject to the local transformations of the $\mathrm{SU}(2)_L$ group. These represent rotations in the two-dimensional weak isospin

space. A general rotation in this space can be expressed by a decomposition into the PAULI matrices, τ_i, which form a basis of the $\mathrm{SU}(2)_L$ group.

The invariance of the Lagrangian from Equation 2.2 under the transformations of Equations 2.4 and 2.5 is attained by the introduction of the fields W_μ^i and B_μ. These are the fundamental gauge fields of the electroweak interaction, which mix to become the physically measurable fields

$$W_\mu^+ = \frac{1}{\sqrt{2}}\left(W_\mu^1 - iW_\mu^2\right) , \tag{2.6}$$

$$W_\mu^- = \frac{1}{\sqrt{2}}\left(W_\mu^1 + iW_\mu^2\right) \text{ and} \tag{2.7}$$

$$\begin{pmatrix} A_\mu \\ Z_\mu \end{pmatrix} = \begin{pmatrix} \cos\vartheta_\mathrm{W} & \sin\vartheta_\mathrm{W} \\ -\sin\vartheta_\mathrm{W} & \cos\vartheta_\mathrm{W} \end{pmatrix} \begin{pmatrix} B_\mu \\ W_\mu^3 \end{pmatrix} . \tag{2.8}$$

These fields represent the W^+, W^-, γ and Z^0 bosons that mediate electroweak interactions. The size of the mixture between the gauge singlet field B_μ and W_μ^3 is given by the WEINBERG angle $\sin^2\vartheta_\mathrm{W} \approx 0.231$ [3]. In this representation of the photon field A_μ, the electroweak couplings are related to the electromagnetic charge e by

$$g\sin\vartheta_\mathrm{W} = g'\cos\vartheta_\mathrm{W} = e . \tag{2.9}$$

The structure of strong interactions is more complicated. The local transformations for electroweak interactions are in one-dimensional space for the hypercharge Y and in two dimensions for the weak isospin. The fundamental characteristic of a fermion that causes the particle to participate in strong interactions is its color. Since there are three colors realized in Nature, the Lagrangian has to be invariant under local $\mathrm{SU}(3)_C$ transformations, where C refers to the term *color*. In the corresponding gauge theory, Quantumchromodynamics (QCD), eight fields, the gluons, are needed to preserve invariance.

The coupling strength of QCD exceeds the ones of electroweak theory considerably and hence the phenomenology of colored particles is nearly completely dominated by QCD. The strong binding among colored particles also leads to confinement, i.e. they cannot be freely observed but instantly form color neutral states. This process of hadronization is an important aspect at hadron colliders like the LHC.

2.1.2 Hierarchy and Fine Tuning in the Higgs Sector

Since any mass term for the bosons in the Lagrangian from Equation 2.2 would violate gauge invariance, the masses of the electroweak gauge bosons are predicted to vanish by pure electroweak theory. This is in contradiction to experimental observations, that measure masses in the order of 10^2 GeV for the $W^\pm$ and Z^0. In addition, the $\mathrm{SU}(2)_L$ transformations of Equation 2.4 violate invariance for any mass term

$$m_\Psi\left(\overline{\Psi}_L\Psi_R + \overline{\Psi}_R\Psi_L\right) . \tag{2.10}$$

The HIGGS mechanism [4–6] is a promising theory to explain the occurrence of massive gauge bosons and fermions under conservation of gauge invariance. Within this theory, the HIGGS boson is described by the potential

$$V = \mu^2\left|\Phi_H\right|^2 + \lambda\left|\Phi_H\right|^4 . \tag{2.11}$$

To guarantee a non-vanishing vacuum expectation value $V_{\text{min}} \neq 0$ at the minimum

$$\langle \Phi_H \rangle = \sqrt{\frac{-\mu^2}{2\lambda}} =: \frac{1}{\sqrt{2}} v \,, \tag{2.12}$$

the potential of Equation 2.11 must satisfy $\mu^2 < 0$ and $\lambda > 0$. Expanding the field Φ_H around the minimum v with

$$\Phi_H = \frac{1}{\sqrt{2}} \left[v + h(x) \right] \tag{2.13}$$

leads to electroweak symmetry breaking. This gives a massless photon and massive $W^{\pm}$, Z^0 and Higgs bosons with the masses

$$m_{W^{\pm}} = \frac{1}{2} v g \,, \qquad m_{Z^0} = \frac{1}{2} v \sqrt{g^2 + g'^2} \,, \qquad m_H = \sqrt{2 v^2 \lambda} \qquad \text{and} \qquad m_\gamma = 0 \,. \tag{2.14}$$

The Equations 2.14 also predict for the mass ratio of the Z^0 and $W^{\pm}$ bosons

$$\frac{m_{W^{\pm}}}{m_{Z^0}} = \frac{g}{\sqrt{g^2 + g'^2}} = \cos \vartheta_{\text{W}} \,, \tag{2.15}$$

which is in good agreement with the measured values.

In addition, a scalar field like the Higgs could restore unitarity in the scattering of longitudinally polarized massive $W^{\pm}$ bosons: The amplitude of this process diverges with increasing scattering energies and could be extenuated with an additional scalar particle that mediates the interaction [7–9]. If no other new physics phenomena retain unitarity in this process, the required Higgs mass has to be at the electroweak scale on the order of 10^2 GeV. This is also supported by indirect experimental constraints on the Higgs mass [10, 11] that prefer a mass below the TeV-scale. Indeed, recent observations at the LHC experiments suggest that there is a Higgs boson with a mass of about 125 GeV [12, 13]. Therefore, even though still not finally confirmed, the Higgs boson plays an important role in the SM.

The presence of a sub-TeV-mass scalar particle gives rise to the so-called hierarchy problem [14–16]. The mass scale for the Higgs boson, as given by the unitarity bounds in $WW \rightarrow WW$ scattering, is determined by the electroweak scale $M_{\text{ew}} = 10^2$ GeV. The bare mass of the Higgs, as given from the Higgs mechanism in Equation 2.14, $m_H^2 = 2v^2\lambda$, is subject to loop corrections from intermediate particles. Possible contributions from a single fermion or scalar loop are shown in Figure 2.2. For a fermion f that couples to the Higgs with $\lambda_f H \bar{f} f$, the correction is given by [17]

$$\Delta m_H^2 = -\frac{|\lambda_f|^2}{8\pi^2} \left[\Lambda^2 - 3 m_f^2 \ln \left(\frac{\Lambda}{m_f} \right) + \dots \right] \,, \tag{2.16}$$

whereas a scalar particle $\widetilde{f}$ that couples via $\lambda_{\widetilde{f}} |H|^2 |\widetilde{f}|^2$ contributes with [17]

$$\Delta m_H^2 = \frac{\lambda_{\widetilde{f}}}{16\pi^2} \left[\Lambda^2 - 2 m_{\widetilde{f}}^2 \ln \left(\frac{\Lambda}{m_{\widetilde{f}}} \right) + \dots \right] \,. \tag{2.17}$$

The energy Λ in these equations represents a cut-off scale where the mass corrections are not any longer correctly described by the SM. The limits of the SM are reached at the latest with the Planck scale $M_{\text{Planck}} = 10^{19}$ GeV, where the strength of gravity becomes comparable to the electroweak forces. To

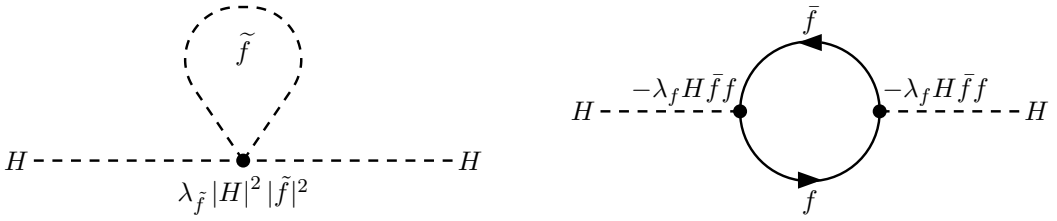

(A) Bosonic loop (B) Fermionic loop

FIGURE 2.2 Possible loop corrections to the mass of the HIGGS boson coming from scalar particles (A) or fermionic particles (B).

ensure a HIGGS mass at $M_{\text{ew}} \ll M_{\text{PLANCK}}$, there must be a very precise cancellation of the large corrections and the bare HIGGS mass $2v^2\lambda$ itself to obtain $m_H \approx M_{\text{ew}}$. This fine tuning appears unnatural, but finds a solution within SUSY: Since SUSY postulates two scalar fields for each fermion,[1] the quadratic divergences in Equations 2.16 and 2.17 exactly cancel out. Hence, the stability of the HIGGS mass with respect to the ultraviolet corrections is usually achieved in SUSY models.[2] Moreover, it can be shown that even higher order loop corrections to the HIGGS mass compensate [18–20]. This makes SUSY to a theoretically well motivated extension of the SM.

2.1.3 Unification of the Forces: GUT and TOE with Supersymmetry

One of the major achievements of the SM is the unification of the electromagnetic and the weak force. Prior to that, electromagnetism was embedded in the theoretical framework of quantum electrodynamics (QED) [21]. The weak force, which is responsible for the nuclear β decay, had been described by a four-fermion interaction in the FERMI model [22]. FERMI's model of weak interactions predicted a diverging cross section with increasing energy $\sigma \propto E^2$. This constrained the model's range of validity below the 10^2 GeV scale.

In the early 1960s, proposals were made to embed these two interactions in the formalism of a common electroweak theory [23–26]. This unification suggested that QED and weak interactions are both a low energetic approximation of the more general interactions of the $\text{SU}(2)_L \times \text{U}(1)_Y$ symmetry group, as described in Section 2.1.1. Beyond the photon γ, as carrier of the electromagnetic forces, it predicted the existence of charged and neutral weak currents, the $W^{\pm}$ and Z^0 bosons, all together mediating electroweak interactions.

In the years 1973 and 1974, the first indirect hints for this additional neutral Z^0 were found [27, 28] and about ten years later direct evidence for the existence of the $W^{\pm}$ [29, 30] and Z^0 [31, 32] could be seen. This unification involved a new free parameter in the theory: The mixing of the fundamental gauge bosons to the measurable mass eigenstates, which is parameterized by $\sin^2 \vartheta_{\text{W}}$ (see Equations 2.6 to 2.9). It could not be predicted by pure electroweak theory, but is predicted by SUSY to be $\sin^2 \vartheta_{\text{W}}(m_{Z^0}) = 0.2333 \pm 0.0008$ [33] if SUSY masses are below the TeV-scale. This is in outstanding agreement with the measurement of $\sin^2 \vartheta_{\text{W}}(m_{Z^0}) = 0.231\,16 \pm 0.000\,12$ [3].

The consolidation of two differently structured theories into a single model that gives the correct predictions in the domains of both unified theories is a theoretically very attractive development. Hence, it comes to no surprise that there have been attempts to include the $\text{SU}(3)_C$ group of strong interactions as

[1] The symmetry requires the same degrees of freedom for fermions and their superpartners and hence there is a scalar partner for f_L and f_R.

[2] Clearly, this already assumes $|\lambda_f|^2 = \lambda_{\tilde{f}}$ and sufficiently low SUSY masses.

well. The efforts to interpret electroweak and strong interactions as effective low energy approximations of a combined high energy theory are referred to as *grand unified theories* (GUTs) [34–36].

There are several proposals to incorporate SUSY models into a GUT [37, 38]. In either case, the unification of the fundamental gauge couplings of the SM is among the most compelling arguments that support SUSY. At currently accessible energies, the couplings are quite different, i.e. the strong interaction exceeds the strength of electroweak interactions considerably. However, a common symmetry group for all interactions in GUT would imply a single coupling of all forces at the energy scale of GUT.

In the field theory of the SM, the measured couplings are represented by superposition of Feynman diagrams to all orders of perturbation theory. In addition to tree level processes, there are diagrams including fermion loops in the boson propagator. These result in diverging contributions to the coupling of the interaction with increasing momentum transfer q^2. The divergence can be avoided by a renormalization of the coupling α at a momentum scale q^2 such that the infinite terms cancel out to all orders. This gives rise to energy dependent couplings of the three fundamental gauge groups. Within the SM, the extrapolation of the couplings to higher energies does not converge into a single combined coupling (as shown by the dashed lines in Figure 2.5(a) (p. 18) in Section 2.2.3).

If the additional field content of SUSY is assumed, the renormalization group running of the couplings is found to match rather accurately at about 10^{16} GeV [33, 39–41] (as displayed in the solid lines in Figure 2.5(a) in Section 2.2.3). Therefore, the SUSY field content predicts a unification of the couplings if SUSY is realized in Nature at the TeV scale. This is a promising hint that SUSY could be found at TeV colliders like the LHC.

Although there is no generally accepted GUT that could yet be confirmed experimentally, there are also efforts beyond the scope of GUT. These aim at the unification of gravity, the third known interaction, as well. This *theory of everything* (TOE) should consolidate the conceptual principles of gauge theories and general relativity in a conjoint quantum field theory. There are promising approaches to do so in supergravity theories [42–44], which are based on the principles of SUSY. Thereby, SUSY also provides a canonical link to gravity and hence might turn out to be a theoretical development towards a theory of unified interactions in a single model.

2.1.4 Particle Physics in Cosmology

Although the domains of cosmology are the large scale structures of the universe and their formation, there are several observations with an impact on particle physics. One of the most important is the indirect observation of *dark matter*. The measurement of rotational velocities in galaxies indicates that the gravity of the baryonic mass in galaxies is not sufficient to compensate for the centrifugal forces. Hence, additional mass is needed to stabilize these galaxies [45, 46]. The kinematic argument of missing mass is seen as well in the dynamics of galaxy clusters [47, 48] and there is also evidence for unseen matter in gravitational lensing [49, 50]. Furthermore, dark matter manifests itself as well on the cosmological scale. Global fits of the anisotropies in the cosmic microwave background hint at a substantial fraction of dark matter in the universe [51, 52]. Moreover, the simulation of the formation of large scale structures in the early universe supports the presence of dark matter [53–55].

The SM contains no particle that could be a candidate for dark matter. Since there has been no confirmed direct observation of dark matter so far, it is widely believed that only a purely weakly interacting particle could be a candidate. More precisely, it must at least interact gravitationally but might interact weakly as well. An electrically charged or colored particle with the measured dark matter density in the universe would have been observed already. The only purely weakly interacting particle in the SM is the neutrino. Simple model calculations show that the resulting relic density of the SM neutrinos result in an insufficiently low abundance to explain the observed amount of dark matter. Furthermore, their

extremely small masses are in contradiction to the preferred *cold dark matter* scenarios, which require more massive candidates [56, 57].

In SUSY theories, there could be a candidate for a massive but only weakly interacting particle. The stability of the proton motivates so-called R-*parity* conservation (see Section 2.2.2). It forbids a SUSY particle to decay into SM particles only. As a direct consequence, the lightest supersymmetric particle (LSP) must be stable. Since an electrically charged or colored stable SUSY particle would have been detected already,[3] the LSP should be only weakly interacting and therefore is a promising candidate to explain dark matter [58–60].

SUSY might also play a role in the interpretation of the *cosmological constant*. Observations of supernovae suggest an accelerated expansion of the universe [61, 62], which could be explained by a non-vanishing intrinsic energy density in the universe, the cosmological constant Λ [63]. From the viewpoint of quantum field theory, this could be interpreted as a vacuum energy. However, these approaches lead to predictions for Λ at very high energies, e.g. the PLANCK scale [64], which exceeds the measured one by many orders of magnitude. It can be shown that exact supersymmetric theories actually predict a vanishing cosmological constant [65], resembling the solution of the hierarchy problem. However, broken SUSY still predicts too large Λ but might be an explanation why the cosmological constant is below the PLANCK scale.

2.2 Minimal Supersymmetric Extension of the Standard Model

Since its primary proposal in the 1960s [66–70], SUSY [17, 71–74] persistently remained one of the foremost candidates for an extension of the SM. The questions related to the problems of the SM in Sections 2.1.2 to 2.1.4 already gave a brief glance to its structure, which is completed in the following. Given its long history of development, a complete description is beyond the scope of this thesis. After a short general definition of SUSY, this section concentrates on those aspects that are important for SUSY searches at the LHC. In the first instance, SUSY breaking and R-parity are explained. They motivate the search for decay chains of heavy SUSY particles with missing transverse energy final states. Moreover, the mass hierarchy among SUSY particles and their mixings are discussed. These are important for the search signatures of jets and tau leptons, respectively.

2.2.1 Fundamentals: Supertransformations and Particle Content

In general, symmetry denotes the invariance of a system's behaviour under a transformation. This is the case as long as the equations of motion of the given system remain unchanged. Particularly, if the action

$$S = \int \mathrm{d}x^4 \mathcal{L} \,, \tag{2.18}$$

does not alter, Equation 2.1 remains the same since it is derived by the variation of S by

$$\delta S \stackrel{!}{=} 0 \,. \tag{2.19}$$

For a given transformation T, the invariance is guaranteed if the Lagrangian $\mathcal{L}$ transforms as

$$T \;:\quad \mathcal{L} \to \mathcal{L}' = \mathcal{L} + \partial_\mu F^\mu \,. \tag{2.20}$$

[3] This assumes that SUSY particles have been produced in a sufficient abundance in the early hot universe.

The last term with the derivative vanishes in the action from Equation 2.18 using the Gauss divergence theorem.

Invariance might be postulated for very different transformations, e.g. the invariance under the space-time transformations of the Poincaré group are required by special relativity. A more general transformation can be written as

$$\Psi \to \Psi' = T\Psi = \exp\left(i \sum_{n=1}^{N} \alpha_n T_n\right) \Psi \,, \tag{2.21}$$

where T_n are the generators of the symmetry group and $\alpha_n \in \mathbb{R}$. SUSY denotes the invariance of a system if a boson is transformed into a fermion and vice versa. Hence, the generator $\mathcal{Q}$ of this group changes a fermionic state into a bosonic state and vice versa:

$$\mathcal{Q}\,|\text{fermion}\rangle = |\text{boson}\rangle \qquad \text{and} \qquad \mathcal{Q}\,|\text{boson}\rangle = |\text{fermion}\rangle \,. \tag{2.22}$$

This already requires the generator $\mathcal{Q}$ to be fermionic, otherwise it could not relate bosonic and fermionic states in the sense of Equation 2.22. The possible existence of such a symmetry and its theoretical constraints are postulated by the Coleman-Mandula theorem [75] and its supersymmetric specification by Haag, Lopuszanski and Sohnius [76]. In a theory with chiral fermions, the generators satisfy the set of (anti-)commutator equations [17]

$$\left\{\mathcal{Q}, \mathcal{Q}^\dagger\right\} = P^\mu \,, \qquad \left\{\mathcal{Q}^\dagger, \mathcal{Q}^\dagger\right\} = \{\mathcal{Q}, \mathcal{Q}\} = 0 \qquad \text{and} \qquad [P^\mu, \mathcal{Q}] = [\mathcal{Q}, P^\mu] = 0 \,. \tag{2.23}$$

The operators $\mathcal{Q}$ and $\mathcal{Q}^\dagger$ also commute with the generators of the gauge transformations. Therefore, particles and their superpartners have the same charge, weak isospin and color and participate in the same interactions. In a similar manner, the partners can be shown to have the same number of degrees of freedom and therefore differ only by spin.

Since there is no pair of a boson and a fermion in the SM that only differs by spin $1/2$, SUSY consequently at least doubles the number of particles. The minimal supersymmetric extension of the SM (MSSM) assumes no additional fields other than the superpartners to the known SM particles. Hence, it is minimal in the sense of field content. The naming convention for the new SUSY particles is as follows: The superpartners of the SM particles are labelled by a tilde above its symbol. Bosonic particle names are extended by the suffix *ino*, whereas to fermionic particle names an *s* is attached at the beginning.

The particle content of the MSSM can be seen in Table 2.1. Since particles and their superpartners have the same number of degrees of freedom, there are two superpartners for the charged leptons and the quarks for left- and right-chiral states. Thus, the sfermion indices R and L refer to the superpartner's chirality and not to spin, because sfermions are scalar particles. However, they participate in the same interactions, e.g. a $\widetilde{\ell}_R$ has weak isospin $I = 0$ and does not interact with the $W^\pm$, whereas the $\widetilde{\ell}_L$ with $I = 1/2$ does.

In addition, the Higgs sector needs an extension in supersymmetric theories. It can be shown that a single SM Higgs boson might cause triangle gauge anomalies [77] in SUSY, i.e. gauge invariance is violated by chiral loops in three-boson interaction. In the SM, these loops exactly cancel out if the contributions from its particle content are summed up. This guarantees anomaly freedom to all orders. The chiral Higgsino, i.e. the superpartner of the Higgs boson, extends the sum by an additional chiral field that leaves a finite contribution. This can be eliminated by the introduction of two chiral superfields with opposite hypercharge.

R-Parity$=+1$			R-Parity$=-1$		
Particle	Symbol	Spin	Particle	Symbol	Spin
Quark	q	$1/2$	Squark	$\widetilde{q}_L$, $\widetilde{q}_R$	0
Neutrino	ν_ℓ	$1/2$	Sneutrino	$\widetilde{\nu}_\ell$	0
Lepton	ℓ	$1/2$	Slepton	$\widetilde{\ell}_L$, $\widetilde{\ell}_R$	0
Gluon	g	1	Gluino	$\widetilde{g}$	$1/2$
Photon	γ	1	Photino	$\widetilde{\gamma}$	$1/2$
$W^\pm$ boson	$W^\pm$	1	Wino	$\widetilde{W}^\pm$	$1/2$
Z^0 boson	Z^0	1	Zino	$\widetilde{Z}^0$	$1/2$
Higgs	H_u^0 , H_u^+	0	fermionic	$\widetilde{H}_u^0$, $\widetilde{H}_u^+$	$1/2$
bosons	H_d^0 , H_d^-	0	Higgsino	$\widetilde{H}_d^0$, $\widetilde{H}_d^-$	$1/2$

Table 2.1 The field content of the minimal supersymmetric extension of the Standard Model. R-parity is described in Section 2.2.2

Furthermore, a single Higgs doublet can be proven to be insufficient to generate the masses of the SM quarks and leptons in the supersymmetric extension of the Yukawa couplings. The Yukawa coupling to up-type quarks is only possible for a Higgs with hypercharge $Y = 1$ (H_u), whereas down-type quarks require $Y = -1$ (H_d). Therefore, the two weak isospin states, $T_3 = \pm 1/2$, and the two hypercharge states, $Y = \pm 1$, add up to the four complex fields

$$H_u = \left(H_u^+ \,,\; H_u^0\right) \qquad \text{and} \qquad H_d = \left(H_d^0 \,,\; H_d^-\right) \,, \tag{2.24}$$

of which two are neutral and two are charged according to

$$Q = T_3 + \frac{Y}{2} \,. \tag{2.25}$$

In total, the four complex fields have eight degrees of freedom, where three of them are needed for the longitudinal states of the $W^\pm$ and Z^0. The remaining five states build two CP-even (h_0, H_0), one CP-odd (A_0) and two charged ($H^\pm$) Higgs-bosons [78].

At tree level, the masses of the neutral final states are related by [79]

$$m^2_{h_0,H_0} = \frac{1}{2}\left[\, m^2_{A_0} + m^2_{Z^0} \mp \underbrace{\sqrt{\left(m^2_{A_0} + m^2_{Z^0}\right)^2 - 4 m^2_{A_0} m^2_{Z^0} \sin^2 2\beta}}_{m^2_{A_0} - m^2_{Z^0} \,\leq\, [\ldots] \,\leq\, m^2_{A_0} + m^2_{Z^0}} \,\right] \,, \tag{2.26}$$

where

$$\tan\beta = \frac{\langle H_u^0 \rangle}{\langle H_d^0 \rangle} \tag{2.27}$$

is the ratio of the vacuum expectation values of the neutral fields from Equation 2.24. Equation 2.26 already implies $m_{h_0} < m_{Z^0}$ at tree level, which can be increased only by radiative corrections [80]. Due to their large Yukawa coupling, third generation loops have typically the biggest contribution [81].

2.2.2 Experimental Constraints: Supersymmetry Breaking and *R*-Parity

The last equality in Equation 2.23 has one of the most influential consequences for SUSY model building: The statement that a particle and its superpartner have equal mass in an exact SUSY. For a bosonic $|\Psi_b\rangle$ and a fermionic state $|\Psi_f\rangle$ that are related via Equation 2.22 and with the masses m_b and m_f, the following equalities hold:

$$\begin{aligned} m_b^2|\Psi_b\rangle &= P_\mu P^\mu|\Psi_b\rangle = P_\mu P^\mu \mathcal{Q}|\Psi_f\rangle = P_\mu \mathcal{Q} P^\mu|\Psi_f\rangle \\ &= \mathcal{Q} P_\mu P^\mu|\Psi_f\rangle = \mathcal{Q} m_f^2|\Psi_f\rangle = m_f^2 \mathcal{Q}|\Psi_f\rangle = m_f^2|\Psi_b\rangle \,. \end{aligned} \tag{2.28}$$

It follows that $m_f = m_b$ and hence particles and their superpartners must have equal mass. This is a very strict statement, which already suspends exact SUSY to be present in Nature. E.g. a light, electrically charged scalar particle, as the superpartner of the electron would be, should be easy to measure, but is not observed in Nature. Therefore, SUSY is usually supposed to be broken, i.e. a certain mechanism might generate different masses for particles and their superpartners. This would allow for higher masses of the non-SM SUSY partners. Still, the scale for the SUSY masses, in the following denoted as M_{susy}, is not arbitrary. The required solution of the hierarchy problem (see Section 2.1.2) and the unification of the SM interactions at a common GUT scale (see Section 2.1.3) already prefers low-mass SUSY partners, i.e.

$$M_{\text{susy}} \not\gtrsim 1\ \text{TeV} \,. \tag{2.29}$$

There are manifold possible mechanisms that explain the origin of this symmetry breaking, which give rise to a diversity of SUSY models [82]. Although all of these different SUSY theories underlie the same experimental constraints, the restrictions on SUSY models are not very tight at present times. This can be mostly attributed to the lack of experimental data in the high energy regime, where these theories gain importance.

Nevertheless, a phenomenological model can be constructed, without any particular assumption about the origin of SUSY breaking. This is accomplished by the introduction of explicit, soft supersymmetry breaking terms in the Lagrangian, where the breaking is communicated by some unspecified dynamics. The term *soft* refers to the fact that the mass scale has to fulfill the bounds from Equation 2.29 and the SUSY particles are protected against masses that exceed the expected limit.

The rather generic constitution of SUSY masses by explicit terms in the Lagrangian comes at the prize of numerous additional parameters that are not specified by the underlying theory. The SM itself has already various parameters, which are not inherently predicted by the theory. Among them are the particles' masses, the fundamental couplings of the $\mathrm{SU}(2)_L \times \mathrm{U}(1)_Y \times \mathrm{SU}(3)_C$ symmetry groups, angles and phases from the CKM matrix [83–85] and neutrino mixing [86–88], as well as the electroweak mixing angle and the Higgs mass. Adding explicit mass terms to the Lagrangian by

$$\mathcal{L}_{\text{susy}} = \mathcal{L}_{\text{interaction}} + \mathcal{L}_{\text{soft}} \tag{2.30}$$

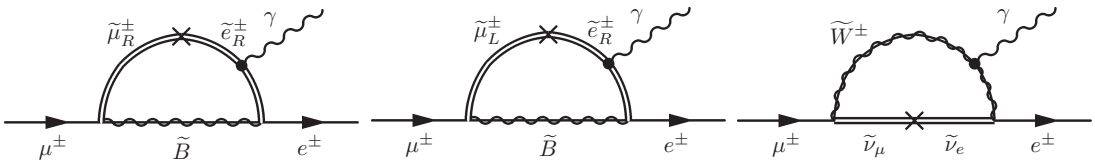

FIGURE 2.3 Lepton flavour violating SUSY loops in the process $\mu \to e\gamma$.

vastly expands the list of parameters. The first term includes the interactions of the (SUSY) particles, whereas the second generates the masses. The soft supersymmetry breaking terms are [71]

$$\begin{aligned}
\mathcal{L}_{\text{soft}} = & \underbrace{-\frac{1}{2}\left(M_3\widetilde{g}^{\alpha}\cdot\widetilde{g}_{\alpha} + M_2\widetilde{W}^{\beta}\cdot\widetilde{W}_{\beta} + M_1\widetilde{B}\cdot\widetilde{B} + \text{h.c.}\right)}_{\text{gaugino masses}} && \alpha\in\{1,\ldots,8\} \quad \beta\in\{1,2,3\} \\
& \underbrace{-\left(\mathbf{m}^2_{\widetilde{Q}}\right)_{ij}\widetilde{Q}_i^{\dagger}\cdot\widetilde{Q}_j - \left(\mathbf{m}^2_{\widetilde{u}}\right)_{ij}\widetilde{\overline{u}}_i^{\dagger}\widetilde{\overline{u}}_j - \left(\mathbf{m}^2_{\widetilde{d}}\right)_{ij}\widetilde{\overline{d}}_i^{\dagger}\widetilde{\overline{d}}_j}_{\text{squark masses}} && i,j\in\{1,2,3\} \\
& \underbrace{-\left(\mathbf{m}^2_{\widetilde{L}}\right)_{ij}\widetilde{L}_i^{\dagger}\cdot\widetilde{L}_j - \left(\mathbf{m}^2_{\widetilde{e}}\right)_{ij}\widetilde{\overline{e}}_i^{\dagger}\widetilde{\overline{e}}_j}_{\text{slepton masses}} && i,j\in\{1,2,3\} \\
& \underbrace{-(\mathbf{a}_u)^{ij}\widetilde{\overline{u}}_i\widetilde{Q}_j\cdot H_u + (\mathbf{a}_d)^{ij}\widetilde{\overline{d}}_i\widetilde{Q}_j\cdot H_d + (\mathbf{a}_e)^{ij}\widetilde{\overline{e}}_i\widetilde{L}_j\cdot H_d + \text{h.c.}}_{\text{trilinear couplings}} && i,j\in\{1,2,3\} \\
& \underbrace{-m^2_{H_u}H_u^{\dagger}\cdot H_u - m^2_{H_d}H_d^{\dagger}\cdot H_d - (bH_u\cdot H_d + \text{h.c.})}_{\text{HIGGS masses}}\,, && (2.31)
\end{aligned}$$

where the content of the supermultiplets $\widetilde{Q}$, $\widetilde{L}$, $\widetilde{\overline{u}}$, $\widetilde{\overline{d}}$, $\widetilde{\overline{e}}$, H_u and H_d are described in Table 2.2. With this SUSY breaking, the masses of SUSY particles are no longer generated by the HIGGS mechanism as the masses of their SM partners. SUSY masses are described by explicit mass terms of the form $m^2_{\Phi}\Phi_{\mu}\Phi^{\mu}$. The index α enumerates the eight superpartners of the gluons, β the three superpartners of the W^k fields and i and j are family indices. In this approach, the five complex mass matrices for the sfermions, the matrices $\mathbf{a}_{u,d,e}$ and the six mass parameters for the gaugino and HIGGS-fields introduce more than 100 new parameters that are unspecified by the theory [89].

However, the choice of parameters is by no means arbitrary. Off-diagonal elements in $\mathbf{m}^2_{\widetilde{e}}$ might cause mixing terms between different sleptons, e.g. between $\widetilde{e}_R$ and $\widetilde{\mu}_R$. This would violate flavour conservation in the slepton sector, which could be propagated to the lepton sector by virtual sparticle loops. An example is displayed in Figure 2.3, which shows SUSY loop contributions to the process $\mu \to e\gamma$. Furthermore, there are several experimental constraints from lepton flavour conservation with implications for SUSY, e.g. [90–94].

particles		spin-0	spin-1/2	B	L	
Quarks & Squarks	$\widetilde{Q}$	$\widetilde{u}_L\ \widetilde{d}_L$	$u_L\ d_L$	$1/3$	–	$\times$ 3 families
	$\widetilde{\bar{u}}$	$\widetilde{\bar{u}}_R$	$\bar{u}_R$	$-1/3$	–	
	$\widetilde{\bar{d}}$	$\widetilde{\bar{d}}_R$	$\bar{d}_R$	$-1/3$	–	
Leptons & Sleptons	$\widetilde{L}$	$\widetilde{\nu}\ \widetilde{e}_L$	$\nu\ e_L$	–	1	$\times$ 3 families
	$\widetilde{\bar{e}}$	$\widetilde{\bar{e}}_R$	$\bar{e}_R$	–	-1	
Higgs & Higgsinos	H_u	$\widetilde{H}_u^+\ \widetilde{H}_u^0$	$H_u^+\ H_u^0$	–	–	
	H_d	$\widetilde{H}_d^0\ \widetilde{H}_d^-$	$H_d^-\ H_d^0$	–	–	

Table 2.2 The particle content of the supermultiplets in the minimal extension of the Standard Model and their baryon and lepton numbers.

In addition to the soft breaking terms in the Lagrangian of Equation 2.30, there are also interaction terms including gauge and non-gauge interactions, i.e. Yukawa couplings of the supermultiplets. In the MSSM, the Yukawa couplings are described by the superpotential, which is given by [17]

$$W_{\text{MSSM}} = \widetilde{\bar{u}}\mathbf{y_u}\widetilde{Q}H_u - \widetilde{\bar{d}}\mathbf{y_d}\widetilde{Q}H_d - \widetilde{\bar{e}}\mathbf{y_e}\widetilde{L}H_d + \mu H_u H_d\,. \tag{2.32}$$

The matrices $\mathbf{y}$ are dimensionless and in three dimensional family space. Equation 2.32 is not the most general allowed form for these interactions. There are more possible terms that preserve gauge invariance, among them lepton and baryon number violating terms like [95]

$$W_{\Delta L=1} = \frac{1}{2}\lambda_{ijk}\widetilde{L}^i\widetilde{L}^j\widetilde{\bar{e}}^k + \lambda'_{ijk}\widetilde{L}^i\widetilde{Q}^j\widetilde{\bar{d}}^k + \mu'_i\widetilde{L}^i H_u \quad \text{and} \tag{2.33}$$

$$W_{\Delta B=1} = \frac{1}{2}\lambda''_{ijk}\widetilde{\bar{u}}^i\widetilde{\bar{d}}^j\widetilde{\bar{d}}^k\,, \tag{2.34}$$

where i, j and k are family indices. If these terms are not suppressed in Nature, lepton and baryon number violating processes could be caused by intermediate SUSY particles states. The most prominent example is the proton decay [96, 97]. It could be realized with the couplings from Equations 2.33 and 2.34 as shown in Figure 2.4. Since the proton's lifetime can be measured to be longer than 10^{29} years [3], at least one of the two couplings in Figure 2.4 must be strongly suppressed. Beyond the stability of the proton, there are further constraints on possible violations of lepton and baryon number in supersymmetric processes [98–101].

The lepton and baryon number violating processes can be avoided by the introduction of R-parity conservation [102, 103]. It is a multiplicative quantum number defined by

$$R = (-1)^{3B+2S+L}\,, \tag{2.35}$$

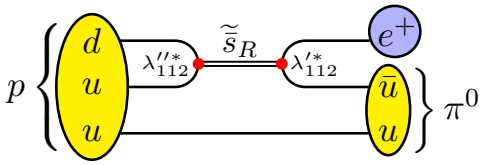

FIGURE 2.4 Possible decay of the proton via an intermediate $\widetilde{\bar{s}}_R$ into a positron and a neutral pion.

where S, B and L are the spin, baryon and lepton number, respectively, as given in Table 2.2. Assuming R-parity conservation, the first coupling in Figure 2.4 cannot take place since

$$R(u) \cdot R(d) = (-1)^{1+1+0} \cdot (-1)^{1+1+0} = +1 \neq -1 = (-1)^{-1+0+0} = R\left(\widetilde{\bar{s}}\right) \tag{2.36}$$

and the stability of the proton is restored by R-parity conservation. There are also other mechanisms that stabilize the proton in SUSY theories beyond R-parity [104].

Following Equation 2.35, the SM particles and their supersymmetric partners always differ by a factor -1 in R-parity since SUSY transformations change their spin by $1/2$, as already noted in Table 2.1. The assumption of R-parity conservation has strong phenomenological consequences for SUSY. Since SUSY particles carry $R = -1$, there must be an even number of SUSY particles at each interaction vertex. Particularly, a SUSY particle cannot decay into only SM particles and hence the lightest SUSY particle must be stable. This already provided a dark matter candidate as noted in Section 2.1.4. Moreover, it was also argued that this LSP should only be weakly interacting, if at all, since it would have been already observed otherwise.[4] A purely weakly interacting, stable and massive SUSY particle does not only provide a candidate for dark matter. It also has strong impact on the appearance of SUSY at collider experiments, as will be shown in Section 2.3.

Within this work, only R-parity conserving SUSY models will be considered. Models that allow for R-parity violation are also under investigation [95, 105–107], but demand for other experimental strategies and hence are not discussed here.

2.2.3 Theoretical Implications: Couplings, Masses and Mixings

Besides the experimental restrictions on the parameters in Equation 2.31, there are also theoretical considerations with consequences for the SUSY masses at the TeV-scale. The mass hierarchy among the SUSY particles will have a huge impact on the collider phenomenology and hence is explained in more detail in the following. Moreover, the masses and couplings among SUSY particles are largely affected by sparticle mixings, which are described subsequently.

The particle masses and couplings in SUSY have a momentum scale dependence that is given by the renormalization group equations (RGEs) [108, 109]. It was already mentioned in Section 2.1.3 that the unification of the gauge couplings can be achieved with the additional SUSY field content. The running of these couplings at one-loop level is described by [17]

$$\frac{\mathrm{d}}{\mathrm{d}t} g_a = \frac{1}{16\pi^2} b_a g_a^3 \quad \text{where} \quad \begin{pmatrix} b_1 & b_2 & b_3 \end{pmatrix} = \begin{cases} \begin{pmatrix} 41/10 & -19/6 & -7 \end{pmatrix} & \text{Standard Model} \\ \begin{pmatrix} 33/5 & 1 & -3 \end{pmatrix} & \text{MSSM.} \end{cases} \tag{2.37}$$

[4] Strictly speaking, an undetected LSP should be colorless and electrically neutral but does not necessarily interact weakly. In GMSB, the LSP is a gravitino, which does not even participate in weak interactions.

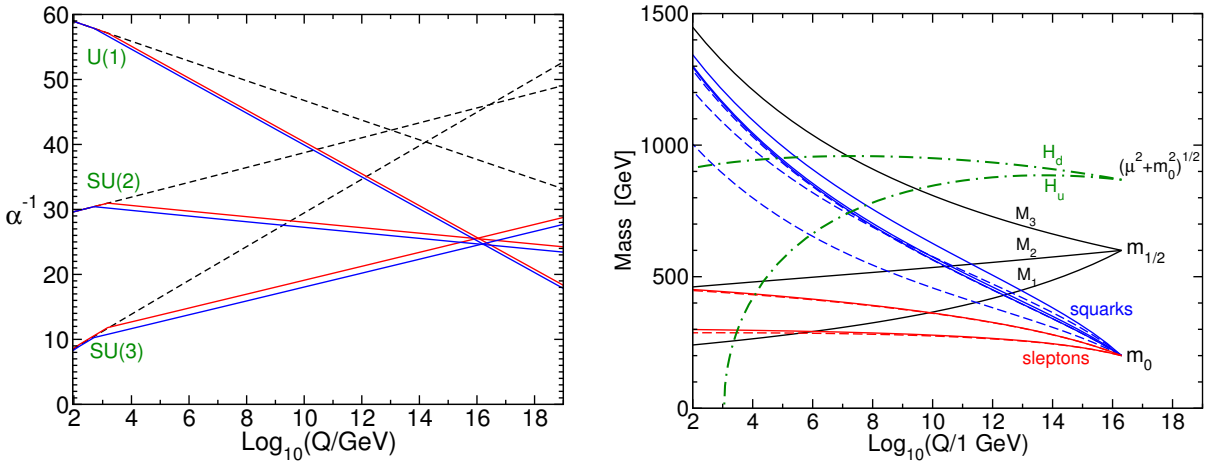

(A) Running gauge couplings (B) Running SUSY masses

Figure 2.5 (A): The running coupling constants of the three gauge groups in the Standard Model (dashed line) and in the minimal supersymmetric extension of the Standard Model for common sparticle masses at 500 GeV *(blue) and* 1.5 TeV *(red). (B): The running SUSY masses in a mSUGRA scenario. Graphics are taken from [17].*

Here, $t = \ln(Q/Q_0)$, Q is the renormalization scale and Q_0 a reference scale. The couplings g_a are connected to the fundamental gauge couplings g and g' from Equation 2.2 and to g_s from strong interactions by

$$g_1 = \sqrt{\frac{5}{3}}\,g' \qquad g_2 = g \qquad g_3 = g_s \qquad \text{and} \qquad \alpha_a := \frac{g_a^2}{4\pi}\,. \tag{2.38}$$

The factor $\sqrt{5/3}$ for g' is needed for a proper normalization of the couplings [71, 110].[5] The reciprocal quantity α_a^{-1} then fulfills

$$\begin{aligned}\frac{\mathrm{d}}{\mathrm{d}t}\alpha_a^{-1} &= \frac{\mathrm{d}}{\mathrm{d}t}\frac{4\pi}{g_a^2} = 4\pi\frac{\mathrm{d}}{\mathrm{d}t}\frac{g_a}{g_a^3} = 4\pi\left(\frac{1}{g_a^3}\frac{\mathrm{d}}{\mathrm{d}t}g_a + g_a\frac{\mathrm{d}}{\mathrm{d}t}\frac{1}{g_a^3}\right) = 4\pi\left(\frac{1}{g_a^3}\frac{\mathrm{d}}{\mathrm{d}t}g_a - 3g_a\frac{1}{g_a^4}\frac{\mathrm{d}}{\mathrm{d}t}g_a\right)\\ &= 4\pi\left(\frac{1}{g_a^3}\frac{\mathrm{d}}{\mathrm{d}t}g_a - 3\frac{1}{g_a^3}\frac{\mathrm{d}}{\mathrm{d}t}g_a\right) = -8\pi\left(\frac{1}{g_a^3}\frac{\mathrm{d}}{\mathrm{d}t}g_a\right) = -\frac{b_a}{2\pi} = \text{const}\,,\end{aligned} \tag{2.39}$$

where Equation 2.37 has been used in the last equality. Therefore, α_a^{-1} has linear dependence on the logarithmic renormalization scale t, as can be seen in Figure 2.5(A). Whereas there is no common intersection in the SM (dashed lines), the gauge couplings unify at about 10^{16} GeV due to different field content and hence different b_a in SUSY [33, 39–41]. The two colored lines for SUSY depict the evolution for common SUSY particle masses of 500 GeV (blue) and 1.5 TeV (red).

The matching gauge couplings at about 10^{16} GeV can be interpreted as a possible unification of the SM interactions in a common gauge group. Following this interpretation, it appears natural to unify the

[5] This factor depends on the chosen symmetry group in which the gauge interactions are unified. The used one results from the embedding of the SM $\mathrm{U}(1)_Y \times \mathrm{SU}(2)_L \times \mathrm{SU}(3)_C \subseteq \mathrm{SU}(5)$ [111].

masses of the SUSY fermions and bosons as well to a common fermionic ($m_{1/2}$) and bosonic mass (m_0) at the GUT scale, where

$$\left.\begin{array}{l} g_1 = g_2 = g_3 = g_U \\ M_1 = M_2 = M_3 = m_{1/2} \\ \mathbf{m}^2_{\widetilde{Q}} = \mathbf{m}^2_{\widetilde{\bar{u}}} = \mathbf{m}^2_{\widetilde{\bar{d}}} = \mathbf{m}^2_{\widetilde{\bar{e}}} = \mathbf{m}^2_{\widetilde{L}} = m_0^2 \mathbb{1} \end{array}\right\} \quad \text{at} \quad Q = M_{\text{GUT}} \approx 10^{16}\,\text{GeV} \tag{2.40}$$

holds. These unified parameters evolve with Q^2 according to the RGEs and thereby split up to their measurable low-energy values. Similarly to Equation 2.37, the first-order running of the gaugino mass parameters M_a can be expressed by [17]

$$\frac{\mathrm{d}}{\mathrm{d}t} M_a = \frac{1}{8\pi^2} b_a g_a^2 M_a \qquad \text{where} \qquad b_a = \begin{cases} {}^{33}/_5 & \text{for} \quad a = 1 \\ 1 & \text{for} \quad a = 2 \\ -3 & \text{for} \quad a = 3\,. \end{cases} \tag{2.41}$$

This leads to scale dependent gaugino mass parameters M_1, M_2 and M_3 in Equation 2.31. The running of the gauge couplings and their corresponding gaugino mass parameters lead to a striking relation for their ratio:

$$\begin{aligned} \frac{\mathrm{d}}{\mathrm{d}t}\frac{M_a}{g_a^2} &= \frac{1}{g_a^2}\frac{\mathrm{d}}{\mathrm{d}t} M_a + M_a \frac{\mathrm{d}}{\mathrm{d}t}\frac{1}{g_a^2} = \frac{1}{g_a^2}\frac{1}{8\pi^2} b_a g_a^2 M_a + \frac{M_a}{4\pi}\frac{\mathrm{d}}{\mathrm{d}t}\frac{1}{\alpha_a} \\ &= \frac{b_a M_a}{8\pi^2} - \frac{M_a}{4\pi}\frac{b_a}{2\pi} = 0\,. \end{aligned} \tag{2.42}$$

Here, Equations 2.41 and 2.38 have been used in the second equality and Equation 2.39 in the third step. The vanishing derivative shows that the ratio is independent of the considered scale. Assuming the unification at the GUT scale from Equation 2.40, the ratio of each gaugino mass parameter to the corresponding squared gauge coupling is equal for all three gauge groups. Hence,

$$\frac{M_1}{g_1^2} = \frac{M_2}{g_2^2} = \frac{M_3}{g_3^2} = \frac{m_{1/2}}{g_U} \qquad \text{or} \qquad M_3 = \frac{\alpha_\text{s}}{\alpha_\text{em}} \sin^2\vartheta_\text{W} M_2 = \frac{3}{5}\frac{\alpha_\text{s}}{\alpha_\text{em}} \cos^2\vartheta_\text{W} M_1 \tag{2.43}$$

holds at all scales. In the second part of Equation 2.43, the Equations 2.9 and 2.38 have been used to express the gauge couplings in terms of the electromagnetic fine structure constant α_em. This gives an approximate proportionality among the mass parameters of

$$M_3 \;:\; M_2 \;:\; M_1 \approx 6 \;:\; 2 \;:\; 1\,. \tag{2.44}$$

The physical gluino mass heavily depends on the mass parameter M_3 by [112]

$$m_{\tilde{g}} = M_3 \left(1 + \frac{\alpha_\text{s}}{4\pi}\left[15 + 6\ln\left\{\frac{Q}{M_3}\right\} + \ldots\right]\right)\,. \tag{2.45}$$

Due to the strong coupling of QCD at the electroweak scale, M_3 has to increase considerably more than the bino and wino mass parameters, when going from GUT to electroweak scale, in order to fulfill Equation 2.43. Hence, the gluino is typically the heaviest SUSY particle.

Similarly, there are RGEs for all scalars from the supermultiplets $\widetilde{Q}$, $\widetilde{L}$, $\widetilde{\bar{u}}$, $\widetilde{\bar{d}}$, $\widetilde{\bar{e}}$. They split up from the common m_0 at GUT scale to the squark and slepton masses at the TeV scale. Figure 2.5(B) shows an

example for the running masses. It displays the sfermion masses and gaugino and Higgs mass parameters as a function of logarithmic momentum scale Q. In this plot, a mSUGRA model [113–115] with the five parameters

$$m_0 = 200\,\text{GeV} \quad m_{1/2} = 600\,\text{GeV} \quad A_0 = -600\,\text{GeV} \quad \tan\beta = 10 \quad \text{and} \quad \operatorname{sgn}\mu = + \tag{2.46}$$

is used. The masses m_0 and $m_{1/2}$ are defined in Equation 2.40, A_0 is the common trilinear coupling (explained in Equation 2.55), $\tan\beta$ is the ratio of the two Higgs doublets' vacuum expectation values (see Equation 2.27) and μ is the Higgs mass parameter from Equation 2.32. The evolution of the masses leads to a sparticle mass spectrum at the TeV scale with

$$m_{\tilde{g}} > m_{\tilde{q}} > M_2 > m_{\tilde{\ell}} > M_1\,. \tag{2.47}$$

The mass hierarchy among the SUSY particles has a large impact on the expected phenomenology, as will be explained in Section 2.3.

Another theoretical aspect of SUSY is related to the mixing of sparticle states. In Section 2.2.1, it was already mentioned that the Higgs sector in SUSY needs to be extended to four Higgs fields. Together with the fields from Equations 2.6 to 2.8 (p. 7) and those of Equation 2.24 (p. 13), there are eight bosonic fields, each having a superpartner:

$$\begin{array}{lcccccccc} & \overbrace{\qquad\qquad\qquad\qquad}^{R\text{-parity}=+1} & & & & \overbrace{\qquad\qquad\qquad\qquad}^{R\text{-parity}=-1} & & & \\ \text{charged:} & W^+ & W^- & H_u^+ & H_d^- & \widetilde{W}^+ & \widetilde{W}^- & \widetilde{H}_u^+ & \widetilde{H}_d^- \\ \text{neutral:} & B & W^3 & H_u^0 & H_d^0 & \widetilde{B} & \widetilde{W}^3 & \widetilde{H}_u^0 & \widetilde{H}_d^0 \end{array} \tag{2.48}$$

In general, the neutral fields of the SM partners can interfere and manifest themselves as four mixed mass eigenstates $\widetilde{\chi}_i^0$, the so-called *neutralinos* [116]. In the basis of the neutral bino, wino and Higgsino fields, this is described by the mass matrix

$$\mathbf{M}_{\widetilde{\chi}^0} = \begin{pmatrix} M_1 & 0 & -\,\mathrm{c}_\beta\,\mathrm{s}_{\vartheta_\mathrm{W}}\,m_Z & \mathrm{s}_\beta\,\mathrm{s}_{\vartheta_\mathrm{W}}\,m_Z \\ 0 & M_2 & \mathrm{c}_\beta\,\mathrm{c}_{\vartheta_\mathrm{W}}\,m_Z & -\,\mathrm{s}_\beta\,\mathrm{c}_{\vartheta_\mathrm{W}}\,m_Z \\ -\,\mathrm{c}_\beta\,\mathrm{s}_{\vartheta_\mathrm{W}}\,m_Z & \mathrm{c}_\beta\,\mathrm{c}_{\vartheta_\mathrm{W}}\,m_Z & 0 & -\mu \\ \mathrm{s}_\beta\,\mathrm{s}_{\vartheta_\mathrm{W}}\,m_Z & -\,\mathrm{s}_\beta\,\mathrm{c}_{\vartheta_\mathrm{W}}\,m_Z & -\mu & 0 \end{pmatrix} \tag{2.49}$$

$$\text{with} \quad \mathrm{c}_{\vartheta_\mathrm{W}} = \cos\vartheta_\mathrm{W}\,, \quad \mathrm{s}_{\vartheta_\mathrm{W}} = \sin\vartheta_\mathrm{W}\,, \quad \mathrm{c}_\beta = \cos\beta \quad \text{and} \quad \mathrm{s}_\beta = \sin\beta\,. \tag{2.50}$$

M_1 and M_2 are the bino and wino mass parameters from Equation 2.31, μ is the Higgsino mass parameter from Equation 2.32 and $\tan\beta$ is the ratio of the vacuum expectation values of the two neutral Higgs-bosons from Equation 2.27. The four parameters reduce to three if Equation 2.43 is assumed. Since $\mathbf{M}_{\widetilde{\chi}^0}$ is symmetric, it can be diagonalized by a single unitary matrix $\mathbf{N}_{\widetilde{\chi}^0}$, which rotates the bino-, wino- and Higgsino basis into the pure neutralino states:

$$\begin{pmatrix} \widetilde{\chi}_1^0 \\ \widetilde{\chi}_2^0 \\ \widetilde{\chi}_3^0 \\ \widetilde{\chi}_4^0 \end{pmatrix} = \mathbf{N}_{\widetilde{\chi}^0} \begin{pmatrix} \widetilde{B} \\ \widetilde{W}^0 \\ \widetilde{H}_d^0 \\ \widetilde{H}_u^0 \end{pmatrix} = \begin{pmatrix} N_{11}^0 & N_{12}^0 & N_{13}^0 & N_{14}^0 \\ N_{21}^0 & N_{22}^0 & N_{23}^0 & N_{24}^0 \\ N_{31}^0 & N_{32}^0 & N_{33}^0 & N_{34}^0 \\ N_{41}^0 & N_{42}^0 & N_{43}^0 & N_{44}^0 \end{pmatrix} \begin{pmatrix} \widetilde{B} \\ \widetilde{W}^0 \\ \widetilde{H}_d^0 \\ \widetilde{H}_u^0 \end{pmatrix}\,. \tag{2.51}$$

The matrix Equation 2.51 determines the contributions from the bino-, wino- and Higgsino fields to the measurable mass eigenstates, i.e. the neutralinos. Their masses are given in terms of the mass parameters in $\mathbf{M}_{\tilde{\chi}^0}$ by

$$\left[\mathbf{N}^*_{\tilde{\chi}^0}\mathbf{M}_{\tilde{\chi}^0}\mathbf{N}^\dagger_{\tilde{\chi}^0}\right]_{ij} = m_{\tilde{\chi}^0_i}\delta_{ij}\ . \tag{2.52}$$

In the same way, the charged fields that carry the same quantum numbers can mix to the four mass eigenstates $\widetilde{\chi}^\pm_k$, the *charginos* [117]. Their mass matrix is given by

$$\mathbf{M}_{\tilde{\chi}^\pm} = \begin{pmatrix} 0 & 0 & M_2 & \sqrt{2}\cos\beta m_W \\ 0 & 0 & \sqrt{2}\sin\beta m_W & \mu \\ M_2 & \sqrt{2}\sin\beta m_W & 0 & 0 \\ \sqrt{2}\cos\beta m_W & \mu & 0 & 0 \end{pmatrix}\ . \tag{2.53}$$

The non-symmetric form of the block matrices in Equation 2.53 requires two unitary transformations in order to rotate the matrices into the mass eigenstates, solutions can be found in [118, 119]. In addition, the two matrices have different form and hence mixing can be different in the positively and negatively charged chargino sector [120]. However, since the matrices are transposed to each other, they have the same eigenvalues and hence the masses of positive and negative $\widetilde{\chi}^\pm_i$ are degenerate.

The SUSY partners of the fermions are also subject to mixings. The superpotential (Equation 2.32) allows for couplings of $\widetilde{f}_L$ and $\widetilde{f}_R$ with the Higgs fields. For instance, the supermultiplets in the term $\widetilde{\bar{u}}\mathbf{y_u}\widetilde{Q}H_u$ contain superpartners to left- and right-chiral particles, see Table 2.2. Since particles and their superpartners have the same Yukawa coupling, the mixing is expected to be dominated by third generation sfermions and hence the approximations

$$\mathbf{y}_u = \begin{pmatrix} 0 & 0 & 0 \\ 0 & 0 & 0 \\ 0 & 0 & y_t \end{pmatrix} \qquad \mathbf{y}_d = \begin{pmatrix} 0 & 0 & 0 \\ 0 & 0 & 0 \\ 0 & 0 & y_b \end{pmatrix} \qquad \mathbf{y}_e = \begin{pmatrix} 0 & 0 & 0 \\ 0 & 0 & 0 \\ 0 & 0 & y_\tau \end{pmatrix} \tag{2.54}$$

hold. The trilinear couplings in the soft SUSY breaking Lagrangian in Equation 2.31 also contribute to the mixing between the superpartners of left- and right-chiral fields. It has been argued that experimental constraints already exclude SUSY with large mixing between different flavour sleptons. So, whatever the cause of SUSY breaking might be, there should be a natural suppression of the flavour mixing terms. A frequently made assumption is that the trilinear couplings from Equation 2.31 are proportional to the Yukawa couplings:

$$\mathbf{a}_u = A_0\mathbf{y}_u \qquad \mathbf{a}_d = A_0\mathbf{y}_d \qquad \text{and} \qquad \mathbf{a}_e = A_0\mathbf{y}_e\ . \tag{2.55}$$

This suppresses flavour mixings if Equations 2.54 are assumed. Therefore, also L-R mixing is expected predominantly in the $\widetilde{t}$, $\widetilde{b}$ and $\widetilde{\tau}$ sector. Figure 2.6 shows possible Feynman diagrams for the mixings.

The possible mixing terms between the $\widetilde{f}_L$ and $\widetilde{f}_R$ fields in the Lagrangian can be written as

$$\mathcal{L}_{m_{\widetilde{f}}} = -\begin{pmatrix}\widetilde{f}^*_L & \widetilde{f}^*_R\end{pmatrix}\mathbf{M}^2_{\widetilde{f}}\begin{pmatrix}\widetilde{f}_L \\ \widetilde{f}_R\end{pmatrix}\ , \tag{2.56}$$

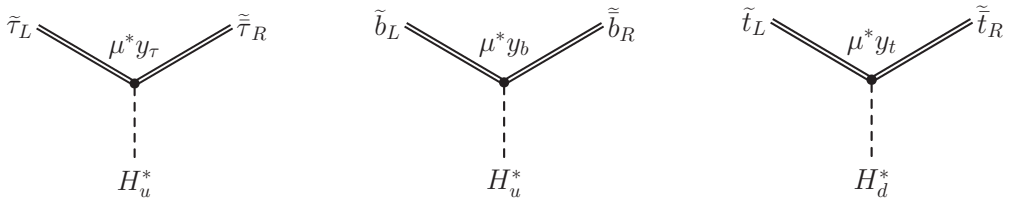

(A) $\mu^* \widetilde{\bar{\tau}} y_\tau \widetilde{\tau} H_u^{0*}$ (B) $\mu^* \widetilde{\bar{b}} y_b \widetilde{b} H_u^{0*}$ (C) $\mu^* \widetilde{\bar{t}} y_t \widetilde{t} H_d^{0*}$

Figure 2.6 Possible mixings between R and L fields in the (A) $\widetilde{\tau}$, (B) $\widetilde{b}$ and (C) $\widetilde{t}$ sector.

where the off-diagonal elements in the matrix $\mathbf{M}^2_{\widetilde{f}}$ allow for mixing of $\widetilde{f}_L$ and $\widetilde{f}_R$. In the case of staus, the matrix is given by [71]

$$\mathbf{M}^2_{\widetilde{\tau}} = \begin{pmatrix} m^2_{\widetilde{\tau}_L} + m^2_\tau + \Delta_L & m_\tau \left(A_0 - \mu \tan\beta\right) \\ m_\tau \left(A_0 - \mu \tan\beta\right) & m^2_{\widetilde{\tau}_R} + m^2_\tau + \Delta_R \end{pmatrix} , \tag{2.57}$$

where A_0 is the common trilinear coupling from Equation 2.55,

$$\Delta_L = \left(-\frac{1}{2} + \sin^2\vartheta_\mathrm{W}\right) m_Z^2 \cos 2\beta \qquad \text{and} \qquad \Delta_R = \frac{1}{3}\sin^2\vartheta_\mathrm{W} m_Z^2 \cos 2\beta \,. \tag{2.58}$$

The off-diagonal elements from the mass matrix in Equation 2.57 are proportional to $\tan\beta$ and hence the mixing is sensitive to the ratio from Equation 2.27. The mixture of the fundamental fields $\widetilde{\tau}_R$ and $\widetilde{\tau}_L$ to the measurable mass eigenstates $\widetilde{\tau}_1$ and $\widetilde{\tau}_2$ is obtained by diagonalization of the symmetric matrix from Equation 2.57 with a unitary matrix $\mathbf{N}_{\tilde{\tau}}$

$$\begin{pmatrix} m^2_{\widetilde{\tau}_1} & 0 \\ 0 & m^2_{\widetilde{\tau}_2} \end{pmatrix} = \mathbf{N}_{\tilde{\tau}} \mathbf{M}^2_{\widetilde{\tau}} \mathbf{N}^T_{\tilde{\tau}} \,, \qquad \text{where} \qquad \mathbf{N}_{\tilde{\tau}} = \begin{pmatrix} \cos\vartheta_{\tilde{\tau}} & \sin\vartheta_{\tilde{\tau}} \\ -\sin\vartheta_{\tilde{\tau}} & \cos\vartheta_{\tilde{\tau}} \end{pmatrix} . \tag{2.59}$$

Since the mixing takes place in two-dimensional isospin space, the representation of the mass eigenstates

$$\begin{pmatrix} \widetilde{\tau}_1 \\ \widetilde{\tau}_2 \end{pmatrix} = \mathbf{N}_{\tilde{\tau}} \begin{pmatrix} \widetilde{\tau}_R \\ \widetilde{\tau}_L \end{pmatrix} \tag{2.60}$$

can be parameterized by a single angle $\vartheta_{\tilde{\tau}}$. Due to this mixing, the masses $m_{\tilde{\tau}_L}$ and $m_{\tilde{\tau}_R}$ are shifted to $m_{\tilde{\tau}_1}$ and $m_{\tilde{\tau}_2}$. In many SUSY models, this results in one rather light stau compared to the lighter smuon or selectron. The same formalism can be applied to the $\widetilde{b}$ and especially the $\widetilde{t}$ sector [121], which might lead to a very light $\widetilde{t}_1$. The $\widetilde{t}$ mixing is described by the matrix

$$\mathbf{M}^2_{\widetilde{t}} = \begin{pmatrix} m^2_{\widetilde{t}_L} + m^2_t + \Delta_L & m_t \left(A_0 - \mu \cot\beta\right) \\ m_t \left(A_0 - \mu \cot\beta\right) & m^2_{\widetilde{t}_R} + m^2_t + \Delta_R \end{pmatrix} \qquad \text{with} \tag{2.61}$$

$$\Delta_L = \left(\frac{1}{2} - \frac{2}{3}\sin^2\vartheta_\mathrm{W}\right) m_Z^2 \cos 2\beta \qquad \text{and} \qquad \Delta_R = -\frac{2}{3}\sin^2\vartheta_\mathrm{W} m_Z^2 \cos 2\beta \,. \tag{2.62}$$

2.3 SUSY Phenomenology at Hadron Colliders

This section discusses the expected signatures of collisions with SUSY particles being produced at hadron colliders. As already mentioned, different SUSY models might have very different signatures. In general, an inclusive search for multiform SUSY phenomenology might suffer from inefficient usage of the conceivable discovery potential. Peculiar signatures with promising detectability, which are realized for only limited SUSY models, could not be fully exploited. Therefore, focus is put solely on R-parity conserving models. In the following, the searched signatures are justified step by step based on the presented aspects of SUSY. Finally, the searched SUSY model that realizes these signatures is described.

2.3.1 SUSY Production at the LHC

As already mentioned in Section 1.2, this analysis searches for directly produced SUSY particles in proton-proton collisions at the LHC. The collider will be described in Section 3.1. However, the expected SUSY physics in proton-proton collisions can be discussed without knowledge of the collision's instrumental realization. Since the proton is no elementary particle itself, its constituents, the partons, are the actual participants in the interactions, and hence produce any new or known particle.

The proton is made up of three valence quarks, two up quarks u and one down quark d and the binding gluons. The latter can produce sea quarks by quark-antiquark creations. The total momentum of the proton is shared among the valence- and sea quarks, $q_{\mathrm{v,s}}$ and the gluons g [122]. Each of them carries a fraction of the total momentum:

$$x_{q_{\mathrm{v,s}},g} = \frac{p_{q_{\mathrm{v,s}},g}}{p_p} \qquad \text{with} \qquad p_p = \sum_{q_{\mathrm{v}},\, q_{\mathrm{s}},\, g} p_{q_{\mathrm{v,s}},g}\,. \tag{2.63}$$

The probability density to find a particular parton with the given momentum fraction $x_{q_{\mathrm{v,s}},g}$ is described by the parton distribution functions (PDFs). They give the availability of colliding partons and their momentum and hence characterize the collision's kinematics. There are several different sets of PDFs, which are either derived from different methods and/or from different data, e.g. `CTEQ` [123, 124], `MRST` [125, 126], `NNPDFs` [127, 128] or from the HERA experiment [129, 130].

Possible SUSY particles can then be produced in the collision of the partons. Since SUSY transformations conserve all quantum numbers beside the spin, also the superpartners of the partons, the squarks and gluinos, interact strongly. Consequently, the strong interaction dominates the possible production of SUSY particles and preferably creates colored SUSY particles.

Figure 2.7 shows Feynman diagrams for the production of squarks and gluinos by the interaction of the partons. The couplings in these diagrams are determined by QCD and hence fixed by the SM. However, the masses of intermediate and final SUSY particles enter the corresponding calculations for the cross section. Hence, the prediction about the contribution from the individual graphs and the total production rate is model dependent. E.g. if the gluino mass exceeds the squark mass significantly, the production of gluinos might be minor compared to squarks.

Also the PDFs play an important role in the production yield of each diagram: On average, valence quarks carry a larger fraction of the proton momentum and thereby provide more energy to the hard collision. Calculations of total and differential cross sections for strong SUSY production in hadronic collisions can be found in [131–133]. Extensions to models with different masses for $\widetilde{q}_L$ and $\widetilde{q}_R$ [134] and to next-to-leading order corrections [135] are also available.

In addition to strong production, there are also possible electroweak contributions. Feynman graphs for pure electroweak production are displayed in Figure 2.8. Their couplings are determined by either electroweak or Yukawa interactions and hence play a minor role compared to QCD. However, the weaker

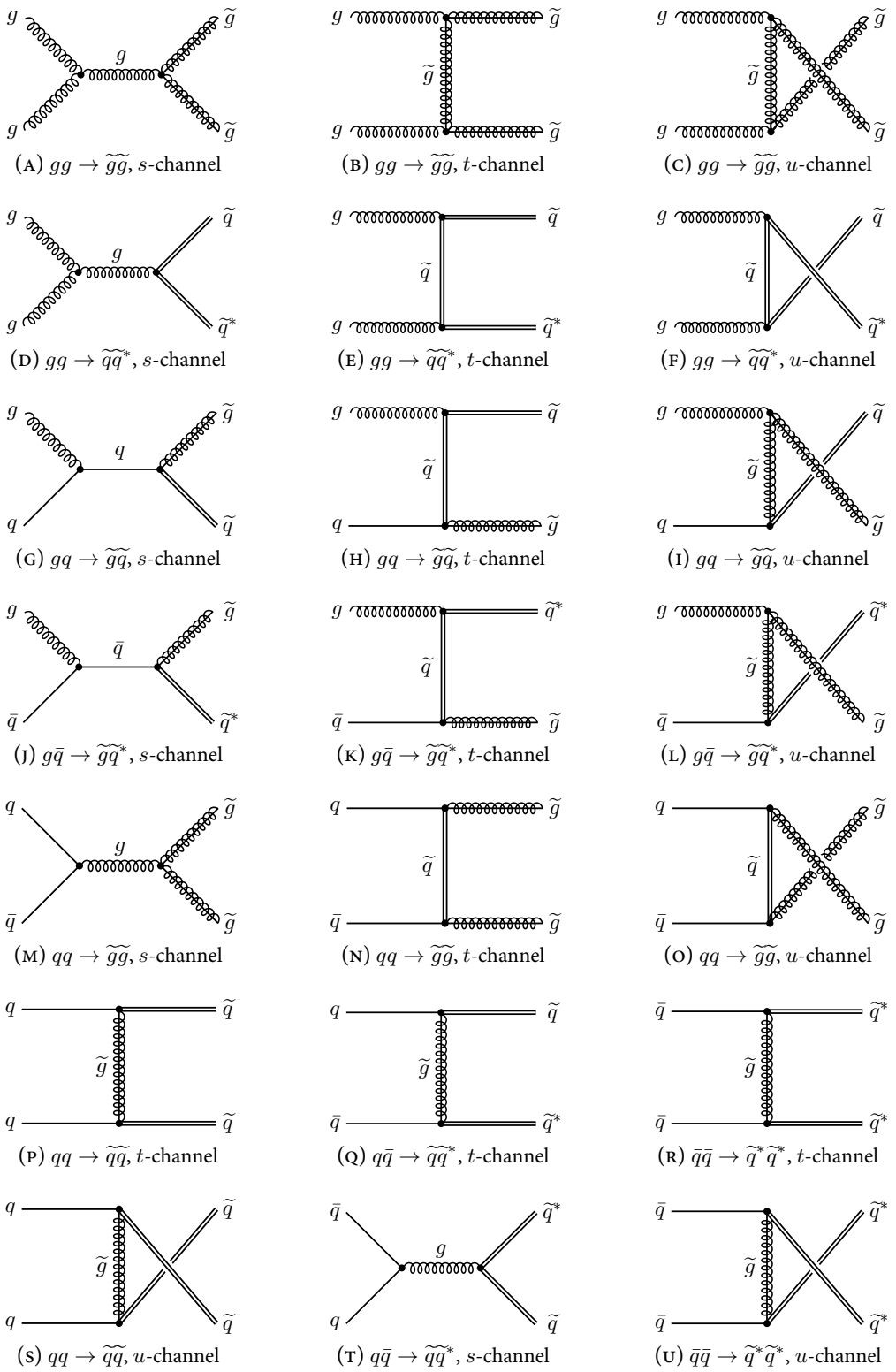

(A) $gg \to \widetilde{g}\widetilde{g}$, s-channel (B) $gg \to \widetilde{g}\widetilde{g}$, t-channel (C) $gg \to \widetilde{g}\widetilde{g}$, u-channel

(D) $gg \to \widetilde{q}\widetilde{q}^*$, s-channel (E) $gg \to \widetilde{q}\widetilde{q}^*$, t-channel (F) $gg \to \widetilde{q}\widetilde{q}^*$, u-channel

(G) $gq \to \widetilde{g}\widetilde{q}$, s-channel (H) $gq \to \widetilde{g}\widetilde{q}$, t-channel (I) $gq \to \widetilde{g}\widetilde{q}$, u-channel

(J) $g\bar{q} \to \widetilde{g}\widetilde{q}^*$, s-channel (K) $g\bar{q} \to \widetilde{g}\widetilde{q}^*$, t-channel (L) $g\bar{q} \to \widetilde{g}\widetilde{q}^*$, u-channel

(M) $q\bar{q} \to \widetilde{g}\widetilde{g}$, s-channel (N) $q\bar{q} \to \widetilde{g}\widetilde{g}$, t-channel (O) $q\bar{q} \to \widetilde{g}\widetilde{g}$, u-channel

(P) $qq \to \widetilde{q}\widetilde{q}$, t-channel (Q) $q\bar{q} \to \widetilde{q}\widetilde{q}^*$, t-channel (R) $\bar{q}\bar{q} \to \widetilde{q}^*\widetilde{q}^*$, t-channel

(S) $qq \to \widetilde{q}\widetilde{q}$, u-channel (T) $q\bar{q} \to \widetilde{q}\widetilde{q}^*$, s-channel (U) $\bar{q}\bar{q} \to \widetilde{q}^*\widetilde{q}^*$, u-channel

Figure 2.7 Possible production of colored SUSY particles at the LHC via strong interactions.

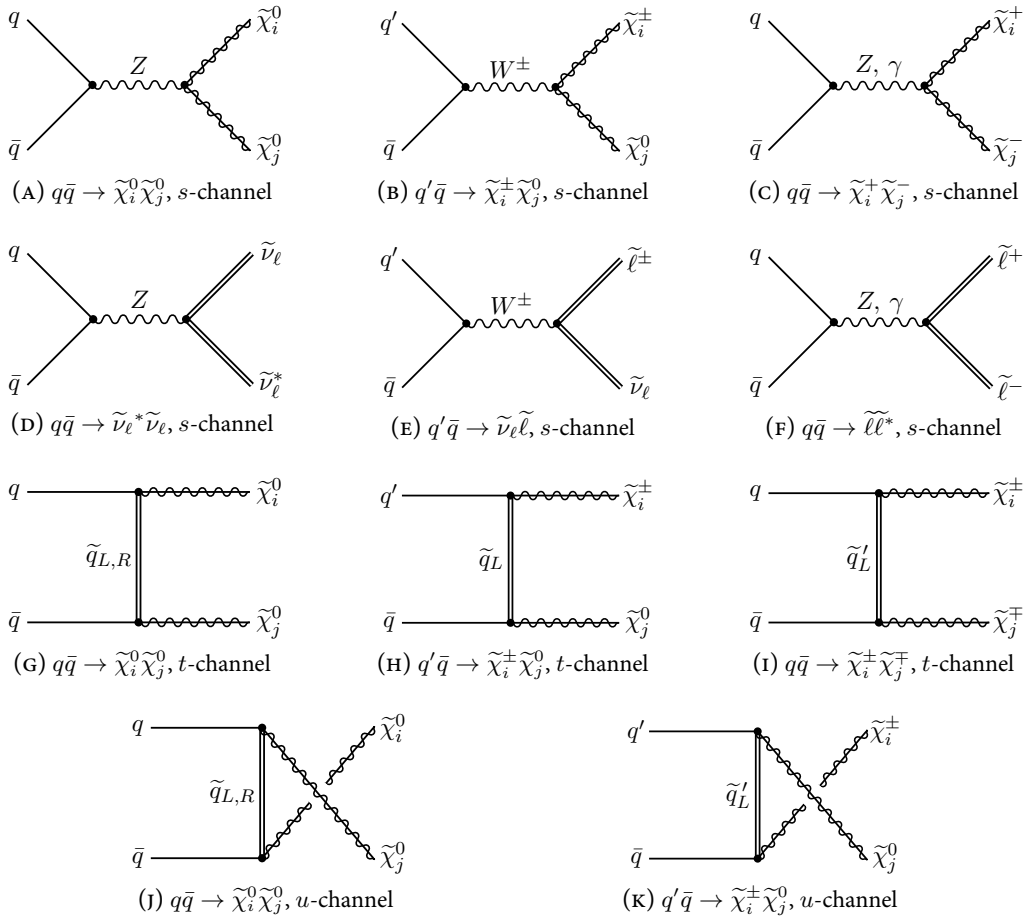

(A) $q\bar{q} \to \widetilde{\chi}_i^0\widetilde{\chi}_j^0$, s-channel (B) $q'\bar{q} \to \widetilde{\chi}_i^\pm\widetilde{\chi}_j^0$, s-channel (C) $q\bar{q} \to \widetilde{\chi}_i^+\widetilde{\chi}_j^-$, s-channel

(D) $q\bar{q} \to \widetilde{\nu}_\ell{}^*\widetilde{\nu}_\ell$, s-channel (E) $q'\bar{q} \to \widetilde{\nu}_\ell\widetilde{\ell}$, s-channel (F) $q\bar{q} \to \widetilde{\ell}\widetilde{\ell}^*$, s-channel

(G) $q\bar{q} \to \widetilde{\chi}_i^0\widetilde{\chi}_j^0$, t-channel (H) $q'\bar{q} \to \widetilde{\chi}_i^\pm\widetilde{\chi}_j^0$, t-channel (I) $q\bar{q} \to \widetilde{\chi}_i^\pm\widetilde{\chi}_j^\mp$, t-channel

(J) $q\bar{q} \to \widetilde{\chi}_i^0\widetilde{\chi}_j^0$, u-channel (K) $q'\bar{q} \to \widetilde{\chi}_i^\pm\widetilde{\chi}_j^0$, u-channel

Figure 2.8 Possible production of SUSY particles at the LHC via electroweak and Yukawa interactions.

coupling might be partly compensated by phase space arguments: If squark and gluino masses are near or even above the center-of-mass energy threshold, gauginos or sleptons might be the only kinematically accessible SUSY particles.

The couplings in the electroweak diagrams are either gauge or Yukawa couplings. Therefore, only the gaugino or Higgsino content of charginos and neutralinos participate in the interaction, see Equations 2.51 and 2.53. For instance, the couplings in Figure 2.8(I) change the quark flavour and are only possible through the wino content of the chargino. Contrary, $Z \to \widetilde{\chi}_i^0\widetilde{\chi}_j^0$, see Figure 2.8(A), is only possible via the Higgsino contributions to $\widetilde{\chi}^0$. In addition, baryon number conservation forces the t-channel diagrams in gaugino production to be mediated by a squark, see Figure 2.8(G) to (K). If squarks should be much more massive than the gauginos, these processes take a subleading role compared to the s-channel production. The latter can be mediated by the lighter electroweak gauge bosons, see Figure 2.8(A) to (F). Cross sections for electroweak gaugino and slepton production can be found in [136].

All shown Feynman diagrams for strong and electroweak production conserve R-parity, as explained in Section 2.2.2. Therefore, all of the vertices have an even number of SUSY particles. Since there are no SUSY particles in the initial state, all s-channel diagrams have to be mediated by a SM particle. With the same line of argument, the initial SM particles in all t- and u-channel diagrams interact by the exchange of a SUSY particle. The pairwise occurrence of SUSY particles at each vertex is also reflected in an even

number of primarily produced SUSY particles. Other SUSY particles might then be created by their decay.

2.3.2 SUSY Particle Decays

As shown above, the requirement for R-parity conservation leads to the production of an even number of SUSY particles, so in most cases exactly two. In each collision where SUSY particles are created, these two initial SUSY particles then might decay. Depending on the sparticle types, this gives rise to very different SM and SUSY particles and hence very different collision topologies. At a proton-proton collider, the production of colored sparticle is expected to dominate in a large area of the SUSY parameter space and hence shall be considered.

Strong SUSY production, as shown in Figure 2.7, leads to a pair of either squarks or gluinos or to one of either:

$$\widetilde{q}\widetilde{q} \qquad \widetilde{g}\widetilde{g} \qquad \text{or} \qquad \widetilde{g}\widetilde{q}\,. \tag{2.64}$$

These particles will preferably decay strongly into other colored SUSY particles. A two-body decay into a lighter SUSY particle and a SM particle has the biggest phase space, but the available SUSY particles are very model dependent. E.g. if the squark is lighter than the gluino, the decay

$$\widetilde{g} \to \widetilde{q}\bar{q} \tag{2.65}$$

could take place.[6] If the mass hierarchy among squarks and gluinos is inverted, i.e. $m_{\tilde{g}} < m_{\tilde{q}}$, the decay from Equation 2.65 is forbidden by kinematic constraints but

$$\widetilde{q} \to \widetilde{g}q \tag{2.66}$$

can appear. In any case, the produced SM particle is a quark, which will manifest itself as a jet of colored particles. Thus, strong decays of colored SUSY particles will produce hadronic particle jets as a visible signature. The energy of the jet strongly depends on the mass difference of the two SUSY particles. In the rest frame of the decaying sparticle, the quark energy from the two-body decay is

$$E_q = \frac{m_{\tilde{g}}^2 + m_q^2 - m_{\tilde{q}}^2}{2m_{\tilde{g}}} \approx \frac{m_{\tilde{g}}^2 - m_{\tilde{q}}^2}{2m_{\tilde{g}}} \qquad \text{for} \qquad m_{\tilde{g}} > m_{\tilde{q}} \qquad \text{or} \tag{2.67}$$

$$E_q = \frac{m_{\tilde{q}}^2 + m_q^2 - m_{\tilde{g}}^2}{2m_{\tilde{q}}} \approx \frac{m_{\tilde{q}}^2 - m_{\tilde{g}}^2}{2m_{\tilde{q}}} \qquad \text{for} \qquad m_{\tilde{g}} < m_{\tilde{q}}\,. \tag{2.68}$$

Therefore, the visible energy of the quark jet is proportional to the difference of the squared sparticle masses.

Besides the decays in Equation 2.65 and 2.66, there are no other strong decays among gluinos and squarks. Although there might be rather large mass differences among the squarks, decays of squarks into other squarks would premise a change in quark flavour, which is only possible in weak interactions. If either the lighter of the squark or gluino has been directly produced, or the more massive already decayed into the lighter colored state, no other strong decay is possible.

[6] Here, the quark is assumed to be massless, or at least $m_q \ll m_{\tilde{q},\tilde{g}}$.

Assuming a common scalar and fermionic mass at the GUT scale, the RGEs suggest that the mass hierarchy

$$m_{\tilde{g}} > m_{\tilde{q}} > m_{\tilde{\chi}} \,,\; m_{\tilde{\ell}} \,,\; m_{\tilde{\nu}_\ell} \,. \tag{2.69}$$

is natural, see Equation 2.47 or Figure 2.5(B). Therefore, the next lighter SUSY particles are accessible only via electroweak interactions. Since the gluino neither couples to any of the gauginos or sleptons nor has any YUKAWA coupling, it could decay only via a virtual squark into neutralinos or charginos. Possible squark decays are

$$\widetilde{q} \to \widetilde{\chi}_i^0 q \qquad \text{or} \qquad \widetilde{q} \to \widetilde{\chi}_i^\pm q' \,. \tag{2.70}$$

They produce a quark and in addition either a neutralino or a chargino, where the quark will show up as a jet. The subsequent decays of the electroweak gauginos strongly depend on the mass hierarchy among gauginos and sleptons. Common to all decay chains is the final decay into the lightest SUSY particle, which is stable as predicted by R-parity conservation. Since this particle is expected to be only weakly interacting, see Section 2.2.2, the sneutrinos $\widetilde{\nu}_\ell$ [137–139] or the lightest neutralino $\widetilde{\chi}_1^0$ are possible candidates. Depending on the SUSY model, Equation 2.51 might predict the lightest neutralino to be either bino- [140], wino- [141, 142] or HIGGSino-dominated [143, 144] or a more general mixed state [145]. Furthermore, the superpartner of the graviton might be a candidate for the LSP.

In any case, the LSP will show up as missing transverse momentum: Although the center-of-mass energy of the colliding partons is not known on a collision-by-collision basis, the transverse momentum of the incoming partons vanishes to very good approximation. Hence, also the transverse momenta of the produced particles sum up to zero. An undetected particle like the LSP will result in an imbalance of the transverse momentum and therefore appears as missing transverse momentum. This is a general feature of only weakly interacting particles.

So far, the SUSY signatures have been quark jets and missing transverse momentum. At a proton collider, the occurrence of charged leptons is also a striking signature. Since interactions among the partons are completely QCD-dominated, direct leptons from the proton interactions are a rare product at the LHC. In contrast to that, the decay of the electroweak gauginos and sleptons can produce leptons, which might help to find SUSY events.

Figure 2.9 shows electroweak decays of gauginos and sleptons that could contribute to the appearance of leptons. However, all depicted FEYNMAN diagrams are not possible in a common SUSY model. E.g. Figure 2.9(K) assumes $m_{\tilde{\ell}} > m_{\tilde{\nu}_\ell} + m_W$, whereas Figure 2.9(N) premises $m_{\tilde{\nu}_\ell} > m_{\tilde{\ell}} + m_W$. Principally, all of these decays can be chained as long as the mass of the incoming particle exceeds the sum of the outgoing particles' masses. This might lead to long decay chains, which all finally end with the decay into the LSP. Produced charged leptons are well detectable and therefore a promising signature to look for.

2.3.3 Tau Leptons in SUSY Models

Despite lepton universality, the tau lepton might be a unique probe for supersymmetric theories and hence demands for special attention. The appearance of leptons is predicted in a wide range of the SUSY parameter space, but for some theories, tau leptons are produced preferably. The fundamental reason for this is the enhanced YUKAWA coupling of tau leptons compared to the first and second generation leptons. Within the SM, this shows up as a much higher tau mass:

$$m_\tau = 1776.82\,\text{MeV} \quad \gg \quad m_\mu = 105.66\,\text{MeV} \quad \gg \quad m_e = 0.51\,\text{MeV} \,. \tag{2.71}$$

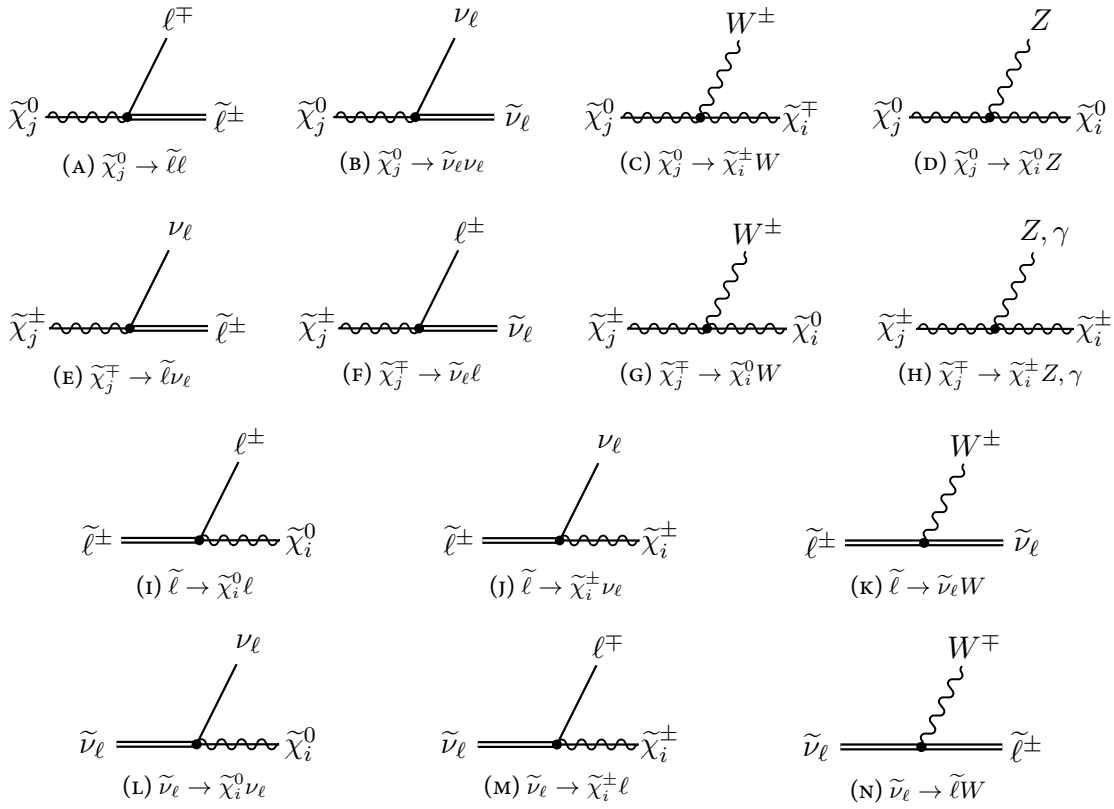

Figure 2.9 Possible decays of sleptons and gauginos, which might contribute to the appearance of leptons.

In SUSY, there are two important aspects that follow from the stronger Yukawa coupling of the tau. The first is related to kinematics in the decay chains and has already been shown in Equation 2.57. The off-diagonal elements of the mass matrix give rise to rather large corrections of $m_{\tilde{\tau}_R}$ and $m_{\tilde{\tau}_L}$ to $m_{\tilde{\tau}_1}$ and $m_{\tilde{\tau}_2}$. This might cause the lighter stau, the $\widetilde{\tau}_1$, to be much lighter than the unmixed states of the first and second generation, i.e.

$$m_{\tilde{\tau}_1} < m_{\tilde{\mu}_{L,R}} \qquad \text{and} \qquad m_{\tilde{\tau}_1} < m_{\tilde{e}_{L,R}} \,. \tag{2.72}$$

In such a case, by pure kinematic phase space considerations, decays like the ones displayed in Figure 2.9(a) or (e) will preferably happen with third generation leptons and hence give rise to tau-rich SUSY signatures.

The second influential effect is connected to the SUSY particle's couplings and has its origin as well in the mixing from Equation 2.60. The superpartners of the right- and left-chiral electron and those of the right and left-chiral muon occur (nearly) unmixed, so that the measurable mass eigenstates are the unmixed weak isospin states. This might not be the case for staus, whose mass eigenstates have contributions from each weak isospin state by Equation 2.60. If the mixing among the neutralinos from Equation 2.51 is not too strong, the Equations 2.49 and 2.44 lead to

$$m_{\tilde{\chi}_1^0} \approx M_1 < M_2 \approx m_{\tilde{\chi}_2^0} \qquad \text{with} \qquad \left|\widetilde{\chi}_1^0\right\rangle \approx \left|\widetilde{B}\right\rangle \qquad \text{and} \qquad \left|\widetilde{\chi}_2^0\right\rangle \approx \left|\widetilde{W}\right\rangle \,, \tag{2.73}$$

Tau Lepton Decays				
decay product	probability [%]	resonance	$\sum$ prongs	$\sum$ BR [%]
$e\nu_e\nu_\tau$	17.84	–	1	35.16
$\mu\nu_\mu\nu_\tau$	17.32	–	1	
$\pi\nu_\tau$	10.83	–	1	49.42
$\pi\pi^0\nu_\tau$	25.47	ρ	1	
$\pi\pi^0\pi^0\nu_\tau$	9.24	a_1	1	
$\pi\pi^0\pi^0\pi^0\nu_\tau$	0.98	–	1	
1-pr. with K	2.9	–	1	
$\pi\pi\pi\nu_\tau$	9.04	a_1	3	14.62
$\pi\pi\pi\pi^0\nu_\tau$	4.59	–	3	
$\pi\pi\pi\pi^0\pi^0\nu_\tau$	0.39	–	3	
$\pi\pi\pi\pi^0\pi^0\pi^0\nu_\tau$	0.01	–	3	
3-pr. with K	0.59	–	3	
others	0.8	–	–	0.8

Table 2.3 The most important leptonic and hadronic decay modes of the tau lepton and intermediate meson resonances if known. The number of prongs are the number of charged particles. Branching ratios are taken from [146].

with a wino-dominated $\widetilde{\chi}_2^0$. This can decay into the lighter $\widetilde{\chi}_1^0$ via intermediate SUSY particles, e.g. a slepton by the combination of Figure 2.9(A) and (I). This would result in a pair of leptons

$$\widetilde{\chi}_2^0 \to \widetilde{\ell}\ell \to \ell\ell\widetilde{\chi}_1^0 \,. \tag{2.74}$$

In general, assuming the unification of masses at the GUT scale in the sense of Equation 2.40, the renormalization group equations for the sleptons result in a higher mass for the $\widetilde{\ell}_L$ than for the $\widetilde{\ell}_R$. This is driven by contributions to the running masses from the $\mathrm{SU}(2)_L$ couplings, which are not present for the $\widetilde{\ell}_R$ states. If the heavier $\widetilde{\mu}_L$ and $\widetilde{e}_L$ are kinematically inaccessible in the $\widetilde{\chi}_2^0$ decay of Equation 2.74, the only possible decay would be via the $\widetilde{\tau}_1$.[7] A wino-only $\widetilde{\chi}_2^0$ would not couple to the $\widetilde{\ell}_R$ states and only the $\widetilde{\tau}_1$ has a sizable $\widetilde{\tau}_L$ component. The same line of argument holds for a wino-like $\widetilde{\chi}_i^\pm$ in decays like the one from Figure 2.9(E), which would result in an enhanced production of tau leptons compared to electrons and muons.

Unfortunately, tau leptons also require more experimental effort due to their decay. The lifetime of the τ

$$\tau_\tau = 290.6 \cdot 10^{-15}\,\mathrm{s} \qquad \text{or} \qquad c\tau_\tau = 87.11\,\mu\mathrm{m}\,, \tag{2.75}$$

[7] Decays into squarks are also not possible if Equation 2.69 is assumed.

leads to a flight length of about half a millimeter per 10 GeV of energy. Therefore, tau leptons typically decay before they reach the ATLAS detector and hence are not directly visible. The most important decay modes are given in Table 2.3 along with their probabilities. The numbers are taken from [146].

There are two basic kinds of decay modes: Leptonic decays, producing either an electron or a muon, or hadronic decays, which result in a jet of hadrons. In any case, at least one neutrino is produced, in leptonic decays there are two of them. This impedes the reconstruction of the full tau's four-momentum since the neutrinos escape detection. Furthermore, tau leptons have to be identified by their decay products. This comes along with the experimentally challenging task of tau lepton reconstruction, as will be explained in Section 3.3.4. However, the decay of the tau provides sensitivity to its SUSY parameter dependent polarization [147–149], which can also be exploited experimentally [150].

2.4 Gauge Mediated SUSY Breaking

In the previous section, the search for SUSY with jets, missing transverse momentum and leptons was motivated, where the special role of tau leptons has been emphasized. Although the experimental goal is the design of a generic search of this signatures, a reference model is needed for some aspects. One of them is the adjustment of free analysis related parameters. For a promising sensitivity, SUSY benchmarks are needed to optimize any free parameter in the analysis outline. In addition, the interpretation of results with respect to exclusion can be solely done with a specific SUSY model that gives a comprehensive and complete prediction.

Although attention is paid to only strong SUSY production in R-parity conserving models, SUSY parameter space is enormous. Therefore, a model with only few parameters is chosen. The choice of the model is obviously restricted by the demand for the considered search signatures. Especially, it should manifest itself by a copious production of tau leptons, which has been shown to be a well motivated search signature. Within this thesis, the Gauge Mediated Supersymmetry Breaking (GMSB) model [151–155] is chosen, which is described in the following.

2.4.1 Breaking Mechanism

In the MSSM, the SUSY particle masses have been included by explicit mass terms in the Lagrangian in Equation 2.31. This was done without giving any specific cause for the mass symmetry breaking between SM particles and their superpartners. It can be argued that the source of this symmetry breaking cannot be inhered in the MSSM itself [17]. Hence, its origin evidently emanates from another sector, the so-called *hidden sector*. The breaking is communicated to the MSSM sector by an interaction that couples to the hidden as well as to the MSSM sector and thereby generates the mass symmetry breaking.

In GMSB, this breaking is mediated dynamically by the gauge bosons of the SM by the ordinary $\mathrm{U}(1)_Y \times \mathrm{SU}(2)_L \times \mathrm{SU}(3)_C$ interactions. Since the gauge interactions are flavour blind, also SUSY breaking has to be flavour blind in the same sense. Therefore, GMSB already provides flavour independent SUSY masses for the sfermions, i.e. the masses depend only on the sfermion's $\mathrm{U}(1)_Y \times \mathrm{SU}(2)_L \times \mathrm{SU}(3)_C$ quantum numbers. In addition, the non-SM-like flavour violations, e.g. the off-diagonal terms in the soft SUSY breaking Lagrangian in Equation 2.31, are suppressed naturally and

$$\mathbf{m}^2_{\tilde{Q}} = m^2_{\tilde{Q}}\mathbb{1} \qquad \mathbf{m}^2_{\tilde{u}} = m^2_{\tilde{u}}\mathbb{1} \qquad \mathbf{m}^2_{\tilde{d}} = m^2_{\tilde{d}}\mathbb{1} \qquad \mathbf{m}^2_{\tilde{L}} = m^2_{\tilde{L}}\mathbb{1} \qquad \mathbf{m}^2_{\tilde{e}} = m^2_{\tilde{e}}\mathbb{1} \tag{2.76}$$

follows, where $\mathbb{1}$ is the unity matrix. The inherent restrain of flavour violation in GMSB also motivates the assumptions about the suppression of off-diagonal elements in the matrices from equation 2.54 and 2.55. This makes GMSB to a well motivated model among possible SUSY realizations.

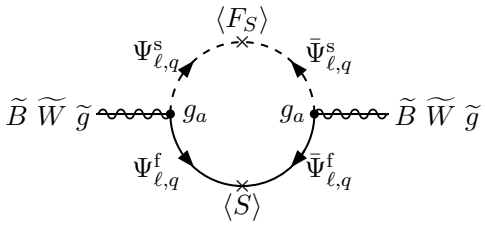

Figure 2.10 A Feynman diagram contributing to the generation of the gaugino masses in Gauge Mediated Supersymmetry Breaking.

The mechanism to generate the higher SUSY masses starts in the hidden sector, where SUSY is broken. In this hidden sector, left-handed chiral supermultiplets Φ_ℓ, $\bar{\Phi}_\ell$, Φ_q and $\bar{\Phi}_q$ exist. They contain messenger and scalar leptons, as well as messenger and scalar quarks, respectively. Their masses are generated by the coupling to a gauge singlet chiral supermultiplet S

$$W_{\text{mass}} = y_\ell S \Phi_\ell \bar{\Phi}_\ell + y_q S \Phi_q \bar{\Phi}_q \,, \tag{2.77}$$

where the scalar component of S and the one of its auxiliary F-term acquire non-vanishing vacuum expectation values

$$\langle S \rangle \neq 0 \qquad \text{and} \qquad \langle F_S \rangle \neq 0 \,. \tag{2.78}$$

This can be shown to generate mass terms in the Lagrangian for the fermions and scalars of the form

$$\mathcal{L}_{\text{fermionic mass}} = - y_\ell \langle S \rangle \, \Phi^{\mathrm{f}}_\ell \bar{\Phi}^{\mathrm{f}}_\ell - y_q \langle S \rangle \, \Phi^{\mathrm{f}}_q \bar{\Phi}^{\mathrm{f}}_q \tag{2.79}$$

$$\mathcal{L}_{\text{scalar mass}} = - \begin{pmatrix} \Phi^{\mathrm{s}}_\ell & \bar{\Phi}^{\mathrm{s}}_\ell \end{pmatrix} \begin{pmatrix} |y_\ell \langle S \rangle|^2 & -y^*_\ell \langle F^*_S \rangle \\ -y_\ell \langle F_S \rangle & |y_\ell \langle S \rangle|^2 \end{pmatrix} \begin{pmatrix} \Phi^{\mathrm{s}}_\ell \\ \bar{\Phi}^{\mathrm{s}}_\ell \end{pmatrix} \tag{2.80}$$

$$- \begin{pmatrix} \Phi^{\mathrm{s}}_q & \bar{\Phi}^{\mathrm{s}}_q \end{pmatrix} \begin{pmatrix} |y_q \langle S \rangle|^2 & -y^*_q \langle F^*_S \rangle \\ -y_q \langle F_S \rangle & |y_q \langle S \rangle|^2 \end{pmatrix} \begin{pmatrix} \Phi^{\mathrm{s}}_q \\ \bar{\Phi}^{\mathrm{s}}_q \end{pmatrix} \,, \tag{2.81}$$

where the superscripts ‘f’ and ‘s’ denote the fermionic and scalar content of the supermultiplets. Diagonalizing the mass matrices from Equations 2.80 and 2.81 leads to the masses

$$\Phi_\ell \,, \ \bar{\Phi}_\ell \ : \qquad m^2_{\mathrm{f}} = |y_\ell \langle S \rangle|^2 \qquad \text{and} \qquad m^2_{\mathrm{s}} = |y_\ell \langle S \rangle|^2 \pm |y_\ell \langle F_S \rangle| \,, \tag{2.82}$$

$$\Phi_q \,, \ \bar{\Phi}_q \ : \qquad m^2_{\mathrm{f}} = |y_q \langle S \rangle|^2 \qquad \text{and} \qquad m^2_{\mathrm{s}} = |y_q \langle S \rangle|^2 \pm |y_q \langle F_S \rangle| \,. \tag{2.83}$$

For $\langle F_S \rangle \neq 0$, the mass symmetry between fermionic and scalar superpartners within a supermultiplet is evidently broken. This breaking is then propagated to the MSSM fields via radiative loop diagrams. Figure 2.10 shows a possible Feynman diagram for a loop contribution to the gaugino masses. The couplings are the gauge couplings of the SM from Equation 2.38 and the intermediate loop consists of the scalar and fermionic components of the messenger supermultiplets.

At one-loop level the resulting mass parameters for the gauginos in the soft supersymmetry breaking Lagrangian can be shown to be [154]

$$M_a = \frac{\alpha_a}{4\pi}\Lambda N_5 = \frac{\alpha_a}{4\pi}\frac{\langle F_S\rangle}{\langle S\rangle}N_5 \qquad \text{where} \qquad \alpha \in \{1,\ 2,\ 3\}\ , \tag{2.84}$$

and N_5 is the number of messenger supermultiplets. The index '5' denotes that the gauge couplings of the SM are expected to be unified at the GUT scale in the SU(5) group. The masses of scalar particles, e.g. sfermions, are only possible via two-loop contributions and are given by [154]

$$m^2_{\text{scalar}} = 2\Lambda^2 N_5 \sum_{k=1}^{3}\left(\frac{\alpha_k}{4\pi}\right)^2 C_k(i) \qquad \text{where} \qquad C_k(i) = \begin{cases} 4/3 & k=3 & \text{SU}(3)_C \\ 3/4 & k=2 & \text{SU}(2)_L \\ 3Y^2/5 & k=1 & \text{U}(1)_Y\ . \end{cases} \tag{2.85}$$

The factors $C_k(i)$ are zero if the particle does not participate in the corresponding gauge interaction. It follows directly from Equation 2.85 that the partners of left-handed fermions are heavier due to their $\text{SU}(2)_L$ couplings and strongly interacting particles are the most massive ones due to the large $\alpha_s = \alpha_3$.

2.4.2 Phenomenology and Parameters

GMSB models typically predict the gravitino, the superpartner of the graviton, as the lightest supersymmetric particle with the mass

$$m_{3/2} \propto \frac{\langle F_S\rangle}{M_{\text{Planck}}}\ . \tag{2.86}$$

Due to the high Planck scale, the gravitino is expected to be much lighter than the other SUSY particles. Hence, the GMSB phenomenology is largely dominated by the decay of the NLSP into the LSP, the gravitino. From Equations 2.84 and 2.85 it can be seen that scalar masses increase with $\sqrt{N_5}$, whereas the gaugino masses are proportional to N_5. This is a consequence of the fact that gaugino masses are generated at one-loop level, whereas scalar masses need two-loop contributions. Hence, for larger N_5, the masses of gauginos get heavier compared to the sfermions and the NLSP typically changes from a neutralino to a sfermion. Since right-chiral sleptons neither carry color nor weak isospin, they are the lightest sfermions according to Equation 2.85. For high $\tan\beta$ models, the $\widetilde{\tau}_1$ becomes the lightest slepton due to the mixing of Equation 2.57 and the SUSY decay chains typically end with

$$N_5 = 1: \qquad \widetilde{\chi}^0_1 \to \widetilde{G}\gamma \tag{2.87}$$

$$N_5 = 3: \qquad \widetilde{\tau}_1 \to \widetilde{G}\tau\ . \tag{2.88}$$

The model is then characterized by only six parameters, which determine the complete SUSY phenomenology:

- Λ The SUSY breaking scale. It is the ratio from the SUSY breaking order parameter $\langle F_S\rangle$ to the messenger mass scale $\langle S\rangle$, $\Lambda = \langle F_S\rangle\ /\ \langle S\rangle$.
- $\langle S\rangle$ The mass scale of the messenger fields.
- $\tan\beta$ The ratio of the two Higgs doublets vacuum expectation values from Equation 2.27.

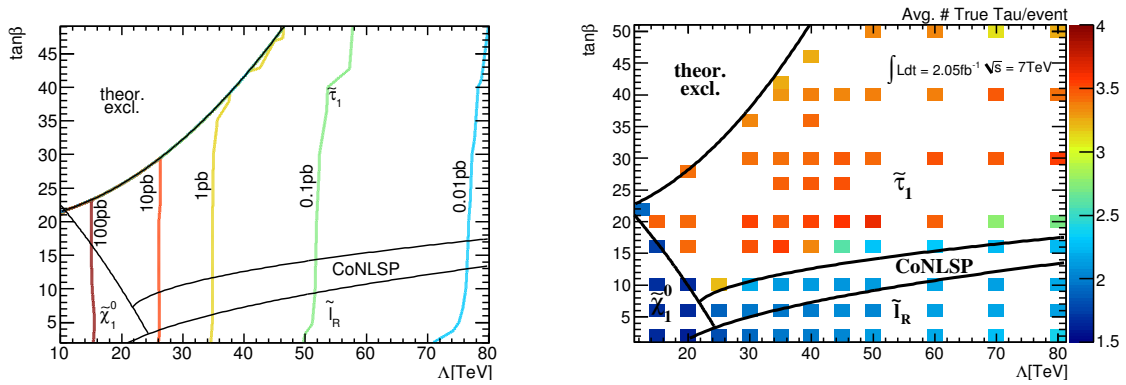

(A) NLO cross sections

(B) Average number of tau leptons

FIGURE 2.11 GMSB cross sections and tau multiplicity [156]. (A): The next-to-leading order cross sections in the GMSB parameter plane of $\tan\beta$ *and* Λ*. (B): The average number of expected tau leptons per generated SUSY event. The granularity is determined by the considered model points.*

N_5 The number of messenger fields.

$\operatorname{sgn}\mu$ The sign of the HIGGS mass term.

$C_{\tilde{G}}$ The gravitino mass scale factor. It determines the lifetime of the NLSP before it decays into the gravitino. In nearly all models, the lifetime is short and the NLSP decays promptly compared to detector scale. Hence, this parameter will not change the phenomenology as long as the NLSP decays within the detector.

Even if only five parameters determine the whole model, the consideration of all their possible combinations is not feasible. Therefore, three of the parameters are fixed and only two are treated separately as free parameters. Within this work, N_5 will be set to three, which lead to $m_{\tilde{\tau}} < m_{\tilde{\chi}_1^0}$, see Equation 2.88. Furthermore, the masses of the SUSY particles are determined by Λ, but not by the absolute messenger mass scale $\langle S \rangle$, see Equations 2.84 and 2.85. Although $\langle S \rangle$ defines the mass scale of the hidden sector, the resulting low energy SUSY masses depend only the breaking in the hidden sector, see Equations 2.82 and 2.83. Therefore, $\langle S \rangle$ is fixed at a scale at sufficiently high energies beyond the experimental reach by $\langle S \rangle = 250$ TeV. The gravitino mass scale factor and the sign of μ do not have strong implications for the low energy SUSY appearance and hence are fixed to $C_{\tilde{G}} = 1$ and $\operatorname{sgn}\mu = +1$. The used set of parameters is then

$$N_5 = 3 \qquad C_{\tilde{G}} = 1 \qquad \operatorname{sgn}\mu = +1 \qquad \langle S \rangle = 250\,\text{TeV}\,, \tag{2.89}$$

leaving only $\tan\beta$ and Λ as free inputs. They are varied in nearly 100 different combinations in the range of

$$\tan\beta = 2 \ldots 70 \tag{2.90}$$

$$\Lambda = 10\,\text{TeV} \ldots 80\,\text{TeV}\,. \tag{2.91}$$

Figure 2.11(A) shows the total expected next-to-leading order production cross sections in the parameter plane, which is steeply falling with increasing Λ. This is driven by the increasing masses of produced SUSY particles, as given by Equations 2.84 and 2.85. Both increase linearly with Λ. Figure 2.11(B) shows

the expected average number of taus that appear per produced SUSY event. For high $\tan\beta$ the mixing in the stau sector leads to a very light $\widetilde{\tau}_1$ and hence decay chains like

$$\widetilde{q} \to \widetilde{\chi}_i^0 q \to \widetilde{\tau}_1 \tau q \to \widetilde{G} \tau \tau q \tag{2.92}$$

produce two taus. This might happen for both initial SUSY particles, e.g. from squark-antisquark pair production. The abundance of tau leptons decreases for lower $\tan\beta$, where the sleptons become degenerate, i.e. the mass difference between first and third generation sleptons is smaller than the tau mass. In this CoNLSP region, taus are no longer preferably produced, but still have sizable contributions. This choice of SUSY model parameterization specifies the phenomenology by two parameters: Whereas Λ sets the mass scale of the SUSY particles, $\tan\beta$ governs the tau richness of the model.

Given the considerations above, this thesis aims at SUSY models, where decay chains produce jets, multiple taus and missing transverse momentum from the escaping LSP. Besides this theoretical motivation, the final specification of this search signatures also succumbs to several experimental issues. They will be explained in the next Chapter 3. Therefore, the final outline in the object selection is established in Section 4.1, after the experimental challenges with tau final states are discussed.

Summary

The SM has shortcoming that might be solved by its supersymmetric extension. At hadron colliders, SUSY may be discovered in collisions with jets, missing transverse momentum and leptons. While tau leptons are experimentally challenging, they likely occur in such collisions. This phenomenology can be found in GMSB models, which can be specified by only two free parameters, Λ and $\tan\beta$.

Chapter 3

The Experimental Setup

Event Reconstruction with ATLAS at the LHC

The direct production of supersymmetric particles and the detection of their decay products is an attractive, but also ambitious and challenging way to search for SUSY. Since SUSY particles are supposed to be very massive and rarely produced, the unprecedented center-of-mass energy of 7 TeV and extraordinary luminosity of the LHC provide encouraging conditions for a potential discovery of SUSY. The collider, as well as the ATLAS detector used for the reconstruction of the collisions, shall be introduced in the following. Furthermore, their simulation, used for comparison to observation, will be explained.

3.1 The Large Hadron Collider

The Large Hadron Collider (LHC) [157–161] is a proton-proton collider[1] at the Swiss-French border near Geneva. It consists of several subsequent accelerator elements, which finally inject two counter-rotating beams of protons into the main component: A 27 km long circular accelerator that ramps up the proton beams to a center-of-mass energy of 7 TeV.

The sequence of accelerating elements is shown in Figure 3.1: The protons are collected from a hydrogen source, boosted in a linear accelerator to 50 MeV and then injected into a series of three circular pre-accelerators: the PSB [164], PS [165] and SPS [166, 167].[2] Here, their energies are raised to 1.4 GeV, 25 GeV and 450 GeV, respectively. After the protons reach their final energy in the SPS, two beams are branched off and injected in opposed direction into the LHC. The both beams' energies are increased up to 3.5 TeV and finally intersected at the experiments. Figure 3.1 shows only the two biggest experiments, ATLAS and CMS, and does not claim scale preservation.

The basic principle of the acceleration is electromagnetic attraction, where a particle with charge q obtains the energy

$$E_{\text{kin}} = \int_{\vec{s}} \left(\vec{F} \cdot \mathrm{d}\vec{s} \right) = q \int_{\vec{s}} \left(\vec{E} \cdot \mathrm{d}\vec{s} \right) \ , \tag{3.1}$$

on the path $\vec{s}$ through an electric field $\vec{E}$. A final energy in the TeV-range by the use of current linear accelerators technologies would either demand for an extremely strong electromagnetic field or excessive long colliders. Therefore, circular designs have proven to be successful, where a particle can cycle the same path again and again until it reaches the needed energy. Certainly, this cannot be exploited ad infinitum, as will be explained.

The linear accelerator elements consist of drift tubes in a Wideröe structure [168], where adjacent tube elements have opposite polarity. A passing particle will be attracted by the next tube and hence accelerated. As soon as the next one is reached, polarity changes and acceleration will continue to the next one and so forth. In the circular elements, the acceleration is performed by cavities that form high frequency

[1] The LHC has a heavy ion program as well [162, 163], which is not used within this work and hence will not be put on record.
[2] The acronyms stand for: (PBS) Proton Synchrotron Booster; (PS) Proton Synchrotron; (SPS) Super Proton Synchrotron.

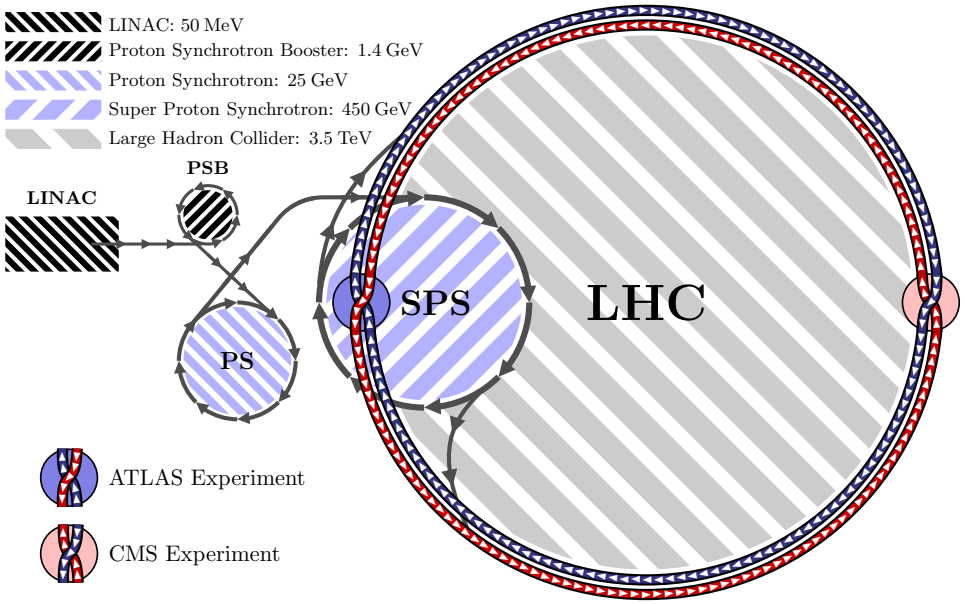

Figure 3.1 Schematic sketch of the LHC accelerator system at CERN and the two biggest experiments.

stationery waves. Depending on the stimulation frequency and the cavity's geometry, an oscillating longitudinal wave along the central axis of the cavity is created. If the particle arrives in phase with the wave, it is accelerated, but otherwise might be decelerated.

The requirement of in-phase arrival of the particle with the oscillation of the cavity makes high demands on the tuning of frequency and the particle's velocity. Fortunately, for highly relativistic particles, the increase in energy does not translate into a noteworthy change in velocity and hence the main circular accelerators can operate at a fixed frequency. In addition to acceleration, the PS also gives a bunch structure to the beam. The LHC beam is segmented into about 1000 to 2800 bunches[3], each of which contains approximately 10^{11} protons [169].

The protons are bent onto the circular path of the accelerator by dipole magnets. This is based on electromagnetic deflection, where a particle with charge q experiences the force

$$\vec{F} = q\left[\vec{v} \times \vec{B}\right] \ , \tag{3.2}$$

when it traverses a magnetic field $\vec{B}$ with a velocity $\vec{v}$. Due to the exceptionally high energies of the protons, magnetic fields up to 8.36 T from 1232 dipoles are needed in the LHC to keep the protons in the beam pipes. This is only possible with superconducting magnets [170, 171], which require to be cooled down to 1.9 K.

The deflection of the protons in a magnetic field leads to synchrotron radiation. The energy loss of a proton per turn is

$$\Delta E_p = \frac{e^2 E_{\text{beam}}^4}{3\epsilon_0 R (m_p c^2)^4} \ , \tag{3.3}$$

[3] The exact number of bunches depends on the actual run conditions. At design luminosity it should reach $2.8 \cdot 10^3$ bunches.

where R is the ring radius and E_{beam} the particle's energy in the circular storage ring. Equation 3.3 reveals one of the benefits of storing protons rather than electrons: Since their mass is much higher, radiative energy losses per circle are reduced by a factor

$$\frac{\Delta E_p}{\Delta E_e} = \left(\frac{m_e}{m_p}\right)^4 \approx 8.8 \cdot 10^{-14} \,. \tag{3.4}$$

At the LHC, the loss of energy due to this effect is about 6.7 keV [172] per proton and turn.

To achieve the extremely high luminosity, the storage rings also have to focus the beam in addition to its acceleration and deflection. Due to electrostatic repulsion of the positively charged beam, it would diverge without any mechanism that compensates for the Coulomb force. The narrow beam profile is restored by a series of rotated quadrupoles whose deflections result in a focussing effect. The LHC also has higher order multipole magnets for several other beam profile corrections. E.g. the dipole deflection of the protons depends on their momentum. Due to the finite momentum spread of the beam's protons, there are different deflections and hence beam divergencies. These are re-focused by sextupole magnets.

The narrow transverse width of the intense proton beam at the interaction points is one of the key features of the LHC. The extreme proton density ensures a high collision rate, which is described by the instantaneous luminosity $\mathcal{L}$[4]

$$\frac{\mathrm{d}}{\mathrm{d}t} N = \mathcal{L}\sigma \,. \tag{3.5}$$

It is the proportionality of the production rate to the cross section for a given process and parameterizes the beam conditions at the intersection. For a ring accelerator with N_b bunches of N_p particles, it is given by

$$\mathcal{L} = f_{\text{rev}} \frac{N_\mathrm{b} N_p^2}{\sigma_x \sigma_y} \,. \tag{3.6}$$

Here, f_{rev} is the revolution frequency and $\sigma_{x,y}$ are the root mean square beam sizes at the collision point in x- and y-direction, respectively.

The beams are intersected at dedicated interaction points, which are surrounded by the detectors. Due to the extended beam geometry, the collisions take place in a volume around this point. The transverse size of this volume is largely dominated by the beam spread, whereas the longitudinal elongation is determined by the crossing angle of the intersecting beams. At the LHC, this angle is $\varphi_{\text{cross}} \approx 200\,\mu\text{rad}$, which also slightly changes the effective transverse intersection area. Assuming a Gaussian transverse beam distribution, the instantaneous luminosity for crossed beams from Equation 3.6 reads [161, 173]

$$\mathcal{L} = f_{\text{rev}} \frac{N_\mathrm{b} N_p^2}{\sigma_x \sigma_y \sqrt{1 + \left(\frac{\sigma_z}{\sigma_\mathrm{T}} \tan\frac{\varphi_{\text{cross}}}{2}\right)^2}} \,, \tag{3.7}$$

where σ_z and σ_T are the root mean squares of the longitudinal bunch length and the transverse beam size at the interaction point, respectively. The design luminosity of the LHC is

$$\mathcal{L} = 10^{34}\,\text{cm}^2\text{s}^{-1} \,. \tag{3.8}$$

[4] The symbol '$\mathcal{L}$' will be used for Lagrangians as well as for the instantaneous luminosity. This ambiguity is accepted to follow the usual naming conventions and the respective meaning will be clarified in the context of each use.

The products of the collisions are measured at four main experiments: CMS [174], ALICE [175], LHCb [176] and ATLAS, where the latter will be explained in detail in the following section. ATLAS and CMS are both general purpose experiments. Principally, they have a similar physics programs and hence can confirm observations of the other experiment independently. In doing so, both experiments are differently outlined with emphasize on distinct aspects in the collision reconstruction. To some extend, this results in a complementary interplay and a minimal overlap in experimental techniques.

LHCb and ALICE are also multipurpose experiments, but have more specific physics programs. ALICE is designed to investigate QCD related questions like quark-gluon plasma at extremely high energies. It is outlined for the heavy ions program of the LHC, but it can be run as well in proton collisions. The domain of b-physics, like precision measurements of CP violation and rare decays of hadrons with b-quarks, is subject of the LHCb experiment.

In addition to the four main experiments at the interaction points, there are also two more without their own interaction point. TOTEM [177] is located nearby the CMS detector and measures collision products from the CMS intersection point in the very forward direction. It is designed to monitor the LHC luminosity and is used for a precise determination of the proton size. The LHCf experiment [178] uses very forward collision products from the ATLAS experiment. It investigates cosmic-ray-like products from the proton collisions.

3.2 The ATLAS Detector

The ATLAS detector [179, 180] is one of the general purpose experiments at the LHC and is the experimental environment in which the analysis of this thesis is performed. The following sections sketch the design of its substructures and explains how particles and their signatures are measured and interpreted. In general, all instruments exploit the interaction of a particle with the detector material. These interactions produce electric signals, which can be read out.

The identification and measurement of particles requires an efficient discrimination between different particle types and a precise determination of their kinematics. This can be realized by dedicated detector components that measure characteristic properties or patterns of particles. These components should have a maximal coverage of the solid angle and fine granularity, where the latter allows for high spatial resolution.

The mentioned demands suggest to build onion shaped detectors, where each detector layer is dedicated to specific tasks and composed of many structures of the same kind. In ATLAS, the coverage of (nearly) the full solid angle is realized by a *barrel* part, which coveres the transverse region around the interaction point, and two *endcap* parts, covering the forward regions near the beam pipe.

The layers also should be arranged by transmissibility, i.e. lucent to opaque from inner to outer layers. This allows each layer to measure the particle as unaffected as possible by the previous layer. A particle of a certain type should be stopped by the last layer that still gains information about this particle type. This ensures that no information, e.g. about the energy, is lost behind the active detector material.

3.2.1 ATLAS Geometry and Coordinates

A schematic picture of the ATLAS detector and its components is displayed in Figure 3.2(a). The next sections explain the structure and operating mode of the different layers, starting from the inside, near the interaction point, to the outermost detector components. Here, and throughout the whole thesis, the nomenclature of the ATLAS coordinate system is used, which is defined as follows. The nominal intersection point is chosen to be the origin of a right-handed Cartesian coordinate system. The z-axis is aligned along the beam pipe, whereas the x-y plane is perpendicular to the beam pipe. The y-axis is

defined to point upwards, so at increasing altitude, perpendicular to ground level, i.e. the plane defined by the LHC ring. The positive x-axis is chosen to lie within this plane and points towards the center of the accelerator ring. The right-handedness then also specifies the positive and negative orientation of the z-axis.

The Cartesian system can be expressed as well in polar coordinates. The radius r is the distance to the intersection point, the azimuthal angle ϕ is measured clockwise around the z-axis and the polar angle θ is measured from the beam pipe. The coordinates are translated by

$$x = r \sin\theta \cos\phi \qquad y = r \sin\theta \sin\phi \qquad \text{and} \qquad z = r \cos\theta. \tag{3.9}$$

and the corresponding inverse functions. Due to the parton distribution functions, compare 2.3.1, the initial longitudinal boost of the colliding partons is unknown and hence only the transverse components of momenta are considered for some aspects. In this projection, i.e. $\theta = \pi/2$, Equations 3.9 can be translated to momentum space by

$$p_x = p_\mathrm{T} \cos\phi \qquad p_y = p_\mathrm{T} \sin\phi \qquad \text{and} \qquad p_z = 0\,. \tag{3.10}$$

The polar angle is usually given in an equivalent measure, the pseudorapidity. It is defined by

$$\eta = -\ln\tan\left(\frac{\theta}{2}\right) \qquad \text{or} \qquad \theta = 2\arctan\left(e^{-\eta}\right)\,, \tag{3.11}$$

and the longitudinal momentum reads $p_z = p_\mathrm{T} \sinh\eta$.

3.2.2 The Inner Detector

The ATLAS inner detector [181, 182] is a tracking device that reconstructs the trajectory of charged particles. It consists of three subelements: The pixel detectors, the semiconductor tracker (SCT) and a transition radiation tracker (TRT). The complete inner detector is filled with a 2 T solenoidal magnetic field [183, 184] aligned with the beam direction in which charged particles are deflected on circular paths. The curvature radius of the track can be used to identify the particle's transverse momentum if the charge is assumed to be known and the charge's polarity can be identified by the deflection direction. The inner detector can be seen in Figure 3.2(b).

The pixel detector [185, 186] is the innermost part and approaches the interaction point up to 5 cm. It is made up of three concentric layers around the beam axis and three disks in either beam direction. These elements are equipped with 1750 modules in total, each of which has about 47 000 pixels. The high pixel density guarantees an extremely high spatial resolution of about 14 µm in the highly occupied vicinity of the interaction point. At the same time, the pixels are designed to show good resistance to the radiation dose from the collisions, to minimize multiple scattering and to have a very efficient response.

The pixel detector is surrounded by five layers of silicon strips, the SCT [187, 188]. It extends the transverse reach of the tracking from 30 cm to 50 cm with about $6.3 \cdot 10^6$ readout channels. The spatial resolution can effort to decrease to 80 µm due to the diverging, and hence lower density of tracks.

The outermost part of the inner detector is filled with the radiation transition tracker [189, 190]. It consists of 350 000 Xenon filled straw tubes, which have an anode wire along its central axis. A charged particle passing through the tube will ionize the gas along its path and produced electrons. These drift towards the anode wire and cause an electric signal. This geometry only allows for a two-dimensional positioning in space. The straws in the barrel are aligned along the z-axis, which disregards any η information. In any case, the η information is of no avail for the transverse momentum measurement.

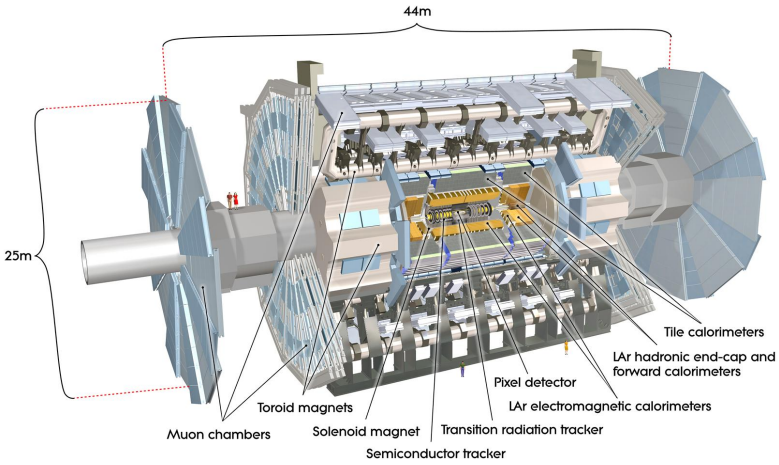

(A) The ATLAS detector

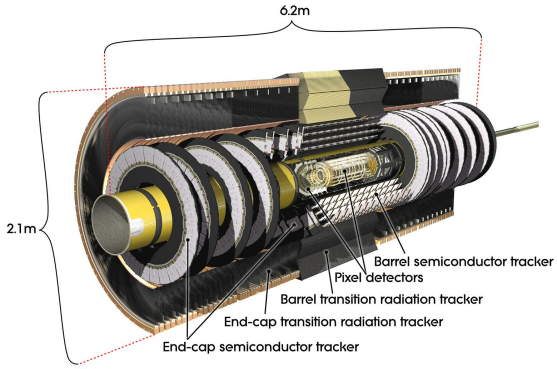

(B) Inner detector

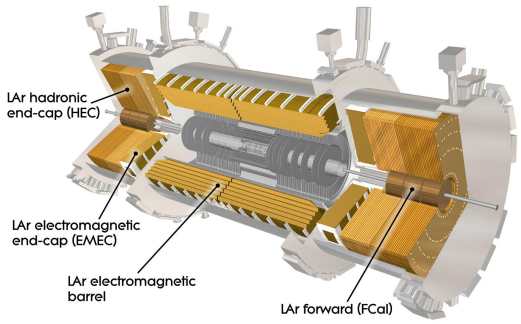

(C) LAr calorimeter

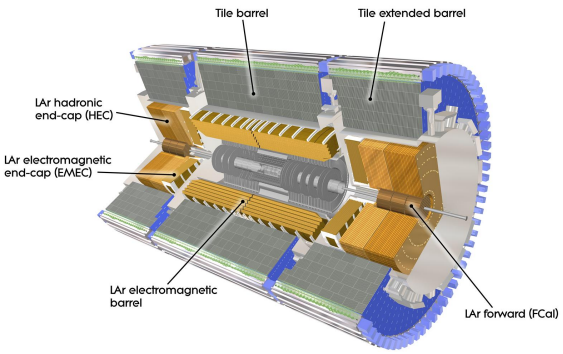

(D) Calorimeters

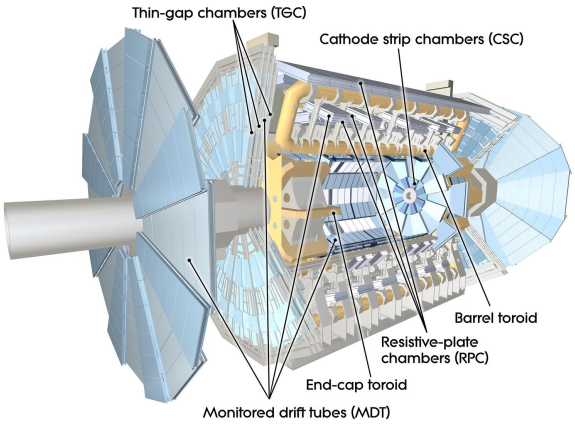

(E) Muon system

Figure 3.2 Cut-away views of the ATLAS detector and its subsystems. Pictures are taken from http://www.atlas.ch/photos/index.html.

In addition, the space in between the straws is filled with a material, in which electrons produce transition radiation, which can be used to identify electrons [191]. There are also possibilities to identify particles via the measurement of energy loss per distance, which is sensitive to the particle's mass [192]. The TRT has the biggest active volume of the inner detector components and allows a wide-ranging trace of charged particles. The large spatial coverage can be afforded since it is a gaseous detector with a long radiation length.

3.2.3 Calorimetry

The calorimeters measure the total energy of a particle. In principle, they consist of absorbers and sensing layers: In the absorbers, the incoming particles interact with the material and create showers of particles. Thereby, the initial particle is decelerated until it is stopped. The absorbers are ordered alternately with sensor layers, in which the showers are detected as electric signals. There are two calorimeter systems in ATLAS: One aims at the measurement of energy depositions from electromagnetic interacting particles and one at energy carried by hadrons.

The electromagnetic calorimeter [193, 194] is responsible for the measurement of particles that interact electromagnetically, i.e. charged particles and photons. A schematic picture can be seen in Figure 3.2(C). Due to their short radiation length, lead panels and stainless steel are used as absorbers, in which particle showers are created. These are immersed in the sensing layers filled with liquid argon, which needs to be cooled down to $-180\,^{\circ}\mathrm{C}$. The argon atoms are ionized by the particles and thereby release electrons, which drift to copper electrodes in an applied electric field. Here, they induce an electric signal that is proportional to the initial particle's energy. A correct calibration that relates the measured signal to the particle's energy is crucial for a reliable operation. Unfortunately, the high luminosity does not allow for a full readout of the calorimeter signals in the short time in between two bunch crossings. Therefore, only the initial ionization current is measured, which is proportional to the energy as well.

The barrel part of the liquid argon calorimeter [195] is made of concentric, accordion shaped layers around the beam direction. They are subdivided into smaller structures of fine granularity with 182 468 readout channels in total. This allows for fine spatial resolution of the objects' substructure, e.g. of jets, or the separation of nearby objects. The forward direction is covered by liquid argon endcap calorimeters [196] for $1.375 < |\eta| < 3.2$ and liquid argon forward calorimeters [197] in the range of $3.1 < |\eta| < 4.9$. The forward direction ($1.375 < |\eta| < 3.2$) is also covered by a liquid argon hadronic endcap [198], which is dedicated to the energy measurement of hadrons.

In the barrel part, the energy of hadrons is measured by the tile calorimeter [199, 200]. The absorbers are made of low-carbon steel and the active material are plastic scintillators. The granularity of the tile calorimeter is about 0.1 rad in ϕ and 0.1 in η. Produced particle showers excite the scintillating material, which re-emits the absorbed energy by luminescence. The light is collected by fibre cables and then read out by photomultiplier tubes. The arrangement of the calorimeters can be seen in Figure 3.2(D).

3.2.4 Muon Systems

Muons are special with respect to reconstruction. Due to their high mass, they are minimal ionizing particles and penetrate the calorimeters. Hence, their identification needs a dedicated detector system, the muon spectrometer [201–203]. It is located around the calorimeters and can be seen in Figure 3.2(E). Although they require an additional dedicated detector system, their special behaviour grants them a unique appearance and makes them easy to identify.

The muon spectrometer is an additional tracking device that is filled by a toroidal magnetic field [204, 205] of about $0.5\,\mathrm{T}$ to $1\,\mathrm{T}$ created by superconducting currents. Within this field, the bend tracks of

muons are measured by different systems. Their trajectory is measured by drift tubes (MDT), whose positions are constantly monitored by an optical alignment system [206, 207] and hence their location is known with an accuracy of 30 µm. In the drift tubes, gas is ionized along the muon's path and the produced electrons are collected. Here, drift time information is used to determine the exact starting point of the electrons and hence the muon's location.

In addition to the spatial location, time of flight measurements are also performed by the use of Resistive Plate Chambers (RPC) [208, 209] in the barrel. In these systems, the active gas is shielded with high resistant plates before the anode and cathode. Due to the isolation, only electrons released very close to the cathode produce sufficient energetic showers by gas amplification to be measured at the anode. Therefore, the penetration point can be determined with high spatial resolution. The resistive plates also tolerate very high electric fields in the drift volume, which allows for very high drift velocities. The fast readout can be used for timing measurements.

In the endcap, muon identification typically suffers from high backgrounds of very forward activity. This gives rise to unacceptable high occupancies of the mentioned muon systems. Therefore, Cathode Strip Chambers [210] (CSCs) are used and the RPCs are replaced by Thin Gap Chambers (TGCs) [211]. They are capable to cope with the higher occupancy.

3.3 Object Identification with the ATLAS Detector

The previous sections gave a description of the ATLAS detector and its main components. It it designed to maximize reconstruction efficiency, i.e. particles that have been created should leave signals in the detector. In order to connect the basic measurements to any kind of physics, the signals have to be interpreted in terms of physical objects. The most obvious choice for the interpretation is in terms of particles. In this thesis, the following terminology is chosen: A particle is said to be reconstructed if it leaves any kind of significant signal above noise level. In this sense it can be regarded as detected. The particle is said to be identified if it is also correctly interpreted as the particle it has really been.

With these definitions, identification evidently premises reconstruction and cannot be verified on a per object basis in data. In simulated events, see Section 3.4, the identification decision can be tested with the information from the actual simulated collision products. To some extent, this can be tried as well in data with tag and probe methods. They try to provide a maximally unbiased selection of a certain object that can be assumed to originate indeed from the required particle.

The identification of particles is a complex and challenging exercise. On the one hand, the different detector systems, each of which has a large number of readout channels, provide many possibilities to access information about a reconstructed object. On the other hand, the high luminosity comes along with a constant stream of collisions, which has to be analyzed. Therefore, the huge amount of information demands for fast algorithms that scan the readout signals for characteristic patterns of certain particles. An extensive report on used algorithms can be found in [212, 213].

In ATLAS, most of the pattern recognition algorithms either directly search for an elementary particle, e.g. a muon, or they look for their visible decay products. The latter is needed if the particle decays or hadronizes before the detector arrival, e.g. a tau or quark. The algorithm are designed to have maximal efficiency, i.e. if the particle is present, it should be identified with high probability. At the same time, the fake rate should be small. This means that no object of other origin should be misidentified as the searched object.[5] There is an anticorrelation between mistag probability and identification efficiency that

[5] Technically speaking, the term *fake rate* denotes the mistag probability of a certain object as another object. Hence, it is not a rate in the sense of occasion per time but mistag per occasion of object. However, this expression will be used to follow the conventional nomenclature.

is steered by the strictness of the algorithm: Very tight constraints on the object suppress fakes, but at the same time might reject a candidate that has been the object searched for. Vice versa, looser requirements might have higher efficiencies for the object, but also high mistagging rates.

Basically, the identification strategies for different particles follows the same outline: It starts at some *seed* that is expected to appear for the object, e.g. a track or an energy deposition in the calorimeter that exceeds a specific threshold. From this starting point, it gathers information about the vicinity of the seed, for example additional tracks or topological information about the surrounding energy distribution in the calorimeters. From this information, the algorithm decides which signals are expected to belong to the object. If a well defined object is established, it is investigated for typic characteristics and patterns that are representative for the searched object. For some objects also vetoes are applied if unexpected constellations are seen. In the following, the reconstruction of individual objects are briefly discussed.

3.3.1 Jets

Jets are bundles of hadrons produced by a common origin, e.g. a hadronizing gluon or quark or from hadronically decaying taus. Typically, they show up as topologically connected group of charged tracks, electromagnetic and hadronic energy depositions. In ATLAS, manifold approaches to find jets are used [214]. The one used for this thesis is the anti-$k_\perp$ algorithm [215, 216].

The algorithm defines distances among two entities, d_{ij}, and among the entities and the beam, d_i^B, by

$$d_{ij} = \min\left\{k_{\mathrm{T}i}^{2p}, k_{\mathrm{T}j}^{2p}\right\}\frac{\Delta R_{ij}^2}{R^2} \qquad \text{with} \qquad \Delta R_{ij}^2 = (\eta_i - \eta_j)^2 + (\phi_i - \phi_j)^2 \tag{3.12}$$

$$d_i^B = k_{\mathrm{T}i}^{2p}\,, \tag{3.13}$$

where $k_{\mathrm{T}i}$, η_i and ϕ_i are the transverse momentum, pseudorapidity and azimuthal angle of the objects, respectively. The exponent $2p$ controls the relative impact of the transverse momentum compared to geometric distance and R is an input parameter.

The algorithm compiles a list of all distances[6] from Equation 3.12 and 3.13. In the case that a distance between two entities is the smallest, the two objects are merged and the list is redone. This is repeated until the distance of one entity is closer to the beam than to any other object. In that case, the object is considered to be a complete jet and is not any longer taken into account for the other jet assemblies. The parameter R sets the resolution of the algorithm at which jets are still merged or already considered as individual objects. A large R reduces the size of the object-to-object distance and hence favors more merging before jets are complete, and vice versa for small R.

The anti-$k_\perp$ algorithm sets $p = -1$, and therefore high-p_{T} objects within the radius R are merged first with others. The softer elements follow in the order of their distance since the minimum in Equation 3.12 is governed by the high-p_{T} object. Hence, the initial seed building constituents are less affected by soft radiation of the physical jet. Different radial input parameters R have been tested in ATLAS. The choice of $R = 0.4$ has proven to be a sensible choice with respect to performance on the given detector granularity and expected topology of physical objects [214].

3.3.2 Electrons and Photons

Electron identification is based on measurements from the tracking devices of the inner detector and the electromagnetic calorimeter [217, 218]. The algorithm starts to look for seed clusters in the liquid argon

[6] All distances are in (transverse momentum)^{2p}-space.

calorimeter that exceed an energy threshold of 2.5 GeV. The search is performed by a *sliding window* algorithm [219] with a window size of about 0.075×0.125 in $\eta \times \phi$ space. An electron can be identified if a single high quality track from the inner detector can be assigned to the clusters. Therefore, the track is extrapolated beyond its last point of measurement in the ID to the calorimeter cells, where special attention is paid to the potential loss of energy and deflection of the candidate by Bremsstrahlung. The association of track and calorimeter object is tested by a comparison of track momentum to energy deposition.

For the further suppression of fake electrons from jets, information on the expected shower shape of electrons in the calorimeter is used. The track is also required to have a minimum number of hits in the inner detector and a maximal χ^2 of the track fit to the hits. In addition, the transition radiation of the TRT, see Section 3.2.2, can be used. Depending on the physics scenario in that electrons are searched, isolation is also used. Electrons are said to be isolated if they make up for 90 % of the energy of a larger cone around them.

Due to their electromagnetic interaction in the liquid argon calorimeters, photons have a similar appearance to electrons in the calorimeters and hence their identification follows the outline of the electron identification [220, 221]. Obviously, the main difference is the missing track in the inner detector, which is required to be not present. In addition to directly detected photons, there are also photons that convert in the inner detector by $\gamma \to e^+e^-$. These can be identified by two tracks with opposite curvature that originate from a common point in the inner detector. The two tracks can be tested to be an electron-positron pair by the use of the electron identification.

3.3.3 Muons

Since they are minimal ionizing particles, muons need a special detector system, see Section 3.2.4, and have a unique appearance in the detector. Their distinct signature makes muons to attractive physics objects. They are rather easy to reconstruct and identify and hence have high efficiency and accuracy in their measurement.

The different available reconstruction algorithms for muons [222] all look for signatures in the muon spectrometer (MS), where only muons are expected to appear. Other particles, like high energetic *punch throughs*, which traverse the calorimeters, might fake muon signatures. These are tried to be addressed by the `staco` algorithm [212, 223] by the combination of information from the inner detector (ID) and the MS. In the inner detector, tracks are reconstructed by a Kálmán filter [224], whereas the MS measurements are evaluated by the package `MUONBOX` [225]. The ID tracks are extrapolated to the ones in the MS and compared by the usage of the full covariance matrix of the two independent track fits. Special attention is paid to possible energy losses in the calorimeters.

Likewise for most objects, quality criteria, like minimal number of hits in a detector system and maximal χ^2 for track fits, are applied. Also calorimetric information is used since the muon is expected to have only small energy deposits. This might not be the case for muons close to jets, e.g. muons from heavy flavour quark decays. However, this analysis searches for muons of non-jet origin and hence these candidates are tried to be rejected as well. The association to the primary vertex of the interaction is also checked to reject cosmic muons.

Depending on p_{T} and η of the muon, its identification efficiency is about 90 % to 98 % [228] and the transverse momentum resolution about 2 % to 5 % for p_{T}^{μ} from 10 GeV to 10^2 GeV [227, 229]. Figure 3.3 shows these identification characteristics as a function of the muon transverse momentum. Figure 3.3(a) shows the identification probability of muons from $Z^0 \to \mu\mu$, where the term *chain 1* denotes the identification with the `staco` algorithm, which is used in this work. The efficiencies are about 95 % for muons with $p_{\mathrm{T}}^{\mu} > 20$ GeV. The precision of the transverse momentum measurement can be seen in Figure 3.3(b) for muons in the *barrel* part. The combined uncertainty from inner detector and muon spectrometer

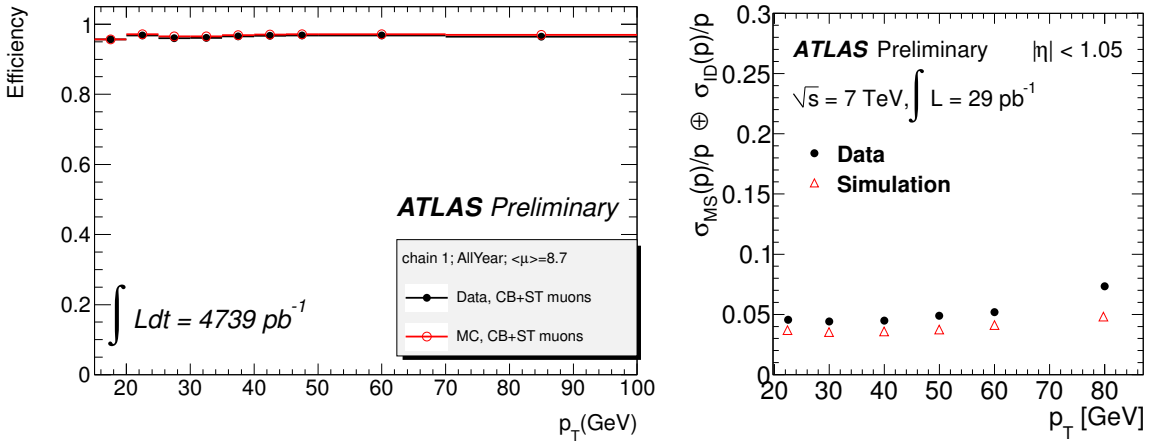

(A) Muon identification efficiency

(B) Muon transverse momentum resolution

FIGURE 3.3 Muon identification performance plots. (A): Muon identification efficiency as a function of transverse momentum [226].(B): The transverse momentum resolution as a function of transverse momentum [227]. Uncertainties from MS and ID measurement are included.

measurement is about 5 % and shows outstanding accuracy. The slightly better resolution in the simulation, see Section 3.4, is corrected by resmearing of the muon momenta in the simulation.

3.3.4 Tau Leptons

Due to their prompt decay, taus are not easy to identify. There are two types of tau decays: Leptonic decays, producing either an electron or a muon, and hadronic decays, see Section 2.3.3. Although parts of the tau's energy is lost by two neutrinos, the leptonic decays are covered by the electron and muon reconstruction algorithms. Unfortunately, its hard to identify, whether they originate from a tau decay or are of other origin.

The hadronic decays lead to jets in the sense of Section 3.3.1, and hence they are reconstructed by the same anti-$k_\perp$ algorithm with $R = 0.4$. The experimental challenge is to disentangle those jets that come from tau decays and those not coming from tau decays. This task is addressed by the tau reconstruction algorithms [230–232]. They look for jets likely to come from tau decays, while they try to reject any other object of non-tau origin. In the context of reconstructed objects, the term *tau* will denote the jet from a hadronically decaying tau in the following. Leptonically decaying taus will be explicitly labelled by their decay mode, e.g. τ_μ. Due to the hadronic jet structure, the most problematic objects that fake taus are QCD jets. They have to be efficiently suppressed due to their frequent abundance at the LHC.

In most cases, tau jets have either one or three tracks, where the sum of charges is either plus or minus one, see Table 2.3. This is already a very effective discriminant for QCD jets since they are not restricted to any number of charged particles. Therefore, some aspects of the identification are split up into one- and multi-track candidates. In the tau identification, the term *prong* is widely used for tracks and will be used as well. Taus can also be separated from jets by their specific and collimated topology in the calorimeter, as well as by their peculiar sharing of energy among its constituents. In addition, they have an impact parameter due to the finite flight length of the tau and its tracks have distinct kinematics.

In principle, all patterns used for the tau identification are motivated by either the tau's decay kinematics or the process of hadronization of colored objects, i.e. gluons or quarks. The properties are quantified by variables, which can be used in multi-variant techniques to obtain an optimal separation of tau jets

and non-tau jets. The tau identification used in this work is based on a *boosted decision tree* (BDT) [233], where the following jet discriminants are used [234]:

$$R_{\text{trk}} = \frac{\sum\limits_{i \in \text{tracks}}^{\Delta R_i < 0.4} p_{\text{T}}^{i} \Delta R_i}{\sum\limits_{j \in \text{tracks}}^{\Delta R_j < 0.4} p_{\text{T}}^{j}}$$

The track radius is the transverse momentum weighted track width, where i and j run over all tracks associated to the tau candidate within $\Delta R < 0.4$. The solid angular distance of each track is measured with respect to the tau candidate axis and p_{T}^{i} is the track transverse momentum. For one-prong candidates, this simplifies to the ΔR of the track to the candidate axis.

$$f_{\text{trk}} = \frac{p_{\text{T}}^{\text{lead. trk}}}{p_{\text{T}}^{\tau}}$$

The leading track momentum fraction is the ratio of the transverse momentum of the leading track to the total transverse momentum of the tau candidate.

$$f_{\text{core}} = \frac{\sum\limits_{i \in \text{cells}}^{\Delta R_i < 0.1} E_{\text{T}}^{i}}{\sum\limits_{j \in \text{cells}}^{\Delta R_j < 0.4} E_{\text{T}}^{j}}$$

The core energy fraction is the ratio of transverse energy within a cone of $\Delta R < 0.1$ to the one in the cone $\Delta R < 0.4$. The index i and j in nominator and denominator run over all calorimeter cells in the respective ΔR range around the candidate axis.

$$N_{\text{trk}}$$

The number of tracks associated to the tau candidate.

$$R_{\text{cal}} = \frac{\sum\limits_{i \in \text{cells}}^{\Delta R_i < 0.4} E_{\text{T}}^{i} \Delta R_i}{\sum\limits_{j \in \text{cells}}^{\Delta R_j < 0.4} E_{\text{T}}^{j}}$$

The calorimeter radius is the transverse energy weighted shower width of the tau candidate in the calorimeter. The index i and j run over all cells within a cone of $\Delta R < 0.4$ around the tau candidate axis in the electromagnetic and hadronic calorimeters.

$$m_{\text{eff}}^{\text{clust.}} = \sqrt{\left(\sum_i E_i\right)^2 - \left(\sum_i \vec{p}_i\right)^2}$$

The cluster mass is the invariant mass computed from all constituent *clusters*. These are substructures of jets that contain merged calorimeter cells, which are assumed to belong to a common object in the jet [219]. The effect of pile-up is minimized by the usage of only certain clusters as defined by a dedicated algorithm [234].

$$m_{\text{eff}}^{\text{trk}} = \sqrt{\left(\sum_i E_i\right)^2 - \left(\sum_i \vec{p}_i\right)^2}$$

The track mass is the invariant mass computed from all tracks of the candidate. The index i runs over all tracks that are associated to the tau candidate and it is only used for multi-prong tau candidates.

$$S_{\text{T}}^{\text{flight}} = \frac{L_{\text{T}}^{\text{flight}}}{\delta L_{\text{T}}^{\text{flight}}}$$

The transverse flight path significance is the significance of the secondary vertex displacement of multi-prong candidates. $L_{\text{T}}^{\text{flight}}$ denotes the decay length in the transverse plane and $\delta L_{\text{T}}^{\text{flight}}$ the corresponding estimated uncertainty.

$$S_{\text{lead. trk}} = \frac{d_0}{\delta d_0}$$

The leading track impact parameter significance is the ratio of distance to uncertainty of the closest approach of the leading track to the reconstructed primary vertex in the transverse plane.

$$f_3^{\text{lead clust.}} = \frac{\sum\limits_{i \in \text{clust.}}^{3} E_i}{\sum\limits_{i \in \text{clust.}}^{N} E_i}$$

The first three leading clusters energy ratio is the ratio of energy in the three leading clusters associated to the candidate divided by the energy of all N associated clusters. In the case of $N \leq 3$ the quantity $f_3^{\text{lead clust.}}$ is always 1.

$$\Delta R_{\text{max}} = \max\left\{\Delta R_i^{\text{trk}}\right\}$$

The maximal ΔR is the maximal solid distance of tracks in η-ϕ-space, where i runs over all tracks. For one-prong candidates it is equal to the track radius and hence not considered.

The BDT is trained separately for one- and multi-prong candidates as well as for different pile-up conditions, where events with equal or less than five or with more than five vertices are considered. The training is performed by the TMVA package [235, 236] with simulated real taus and quark or gluon fakes. The conjoint use of all discriminating quantities leads to a single BDT jet score. It is close to one for tau-like objects and close to zero for non-tau like. The final choice for the BDT jet score cut can then be tuned for each analysis, leaving much freedom in the analysis outline.

In order to provide common numbers and recipes for systematic uncertainties for the tau identification, the continuous BDT jet score cut is limited to three benchmarks of different strictness: loose, medium and tight. They are defined by a signal efficiency for true one-prong taus of 60 %, 50 % and 30 % and true three-prong taus of 65 %, 55 % and 35 %, respectively. The cuts on the BDT that fulfill the required efficiencies are binned in transverse momentum of the reconstructed candidate. This compensates for the p_{T}-dependence of the BDT jet score distribution.

Figure 3.4 shows performance plots of the tau reconstruction. Figure 3.4(A) and (B) display the transverse momentum dependence of the identification probability for BDT medium taus from $Z^0 \to \tau\tau$ in data and MC. The efficiencies are much smaller compared to muons (see Figure 3.3(A)). Also the precision of the transverse momentum measurement in Figure 3.4(E) demonstrates a worse resolution compared to muons (see Figure 3.3(B)). This is particularly true for the p_{T}^{τ} region below 100 GeV, where the uncertainties are bigger by a factor 2 to 3.

Finally, Figure 3.4(C) and (D) show the fake tau rejection versus truth tau efficiency for different cuts on the BDT output. For comparison, a different identification approach that uses a likelihood is given. It shows worse performance and hence the BDT is used for this analysis. For signal efficiencies of about 60 %, approximately 5 % (2.5 %) of one-(multi-)prong non-tau jets are still misidentified as tau jets. These fake tau contributions make high demands on the background estimates. Typically, they are caused by jets from all kinds of QCD processes, underlying event activity, multiple parton scattering and pile-up collisions, which are only known up to limited precision.

In addition to QCD jets, electrons are the second most likely tau-faking objects. The rejection of electrons is based on a different set of variables, where some overlap to the presented exists. These variables are also used by a BDT and optimized on simulated taus and electrons. In general, tau fakes from elec-

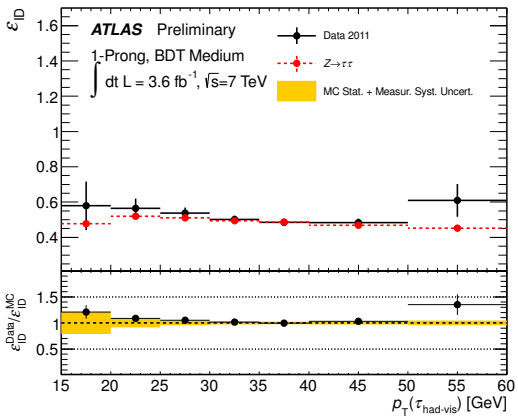

(A) 1-pr.: τ identification eff. for BDT medium

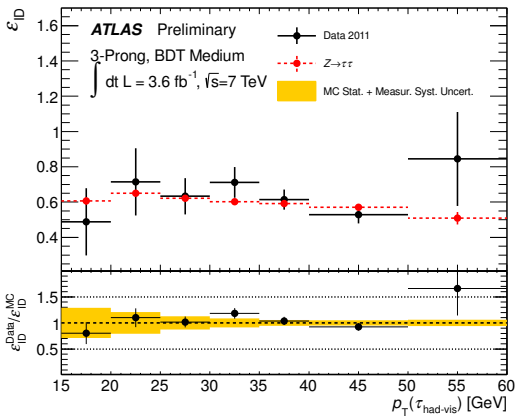

(B) 3-pr.: τ identification eff. for BDT medium

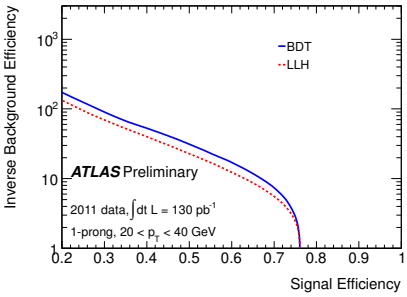

(C) 1-pr.: efficiency vs. rejection

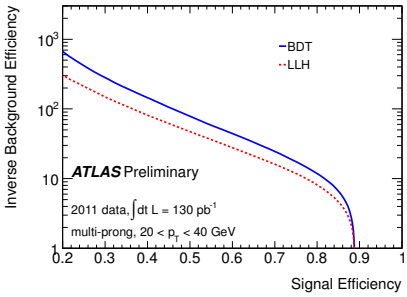

(D) 3-pr.: efficiency vs. rejection

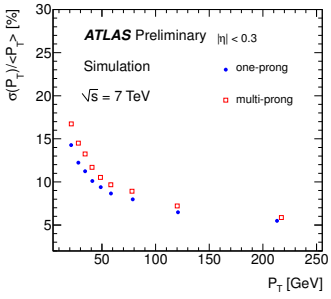

(E) p_{T}^{τ} resolution

Figure 3.4 Tau identification performance plots [231, 237]. The transverse momentum dependence of the tau identification efficiency of BDT medium taus: (A) one-prong and (B) three-prong taus. Fake tau rejection versus truth tau selection efficiency for (C) one-prong and (D) three-prong taus. (E): The transverse momentum resolution of tau reconstruction.

trons have shown to play only a minor role in this analysis and hence are not explained in more detail. Information on implementation and performance can be found in [234].

3.3.5 Missing Transverse Energy

Among many proposals of new physics, as well as for many interesting Standard Model physics, the occurrence of only weakly interacting particles is predicted. Since they escape detection, their energy cannot be measured directly. Nonetheless, their transverse energy can be measured by the assumption that the initial state of interacting partons has no transverse momentum and hence the total transverse momentum of the event should be balanced.

In ATLAS, the missing energy is measured in the following way [238, 239]: After the reconstruction of the full event, the vectorial sum of the transverse energy from all reconstructed objects is calculated. All energy depositions that are not associated to a physical object are also added vectorially in the transverse plane. The total transverse momentum from the objects is then corrected by these *soft terms*. Finally, the missing transverse energy is the remaining, negative imbalance of the summed transverse momenta.

The measurement of the object related energies needs calibration, which varies for different objects. Therefore, the final energy input from any object to the $E_{\mathrm{T}}^{\mathrm{miss.}}$ depends on the interpretation of this object.

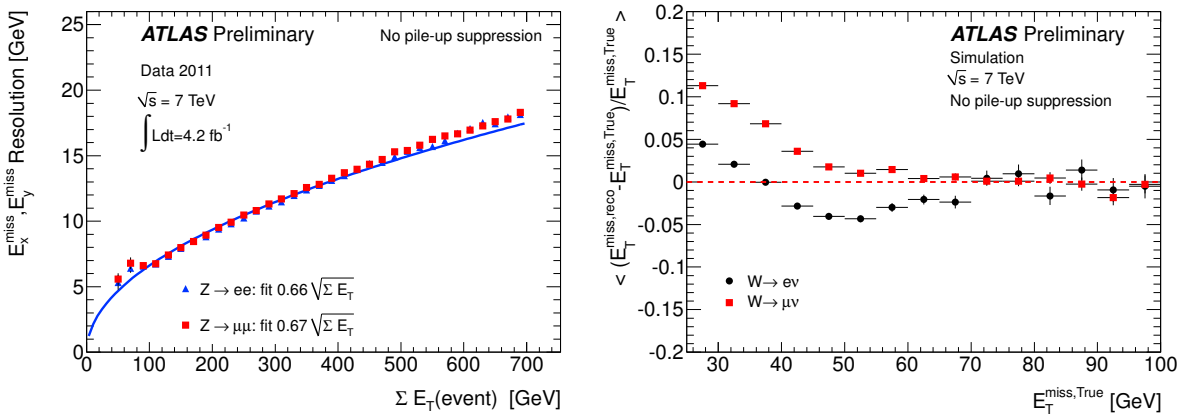

(A) $E_{\mathrm{T}}^{\mathrm{miss.}}$ resolution

(B) $E_{\mathrm{T}}^{\mathrm{miss.}}$ linearity

FIGURE 3.5 Performance plots for the reconstruction of missing transverse energy [239]. (A): $E_T^{miss.}$ resolution in events with no expected missing energy. (B): $E_T^{miss.}$ linearity in MC events with expected missing momentum.

E.g. the same object might have different contribution to the $E_{\mathrm{T}}^{\mathrm{miss.}}$ if it is considered to be an electron or a jet. In particular, muons have to be treated carefully since their energy is not measured in the calorimeters. Their transverse momentum needs to be provided by the muon reconstruction algorithms. If a muon should be missed in the reconstruction, its energy would not contribute to the $E_{\mathrm{T}}^{\mathrm{miss.}}$ calculation and hence an imbalance in the transverse momentum would lead to faked missing energy.

Figure 3.5(A) shows the $E_{\mathrm{T}}^{\mathrm{miss.}}$ resolution as a function of the total transverse energy sum in the event. Here, $Z^0 \to ee/\mu\mu$ data events are selected, where no missing energy is expected. The misreconstructed $E_{\mathrm{T}}^{\mathrm{miss.}}$ is then considered as the expected resolution for the measurement of real missing energy. Due to the finite energy resolution of the object reconstruction, the mismeasurement increases with larger energy sum. In events with large activity, the same relative fluctuations translate into larger absolute uncertainties. The linearity of real $E_{\mathrm{T}}^{\mathrm{miss.}}$ measurement can be seen in Figure 3.5(B). It gives the normalized difference between reconstructed and truth missing energy in $W \to e/\mu$ in the simulation, see Section 3.4. Above $E_{\mathrm{T}}^{\mathrm{miss.}} > 40\,\mathrm{GeV}$ the deviation is below 5 %.

3.3.6 Quark Flavor Tagging

The appearance of heavy flavour quarks is a signature of interesting Standard Model physics, e.g. Top physics, and as well as for searches of new physics like $H \to b\bar{b}$ or SUSY with stops. The tagging of b-quarks is mainly based on the measurement of displaced vertices from long lived hadrons that come from b decays [240, 241]. The track kinematics and the substructure of jets are fitted and information about impact parameter and secondary vertices are gathered. These are used in a neural network by the `JetFitterCombNN` package [242] to obtain maximal discrimination power. The b-tagging performance depends on the event environment, jet kinematics and required strictness of the b-tagging algorithm. Typical reconstruction efficiencies are 60 % [243] with a mistag probability of few percent [244].

3.3.7 Trigger

The LHC collides bunches of protons at the experiments with very high rates. Since the interactions are dominated by QCD, most of the collisions are of no interest for the experiments and can be filtered out.

In ATLAS, this is done by a three staged trigger system [245, 246] that looks for events with potentially interesting physics. At design luminosity, bunches of 10^{11} protons will collide with a frequency of 40 MHz, where about 25 proton-proton collisions are expected per bunch crossing.

This unmanageable amount of data is reduced to roughly 200 Hz in full detector readouts, where each event has approximately the data size of 1.6 MB. The term *event* denotes a concurrent detector readout of all proton-proton collisions from one bunch crossing that was decided to be kept by the trigger chain. Since most analyses are done on a sequence of full detector readouts, the term event will be widely used in the following. It contains several proton-proton collisions from one bunch crossing, where only one is of interest in most cases. The phenomenon of overlaying proton collisions in one readout is called *pile-up* and its conditions are typically given in terms of average p-p interactions per bunch crossing $\langle\mu\rangle$ or the number of reconstructed vertices.

The decision to keep or reject an event is done sequentially in three steps: Level 1 (L1), Level 2 (L2) and the event filer (EF), where each stage reduces the stream of passing events. Since the incoming rate gets smaller from stage to stage, the restrictions on available decision time relax. Hence, the amount of information and algorithm complexity that is used for this selection can be increased from stage to stage. There are numerous different triggers, which either look for certain interesting objects, e.g. high p_{T} leptons or missing transverse energy, or combinations of them. In this sense, triggers make a preliminary decision about what the event is expected to contain. The trigger used for this analysis is a muon trigger, as will explained in Section 4.1.3 after the object selection has been fixed.

3.3.8 SUSY Sensitive Variables

Jets, missing transverse energy and tau leptons have been shown to be promising search patterns. In addition to the particle objects, the entire event topology can be used as a SUSY sensitive signature. Besides the missing energy, the hadronic and leptonic event activity is measured by

$$H_{\mathrm{T}} = \sum_{i=1}^{N} p_{\mathrm{T}}^{\mathrm{jet}} + \sum_{\ell=e,\mu,\tau} p_{\mathrm{T}}^{\ell} \qquad \text{and} \qquad m_{\mathrm{eff.}} = H_{\mathrm{T}} + E_{\mathrm{T}}^{\mathrm{miss.}} \,. \tag{3.14}$$

These variables quantify the associated occurrence of missing transverse energy, hard jets and high-p_{T} leptons. These are expected to be more energetic in SUSY compared to typical transverse momenta of these objects in the Standard Model. In this sense, high H_{T} or $m_{\mathrm{eff.}}$ is considered to be SUSY like, whereas low values are Standard Model like. To reduce influence from pile-up jets, the sum in Equation 3.14 runs only up to $N = 2$ leading jets and both are required to have $p_{\mathrm{T}}^{\mathrm{jet}} > 25$ GeV. In addition, the ratio of $E_{\mathrm{T}}^{\mathrm{miss.}}$ to $m_{\mathrm{eff.}}$

$$\frac{E_{\mathrm{T}}^{\mathrm{miss.}}}{m_{\mathrm{eff.}}} \tag{3.15}$$

quantifies the contribution of missing energy to the total effective mass. In QCD events with high transverse activity, a considerable amount of missing energy could be caused by mismeasured jet energies, see Figure 3.5(a). In that case, the faked missing energy increases with the transverse hadronic activity. Since only the mismeasured energy can be seen as $E_{\mathrm{T}}^{\mathrm{miss.}}$, it is expected to make up a rather small part of the real transverse activity. The latter is the sum of H_{T} (measured sum) and $E_{\mathrm{T}}^{\mathrm{miss.}}$ (missing components), which make up to $m_{\mathrm{eff.}}$. In this sense, the ratio from Equation 3.15 can be considered as a $E_{\mathrm{T}}^{\mathrm{miss.}}$ significance, where small values are QCD like and high values are SUSY like.

Among the backgrounds that can contribute with high $E_{\mathrm{T}}^{\mathrm{miss.}}$ or H_{T}, the most important ones include $W^{\pm}$ bosons, e.g. Top and W+jets. They can be suppressed by cuts on the transverse mass

$$m_{\mathrm{T}}^{\ell} = \sqrt{2p_{\mathrm{T}}^{\ell}E_{\mathrm{T}}^{\mathrm{miss.}}\left\{1-\cos\left[\Delta\phi\left(\ell, E_{\mathrm{T}}^{\mathrm{miss.}}\right)\right]\right\}}\,. \tag{3.16}$$

If the lepton and the missing transverse energy come from a $W \to \ell\nu_{\ell}$ boson decay, the transverse mass is constrained to be below the W mass. In SUSY events, $E_{\mathrm{T}}^{\mathrm{miss.}}$ and leptons can be produced uncorrelated in their kinematics and hence might exceed m_W.

3.4 Simulation of the ATLAS Experiment

The standalone measurements from the data taken at the ATLAS experiment come with the problem of lacking comparability to expectations. A new kind of physics might manifest itself by an excess of rare signatures, but any evidence for this relies on a precise prediction on the level that should be exceeded. In a SUSY search, this level is defined by the background contributions from the SM. Therefore, the complete experiment can be simulated by the use of Monte-Carlo techniques under the conditions of well defined physics in the collisions. This allows to predict the expected signatures for any kind of SM and non-SM physics, which can be compared to the observation.

The computer based replication of a certain physics scenario in proton-proton collisions and the simulation of the detector response on this physics is an extremely complex task, for which the `Athena` software framework [247, 248] has been developed. In the first instance, the simulation of a certain physics scenario necessitates the generation of events of this model. This includes the full event kinematics, the decay of all particles that are unstable on detector scale and the hadronization of all strongly interacting particles in the conditions of overlaying proton-proton collisions. These bare physics events then undergo the detector simulation, where the interaction of all produced particles with all detector components along its path is simulated. The interactions are transferred into the readout signals, which enter the same reconstruction algorithms that are used for the data. In the following, this simulation chain shall be explained a bit more in detail since it is extensively used in the analysis.

3.4.1 LHC Simulation by Event Generators

The first step of the simulation is the generation of the event physics in proton-proton collisions. The considered physics is randomly realized according to its probability of occurrence, with the kinematics, decay and hadronization of all particles that are unstable at detector scale. This can be performed by different event generators [249]:

`HERWIG` [250, 251] starts with the simulation of the hard process, i.e. the interaction of two partons from the colliding protons with a set of outgoing primary particles. The matrix element is computed to lowest order in perturbation theory at the momentum transfer Q. After the hard process, initial and final state parton showers are generated. The initial partons with momentum fraction x can radiate partons with a energy, such that the momentum transfer Q is matched. The outgoing particles also can radiate parton showers, e.g. gluons.

In the next step, decays of particles are considered that have lifetimes smaller than the hadronization time scale. These particles can radiate parton showers as well. After that, all particles that participate in hadronization are present and strongly interacting particles are translated into hadrons. Since QCD perturbation theory is not applicable in the hadronization, a phenomenological model is used. It considers the primary produced particles, all parton showers and the proton

remnant. For the latter, the multi-parton interaction model Jimmy [252] is used. Finally, all other particle decays, e.g. tau decays, are simulated until only particles remain that are stable on detector scale. Spin correlations in the decays are taken into account to guarantee realistic event kinematics. The decay of tau leptons and radiation of photons by charged particles is carried out by TAUOLA [253, 254] and PHOTOS [255], respectively and MRST2007 LO* PDFs [256] are used. HERWIG is used for the generation of all SUSY signal processes.

Pythia [257, 258] features a high variety of hard QCD subprocesses, where the matrix element is calculated in leading order and partons are radiated by the initial and final particles of the hard interaction. Short living particles may decay before hadronization starts, which follows the Lund string model [259, 260]: Diverging colored particles are attached by a string that carries energy proportional to their distance. The string can break up and create new particles, e.g. quark-antiquark pairs. Thereby, the string length between the initial colored particles and their energy is reduced. This is repeated until color neutral objects, i.e. mesons and baryons, are formed. These can either again decay or be stable on detector scale. Since Pythia shows a good description of strong interactions, it is used as event generator for QCD with MRST2007 LO* PDFs.

Alpgen [261] starts with a certain final state configuration, e.g. the multiplicity of final hard partons. Then, all processes leading to this wanted state are considered according to the leading order matrix element calculation. Thereby, leading order matrix elements are used for the hard interaction with up to five additional hard partons. This gives a realistic picture of electroweak gauge boson production in association with high hadronic activity. These events might contribute to the searched SUSY patterns and hence Alpgen is used for W and Z events with additional jets. The hadronization in these events is carried out by HERWIG, which can be interfaced to Alpgen for that purpose. Alpgen uses CTEQ6L1 [123] as PDF set.

MC@NLO [262] calculates matrix elements up to second order. Unfortunately, there is an overlap in the described physics of higher order diagrams and the used parton shower algorithms. Principally, the latter are a phenomenological approximation of higher order predictions. MC@NLO matches the NLO calculation to the parton shower algorithms by subtraction of double counted events on a statistical basis [263]. This is realized by the use of negative event weights. Particularly, the event kinematics of processes that include high mass states are well described by this approach. Hence, it is used for top pair [264], single top [265] and di-bosons production. The used PDF set is CT10 [266], which includes NLO PDFs.

AcerMC [267] is an event generator for Standard Model processes. The matrix element for the hard process is calculated by MadGraph [268, 269] and HELAS [270, 271], where the final phase space of the n-particle system is calculated by the Kajantie-Byckling formalism [272]. Additional parton showers, hadronization and particle decays can be performed either by Pythia or HERWIG via interfaces to the AcerMC output. In the t-channel production of single top, particles tend to have very forward direction, where MC@NLO shows less quality in the description of the event kinematics. Therefore, AcerMC is used for these processes.

The event generation is done when all colored states hadronized only particles remain that are stable on detector scale. From here, the physic event is complete and particles can undergo the detector simulation.

3.4.2 ATLAS Detector Simulation

After the event generation, the four-momenta and quantum numbers of all generated particles are known and their interaction with the detector can be simulated. Starting from the particles origin, the trajectory

of each particle is propagated through the magnetic fields and the flight direction of charged particles is deflected. As soon as a particle reaches a detector component, its interaction is simulated by GEANT4 [273, 274], which is interfaced to a complete virtual geometric replica of all detector components in a computer simulation [275].

The interaction of particles with the detector material releases additional particles, e.g. showers in the calorimeter or free charge carriers in the semiconductor detectors, which are then added to the simulation. By these interactions, particles are either stopped by their energy loss, like electrons in the liquid argon calorimeter, or they move beyond the spatial reach of the detector, e.g. muons. The software propagates the produced primary and secondary particles to the readouts, e.g. in the electric field of applied drift voltages. Here, the induced electric signals are mimicked by the amount of simulated charge carriers and hence the expected physical readouts from the original interaction are estimated.

The predicted detector response on the initial physics event can then undergo the normal reconstruction algorithms, as explained in Section 3.3 and the simulation is finished. This simulation chain has been extensively checked and validated, e.g. [276, 277], to have a reliable detector response for any input physics model. In the following, the reconstructed events that are obtained from simulation will be entitled as Monte-Carlo (MC) in contrast to the measured data from the experiment.

3.4.3 Standard Model Monte-Carlo and Dataset

The data used in this analysis were taken with the ATLAS detector from 22$^{\text{nd}}$ of March to 30$^{\text{th}}$ of October in 2011 and correspond to an integrated luminosity of $4.7\,\text{fb}^{-1}$ [278]. They are subdivided into data-taking periods, run numbers, luminosity blocks and finally events. The used periods are B2 and D to M. The periods A and B1 of the year 2011 are excluded due to non-operating magnet systems in the detector and period C was taken with lower center-of-mass energy. The periods that follow M are heavy ion collisions, which are not considered for this analysis. From Period J onwards, the LHC increased the beam currents, which leads to higher instantaneous luminosity. This is reflected in tighter thresholds for triggers.

All possible contributions from the Standard Model can be evaluated by the MC techniques as explained above. The used samples are summarized in Tables A.1 to A.8 in Appendix A and will be combined to Top, W+jets, Z^0+jets, di-bosons, Drell-Yan and QCD in the following. For the combination of the processes, all samples are summed up with corresponding luminosity weight so that they represent MC simulations of $4.7\,\text{fb}^{-1}$. For all MC and data samples, the production tag p832 is used. This tag specifies the parameter setup in the reconstruction chain and is recommended for 2011 data analysis.

The differences in pile-up conditions in data and the one used for MC generation is corrected by reweighting. The MC events are reweighted so that the distribution of average number of interactions per bunch crossings agree in data and MC. In addition, MC is rescaled on object basis according to the differences in data and MC of electron and muon identification efficiency. The scale factors are estimated data-driven in bins of p_{T} and η by the combined performance groups for these objects. This procedure is also performed for b-tagging, whenever it is used. Potential differences in the tau lepton reconstruction are considered separately in this analysis. Also differences in the trigger efficiencies in data and MC are corrected by data-driven scale factors at event basis.

3.4.4 Analysis Software

Technically, the rescaling and reweighting as well as the object identification definitions are realized by the SUSYTools package.[7] All data and MC samples are analyzed with the version 00-00-67, which is the appropriate tag for the used datasets. The package itself gathers different analysis tools that provide

[7] https://svnweb.cern.ch/trac/atlasoff/browser/PhysicsAnalysis/SUSYPhys/SUSYTools.

recommended definitions of objects and common recipes for the evaluation of systematic uncertainties. Furthermore, the required corrections for pile-up and object rescaling of the MC are provided. The evaluation of the obtained information is done within the analysis framework `root` [279, 280]. It is used for all calculations and the visualization of information.

Chapter 4

Probing the Standard Model

Controlling Backgrounds

This chapter investigates the Standard Model (SM) backgrounds and their contributions to the analysis. The search for taus, missing transverse momentum and jets has already been motivated from a theoretical perspective in Sections 2.3 and 2.4. Since the expected background contributions heavily depend on the outline in the object selection, it shall be derived also under consideration of the instrumental and experimental characteristics, as explained in Chapter 3.

4.1 Baseline Event and Object Selection of the Analysis

The final selection of objects in the SUSY search and the events that contain them succumbs to several demands, which are described in the following. The baseline event and object selection is deduced from data quality requirements, reconstruction and identification issues and the goal to combine the results with other analyses. Particularly, the challenge connected to the identification of hadronically decaying tau leptons is considered.

4.1.1 Pre-Selection

In the first instance, events that enter the analysis are required to be taken under good beam and detector conditions by a good runs list. It rejects any recorded event, where either the reconstruction might have suffered from a non-operating detector component or beam conditions are not appropriate for the analysis. The considered events correspond to an integrated luminosity of $4.7\,\mathrm{fb}^{-1}$ with an uncertainty of $1.8\,\%$ [278, 281]. In addition to the hardware requirements, also a reconstruction based event cleaning is done to avoid fake measurement of jets and $E_{\mathrm{T}}^{\mathrm{miss.}}$ [282] due to badly measured objects. Any further choice in the events is done on this pre-selection.

4.1.2 Particle Objects

In general, high lepton multiplicities might be a powerful discriminant because they are only rarely expected in the SM, but might be copiously present in SUSY. However, the low abundance of these events in the SM impede precise background predictions since rare backgrounds can be studied only with very limited statistics. For tau-rich SUSY models, final states with high tau multiplicity among the leptons might be also well suited for optimal sensitivity. However, the standard tau reconstruction only considers hadronic decays, and pure hadronic final states have high fake contributions at a hadron collider. Furthermore, they increase the experimental challenges related to hadronic tau reconstruction. This situation is illustrated in Table 4.1.

This problem is tackled by the extension of pure hadronic tau searches to final states with at least one leptonically decaying tau. The reconstruction of light leptons can be shown to be much more reliable, e.g. they have much smaller fake rate and higher efficiency, see Section 3.3. In addition, the presence of

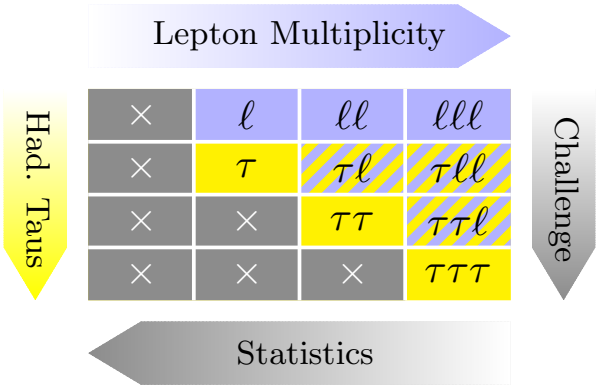

Table 4.1 Lepton and tau multiplicities in SUSY searches. The mixed hadronic tau and light lepton final states are targeted in this analysis.

a light lepton will be shown to be beneficial for many aspects of the analysis. Particularly, it can be used to study the hadronic tau identification in the busy event topologies of SUSY analyses. These results can then be transferred also to other SUSY searches with hadronically decaying taus.

The mixed final state of light leptons and hadronic taus also expands the search pattern of soley hadronic taus [283] and closes the gap to the existing di-lepton searches [284]. The choice of the light lepton flavour could be seen to have a rather large impact on the analysis outline and hence only one flavour is considered. Due to the better muon identification performance, it has been favored over the electron, so that final states with muons and hadronic taus are searched.

The requirements in the object selection are further specified to allow for a common interpretation of results from several analyses. Here, the di-lepton, di-tau and single tau analyses are considered. The statistical combination of different search channels can be achieved by the design of analyses that are free of overlap in their event selection. To evade any correlation among different channels in any aspect of the analysis, this should be instantiated at an early stage in the event selection in a way, such that each analysis can retain its maximal discovery potential. The layout of the object selection is well suited for that purpose. To avoid any overlap to di-lepton final states, exactly one muon is required and events with electrons are vetoed as well to be free of any overlap to the electron with taus search. Since all other tau analyses veto on light leptons, all possible tau multiplicities can be considered. This leads to the requirements

$$N_\mu = 1 \qquad \text{and} \qquad N_e = 0 \qquad \text{and} \qquad N_\tau \geq 1 \tag{4.1}$$

for the object selection.

For low-p_T leptons, fake rates and efficiencies are typically not well modelled in the MC, which is needed for data and MC comparison. Especially tau leptons suffer from these effects and hence they are required to have $p_\mathrm{T}^\tau > 20\,\mathrm{GeV}$. For further suppression of fakes, taus are required to have either one or three tracks with charges that sum up to $q_\tau = \pm 1$. This requires that the tau is in the reach of the trackers $|\eta_\tau| < 2.5$. A BDT based electron veto is applied and the association to the primary interaction vertex is checked to reject fakes from pile-up collisions. The final identification decision is based on the BDT discriminant (see Section 4.3) with either loose, medium or tight strictness. The optimal working point for the tau identification will be given in Section 5.1.3, after a reliable background estimate has been established in this chapter.

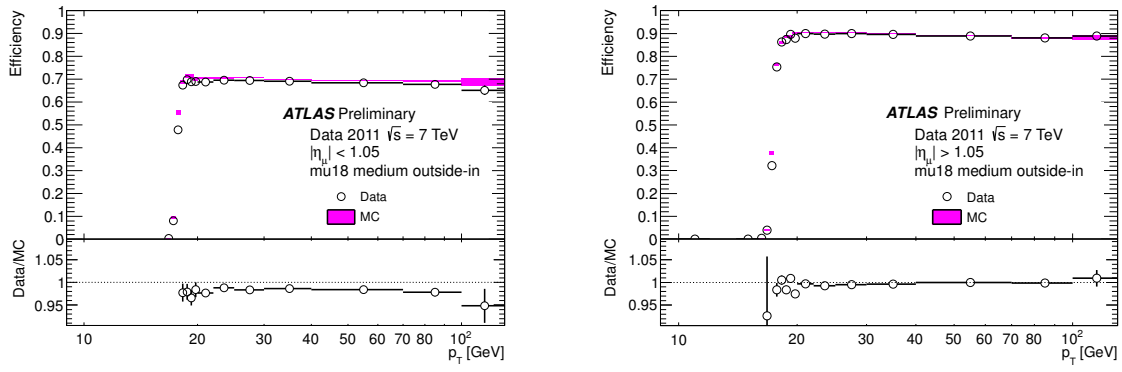

(A) Muon trigger eff.: Barrel

(B) Muon trigger eff.: Endcaps

FIGURE 4.1 Muon trigger efficiency versus reconstructed transverse muon momentum in (A) the barrel and (B) the endcap regions [285]. Data efficiencies are obtained from tag and probe methods in $Z^0 \to \mu\mu$.

The muon identification follows the strategy as given in Section 3.3.3. In addition, muons from tau decays and also prompt muons are expected to be isolated. That means that no significant energy around their track is deposited in the calorimeters. This is not the case for muons from heavy quark decays and muons that are faked by jets. Therefore, muons are required to have less than $1.8\,\text{GeV}$ of energy in a cone of $\Delta R < 0.2$ around their track.

4.1.3 Analysis Trigger

Its striking appearance in the detector suggests to use the muon to trigger the event because muons have a high trigger efficiency [228, 285]. The L1 muon trigger uses the muon spectrometers, where it looks for coincident hits in the RPCs or TGCs. These are validated by the L2 and EF muon trigger with additional information from the MDTs and CSCs as well as from inner detector measurements.

The chosen trigger is designed to detect muons with $p_{\text{T}}^{\mu} > 18\,\text{GeV}$ and the selected muon is required to be matched to the trigger. The trigger efficiency modelling in the MC is corrected by a p_{T} and η dependent scale factor to ensure good data-MC agreement [228]. Softer transverse momentum thresholds, i.e. $p_{\text{T}}^{\mu} < 18\,\text{GeV}$, are affected by erroneous triggering with unaffordable rates. A softer muon transverse momentum might also introduce large systematic uncertainties on trigger efficiencies. Figure 4.1 shows the trigger efficiency for muons as function of their transverse momentum. The efficiency in data is measured by tag and probe techniques in $Z^0 \to \mu\mu$ and the small difference in data and MC is corrected by trigger scale factors [285].

For period J and onwards, the luminosity conditions changed and this trigger got prescaled, i.e. only a subset of its events is recorded. Therefore, triggers with tighter requirements have to be chosen, which can be achieved either by tighter muon criteria or additional objects. Since many aspects of the analysis might be correlated to the muon identification criteria, these should be the same for all data and MC. Any change in the muon trigger might bias the composition of selected muons, so that the muon trigger requirements are maintained for all periods. The muon selection would also suffer from a higher p_{T} threshold because muons from tau decays already lose energy by two neutrinos and hence tend to be soft.

Object	Name	Occurrence	Transverse Momentum
muon trigger	`EF_mu18`	`true`	$p_{\mathrm{T}}^{\text{trig. }\mu} > 18\,\mathrm{GeV}$
muon and jet trigger	`EF_mu18_L1J10`	`true`	$p_{\mathrm{T}}^{\text{trig. jet}/\mu} > 10/18\,\mathrm{GeV}$
jets	`jet_AntiKt4TopoNewEM`	$N_{\text{jet}} \geq 1$	$p_{\mathrm{T}}^{\text{jet}} > 50\,\mathrm{GeV}$
muon	`mu_staco`	$N_{\mu} = 1$	$p_{\mathrm{T}}^{\mu} > 20\,\mathrm{GeV}$
taus	`tau`	$N_{\tau} \geq 1$	$p_{\mathrm{T}}^{\tau} > 20\,\mathrm{GeV}$

Table 4.2 The required objects in the event selection. The field Name *denotes the variable name as used in the ATLAS data format. The single muon trigger is used for periods B2 to I and the muon plus jet trigger for periods J to M.*

The trigger is tightened by a logic *and* with an additional object. This object should have as loose as possible requirements so that still many events with muons are kept. On the other hand, it should ensure enough rejection to allow for unprescaled triggering. Among many possibilities, a combination with a jet trigger has been chosen. With respect to physics, this can be justified by the search for SUSY with additional hadronic activity as explained in Section 2.3: Jets are expected in any case in SUSY and hence will not reduce the final significance of the analysis. From the technical side, the decision was supported by the existence of common systematic recipes and performance studies that can be used for the analysis. The p_{T} for the jets that shall be triggered is 10 GeV.

Though also low-p_{T} objects might be interesting for the analysis, lower bounds on their transverse momenta are needed for technical and experimental reasons. One is related to so-called trigger plateau cuts. The efficiency of a trigger depends on the transverse momentum of the object it is trying to find. This dependence is described by trigger turn-on curves. To guarantee agreement between data and MC, the minimal required transverse momentum of a triggered object is placed in the lower region of the plateau of the turn-on curve. This ensures a robust MC description of the trigger efficiency in data, which could be mismodelled in the turn-on phase.

For muons, this requirement leads to $p_{\mathrm{T}}^{\mu} > 20\,\mathrm{GeV}$, which is only 2 GeV above the design trigger threshold due to the good performance of muon reconstruction. For jets, the turn-on phase is much broader in the momentum spectrum and reaches the plateau above $p_{\mathrm{T}}^{\text{jet}} > 50\,\mathrm{GeV}$. This cut is applied regardless of the data taking period to have a common kinematic selection for all data and MC events. Since the trigger can fire for any jet type, the $p_{\mathrm{T}}^{\text{jet}}$ threshold can be exceeded by the tau as well. In that sense, the reconstructed tau is considered as a jet and either tau jets or non-tau jets can fire the jet trigger. The requirement from Equation 4.1 and the trigger plateau jet constitute the object selection of the analysis and is summarized in Table 4.2.

To avoid ambiguities in the object definitions, reconstructed objects undergo an *overlap removal* before the object selection is required. This avoids that a single object might be considered as two different objects in the analysis. E.g. a jet should not be considered as jet in $m_{\text{eff.}}$ if it is already identified as a tau. Thereby, preference is given to the object interpretation that is assumed to be more reliable. Two different objects, e.g. a tau and a jet, are considered as the same object if they are closer than a given ΔR. If there are such ambiguities, they are removed in the following order:

1. Electrons and muons veto taus within $\Delta R < 0.2$
2. Electrons and taus veto jets within $\Delta R < 0.2$.
3. Jets veto muons within $\Delta R < 0.4$. These muons are assumed to be either fakes or from heavy quark decays.

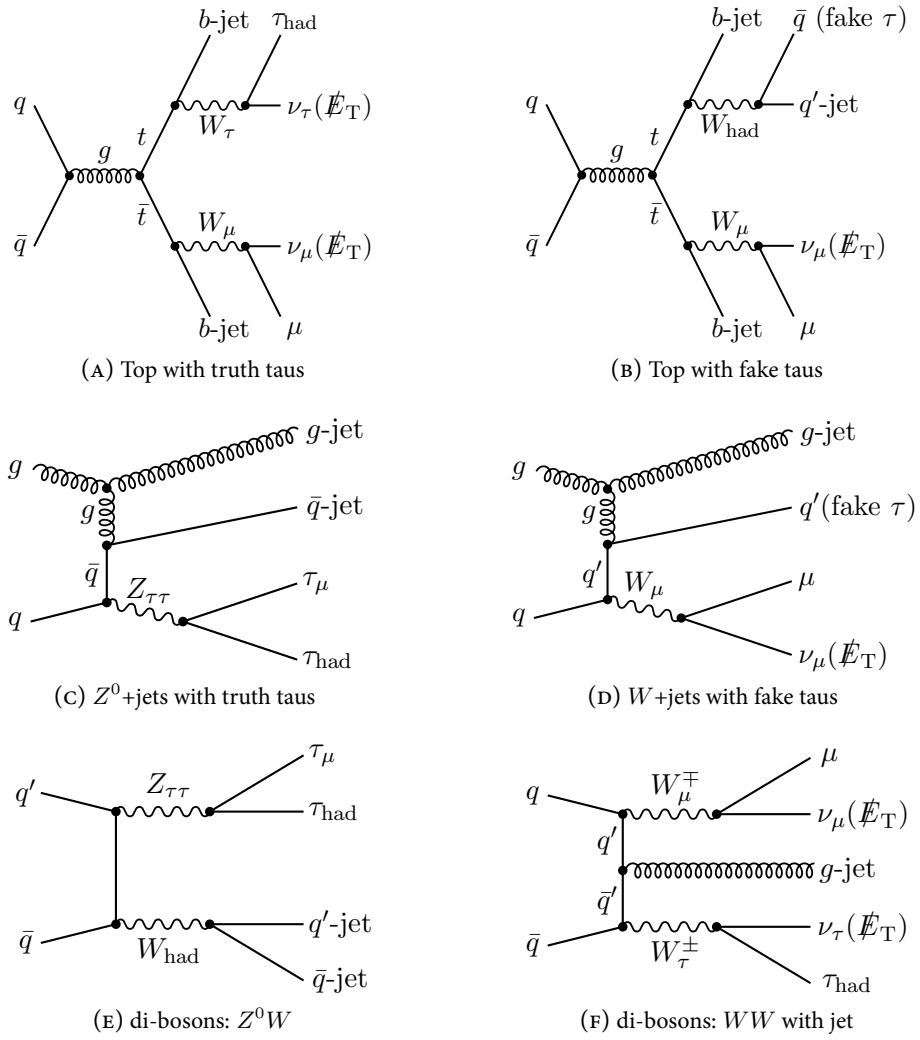

(A) Top with truth taus

(B) Top with fake taus

(C) Z^0+jets with truth taus

(D) W+jets with fake taus

(E) di-bosons: Z^0W

(F) di-bosons: WW with jet

FIGURE 4.2 Possible SM contributions to the search pattern of a muons, taus, jets and missing transverse energy. Subscripts of unstable particles denote the decay mode of the particle.

4.1.4 Contributing Standard Model Processes

The searched SUSY signatures, i.e. jets, $E_{\text{T}}^{\text{miss.}}$, taus and muons, can be realized by different processes in the SM. The appearance of a true tau and a true muon might arise from events with Z^0 bosons, top-pair production or associated production of two electroweak gauge bosons.

In addition to the appearance of real taus and muons, there are also expected fake contributions. In general, the mapping of true physics particles to reconstructed objects suffers from efficiencies below unity, $\epsilon < 1$, and additional fake contributions with rates $f \neq 0$ from all kind of misidentified objects. If there are n different categories of truth objects, each with an abundance of N_i^{truth}, the number of reconstructed objects $N_i^{\text{reco.}}$ is

$$N_i^{\text{reco}} = \epsilon_i N_i^{\text{truth}} + \sum_{j=1}^{n} f_i^j N_j^{\text{truth}} \,. \tag{4.2}$$

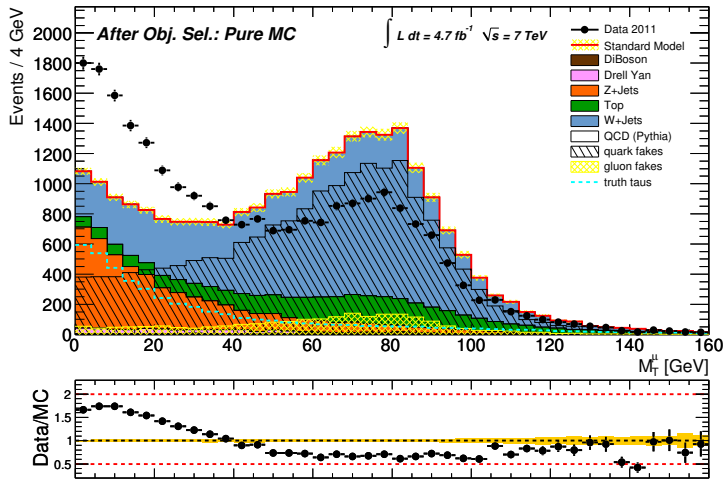

Figure 4.3 Comparison of m_T^μ from pure MC estimate and from data after the object selection with BDT loose taus. Agreement is insufficient.

The first term is diagonal because efficiencies are defined with respect to the truth particle's type. However, principally every object of type j can fake the type i with the mistag probability f_i^j. The dominating fake contribution for any object is hence characterized by two parameters: The mistag probability for an object of other type and the abundance of that object in the data. Clearly, jets are by far the most frequent produced objects at a hadron collider and hence also QCD processes without leptons have to be considered.

The sizable fake rate for taus also allows $W \to \mu\nu_\mu + \tau_{\text{fake}}$ contributions to the event selection. Due to the negligible fake rate for muons, their fake contributions are rare and only contribute by very high cross section processes, i.e. QCD. Figure 4.2 shows possible Feynman diagrams for the most important backgrounds for this analysis. They come from Top, W+jets and di-bosons, as will be shown later in Section 5.1.4.

The SM contributions to the event selection can be quantified by MC techniques. However, this relies on correct handling of all contributing Feynman diagrams to all orders in the event generator. Since this is unfeasible from a technical side, only the most important leading order or also next-to-leading order diagrams are considered and the total cross section is rescaled by k-factors to the extrapolated total cross section. Therefore, some Feynman diagrams might be missing that will not contribute significantly to the total cross section. Still, their differential cross section to appear in the extreme kinematic phase space of the signal region of a SUSY search might give larger relative contribution.

Figure 4.3 shows the transverse mass with the muon as obtained from pure MC simulations and the measured distribution from data. Only pile-up conditions, trigger and lepton efficiencies are corrected. This plot, as well as the following data-MC comparisons, show

- Black dots: measured data.
- Stacked, solid colored histograms: Expected SM contributions from di-bosons, Drell-Yan, Z^0+jets, Top, W+jets and QCD.
- Red line with yellow uncertainties: Sum of expected SM contributions with uncertainties from MC statistics.

- Overlaid black slashed histogram: Expected MC contributions from events where the tau candidate is faked by a quark initiated jet.
- Overlaid yellow hashed histogram: Expected MC contributions from events where the tau candidate is faked by a gluon initiated jet.
- Overlaid dashed cyan line: Expected MC contributions from events, where the tau candidate originates from a truth tau.

The comparison shows that the data are not sufficiently described by pure MC estimations and emphasizes the need for more refined techniques to correctly predict the expected SM contributions. The excess in data at the low m_{T}^{μ} region already hints at a lacking proper QCD estimate, which is expected to accumulate at low p_{T}^{μ} and $E_{\mathrm{T}}^{\mathrm{miss.}}$ and hence low m_{T}^{μ}. The requirement of a $50\,\mathrm{GeV}$ jet, one muon and at least one loose tau already rejects all available MC statistics in the used `Pythia` samples and hence no appropriate estimate is possible. In addition, the region around the JACOBIAN peak is overpredicted in the MC. This already indicates a possible overestimate of the W+jets contributions, which dominate that region. The individual background contributions are investigated in the following.

4.2 Data-Driven Methods for Background Estimates

Despite data-driven corrections for pile-up conditions and object identification efficiencies, a purely MC based estimate of the backgrounds is not sufficient for a reliable background estimate. Therefore, MC predictions shall be either confirmed, corrected or replaced by data-driven techniques. In general, these techniques try to take as much as possible information from measured data to estimate backgrounds, which is complementary to the information obtained from MC. This section explains the used methods.

4.2.1 QCD with the Muon Isolation

Though final states with taus and muons are rarely faked in QCD, it has the by far biggest cross section and hence needs special treatment. The large abundance of QCD would require MC with technically unfeasible statistics to give a representative sample from which the contribution could be predicted. The requirement of a high quality muon and a tau of only loose BDT tightness already rejects all available MC events. Therefore, QCD has to be estimated from data directly.

For that purpose the matrix method [286] is used. It uses the weaker isolation of fake muons compared to true muons. In that sense, it estimates the complete contribution to the event selection that comes from faked muons. Clearly, this is QCD dominated. The method defines two identification criteria: A tight (T) one, which is used in the analysis, and a looser one (L) where the cut on the muon isolation is dropped. The isolation is defined by the energy in the calorimeters in a cone of $\Delta R < 0.2$ around the muon track and should be smaller than $E_{\mathrm{calo.}}^{\Delta R<0.2} < 1.8\,\mathrm{GeV}$. The observed tight and loose muons in data are then either fake (F) or real (R) muons, and hence

$$N_L^{\mathrm{obs.}} = N_L^R + N_L^F \tag{4.3}$$

$$N_T^{\mathrm{obs.}} = N_T^R + N_T^F = \frac{N_T^R}{N_L^R} N_L^R + \frac{N_T^F}{N_L^F} N_L^F = r_R N_L^R + r_F N_L^F \tag{4.4}$$

holds. The last equality of Equation 4.4 assumes the ratio from tight to loose real and fake muons to be known, which can be estimated from control regions. For real muons, these are taken from $Z^0 \to \mu\mu$

control regions, where truth muons can be selected with high purity. This ratio is determined as a function of the muon transverse momentum. For fake muons, the ratio is derived from high statistics QCD control regions, where muons can be assumed to be fakes. This also done in bins of the muon transverse momentum and hence r_R and r_F can be measured.

With these ratios, Equations 4.3 and 4.4 can be solved for

$$N_T^F = \frac{r_F}{r_R - r_F}\left(r_R N_L^{\text{obs.}} - N_T^{\text{obs.}}\right) , \tag{4.5}$$

which is the number of fake muons passing the tight selection. Since the tight selection is used in the analysis, it gives the expected contribution from events with fake muons to the selected data events. In Equation 4.5, an observed tight muon will contribute to $N_L^{\text{obs.}}$ and $N_T^{\text{obs.}}$. For the technical implementation in the analysis, it is more suitable to split the events in disjoint sets: tight muons and muons that are loose but not tight, $N_{L\wedge\neg T}^{\text{obs.}} = N_L^{\text{obs.}} - N_T^{\text{obs.}}$. In this separation Equation 4.5 reads

$$N_T^F = \frac{r_F}{r_R - r_F}\left[r_R N_{L\wedge\neg T}^{\text{obs.}} - (1 - r_R)\, N_T^{\text{obs.}}\right] . \tag{4.6}$$

This method can be used in any data selection that contains a muon. Particularly, the data selection can be split up into subsets that are binned in different quantities. This also provides the expected shape from the fake muon contribution to the quantity, and not only its normalization. For each bin the statistical uncertainties on $N_T^{\text{obs.}}$ and $N_{L\wedge\neg T}^{\text{obs.}}$ are considered and the uncertainties on the ratios r_R and r_L are taken as systematic uncertainty. If not separately given, these are added quadratically and in the following, and QCD will always be given as estimated by this technique.

4.2.2 W+jets with the Muon Charge Asymmetry

The contributions from W+jets can be obtained from the different abundance of positively and negatively charged $W^{\pm}$ bosons at a proton-proton collider [287]. Due to the predominance of up-type quarks in the proton, positively charged W^+ are produced more frequent compared to negative W^- bosons. The observed events can be split up in positive and negative muons, and hence in W^+ and W^-:

$$N_{\text{obs.}}^+ = N_{W^+} + N_{\text{rest}}^+ \qquad \text{and} \qquad N_{\text{obs.}}^- = N_{W^-} + N_{\text{rest}}^- . \tag{4.7}$$

This system of equations can be solved if the ratio

$$r^{\pm} = \frac{\sigma\left(pp \to W^+\right)}{\sigma\left(pp \to W^-\right)} = \frac{N_{W^+}}{N_{W^-}} \tag{4.8}$$

is known and all other contributing processes are produced symmetric with either sign, i.e. $N_{\text{rest}}^- = N_{\text{rest}}^+$. This leads to

$$N_{W^+} = \frac{r^{\pm}\left(N_{\text{obs.}}^+ - N_{\text{obs.}}^-\right)}{r^{\pm} - 1} \qquad \text{and} \qquad N_{W^-} = \frac{N_{\text{obs.}}^+ - N_{\text{obs.}}^-}{r^{\pm} - 1} \tag{4.9}$$

and hence

$$N_W = N_{W^+} + N_{W^-} = \frac{r^{\pm} + 1}{r^{\pm} - 1}\left(N_{\text{obs.}}^+ - N_{\text{obs.}}^-\right) . \tag{4.10}$$

Since the production of positively and negatively charged $W^{\pm}$ are uncorrelated, the statistical uncertainty of Equation 4.10 is given by

$$\Delta N_W^{\text{stat.}} = \frac{r^{\pm}+1}{r^{\pm}-1}\sqrt{N^{+}_{\text{obs.}} + N^{-}_{\text{obs.}}}\,. \tag{4.11}$$

For this method, the ratio $r^{\pm}$ needs to be known. In principle, it could be obtained from theoretical calculations from inclusive $W^{\pm}$ production, but this might introduce a kinematic bias in the estimate. Since the differential cross sections for W^{+} and W^{-} production have different η dependence [288], the ratio might change for different kinematic cuts. Therefore, the ratio $r^{\pm}$ is taken from MC under the assumption that the quantity itself and charge identification is correctly described

$$r^{\pm} = \frac{\sum\limits_{i\in\Omega} \omega^{i,\text{MC}}_{W^{+}}}{\sum\limits_{i\in\Omega} \omega^{i,\text{MC}}_{W^{-}}}\,. \tag{4.12}$$

The nominator (denominator) sums up the event weights of all W^{+} (W^{-}) MC events that are in the kinematic phase space Ω. Ω is defined by the kinematic selection in data, in which the W+jets contributions shall be estimated. This ensures the correct handling of the dependence of $r^{\pm}$ on the event kinematics. The limited MC statistics add an additional systematic uncertainty of

$$\Delta N_W^{\text{syst.}} = \frac{2\Delta r^{\pm}}{\left(r^{\pm}-1\right)^2}\left(N^{+}_{\text{obs.}} - N^{-}_{\text{obs.}}\right) \quad \left(\Delta r^{\pm}\right)^2 = \left(\frac{\Delta N_{W^{+}}}{N_{W^{-}}}\right)^2 + \left(\frac{N_{W^{+}}\Delta N_{W^{-}}}{N^2_{W^{-}}}\right)^2\,, \tag{4.13}$$

where $\Delta N_{W^{\pm}}$ is the square root of the quadratic sum of all considered MC event weights in Equation 4.12. The reliance on the MC modelling of the ratio from Equation 4.12 is no major drawback because many potential systematics cancel out in the ratio, e.g. luminosity, identification efficiencies or the modelling of selection efficiencies of kinematic cuts. In addition, the charge identification is rather easy to model as long as the transverse momenta of muons are not too high so that their curvature in the magnetic field becomes very small.

4.2.3 Data Driven Scale Factors

Backgrounds can also be investigated in control regions (CRs). They are obtained by appliance of kinematic cuts that are designed to enrich a certain background type. In these CRs, the considered background can be investigated individually to understand its behaviour and to seek for any possible mismodelling. The use of that information in the analysis relies on two basic assumptions: The obtained information is applicable beyond the kinematic phase space of the control region and there is no significant contamination from events of different origin. The latter can be estimated to first oder from MC. This implies that there is no fundamental strong mismodelling of the kinematic variables that define the CRs.

An important property of backgrounds is their normalization, i.e. the expected total contribution of a background type to the event selection. The normalization for MC simulation is obtained by theoretical cross sections, simulated detector acceptance and simulated efficiency of cuts. Any deviation between real and simulated detector response or cut efficiency could spoil the correct normalization. This can be restored in CRs by rescaling of the MC prediction to the data observation.

In general, purities of certain background types in control regions will not be 100 %, which might lead to a wrong scale factor ω for that background. Let k denote the number of all contributing backgrounds

and n the number of those that shall be rescaled in n different control regions. Assuming globally valid scale factors ω_i for the n considered backgrounds, their mixtures can be taken into account by the matrix equation

$$n \text{ CRs} \left\{ \begin{pmatrix} N_1'^{\text{obs.}} \\ \vdots \\ N_n'^{\text{obs.}} \end{pmatrix} = \overbrace{\begin{pmatrix} s_{11} & \cdots & s_{1n} \\ \vdots & \ddots & \vdots \\ s_{n1} & \cdots & s_{nn} \end{pmatrix}}^{n \text{ background types}} \begin{pmatrix} \omega_i \\ \vdots \\ \omega_n \end{pmatrix} . \tag{4.14}$$

The matrix $\mathbf{S} = s_{ij}$ gives the MC prediction of each considered background type j to all CRs i. The observation in data is corrected for the $k - n$ backgrounds that are not considered in the matrix from Equation 4.14 by

$$N_i'^{\text{obs.}} = N_i^{\text{obs.}} - \sum_{m=n+1}^{k} s_{im} . \tag{4.15}$$

Here, s_{im} denotes the MC prediction of the remaining background m in the control region i. This is equivalent to an extension of the matrix $\mathbf{S}$ by $k - n$ additional columns with the corresponding MC contributions and the expansion of the vector $\vec{\omega}$ by $k - n$ ones.

For an ideal separation of background types, the matrix $\mathbf{S}$ would be diagonal and the scalings ω_i would be $s_{ii}^{-1} N_i'^{\text{obs.}}$. For more general compositions, the scalings can be derived by inversion of the matrix $\mathbf{S}$ and multiplication to $\vec{N}'^{\text{obs.}}$

$$\vec{\omega} = \mathbf{S}^{-1} \vec{N}'^{\text{obs.}} . \tag{4.16}$$

There is exactly one inverse matrix if the quadratic matrix $\mathbf{S}$ is bijective. This is equivalent to the statement that its rows form a basis of $\mathbb{R}^n$, i.e. $\vec{s}_i^{\,\text{row}} \neq \lambda \vec{s}_j^{\,\text{row}}$ for any i, j and $\lambda \in \mathbb{R}$. Linear independent rows of the matrix $\mathbf{S}$ can be achieved if the control regions have different relative background compositions. This is the case as long as the chosen cuts for the CRs indeed enrich each control region with the wanted event type.

The evaluation of the uncertainties on $\vec{\omega}$ is more complicated. All $n \times n$ matrix elements, as well as the n data observations and the $n(k - n)$ background corrections from Equation 4.15 have individual uncertainties. These sum up to

$$n^2 + n + n(k - n) = n^2 + n + nk - n^2 = n(k + 1) \tag{4.17}$$

contributing parameters. Their uncertainties are taken into account by smearing of all parameters at once within their uncertainties. This new matrix equation can be used to get another set of scalings. This is redone N times and gives distributions for the scalings with a spread according to their uncertainty. This sequential determination of the N collections of n scalings also allows to compute the correlation among the scalings. They are needed for the uncertainty on the total normalization of the composite background in the signal region

$$N_{\text{sum}}^{\text{SR}} = \sum_{i=1}^{n} \omega_i s_i^{\text{SR}} + \sum_{m=n+1}^{k} s_k^{\text{SR}} , \tag{4.18}$$

where s_j^{SR} is the MC prediction of background j in the signal region.

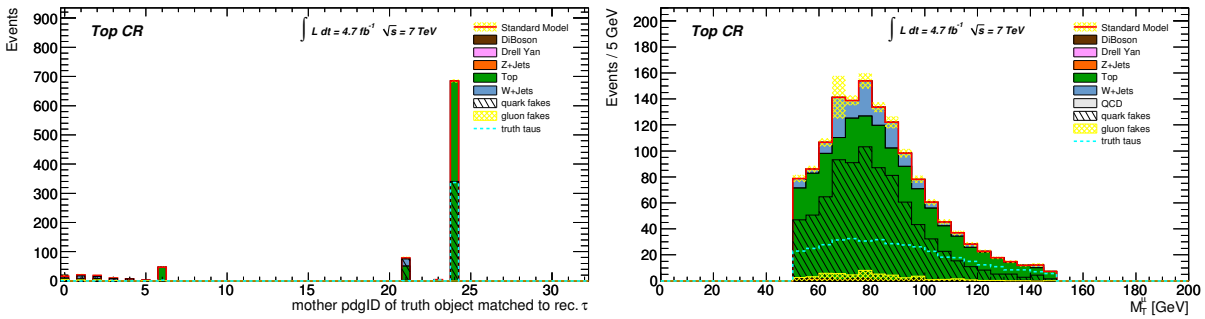

(A) Mother PDG ID of truth object giving the τ

(B) Transverse mass with muon

FIGURE 4.4 Truth and fake taus in the Top CR. (A): The PDG ID of the mother of the truth object that gives the reconstructed tau. (B): The transverse mass with the muon and the $E_T^{miss.}$. Taus are BDT loose.

4.3 Tau Lepton Identification Performance Studies

As mentioned above, mismodelled detector efficiencies for triggers and light leptons are considered by MC rescaling. Due to the sizable fake contributions for taus compared to muons, the description of the tau identification performance in the simulation is even more crucial for the analysis. Since taus can be faked by complex objects like gluon or quark initiated QCD jets, the tau identification algorithms need to be validated. This is done in the context of different backgrounds with different event and jet topologies, as described in the following sections. The final choice for the optimal BDT working point for the SUSY search will be decided later in Section 5.1.3, after the tau identification has been understood.

4.3.1 Considered Background Topologies

The final search pattern with a muon, taus, missing energy and hadronic activity will most likely result from either Top or W+jets. These backgrounds both have real missing transverse energy, real leptons and might be accompanied by hard jets and hence shall be investigated in the following. Since the MC description of the tau identification might be quite different for fake and truth taus, these have to be investigated separately. In W+jets events, either a true muon or a true tau is produced and hence the other object needs to be faked. The by far smaller fake rate for muons, $f_\mu^{\text{jet}} \ll f_\tau^{\text{jet}}$ in the notation of Equation 4.2 (p. 59), leads to a negligible fraction of events with truth taus and hence W+jets background is completely fake tau dominated. In Top events, the truth and fake tau contributions need to be separated.

In the first instance, Top and W+jets enriched CRs require a suppression of QCD and should have minimal contributions from potential SUSY. This can be achieved by cuts on $E_{\text{T}}^{\text{miss.}}$ and m_{T}^{μ}

$$30\,\text{GeV} < E_{\text{T}}^{\text{miss.}} < 100\,\text{GeV} \qquad \text{and} \qquad 50\,\text{GeV} < m_{\text{T}}^{\mu} < 150\,\text{GeV}\,, \tag{4.19}$$

where the lower bounds are for QCD rejection and the upper bounds minimize potential signal contamination. The separation of Top and W+jets events is done with a b-tagging requirement and veto, respectively because b-quarks are only expected to appear in Top events. In W+jets events, no separation of truth and fake taus is needed, and hence this already defines the W+jets control region.

Top events that contain truth and fake taus can be separated by a cut on m_{T}^{μ}. Events with a true tau and a muon have two leptonically decaying W bosons. Hence, there are two hard neutrinos from the W-decays that contribute to the $E_{\text{T}}^{\text{miss.}}$. Fake taus in Top events predominantly come from hadronically

<table>
<tr><td colspan="3">Top and W control region
$30\,\text{GeV} < E_{\text{T}}^{\text{miss.}} < 100\,\text{GeV}$
$50\,\text{GeV} < m_{\text{T}}^{\mu} < 150\,\text{GeV}$</td></tr>
<tr><td colspan="2">Top control region
$N_{b\text{-tag}} \geq 1$</td><td rowspan="2">W control region

$N_{b\text{-tag}} = 0$</td></tr>
<tr><td>Top control region
fake taus
$50\,\text{GeV} < m_{\text{T}}^{\mu} < 100\,\text{GeV}$</td><td>Top control region
true taus
$100\,\text{GeV} < m_{\text{T}}^{\mu} < 150\,\text{GeV}$</td></tr>
</table>

Table 4.3 The chosen control regions for the performance studies of tau identification in W+jets and Top backgrounds.

decaying W bosons, as can be seen in Figure 4.4(a). It shows the PDG ID[1] of the mother of the truth object that has been matched to the reconstructed tau. Fake taus are predominantly from quark initiated jets that originate from hadronically W decays. The gluon initiated fake taus are radiated by quarks (PDG ID: 1 to 5) and fakes from b-jets come from tops (PDG ID: 6). A list of particles with their PDG ID can be found in Appendix A in Table A.9 (p. 148).

If one of the two W bosons decays hadronically, only the muon neutrino constitutes the real $E_{\text{T}}^{\text{miss.}}$. Hence, the transverse mass m_{T}^{μ} of the muon and missing transverse energy is constraint to be below the W mass, see also Figure 4.2(a) and (b). From Figure 4.4(b) it can be seen that the high m_{T}^{μ} tail is indeed dominated by events with truth taus. Therefore, Top events with truth and fake taus can be separated by $m_{\text{T}}^{\mu} \gtrless 100\,\text{GeV}$. Table 4.3 summarizes the chosen control regions.

The separation of truth and fake taus by this kinematic consideration is one of the advantages of muons, which can be assumed to be truth muons. This is a unique feature of the muon, which could not be exploited in an analysis that searches for two hadronically decaying taus. In that case, none of the two taus could be tagged to be a truth tau. Furthermore, the kinematic disentanglement of fake and truth taus is free of any bias to a potentially mismodelled tau identification. It is solely based on the presence of additional missing transverse energy in the case of truth taus. Other criteria, like a cut on the BDT score or the tau transverse momentum, might also have discrimination power between truth and fake taus. However, these might already suffer from a mismodelled tau identification, which is the actual subject of the investigation. Hence, they can not be assumed to give a reliable distinction of fake and truth tau contributions.

The basic kinematic description of loose taus in the control region can be seen in Figures 4.5 and 4.6. In the Top CRs, the shapes of the distributions are reasonably described, but the predicted normalization of W+jets is considerably overestimated in the MC. The spike in the transverse momentum spectrum at 50 GeV in W+jets comes from the jet trigger plateau cut. In these events, the tau is the hardest jet and exceeds the $p_{\text{T}}^{\text{jet}} = 50\,\text{GeV}$ threshold. For taus with softer transverse momentum, at least one additional jet above the jet trigger plateau cut needs to be present. This feature is less pronounced in the Top CRs because here one of the two hard b-jets fulfills the requirement anyway and the tau is not needed.

The plots show that the basic event kinematics in Top, e.g. η_{τ} and isolation with respect to closest nearby jet, are well described. Contrary, the BDT in W+jets hints to a wrongly modelled tau identification for fake taus from W+jets. Table 4.4 shows the origin of taus in the three control regions. The fraction of taus that have been faked by an electron are at permille level in all three control regions. This is seen throughout the whole analysis and hence fake tau contributions from electrons are not investigated in

[1] MC particle identification numbering scheme of the Particle Data Group.

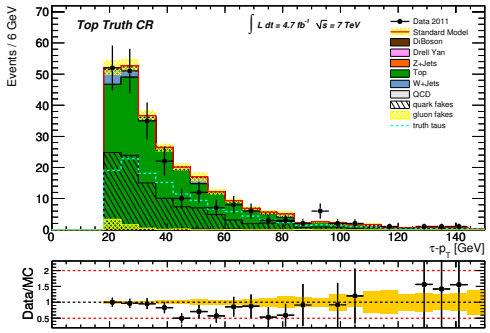

(A) Top Truth CR: p_{T}^{τ}

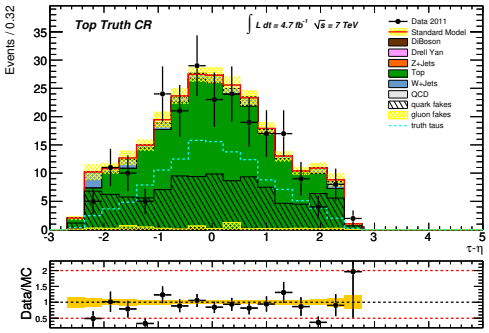

(B) Top Truth CR: η_{τ}

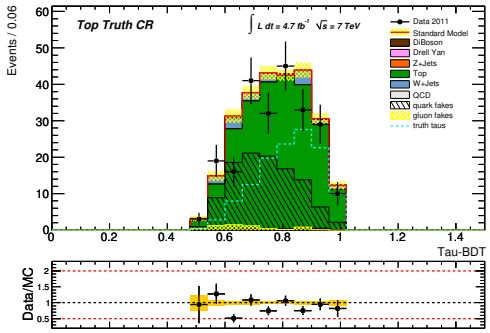

(C) Top Truth CR: BDT

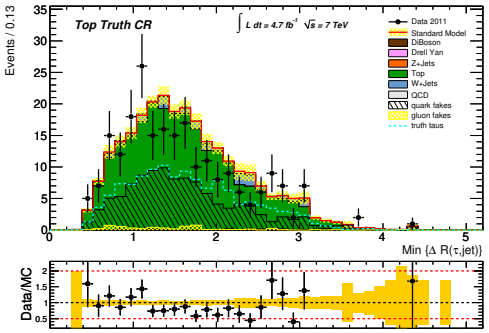

(D) Top Truth CR: Isolation

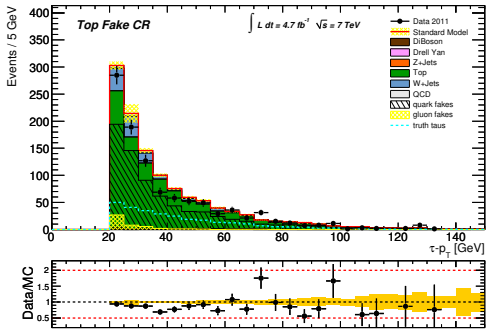

(E) Top Fake CR: p_{T}^{τ}

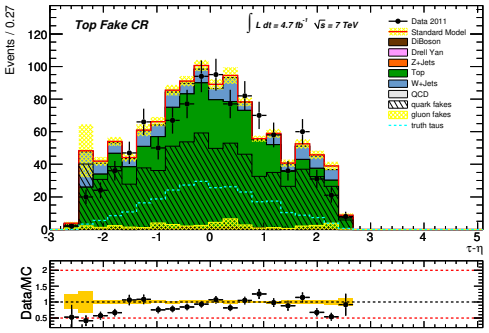

(F) Top Fake CR: η_{τ}

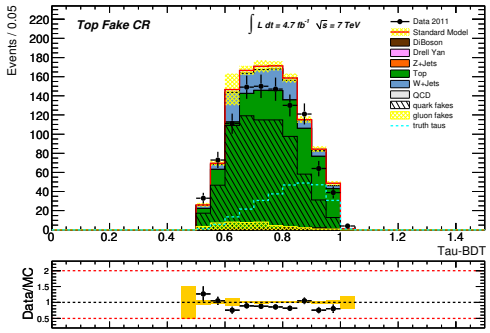

(G) Top Fake CR: BDT

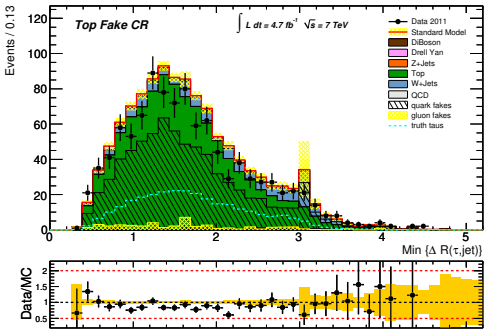

(H) Top Fake CR: Isolation

Figure 4.5 Kinematics of BDT loose taus in the Top with truth and fake taus control regions.

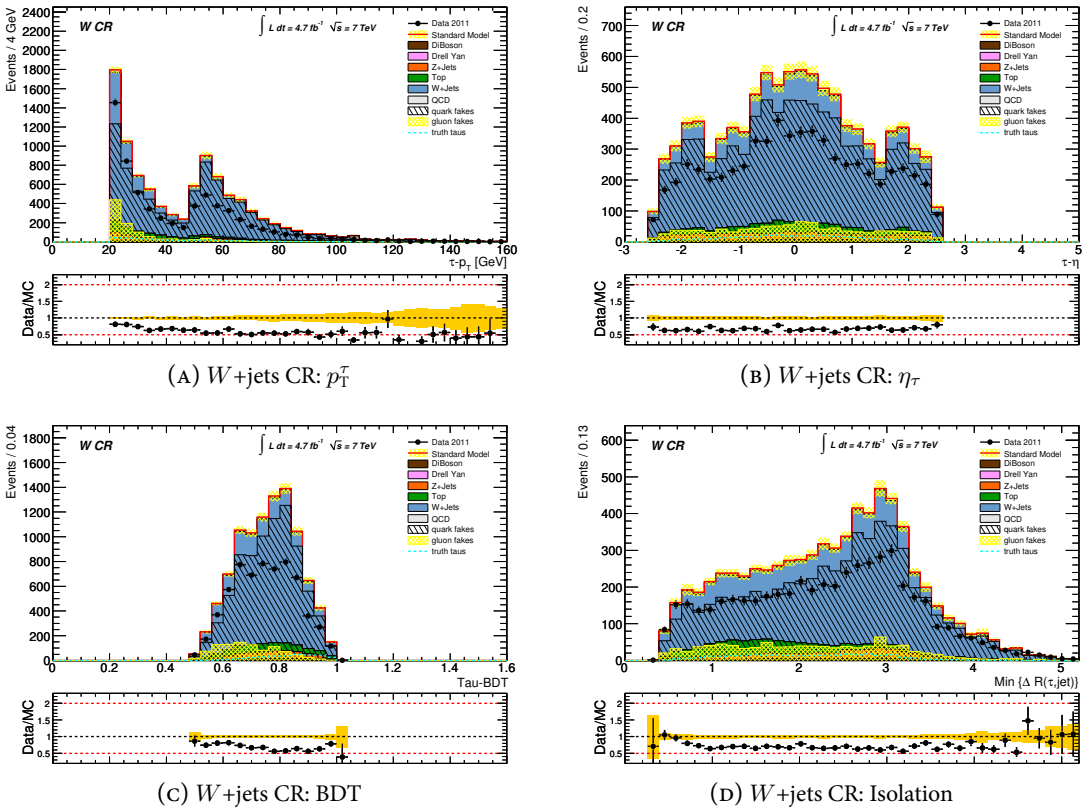

(a) W+jets CR: p_{T}^{τ}

(b) W+jets CR: η_{τ}

(c) W+jets CR: BDT

(d) W+jets CR: Isolation

Figure 4.6 Kinematic variables of BDT loose taus in the W+jets control region. The normalization is overpredicted in the MC. The spike in the transverse momentum spectrum in W+jets comes from the jet trigger plateau cut.

more detail. The table further demonstrates that the cut on m_{T}^{μ} increases the purity of taus in Top by nearly a factor of two.

For a proper background estimate of W+jets, the higher abundance of MC events in the CR is investigated in the following. Table 4.4 quantifies that neither truth taus nor noteworthy electron fakes are expected in W+jets. Therefore, jet initiated fake taus are the most probable candidates as origin of the mismodelling. It shall be clarified whether the different normalization in W+jets is caused by different performance of the tau identification algorithms in MC and data on fake taus.

4.3.2 Tau Substructure Investigation

The observed MC excess in W+jets can be corrected by a rescaling of its contributions. If a single scaling factor is used, it must be shown to be universally applicable, i.e. there is no bias of the scaling factor to the event selection of the analysis. This can be assured if the effect that causes the deviation is found and can be shown to be independent of the event selection.

The rather complicated tau identification has already been noted as a potential origin of the seen discrepancy. To test this hypothesis, the selection is repeated with just at least one tau *candidate*. The candidate is required to fulfill the basic kinematic requirements, e.g. p_{T}^{τ} and η_{τ}, but no tau identification related cut is applied. For the latter, the requirements on track multiplicity, charge and the BDT output are dropped to have a maximally unbiased selection of tau candidates. These can be investigated in the W+jets control region, where the W decayed into a muon and the tau candidate is known to be a fake,

CR		DiBosons	Drell-Yan	Z^0+jets	Top	W+jets	SM
W+jets CR	τ purity [%]	58.4	0	20.6	29.2	0	3.3
	e fakes [%]	0.65	0	0.07	1.14	0.15	0.28
Top fake tau CR	τ purity [%]	26.9	0	42.8	28.5	0	25
	e fakes [%]	0	0	0	0.66	0	0.56
Top truth tau CR	τ purity [%]	78.4	0	11.5	52.7	0	49.3
	e fakes [%]	12	0	0	0	0.58	0.55

TABLE 4.4 The purities of selected taus and the fraction of taus that have been faked by electrons. Taus are BDT loose.

i.e. a non-tau jet. Since (nearly) all taus are fakes in this section, the term jet is used likewise. Both, tau and jet, denote a tau candidate that enters the tau identification.

Figure 4.7 shows data and MC comparisons after the object selection without tau identification. In events with multiple tau candidates, the one with highest p_{T}^{τ} is shown in the plots. The agreement is very good and hence event and basic tau kinematics are described correctly. The small excess in data in the $p_{\mathrm{T}}^{\tau} < 50\,\mathrm{GeV}$ region of Figure 4.7(A) is caused by the jet trigger plateau cut. For these low-momentum taus, at least one second jet with $p_{\mathrm{T}}^{\mathrm{jet}} > 50\,\mathrm{GeV}$ is needed to fulfill the trigger threshold. Figure 4.7(H) shows the jet multiplicity for these low-p_{T}^{τ} events. Evidently, there are less jets in the MC, which leads to a smaller probability to surpass the jet plateau cut.

The good agreement in Figure 4.7 can be attributed to the outstanding reconstruction characteristics of the muon. The plots also demonstrate that W+jets dominates the given event selection. The agreement of the tau's basic kinematic distributions also indicates good MC description of the general kinematics of jets faking taus. Nonetheless, the tau identification algorithms look on the jet substructure. It has much more complicated features that could be mismodelled, as investigated in the following. Since the event selection is well described up to the muon and tau candidate requirement, it allows to study the performance of the tau identification on top of a reliable muon identification.

In the next step, the tau identification related properties of the tau candidate are investigated in the W+jets control region. Therefore, the W+jets CR cuts of Table 4.3 are applied but still no tau identification is required. Contrary to the general event kinematics, Figure 4.8 shows that the properties of the jet that enter the tau identification are not well modelled. Figures 4.8(A) to (C) show calorimetry related variables. The data has more reconstructed clusters for tau candidates with higher reconstructed invariant mass and more spacial extension as simulated in MC. Track related quantities can be seen in Figures 4.8(D) to (F). The multiplicity of associated tracks and their invariant mass are higher in data than in MC. Furthermore, the momentum fraction of the leading track to the total transverse energy is not well described. Finally, Figures 4.8(G) and (H) show wider profiles for the obtained impact parameter and flight path significance.

Summarizing, tau identification related variables can be shown to be mismodelled for jets in the W+jets MC simulation. E.g. the track multiplicity of jets is underestimated and the sharing of energy among charged particles (tracks) and the other constituents are different in MC and data. This can be attributed to the complicated hadronization of colored particles. The simulation underestimates the production of charged and neutral particles. This leads to lower multiplicity of tracks and clusters and more collimated jets in the W+jets MC. These patterns are considered to be tau-like by the tau identification algorithms and hence the fake rate is overestimated in the MC. This leads to more selected W+jets events in the MC.

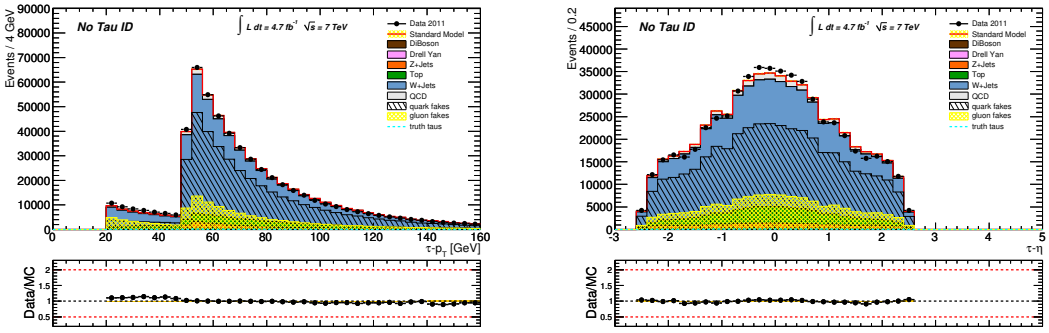

(A) p_{T}^{τ}

(B) η_{τ}

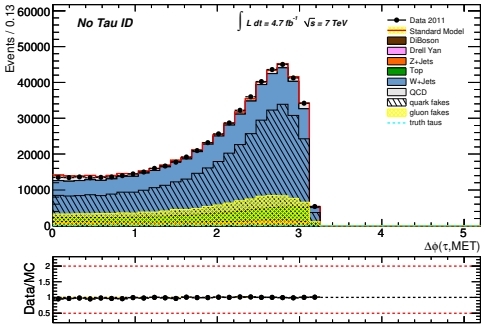

(C) $\Delta\phi\left(\tau, E_{\mathrm{T}}^{\mathrm{miss.}}\right)$

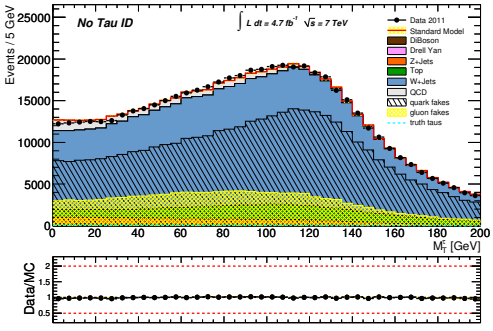

(D) m_{T}^{τ}

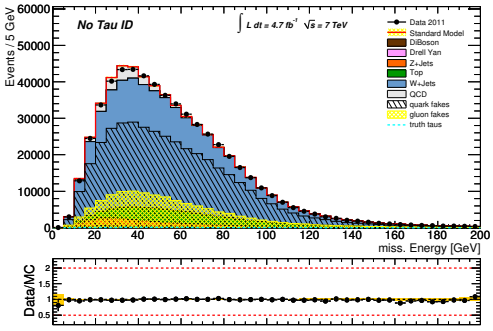

(E) $E_{\mathrm{T}}^{\mathrm{miss.}}$

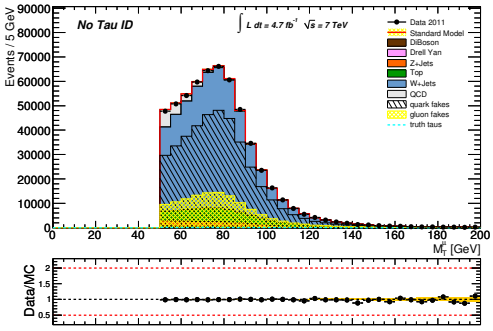

(F) m_{T}^{μ}

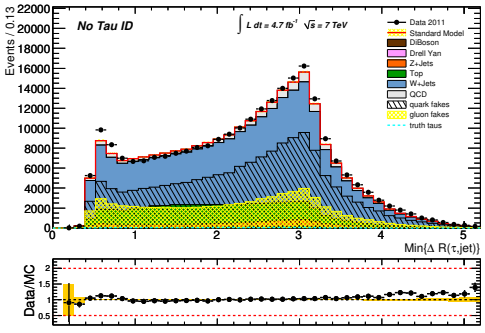

(G) $\min\{\Delta R(\tau, \mathrm{jets})\}$

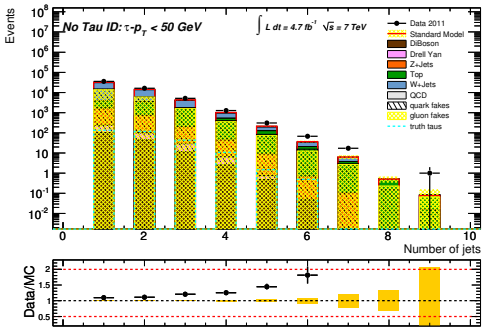

(H) $p_{\mathrm{T}}^{\tau} < 50\,\mathrm{GeV}:\ N_{\mathrm{jets}}$

Figure 4.7 Kinematic modelling of events without applied tau identification after the object selection. Only at least one tau candidate with basic kinematic properties is required. Agreement between data and MC is very good.

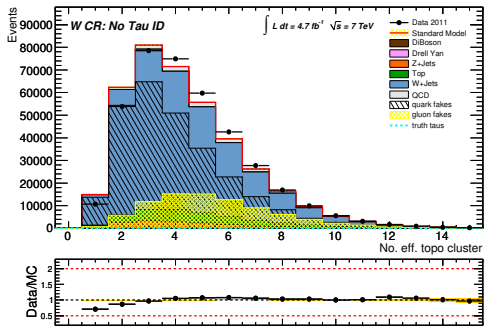

(A) No. eff. clusters

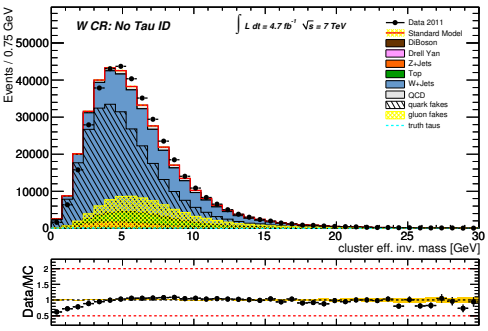

(B) Inv. mass of eff. clusters

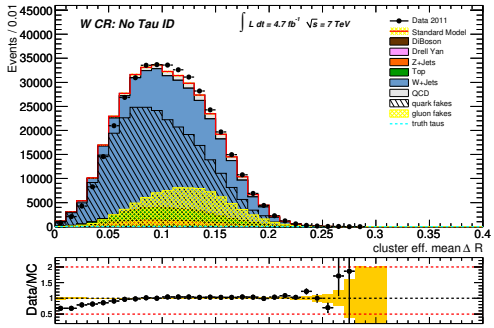

(C) Mean ΔR of eff. clusters

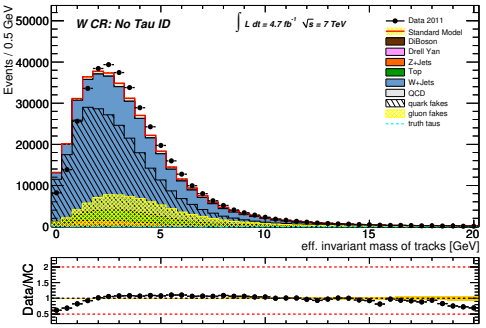

(D) Inv. mass of tracks

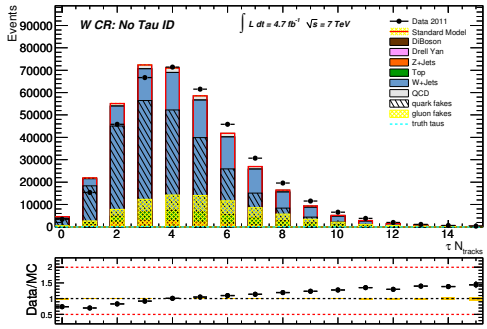

(E) No. of τ-tracks

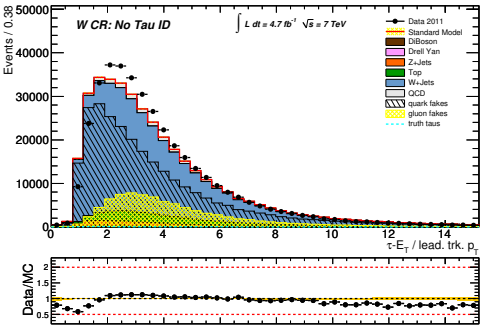

(F) E_{T} / $p_{\mathrm{T}}^{\text{lead. trk.}}$

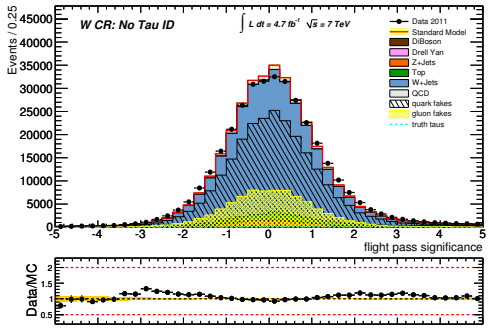

(G) Flight path significance

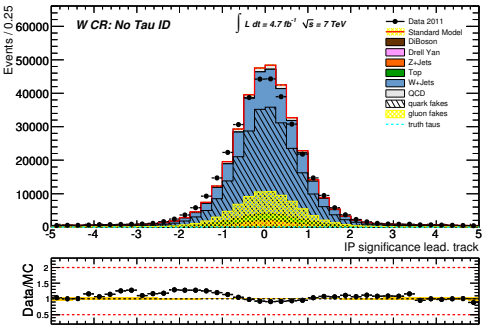

(H) Impact parameter significance

FIGURE 4.8 Data and MC comparisons of tau identification related quantities in the W+jets CR. The substructure of fake tau candidates is less tau-like in data.

Figure 4.9(a) shows the resulting tau BDT jet score distribution. The tau identification in the normal event selection is applied on this distribution. It clearly confirms that jets are more tau-like in MC compared to data, i.e. they have a higher BDT output. The requirement of BDT medium tau rejects nearly all tau candidates with BDT < 0.6. Therefore, the tau fake rate and the estimated contribution from this background is overestimated in the MC. This will be compensated by a rescaling of the MC contributions from W+jets.

To assure that these performance issues, and hence the used scalings, are globally valid, potential biases of the tau identification are investigated as well in Figure 4.9. Figure 4.9(b) shows the BDT in a high effective mass phase space in the W+jets control region. This cut is chosen because $m_{\text{eff.}}$ will be used to define the final search patterns and hence should have no bias to the tau identification. Furthermore, Figure 4.9(c) and (d) show the BDT output separately for high and low transverse momentum taus. There is a correlation of the transverse momentum and BDT score. Low-p_{T} taus have a more pronounced high BDT tail hence have higher fake rate. Contrary, high-p_{T} taus look less tau like. Nevertheless, the data to MC ratio of the high BDT tail is the same for both cases. Hence, no dependence of the mismodelling to the p_{T}^{τ} can be seen.

In Figure 4.9(e) and (f), the BDT distribution can be seen for one- and three-prongs, respectively. As expected, one-prong candidates look more tau-like and are also more effected by the mismodelling. The presence of jets with only one charged particle is rare in QCD but overestimated in the MC, see Figure 4.8e. Still, the performance in the high BDT tail that is used in the analysis shows the same discrepancy.

Finally, plots 4.9(g) and (h) show the BDT distributions for high and low pile-up conditions. They are separated in between five and six reconstructed vertices. Due to the different event environment, the tau identification performance is different in high and low pile-up environments. In both cases, the ratio in the high BDT range succumbs to the same mismatching in data and MC.

In all cases, the high BDT tail is overestimated in W+jets and hence MC contributions have to be scaled down. Any dependence of the used scalings on the event kinematics and conditions will be separately investigated. In any case, the ratio plots from Figure 4.9 already show the same flat behaviour above a BDT of 0.6. This is the region of the BDT output that will be used for the tau identification in the final analysis.

Contrary to W+jets, fake taus in Top could be seen to be better modelled, see Figure 4.5. The different performance in the description of fake taus in Top and W+jets can be explained by the use off different generators from a technical side. Furthermore, there are significant differences related to physics in the production of tau fakes in Top and W+jets. This can be seen in Figure 4.10. Figures 4.10(a) and (b) show the PDG ID of the truth object that has been matched to the reconstructed tau in the Top and W+jets CRs, respectively. In addition, Figures 4.10(c) and (d) are obtained from the same CRs, but they show the PDG ID of the mother of the object that gives the reconstructed tau.

In both, Top and W+jets, tau fakes predominantly come from quark initiated jets. However, in Top these jets arise from hadronically W decays. Since the W is color neutral, the two quarks from its decay only need color exchange among themselves to hadronize. In W+jets, tau fakes are caused by quarks from associated QCD activity. A produced quark needs color exchange with the rest of the event in order to hadronize to a colorless final states. The color exchange with the whole event is much more complicated and could lead to more complex jet structures. They might be more prone to a wrong hadronization modelling.

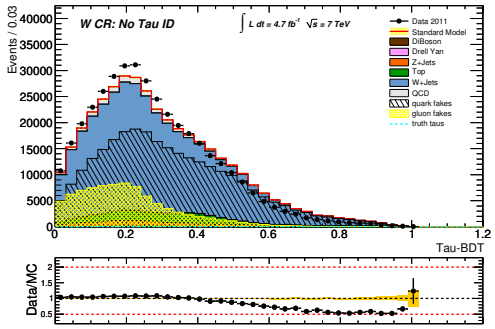

(A) All tau candidates

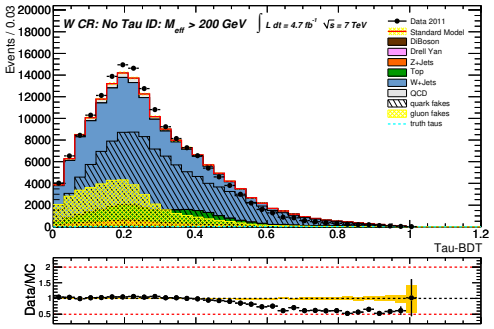

(B) $m_{\text{eff.}} > 200\,\text{GeV}$

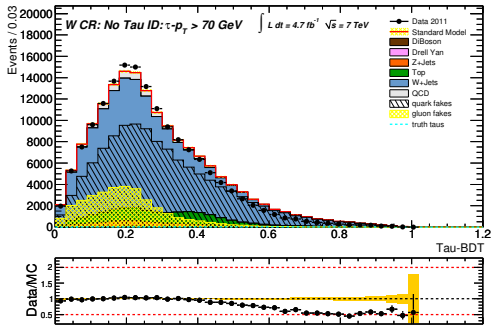

(C) $p_{\text{T}}^{\tau} > 70\,\text{GeV}$

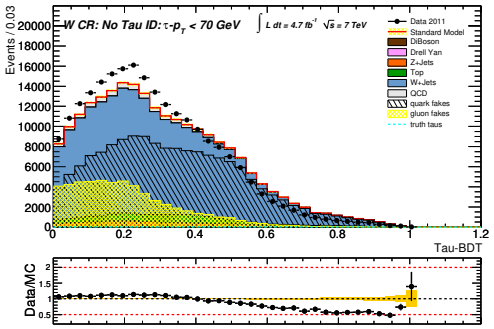

(D) $p_{\text{T}}^{\tau} < 70\,\text{GeV}$

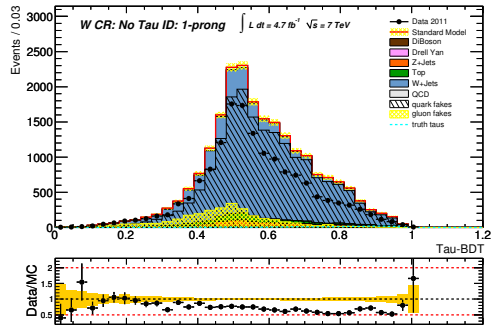

(E) One-prongs

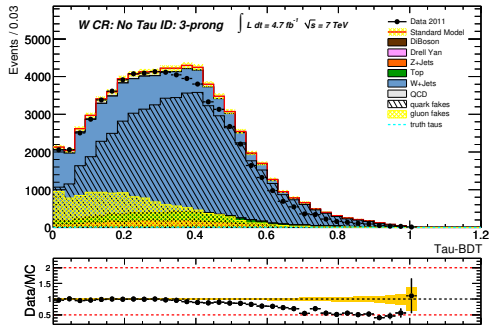

(F) Three-prongs

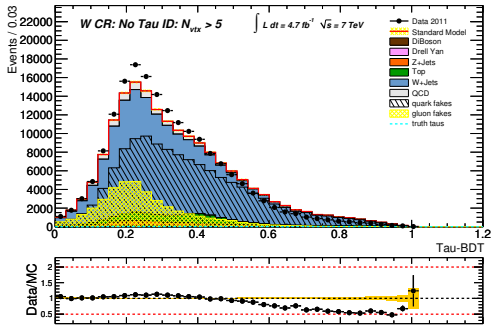

(G) High pile-up

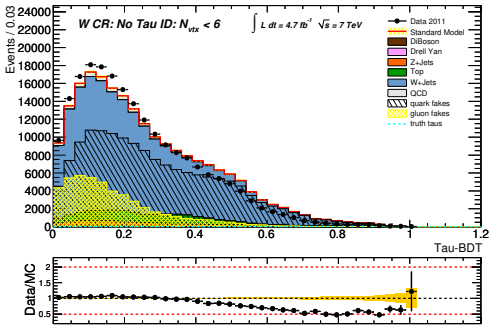

(H) Low pile-up

FIGURE 4.9 The tau BDT distribution of fake tau candidates in the W+jets control region. (A) all candidates, (B) high effective mass, (C) high-p_{T}^{τ}, (D) low-p_{T}^{τ}, (E) one-prongs, (F) three-prongs, (G) high pile-up, (H) low pile-up events.

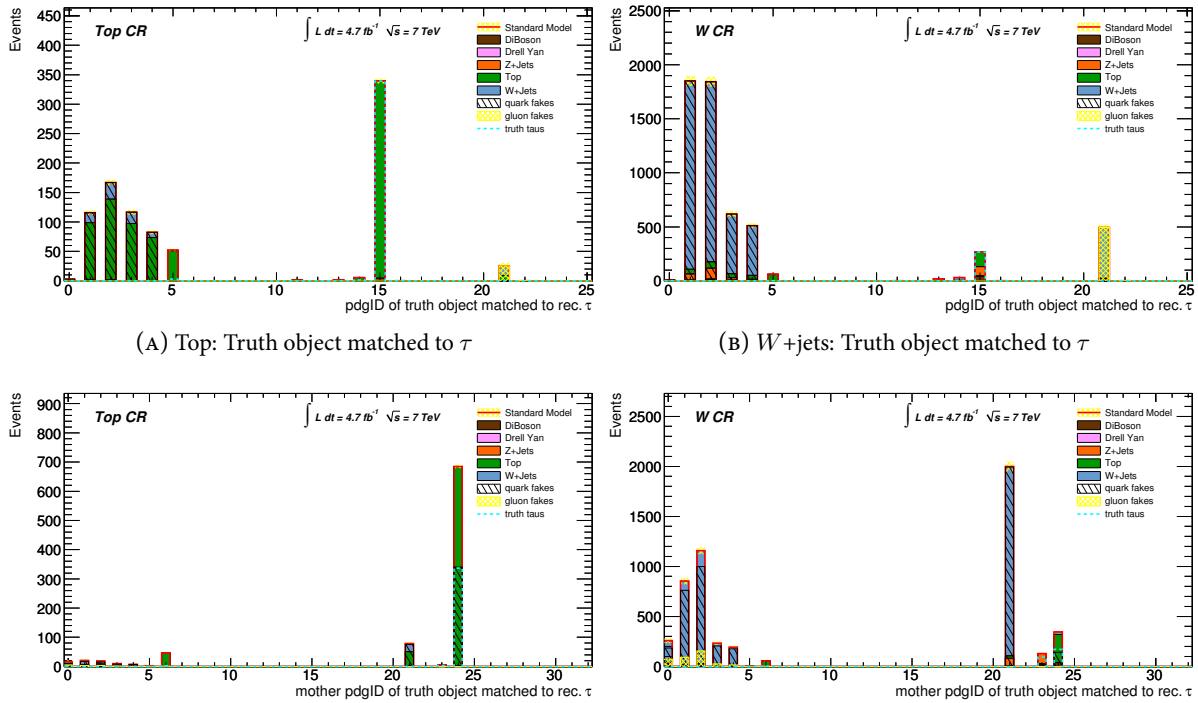

(A) Top: Truth object matched to τ

(B) W+jets: Truth object matched to τ

(C) Top: Mother of truth object matched to τ

(D) W+jets: Mother of truth object matched to τ

Figure 4.10 The PDG ID of the truth object giving the tau in (A) the Top CR and in (B) the W+jets CR. The PDG ID of the mother of the truth object giving the tau in (C) the Top and (D) the W+jets CRs. Taus are BDT medium.

4.4 Standard Model Background Contributions

In this section, the shown techniques from Sections 4.2.1 to 4.2.3 are applied to the different SM backgrounds. The results are presented and verified by cross checks if possible.

4.4.1 Top and W+jets

Top and W+jets backgrounds constitute the major contribution to the final event selection and hence need most attention. In Section 4.3, the performance of the tau identification in events from these backgrounds has already been investigated. It could be seen that the contributions from W+jets need to be rescaled due to wrong tau identification modelling. Since both backgrounds have quite common appearance for this analysis, a strict breakup of these processes in different control regions is not possible. This is particularly true for the separation of truth and fake tau contributions. Therefore, the technique presented in Section 4.2.3 is well suited to simultaneously derive scalings for each of these backgrounds.

Obtained Scalings

The control regions of Table 4.3 have already proven to split up the three background types, Top with truth and fake taus and W+jets, sufficiently well, so that these are chosen. The cutflow into the control regions can be seen in Table 4.5. The upper table shows expected and observed events at each cut stage up to the combined Top and W+jets control region. The lower three tables show the subsequent cutflows to the individual control regions enriched with W+jets, Top with truth and Top with fake taus, respectively.

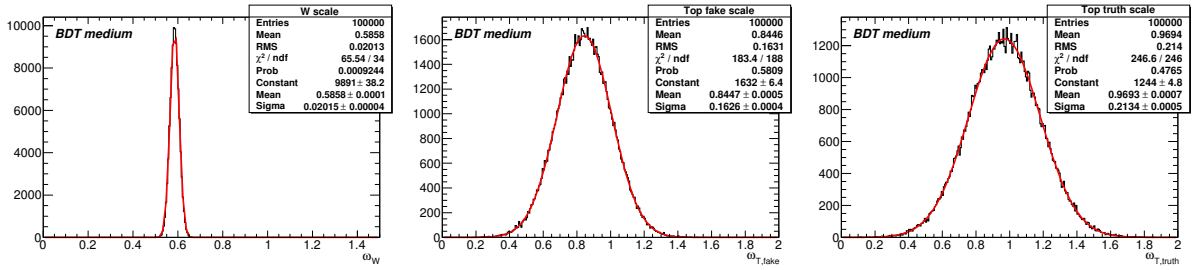

(A) W+jets scaling (B) Top with fake tau scaling (C) Top with truth tau scaling

FIGURE 4.11 The obtained scalings for W+jets, Top with fake taus and Top with truth taus. The tau is required to be of medium tightness in the BDT output.

The last row gives the contribution of events where the leading tau is a truth tau and the last column sums up the SM expectations. The given uncertainty is the squared sum of MC statistical uncertainties and from the data-driven QCD estimate. The tau is required to be at least BDT medium, which will be used for the final selection.

The Table 4.5 provides all numbers for Equation 4.14 (p. 64), which then reads

$$\begin{pmatrix} 3226.62 \\ 616.52 \\ 164.79 \end{pmatrix} = \begin{pmatrix} 4939.79 & 237.65 & 138.03 \\ 82.49 & 404.36 & 233.89 \\ 9.48 & 66.45 & 106.43 \end{pmatrix} \begin{pmatrix} \omega_W \\ \omega_{\mathrm{T,f}} \\ \omega_{\mathrm{T,t}} \end{pmatrix} . \tag{4.20}$$

The left vector with the data observation has been corrected by the data-driven QCD estimate as well as the MC predictions from Z^0+jets, Drell-Yan and di-bosons in the three control regions. The scalings and their uncertainties are derived by the variation of all contribution parameters. The results are

$$\omega_W = 0.586 \pm 0.020 \qquad \omega_{\mathrm{T,f}} = 0.845 \pm 0.163 \qquad \text{and} \qquad \omega_{\mathrm{T,t}} = 0.969 \pm 0.213 \,. \tag{4.21}$$

where ω_W is the scaling for W+jets and $\omega_{\mathrm{T,f}}$ and $\omega_{\mathrm{T,t}}$ are the scalings for Top events with fake and truth taus, respectively. They can be seen in Figure 4.11 with a fitted GAUSSian.

The scalings for the Top backgrounds are close to unity, whereas the scaling for W+jets is about 0.6. These numbers are in very good agreement with the results from Section 4.3. Top has been seen to be well modelled and $\omega_W = 0.586$ reflects the data to MC ratio in the high BDT tails of Figure 4.9 (p. 73). The rather large uncertainties for the Top scalings are more constrained by the correlation among the scalings with the correlation matrix

$$\begin{pmatrix} 1 & -0.144 & 0.057 \\ -0.144 & 1 & -0.907 \\ 0.057 & -0.907 & 1 \end{pmatrix} . \tag{4.22}$$

This can be attributed to the sizable off-diagonal elements of the lower right block in Equation 4.20. An upregulation of the Top fake contributions can partially be compensated by a downregulation of the Top truth contributions and vice versa. This anticorrelation will reduce the total uncertainty on the Top background since it does not allow for independent fluctuation of Top truth and Top fake contributions. Since the scalings are anticorrelated their uncertainties partly counterbalance. The correlation among the scalings will be considered for the uncertainty on the final event selection.

	2011 Data	DiBoson	Drell Yan	Z+Jets	Top	W+Jets	QCD (DD)	SM
GRL	229 373 908	44 253	55 194 030	19 350 596	950 153	145 489 056	–	221 028 089 ± 48 080
Trigger	137 185 828	12 546	231 819	1 766 665	174 229	10 880 125	–	13 065 385 ± 9616
cleaning cuts	134 553 518	12 298	228 107	1 694 491	173 287	10 300 801	–	12 408 984 ± 9261
$N_{\text{jet}}^{50\text{ GeV}} \geq 1$	50 374 151	4997	41 470	248 992	153 694	1 377 472	–	1 826 625 ± 1583
$N_{\mu}^{20\text{ GeV}} = 1$	2 437 754	2988	19 586	99 186	88 532	1 180 140	845 744	2 236 177 ± 209 662
$N_{\tau} \geq 1$	15 194	157	254	3637	2410	9757	2829	19 044 ± 789
$M_{\text{T}}^{\ell} > 50$ GeV	6249	102	43.0	516	1685	6821	104	9270 ± 151
$M_{\text{T}}^{\ell} < 150$ GeV	6121	92.6	42.7	510	1585	6778	104	9113 ± 149
$E_{\text{T}}^{\text{miss}} > 30$ GeV	4940	78.2	15.6	339	1418	5415	71.4	7336 ± 114
$E_{\text{T}}^{\text{miss}} < 100$ GeV	4482	69.2	15.4	320	1187	5032	69.9	6693 ± 109
Top & W+jets CR	4482	69.2	15.4	320	1187	5032	69.9	6693 ± 109
$N_b = 0$	3677	67.7	14.8	313	376	4940	55.1	5766 ± 98
truth taus	–	44.5	0	88.1	138	0	–	271 ± 5
Top & W+jets CR	4482	69.2	15.4	320	1187	5032	69.9	6693 ± 109
$N_b \geq 1$	805	1.53	0.54	6.81	811	92.0	14.8	927 ± 19
$M_{\text{T}}^{\ell} < 100$ GeV	639	1.33	0.54	6.29	638	82.5	14.3	743 ± 16
truth taus	–	0.71	0	3.43	234	0	–	238 ± 3
Top & W+jets CR	4482	69.2	15.4	320	1187	5032	69.9	6693 ± 109
$N_b \geq 1$	805	1.53	0.54	6.81	811	92.0	14.8	927 ± 19
$M_{\text{T}}^{\ell} > 100$ GeV	166	0.20	0	0.52	173	9.49	0.49	184 ± 5
truth taus	–	0.15	0	0.12	106	0	–	107 ± 2

Table 4.5 Cutflow into the control regions used to obtain the scalings. The upper cutflow shows observed and expected events up to combined Top and W+jets control region. The lower three tables are the cutflows to the control regions enriched with W+jets, Top with fake taus and Top with truth taus. The last row gives the events that contain truth taus and the last column the sum of all SM contributions.

The variation of the parameters in Equation 4.20 considers the uncertainties from limited statistics in data and MC as well as the uncertainty of the QCD estimate. Since the control regions do not overlap, all uncertainties are from statistically independent samples and hence smearing is applied uncorrelated. This is not strictly true for the QCD estimate. It contains a systematic contribution, which is correlated among the three control regions. In addition, the statistical uncertainty is correlated to the data uncertainty because QCD is estimated from data. In any case, the overall contribution of QCD is very small. The largest is about 2 % to the Top with fake taus CR (see Table 4.5) and hence QCD has nearly no influence on the final results. Therefore, QCD uncertainties are considered but without any correlation. Correlated variation of the parameters from Equation 4.20, e.g. from jet energy scale uncertainties, are treated separately at a later stage in the analysis, see Section 5.2.

Robustness Tests and Kinematic Dependence

The W+jets scaling has already been shown to be caused by mismodelling of the tau identification in Section 4.3. In addition, the mismodelling was not biased by any effect that could be different in the control regions compared to the remaining kinematic phase space. Still, this is quantified more precisely by the evaluation of the scalings for different input parameters for the method.

The considered influences are the strictness of the tau identification, the pile-up conditions, the used event generators, the definitions of the control regions and additional kinematic cuts to mimic SUSY-like event topologies. The obtained scalings for all variations can be seen in detail in Appendix B in Figures B.1 to B.4 and are summarized in Figure 4.12. It shows the nominal scalings for BDT medium taus as a red line with its uncertainties in yellow and overlaid the obtained scalings for different inputs.

In the final analysis, a common tau identification criterium will be consistently used and hence different scalings for the three BDT benchmarks would be no issue. Though, Figure 4.12 shows stable scalings for all benchmarks. The loose BDT requirement already rejects nearly all taus with BDT jet score below 0.6 (see e.g. Figure 4.5 (p. 67)). The data to MC ratio is constant above this value (see Figure 4.9 for W+jets CR), and hence the three BDT working points are affected in the same manner.

For the evaluation of the pile-up dependence of the scalings, all data and MC samples are split up into a high pile-up ($N_{\text{vtx}} \geq 6$) and low pile-up ($N_{\text{vtx}} \leq 5$) sample. The scalings are then rederived by the use of the two statistical independent samples. This leads to consistent results within the expected uncertainty and no dependence on the pile-up conditions can be seen. Furthermore, the influence of the cut choice on m_{T}^{μ} for the truth and fake tau separation in the Top CR is checked. The strong correlation of the Top related scalings is driven by the sizable mixture of truth and fake contributions in these control regions. Hence, the scalings could be biased by the chosen cut, but Figure 4.12 shows stable behaviour by a variation of the cut by $10\,\text{GeV}$.

The scalings are also derived by the use of different generators for Top and di-bosons. As expected, the use of the `Sherpa` generator for di-bosons shows nearly no influence because the di-bosons contributions are very small in all CRs (see Table 4.5). Also the use of `Alpgen` for Top gives deviations of the scalings that are within the expected statistical uncertainty. Finally, potential impact of the surrounding event kinematics on the scalings is considered. The final search pattern of missing energy and hadronic activity is mimicked in the control regions by additional cuts on $m_{\text{eff.}}$. In the W+jets CR, the remaining statistics is sufficiently high to go up to $m_{\text{eff.}} > 600\,\text{GeV}$, whereas the rather small statistics in the Top CRs only allows for cuts up to $m_{\text{eff.}} > 350\,\text{GeV}$. In any case, no dependence on the kinematics can be seen.

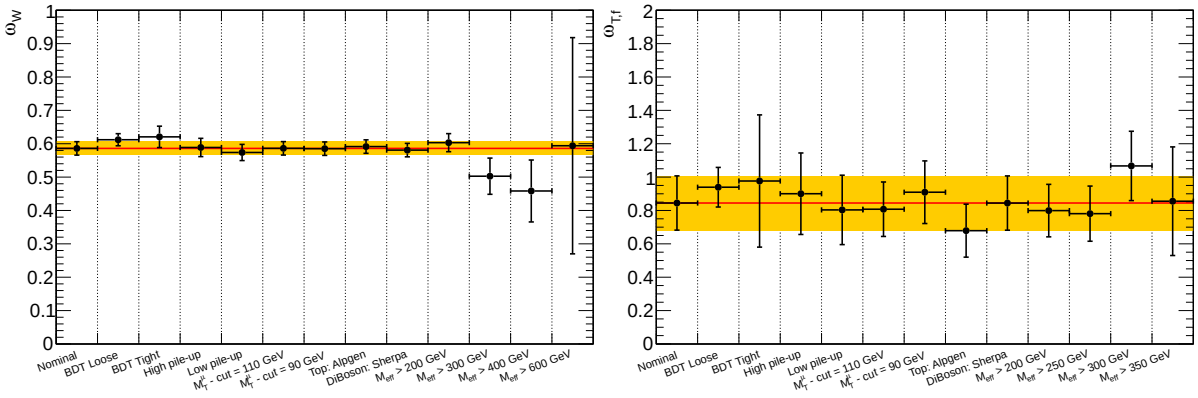

(A) W+jets scaling

(B) Top with fake tau scaling

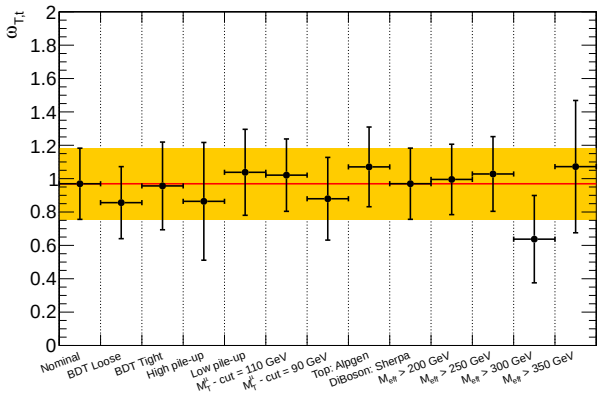

(C) Top with truth tau scaling

Figure 4.12 The obtained scalings for W+jets, Top with fake taus and Top with truth taus for different variations of tau identification, pile-up conditions, kinematic selections and generators. Scalings can be shown to be robust with respect to the nominal value, which is derived from BDT medium taus.

B-Tagging Dependence and Verification in Test Control Region

Further attention has to be paid to any b-tagging related dependence. Since Top and W+jets are separated by a cut on b-tagged jets, the discrepancy for W+jets could be related to any mismodelling of b-tag efficiency and mistag probability. The W+jets CR is defined by a veto on b-tags. Hence, the MC contributions in the W+jets CR could be increased by an underestimated b-tag efficiency. This would lead to larger Top contaminations in the W+jets CR. Also the b-mistag probability could be underestimated. This would veto less W+jets events and hence increase the MC in the W+jets CR as well. Since Top events in the W+jets CR and W+jets events with fake b-tags are both rare, this could hardly explain the difference in observed events by a factor of 0.6. However, there could be some impact that overlays the discrepancies from the tau identification.

The b-tagging performance is checked after the object selection with at least one BDT medium tau. The number of reconstructed b-jets as well as their transverse momentum and pseudorapidity can be seen in Figure 4.13. The good agreement already shows that the Top contributions are well described. The MC excess in the zero b-tag bin can be attributed to the overestimated W+jets contributions and the step in the transverse momentum spectrum is caused by the jet trigger plateau cut. In W+jets events, this step

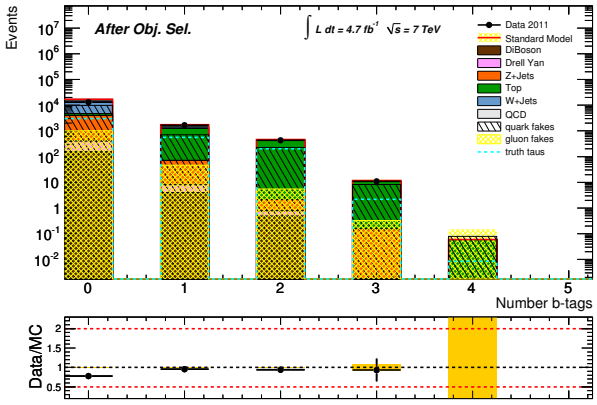

(A) Number of b-tagged jets

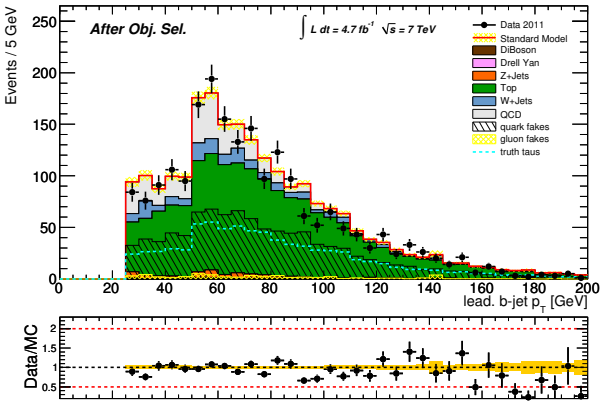

(B) p_{T} of leading b-jet

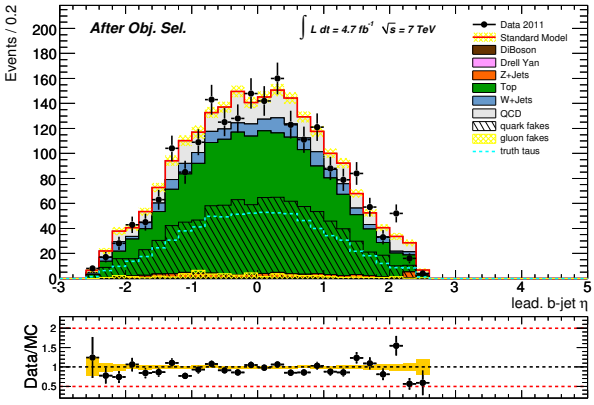

(C) η of leading b-jet

FIGURE 4.13 b-tagging control plots after object selection with BDT medium taus. Agreement is very good, the excess in the zero b-tag bin is due to the overpredicted W+jets contributions and the step in the transverse momentum spectrum is caused by the jet trigger plateau cut.

showed up in the (fake) tau transverse momentum spectrum. Most of the W+jets events do not have an additional jet and the tau needs to surpass this requirement. In Top events, the b-jets from t decays are highly boosted and hence one of them fulfills the trigger plateau cut in most cases.

Any potential bias of the scalings to the use of b-tagging is checked in an additional control region. A test control region is chosen without any applied b-tagging and minimal overlap to the control regions of Table 4.3 by

$$70\,\mathrm{GeV} < E_{\mathrm{T}}^{\mathrm{miss.}} < 150\,\mathrm{GeV}\,. \tag{4.23}$$

Since the available kinematic phase space is limited, a control region with no overlap is only possible with insufficient statistics. Nonetheless, the overlap in $E_{\mathrm{T}}^{\mathrm{miss.}}$ from 70 GeV to 100 GeV between the CRs is moderate. For W+jets, the overlap of 30 GeV to 100 GeV (see Table 4.3 (p. 66)) and 70 GeV to 150 GeV (see Equation 4.23) is not too large (see Figure 4.7(E)) and further suppressed by the $m_{\mathrm{T}}^{\mu} > 50$ GeV cut Table 4.3. The overlap of Top contribution is also largely reduced by the used b-tagging in the CRs of Table 4.3. The cutflow to the test control region can be seen in Table A.10 (p. 149) in Appendix A.

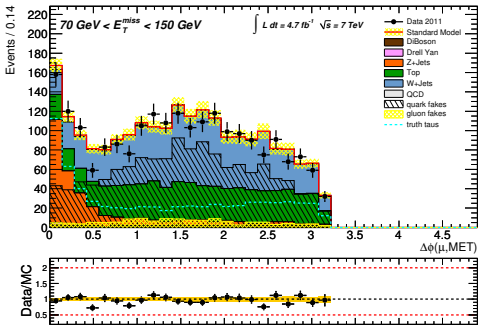

(a) $\Delta\phi\left(\mu, E_{\mathrm{T}}^{\mathrm{miss.}}\right)$

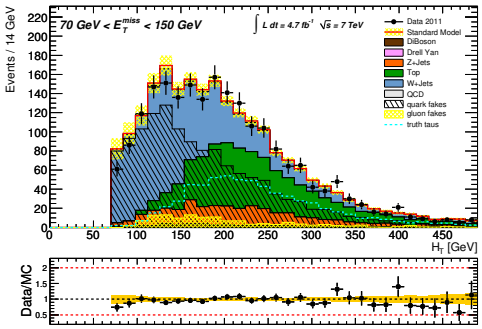

(b) H_{T}

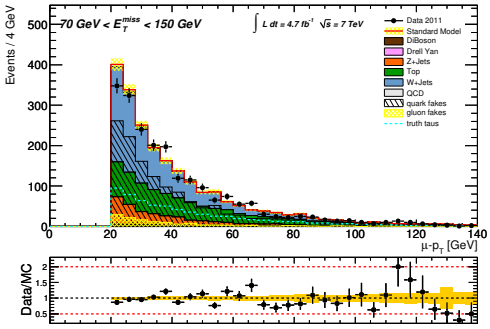

(c) p_{T}^{μ}

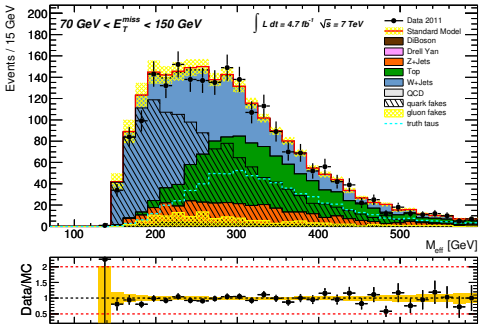

(d) $m_{\mathrm{eff.}}$

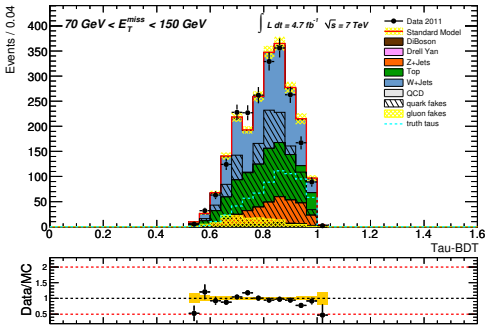

(e) τ BDT jetscore

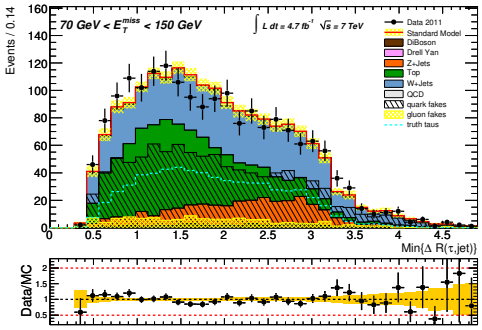

(f) $\min\left\{\Delta R\left(\tau, \mathrm{jets}\right)\right\}$

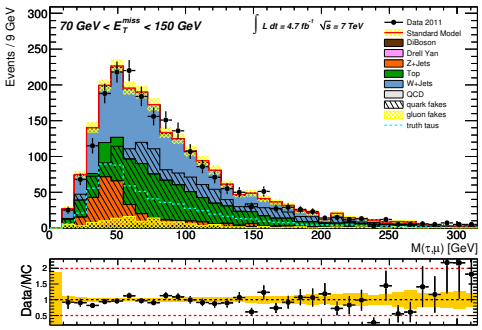

(g) $m_{(\tau,\mu)}$

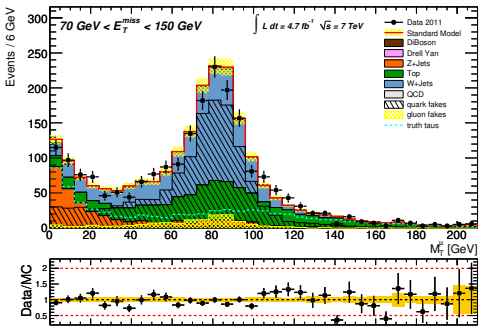

(h) m_{T}^{μ}

Figure 4.14 Data and MC comparisons in the test control region. MC is rescaled and all distributions show good agreement.

Figure 4.14 shows data and MC comparisons in the test control region, where the MC is corrected by the scalings from Equation 4.21. The good agreement shows that the scalings correctly remodel the MC also in events without b-tagging requirement or veto. Hence, no bias of the scalings to the used b-tagging in the control regions of Table 4.3 can be seen. Particularly, Figures 4.14(E) and (D) demonstrate the correct modelling of the tau identification and the $m_{\text{eff.}}$ kinematics after the rescaling. This is an important result since both will be used for the final signal region definition. Furthermore, many of the distributions are dominated by different backgrounds in different ranges, e.g. Figure 4.14(B) or (D). Their good agreement in the shape also shows that the individual contributions, and not only the sum of them, are rescaled properly.

Verification with Muon Charge Asymmetry

The charge asymmetry method, see Section 4.2.2, is also well suited for the estimate of the individual W+jets background contributions. The method relies on a correct modelling of the ratio of positively to negatively charged muons in the W+jets backgrounds. Since this ratio also depends on the W kinematics, it is investigated in the following.

The W transverse momentum, p_{T}^{W}, can be reconstructed by the vectorial sum of the muon's transverse momentum and the $E_{\text{T}}^{\text{miss.}}$. However, its pseudorapidity is experimentally not accessible due to the lacking information on the longitudinal neutrino momentum. Therefore, the η_{μ} is used as a probe since it is the most correlated quantity to the original η_{W}. In addition, m_{T}^{μ} and $\Delta\phi\left(\mu, E_{\text{T}}^{\text{miss.}}\right)$ can be used to test the correct description of the W-decay kinematics in the MC. Since the muon charge should be uncorrelated to the performance of the tau identification, this study is done before the tau requirement to increase available statistics. The chosen object selection only includes the tau candidate without any identification related cut like it was used in Section 4.3.2. It has already been shown that this removes the complications related the tau identification and gives a well described event selection. Since this study targets W+jets events, it is performed in the W+jets CR.

Figures 4.15(A) to (E) show that the W kinematics are correctly modelled in W+jets background. In addition, Figure 4.15(F) is obtained from the combined Top CR[2] and demonstrates the symmetry between positive and negative muons in the Top contributions. This is needed for a correct prediction of the W+jets background.

Though Figure 4.15(A) shows good agreement in the reconstructed muon charge, the high available statistics show a slightly overestimated charge ratio in the MC. This can be seen in Figures 4.15(G) and (H). It displays the charge asymmetry in data and MC as function of η_{μ} and p_{T}^{W}, respectively. The mean deviation of data and MC is about $\Delta r^{\pm} = 0.07$ and will be added as an additional systematic uncertainty via Equation 4.13 (p. 63).

For the test control region from Equation 4.23 this methods predicts a W+jets contribution of

$$N_{W}^{\text{chrg. asym.}} = 1140 \pm 140^{\text{stat.}} \pm 82.7^{\text{MC stat.}} \pm 38.6^{\text{syst.}} = 1140 \pm 167^{\text{tot.}} \,. \tag{4.24}$$

The last systematic comes from the observed mismatch of the charge ratio from the study above. This can be compared to the estimate from the scaled MC prediction

$$N_{W}^{\text{scal. MC}} = (1889 \pm 48) \times (0.586 \pm 0.02) = 1107 \pm 47 \,. \tag{4.25}$$

[2] Combined Top CR means that no separation of truth and fake taus is done. The muon charge is assumed to be uncorrelated to the tau characteristics.

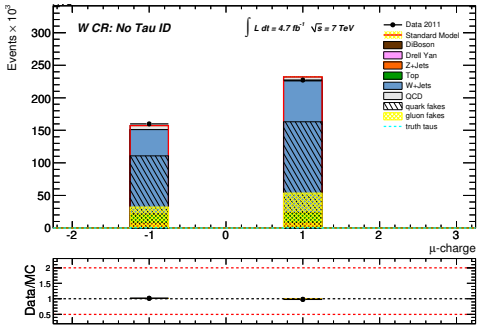

(A) W-CR: Muon charge

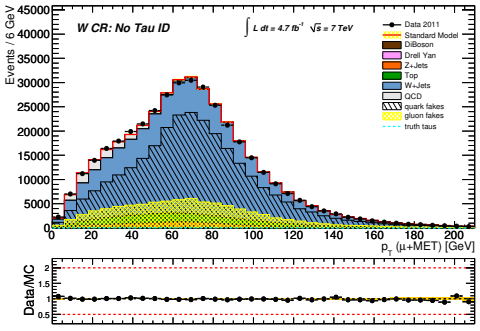

(B) W-CR: rec. W-p_{T}

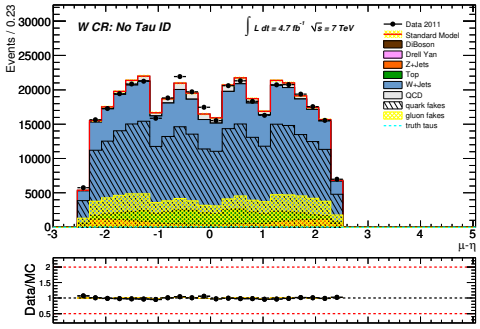

(C) W-CR: η_μ

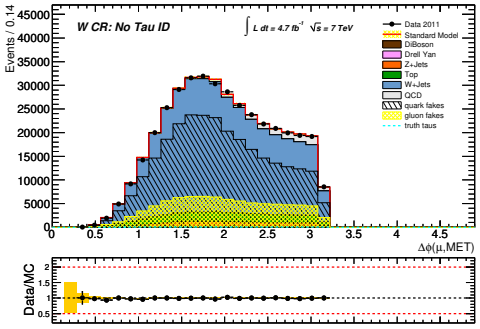

(D) W-CR: $\Delta\phi\left(\mu, E_{\mathrm{T}}^{\mathrm{miss.}}\right)$

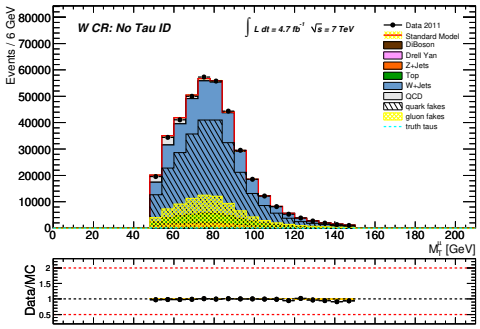

(E) W-CR: m_{T}^{μ}

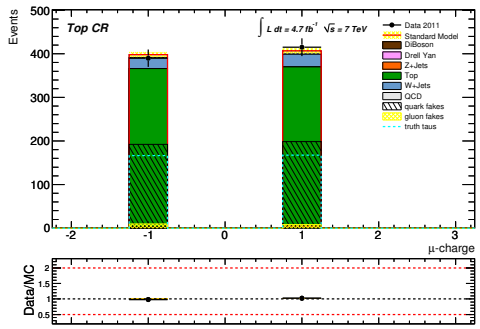

(F) Top-CR: Muon charge

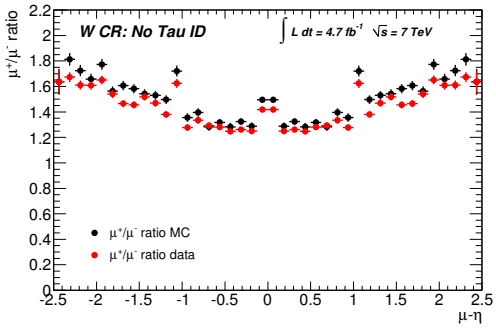

(G) W-CR: $r^{\pm}$ vs. η_μ

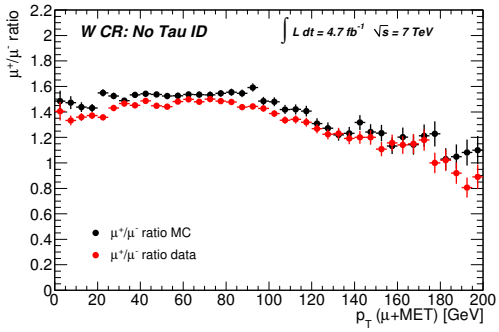

(H) W-CR: $r^{\pm}$ vs. rec. W-p_{T}

Figure 4.15 Control plots for the W charge asymmetry method: (A) to (E) W related kinematics in the W+jets CR before tau identification. (G) and (H): The ratio of negative to positive muons is slightly overestimated in the MC.

The numbers show good agreement and the scaled MC prediction is consistent with the observed charge asymmetry in data. Therefore, the scalings can be confirmed by an independent data-driven method.

Verification by a χ^2 Test

Finally, the method to obtain the scalings is checked by an additional approach. The inversion of the matrix Equation 4.16 (p. 64) solves the system of equations from 4.14. By the variation of all input parameters, a continuum of solutions is obtained, which defines the uncertainties. The existence of an inverse matrix is equivalent to the statement that the rows $\vec{s}_i^{\,\text{row}}$ of the matrix are linearly independent. This means that the control regions must have different relative composition, i.e. $\vec{s}_i^{\,\text{row}} \neq \lambda \vec{s}_j^{\,\text{row}}$ for any i, j and $\lambda \in \mathbb{R}$. This is the case, as long as the chosen cuts have separation power for the considered background types and obviously is true for the matrix in Equation 4.20 (p. 75). Here, each control region is dominated by the wanted background.

The existence of the inverse matrix is also equivalent to the statement that $\mathbf{S}$ is bijective, so there is exactly one set of scalings that fulfills Equation 4.14. All of the smeared matrices will be invertible as long as the uncertainties on the matrix elements are smaller than their differences in the relative compositions. This guarantees linear independent rows in all smeared matrices and exactly one solution for the scalings can be found. Indeed, this is the case for all considered variations of the matrix $\mathbf{S}$. Though one exact solution is obtained for any set of input parameters, it is not obvious whether there might be additional approximate solutions to the equations. These might as well explain the observed data but by different background compositions and with less agreement as the exact solution.

These approximate solutions cannot be found by strict algebraic methods and hence have been looked for by a different approach. One possibility is the simultaneous scan of all scalings and the comparison of their MC prediction with the data observation. The agreement for each set of scalings $\vec{\omega}$ is quantified by a χ^2

$$\chi^2\left(\vec{\omega}\right) = \sum_{i=1}^{3} \left(\frac{N_i'^{\text{obs.}} - \left(\mathbf{S}\vec{\omega}\right)_i}{\sigma_i} \right)^2 , \tag{4.26}$$

where i runs over all CRs and $\mathbf{S}$ is the matrix from Equation 4.14 (p. 64). The uncertainty σ_i includes the uncertainties from the MC predictions $\mathbf{S}$ as well as those from the corrected data observations $\vec{N}'^{\text{obs.}}$. The squared uncertainty on the ith component of the quantity $\mathbf{S}\vec{\omega}$ is

$$\left[\Delta\left(\mathbf{S}\vec{\omega}\right)_i\right]^2 = \left[\Delta\left(\sum_{j=1}^{3} s_{ij}\omega_j\right)\right]^2 = \sum_{k=1}^{3}\left[\underbrace{\frac{\partial}{\partial s_{ik}}\left(\sum_{j=1}^{3} s_{ij}\omega_j\right)}_{=\delta_{jk}\omega_k}\Delta s_{ik}\right]^2 = \sum_{k=1}^{3}\left[\Delta s_{ik}\omega_k\right]^2 \tag{4.27}$$

where Δs_{ik} is the uncertainty on s_{ik}. The squared uncertainty of $\vec{N}'^{\text{obs.}}$ is

$$\left(\Delta N_i'^{\text{obs.}}\right)^2 = N_i^{\text{obs.}} + \sum_{m=n+1}^{k} \left(\Delta s_{im}\right)^2 , \tag{4.28}$$

where m runs over all remaining backgrounds that are not rescaled, i.e. QCD, di-bosons, Drell-Yan and Z^0+jets, see Equation 4.15 (p. 64). The uncertainties from Equation 4.27 and 4.28 are then combined uncorrelated. As explained before, this neglects possible correlations in the uncertainties of the data-driven QCD estimate, which is expected to make no difference due to the small QCD contribution.

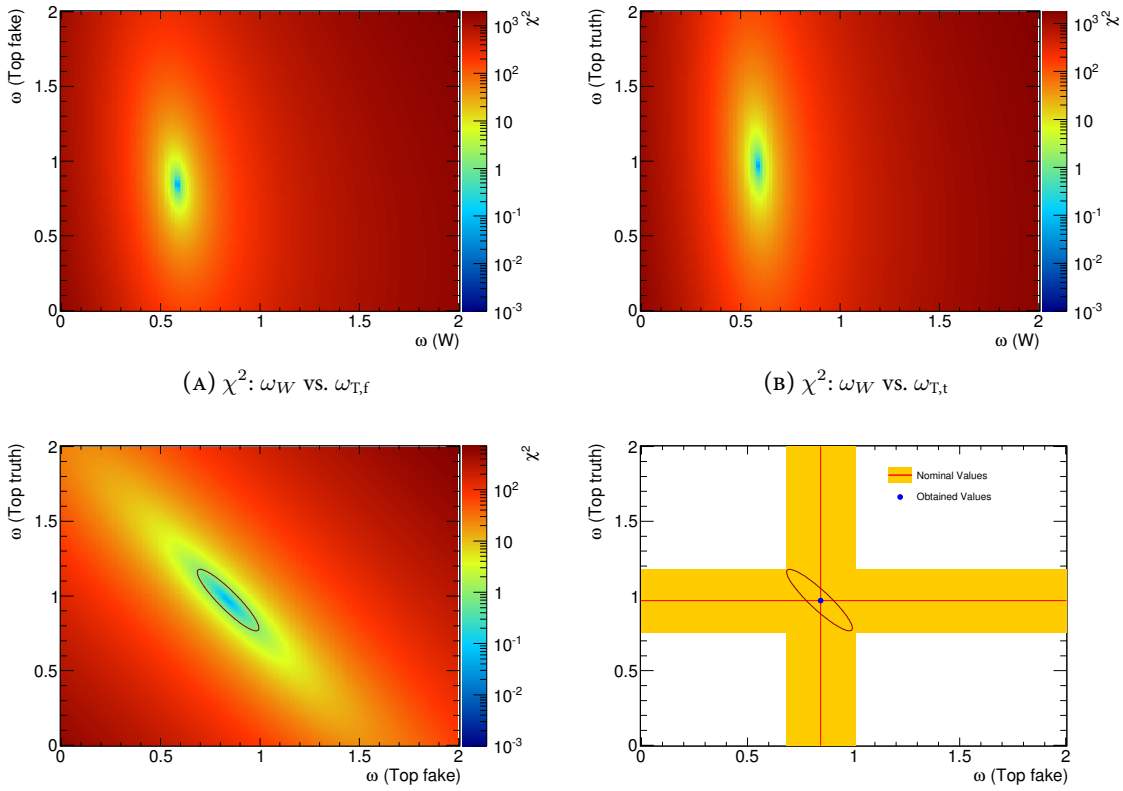

(A) χ^2: ω_W vs. $\omega_{\mathrm{T,f}}$

(B) χ^2: ω_W vs. $\omega_{\mathrm{T,t}}$

(C) χ^2: $\omega_{\mathrm{T,f}}$ vs. $\omega_{\mathrm{T,t}}$

(D) Comparisons of methods

Figure 4.16 The obtained χ^2-distributions from the scan of scalings. The third scaling is always fixed to the value minimizing χ^2. No additional local minima can be seen and uncertainties and correlations are consistent.

The χ^2 is sampled in steps of 0.01 to have sufficient granularity to resolve the expected uncertainty and is scanned in the range of 0 to 2 for each scaling. The scalings with minimal χ^2 are

$$\omega_W = 0.59 \qquad \omega_{\mathrm{T,f}} = 0.84 \qquad \omega_{\mathrm{T,t}} = 0.97\,. \tag{4.29}$$

They reproduce the ones from Equation 4.21 (p. 75) up to the used step width and hence give the same result. Since these scalings are an exact solution, the minimal χ^2 vanishes. This only holds up to very small remaining $\chi^2 \approx 10^{-5}$, since the none of the scanned values exactly matches the solution from Equation 4.21. The obtained three dimensional χ^2-distribution can be seen in Figure 4.16(A) to (C) in two-dimensional slices, where the third scaling is always fixed to the one from Equation 4.29. The distributions show smooth behaviour in all regions and no additional local minima can be seen. A finer search pattern can be found in Appendix B in Figure B.5 (p. 163).

The χ^2-distribution in Figure 4.16(C) also shows the $\Delta\chi^2 = 1$ contour that defines the 1-σ-region around the minimal χ^2. These uncertainties can be compared to the ones from Figure 4.11, as shown in Figure 4.16(D). The yellow bands indicate the uncertainties from the matrix inversion and are in very good agreement with the $\Delta\chi^2 = 1$ contour. Also the expected anticorrelation can be seen. Therefore, the same scalings and uncertainties are obtained by this different approach.

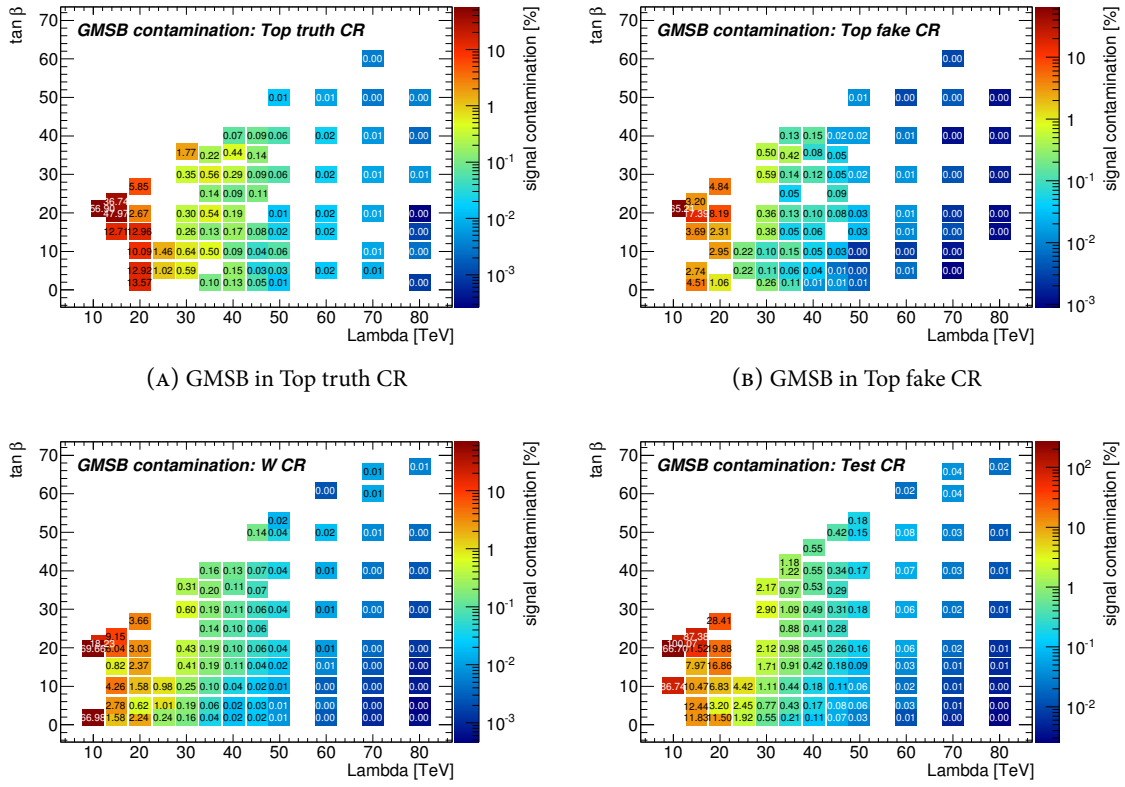

(A) GMSB in Top truth CR

(B) GMSB in Top fake CR

(C) GMSB in W+jets CR

(D) GMSB in test CR

FIGURE 4.17 The expected signal contamination from the considered GMSB model in the control regions for (A): Top with truth taus, (B): Top with fake taus, (C): W+jets and (D): the control region used to test the scalings.

Impact of Potential SUSY Contamination

So far, the scalings have been derived under the background-only hypothesis, i.e. only the SM contributions are considered. In addition, also potential SUSY could contribute to the control regions and hence bias the results. This effect is tried to be minimized by upper bounds on SUSY sensitive variables, i.e. $E_{\mathrm{T}}^{\mathrm{miss.}} < 100\,\mathrm{GeV}$ and $m_{\mathrm{T}}^{\mu} < 150\,\mathrm{GeV}$, where the SM is expected to dominate. However, the influence is quantified more precisely in Figure 4.17. It shows the relative GMSB contamination in the used control regions from the model points defined in Equations 2.89 to 2.91 (p. 33).

The signal points above $\Lambda > 20\,\mathrm{TeV}$ show only small contributions at permille level. These are well below the uncertainties on the scalings. In the Top CRs, Top with truth taus has slightly larger relative SUSY contributions. The kinematic disentanglement of true and fake tau contributions was based on the presence of additional missing energy in the events with truth taus. In that sense, Top with truth taus is more signal-like and has larger GMSB contamination. The largest relative contribution is in the test control region (see Equation 4.23) due to the larger allowed $E_{\mathrm{T}}^{\mathrm{miss.}}$ phase space. However, this region is only used for control tests and not to obtain the scalings.

Summarizing, the derived data-driven scalings can be shown to be robust and to have neither any bias to event kinematics nor the used b-tagging in the control regions. Additionally, the scalings can be confirmed by an independent data-driven method that uses the muon charge asymmetry and by the minimization of a χ^2-function. In the following, Top and W+jets contributions will be always rescaled

if not explicitly stated otherwise. The corrected MC represents the best background estimate and hence should be used for the analysis.

4.4.2 QCD

The data-driven QCD estimate is obtained from the matrix method, see Section 4.2.1, and is validated in the following. Due to the muon and the tau requirement, the QCD contribution after the object selection is already too small to establish a QCD dominated CR. Therefore, variables are considered that have discrimination power between QCD and non-QCD contributions. They can be seen in Figure 4.18.

Figures 4.18(a) and (b) indicate that muons are more aligned with the $E_{\mathrm{T}}^{\mathrm{miss.}}$ in QCD, whereas taus are rather back-to-back to the $E_{\mathrm{T}}^{\mathrm{miss.}}$. This can be explained by the muon identification. A muon in QCD is either faked by a jet or a real muon from heavy quark decays in the jet. The latter case is suppressed by strong isolation requirements, which could be surpassed if essential parts of the primary jet are missed by the reconstruction. If the muon is faked by a jet, parts of its energy could be lost as well because the muon identification vetoes on calorimetric activity around the track. In both cases, energy of the jet that gives the (mis-)identified muon is missing and defines the direction of $E_{\mathrm{T}}^{\mathrm{miss.}}$. This $E_{\mathrm{T}}^{\mathrm{miss.}}$ is then aligned with the muon. In that case, the missing energy and the muon energy should add up approximately the original jet energy.

Since most QCD events are di-jet events, the jet that fakes the tau is expected to be back-to-back with the jet faking the muon. Hence, the tau should be back-to-back to the vectorial transverse momentum sum of the muon and missing energy. This can be seen in Figure 4.18(c), where QCD peaks at $\Delta\phi = \pi$. This signature is also seen in W+jets. Here, the tau is faked by a jet that recoils against the W-boson, which gives the truth $E_{\mathrm{T}}^{\mathrm{miss.}}$ and the muon.

In addition, Figures 4.18(d) to (f) show kinematic variables where QCD and non-QCD appear differently. In all cases, the data-driven QCD estimate closes the missing events between the scaled non-QCD MC and the data observations and hence gives a reliable result. A small underestimate of QCD is seen in the QCD enriched regions, which principally could be corrected with these plots. However, the final event selection will be above $m_{\mathrm{T}}^{\mu} > 100\,\mathrm{GeV}$. In this region, QCD does not contribute significantly and uncertainties on the estimate are well above the slight discrepancy in this plots.

Strictly speaking, the use of scaled non-QCD MC in these plots does not provide a completely unbiased control check for the matrix method. The QCD estimate has already been used to derive the scalings. If the estimate would be wrong, obtained scalings could be influenced. E.g. a strong underestimate of QCD would result in larger scalings since data are less reduced for the QCD contributions. The underestimated QCD could still be hidden in Figure 4.18 because non-QCD contributions would be larger and partly compensate for the missing QCD.

This interplay between the two data-driven estimates is caused by the presence of QCD in the control regions from Table 4.3 and the presence of non-QCD contributions in the plots from Figure 4.18. However, the cross-talk of these methods is strongly suppressed by the small QCD contributions in the Top and W+jets control regions, see Table 4.5. The biggest influence of QCD can be seen in the Top with fake taus CR. Still, it contributes only about 2 % of events to that CR and has nearly no influence on the scalings. In addition, the different shapes of QCD and non-QCD in Figure 4.18 do not allow for their compensation. In that sense, the two methods can be regarded as decoupled and cross checked separately.

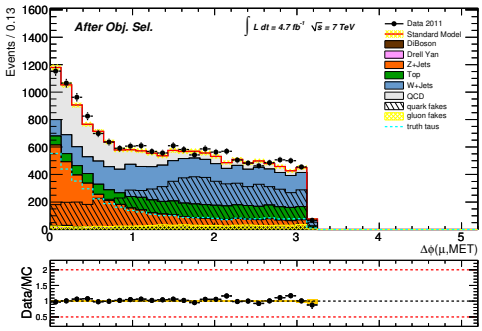

(A) $\Delta\phi\left(\mu, E_{\mathrm{T}}^{\mathrm{miss.}}\right)$

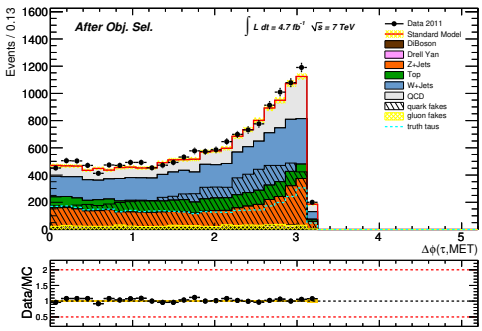

(B) $\Delta\phi\left(\tau, E_{\mathrm{T}}^{\mathrm{miss.}}\right)$

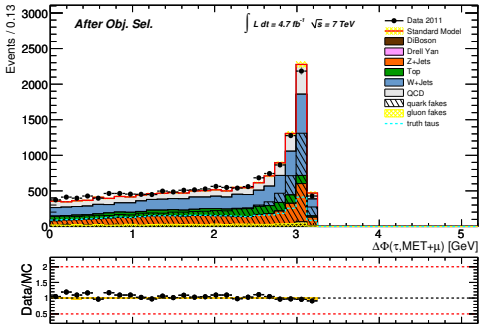

(C) $\Delta\phi\left(\tau, E_{\mathrm{T}}^{\mathrm{miss.}} + \mu\right)$

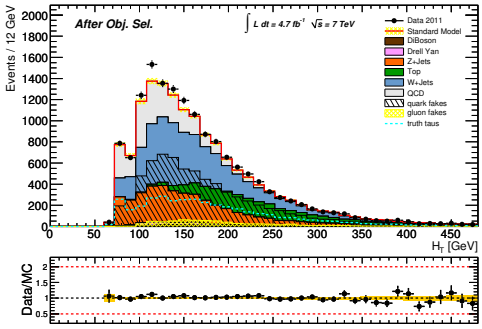

(D) H_{T}

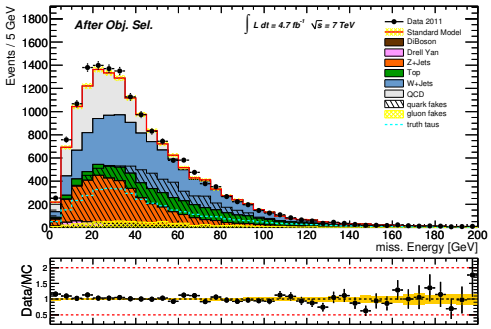

(E) $E_{\mathrm{T}}^{\mathrm{miss.}}$

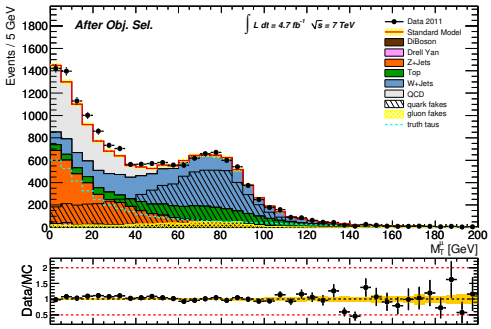

(F) m_{T}^{μ}

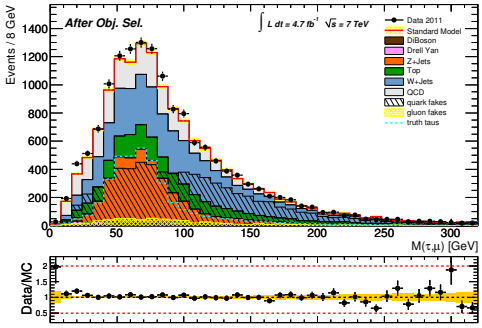

(G) Invariant mass of τ and μ

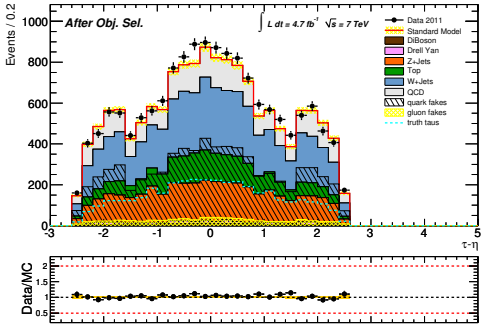

(H) η_{τ}

FIGURE 4.18 QCD control plots after the object selection. W+jets and Top are rescaled and the data-driven QCD estimate closes the gap between rescaled non-QCD MC and the data observation. Tau is BDT medium.

4.4.3 Z^0+jets and Drell-Yan

Although Z^0+jets and Drell-Yan principally originate from the same process, they are listed separately. Objects in Drell-Yan events typically have much smaller transverse momenta and hence very small contributions to the analysis. Likewise, the Z^0+jets contributions will turn out to have no major impact on the final event selection. Their modelling in the MC shall be investigated nonetheless. The treatment of its contributions to the data-driven scalings by pure subtraction of the MC prediction in Equation 4.15 (p. 64) shall be justified.

A Z^0+jets control region is enriched with events where the tau and the muon have opposite charge, as expected from $Z^0 \to \tau^+\tau^-$. Furthermore, Figure 4.18(f) suggests to look on the m_{T}^{μ} region below 40 GeV to suppress Top and W+jets. The large QCD contributions can be reduced by tighter cuts on the muon transverse momentum of $p_{\mathrm{T}}^{\mu} > 30\,\mathrm{GeV}$.

Unfortunately, the taus' decays do not allow for a reconstruction of the Z^0 mass peak and to enrich Z^0 events by a mass window cut. This can be partly compensated by the reconstruction of the invariant mass in the collinear approximation. It assumes that the neutrinos make up the total missing transverse momentum. In the limit of high energetic taus, all their decay products are aligned with the original tau momentum. The two neutrinos of the τ_μ decay and the one neutrino of the τ_{had} then point in the direction of the visible decay products (the muon and the tau jet) and make up the total $E_{\mathrm{T}}^{\mathrm{miss.}}$. The two neutrinos from the τ_μ decay can be treated as one kinematic entity for this considerations since they are both aligned. This gives the following set of relations in the transverse plane

$$\frac{p_y^{\nu_{\tau_{\mathrm{had}}}}}{p_x^{\nu_{\tau_{\mathrm{had}}}}} = \frac{p_y^{\tau}}{p_x^{\tau}} \qquad \frac{p_y^{\nu_{\tau_\mu}}}{p_x^{\nu_{\tau_\mu}}} = \frac{p_y^{\mu}}{p_x^{\mu}} \qquad p_x^{\nu_{\tau_{\mathrm{had}}}} + p_x^{\nu_{\tau_\mu}} = E_x^{\mathrm{miss.}} \qquad \text{and} \qquad p_y^{\nu_{\tau_{\mathrm{had}}}} + p_y^{\nu_{\tau_\mu}} = E_y^{\mathrm{miss.}}\,. \tag{4.30}$$

These four relations can be solved for the four unknown transverse neutrino momenta.[3] The fraction of the undecayed tau's energy that is carried by the visible decay products can then be calculated to

$$z_{\tau_{\mathrm{had}}} = \frac{p_x^{\tau}}{p_x^{\tau} + p_x^{\nu_{\tau_{\mathrm{had}}}}} = \frac{p_y^{\mu} \cdot p_x^{\tau} - p_y^{\tau} \cdot p_x^{\mu}}{p_y^{\mu} \cdot p_x p_y^{\tau} \cdot p_x^{\mu} + p_y^{\mu} \cdot E_x^{\mathrm{miss.}} - p_x^{\mu} \cdot E_y^{\mathrm{miss.}}} \tag{4.31}$$

$$z_{\tau_\mu} = \frac{p_x^{\mu}}{p_x^{\mu} + p_x^{\nu_{\tau_\mu}}} = \frac{p_y^{\mu} \cdot p_x^{\tau} - p_y^{\tau} \cdot p_x^{\mu}}{p_y^{\mu} \cdot p_x^{\tau} - p_y^{\tau} \cdot p_x^{\mu} - p_y^{\tau} \cdot E_x^{\mathrm{miss.}} + p_x^{\tau} \cdot E_y^{\mathrm{miss.}}}\,. \tag{4.32}$$

Finally, the original invariant mass can be reconstructed by

$$m_{(\tau,\mu)}^{\mathrm{CL}} \approx \sqrt{\frac{\left(p^{\tau} + p^{\mu}\right)^2}{z_{\tau_{\mathrm{had}}} \cdot z_{\tau_\mu}}}\,. \tag{4.33}$$

Typically, the transformation only shifts the reconstructed mass peak to the Z^0 mass. The width of the distribution is still broadened by the finite $E_{\mathrm{T}}^{\mathrm{miss.}}$ resolution considerably, so that a mass window cut is not effective. Nevertheless, a requirement on the invariant mass in the collinear limit above 60 GeV is a helpful QCD discriminant.

Furthermore, the invariant mass of the tau and the muon, without any $E_{\mathrm{T}}^{\mathrm{miss.}}$ corrections, is expected below the Z^0 mass in Z^0+jets. In other SM backgrounds, the (fake) tau and the muon are not constrained by that and hence $m_{(\tau,\mu)} < 90\,\mathrm{GeV}$ is required. The cutflow to the Z^0+jets control region can be seen in Table A.11 (p. 150) in Appendix A.

[3] The four degrees of freedom in the transverse plane of the two-neutrino-system from the τ_μ decay reduce to two. They have the same ϕ and only the sum of x- and y-momenta are needed and not the individual contributions.

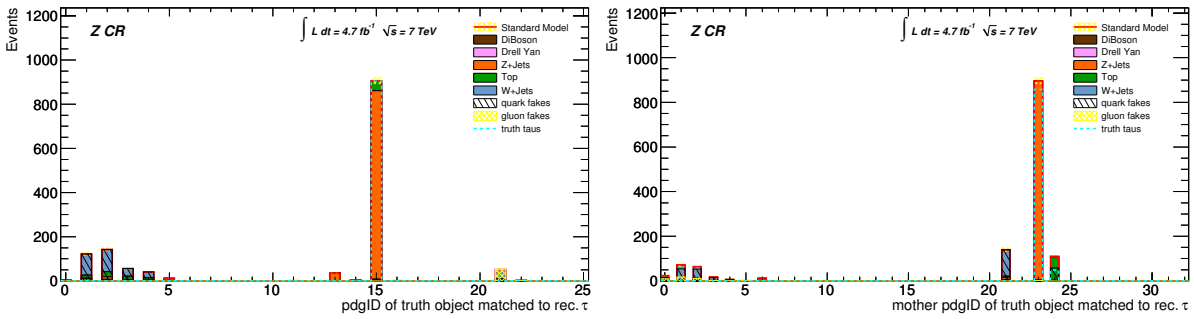

(A) Z^0+jets: Truth object matched to τ (B) Z^0+jets: Mother of truth object matched to τ

FIGURE 4.19 Origin of taus in the Z^0+jets control region. (A): The PDG ID of the truth object matched to the tau candidate and (B): The PDG ID of the mother of the truth object that gives the tau. Most taus are truth taus from Z^0 decays, the fakes are dominantly quark initiated from the Top and W+jets contributions. Tau is BDT loose.

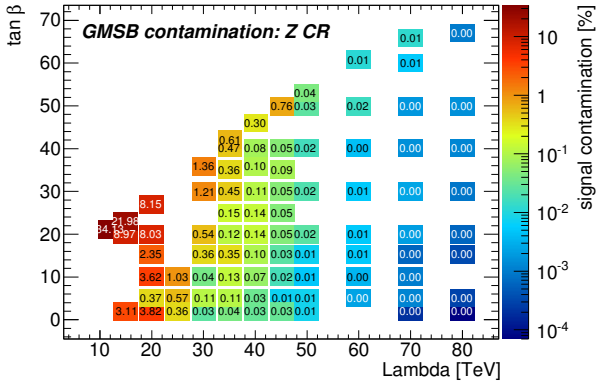

FIGURE 4.20 The relative GMSB contamination in the Z^0+jets control region.

The sum of these cuts decrease the available statistics considerably, so that the study is done with BDT loose taus. Therefore, slightly different scalings than the one for medium taus are used, see Figure 4.12. Since the Z^0+jets contributions are unscaled in this study, the results will still hold for medium taus. This is true as long as the quality of the tau identification description in MC is the same for loose and medium taus. This could already be seen in Figure 4.12 and is even less critical for Z^0+jets, which is true tau dominated. Truth tau related scalings were already shown to be consistent with one in Top.

The composition of the truth objects that give the reconstructed tau can be seen in Figure 4.19. Most taus are indeed true taus that come from Z^0 decays. The fake taus are dominantly quark jet initiated and in most cases either come from the remaining W+jets or Top contributions. Since most taus are truth taus, good agreement is expected. Truth taus could be seen to be well described in the MC. Figure 4.20 also shows the relative GMSB contamination from the considered signal grid in the Z^0+jets control region. Above $\Lambda > 20$ TeV the contributions are at permille level.

Figure 4.21 displays data and MC comparisons in the Z^0+jets control region. Data and MC can be seen to be in good compliance. Figures 4.21(A) and 4.21(B) demonstrate that the muon is more aligned with $E_{\mathrm{T}}^{\mathrm{miss.}}$ than the tau. Since these muons come from tau decays, they are accompanied by two neutrinos, which dominate the $E_{\mathrm{T}}^{\mathrm{miss.}}$. All distributions show good agreement in shape and normalization so that

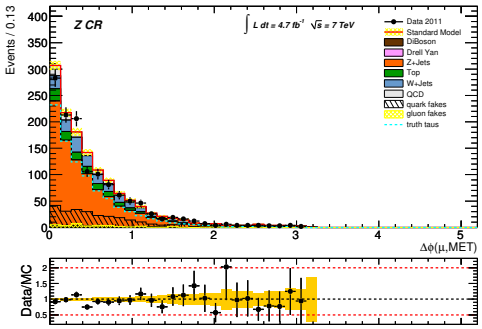

(a) $\Delta\phi\left(\mu, E_{\mathrm{T}}^{\mathrm{miss.}}\right)$

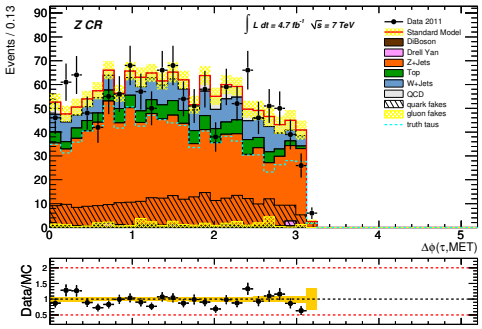

(b) $\Delta\phi\left(\tau, E_{\mathrm{T}}^{\mathrm{miss.}}\right)$

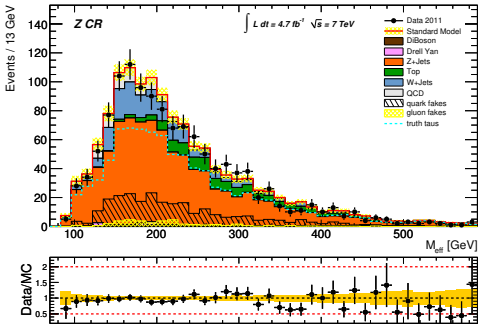

(c) $m_{\mathrm{eff.}}$

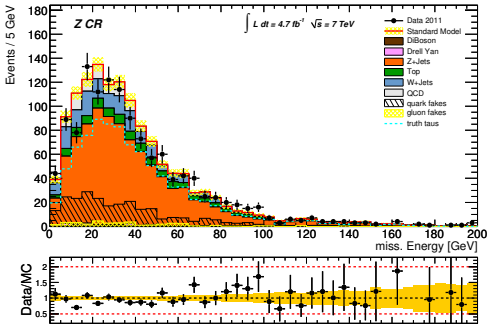

(d) $E_{\mathrm{T}}^{\mathrm{miss.}}$

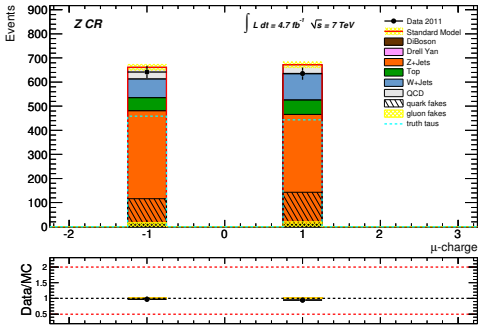

(e) Muon charge

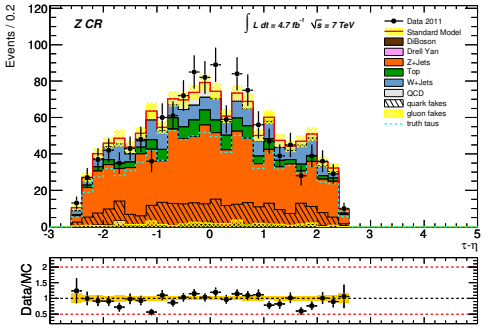

(f) η_{τ}

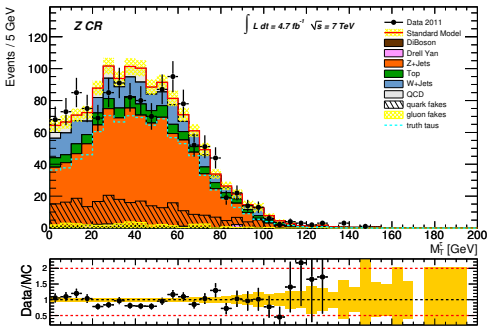

(g) m_{T}^{τ}

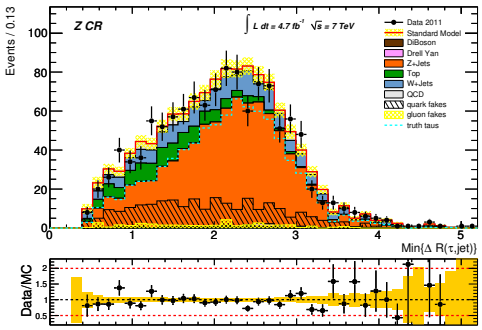

(h) $\min\{\Delta R(\tau, \mathrm{jets})\}$

Figure 4.21 Data and MC comparisons in the Z^0+jets control region. Taus are BDT loose to ensure sufficient event statistics. All quantities show good agreement.

Z^0+jets can be seen to be correctly described. Figure 4.21(E) also shows the symmetry for positive and negative muons, as required for the charge asymmetry method.

The individual investigation of Drell-Yan processes is not possible due to their low-p_{T} objects and hence small contributions. They will have only very small contributions to the analysis (see Section 5.1.4) and hence do not demand for high attention or special data-driven techniques. If MC statistics is lacking, an estimate for their contribution is made by extrapolation. The normalization of its contribution can be predicted under the assumption that kinematic quantities behave as in Z^0+jets by

$$N_{\mathrm{est.}}^{\text{Drell-Yan}}\,(\text{after cut}) = \frac{N_{\mathrm{MC}}^{Z^0\text{+jets}}\,(\text{after cut})}{N_{\mathrm{MC}}^{Z^0\text{+jets}}\,(\text{before cut})} N_{\mathrm{MC}}^{\text{Drell-Yan}}\,(\text{before cut})\ . \tag{4.34}$$

This is a conservative estimate because variables like $m_{\mathrm{eff.}}$ or H_{T} are expected to be softer in Drell-Yan compared to Z^0+jets. Hence, the extrapolation should fall more steeply compared to Z^0+jets.

4.4.4 Di-Bosons

Di-boson events, i.e. WW, WZ^0, Z^0Z^0, can also produce a muon and additional taus. Neutrinos from W, Z^0 or τ decays might provide true $E_{\mathrm{T}}^{\mathrm{miss.}}$ and additional jets might arise from hadronically decaying W and Z^0 or associated QCD processes. Likewise for Z^0+jets, these events could be investigated in dedicated control regions to see if they are correctly described in the MC.

A detailed MC study has been performed to isolate di-boson events with taus [289]. It could be shown that an enrichment of these events is hardly feasible due to two reasons. Firstly, the cross sections are small compared to other SM processes and hence contributions typically drown in other backgrounds. Secondly, the considerable fake rate for taus contaminates the selection with misidentified taus. E.g. $Z^0W \to \mu\mu\tau$ has huge backgrounds from Z^0+jets where the Z^0 decays into muons and the tau is faked. The same is true for $WW \to \tau\mu$, which is superimposed by $W \to \mu$ with fake taus and also $t\bar{t}$ with two leptonically decaying W bosons.

Although a dedicated study in a control region is not possible, the expected origin of selected taus can be studied purely MC based. For that purpose, selected taus from di-boson events have been scrutinized after the object selection. Figures 4.22(A) and (B) show the origin of the taus. Most taus are truth taus from either Z^0 (PDG ID: 23) or W (PDG ID: 24) decays. The few remaining fake taus are completely quark jet dominated where the quarks comes from hadronically Z^0 or W decays. Fakes that originate from W bosons have already been shown to be well modelled in Top, see Section 4.3. Quark initiated fake taus from $Z^0 \to q\bar{q}$ can be expected to have similar properties. The quarks have the same color flow in hadronization like quarks from $W \to qq'$ and strong interactions are blind to the electroweak quantum numbers of the W and the Z^0. Also truth taus could be found to be correctly described in Top, see Section 4.3, and in Z^0+jets, see Section 4.4.3. Hence, no strong mismodelling is expected for di-bosons.

As a further check, the kinematics of the selected taus are investigated. This can be used to see if there are any di-bosons specific kinematic features that could spoil the correct description of the tau identification. This can be seen in Figures 4.22(C) to (H). The low hadronic activity in di-boson events often requires the tau candidate to surpass the jet trigger plateau cut. Therefore, many di-boson events have $p_{\mathrm{T}}^{\tau} > 50\,\mathrm{GeV}$, which explains the spike in the transverse momentum spectrum. The quantities do not show any suspicious behaviour that is different to Top backgrounds, see e.g. Figure 4.5 (p. 67). In addition, the overall contribution from di-bosons is rather small and hence its contribution is estimated purely MC based, without any specific data-driven techniques.

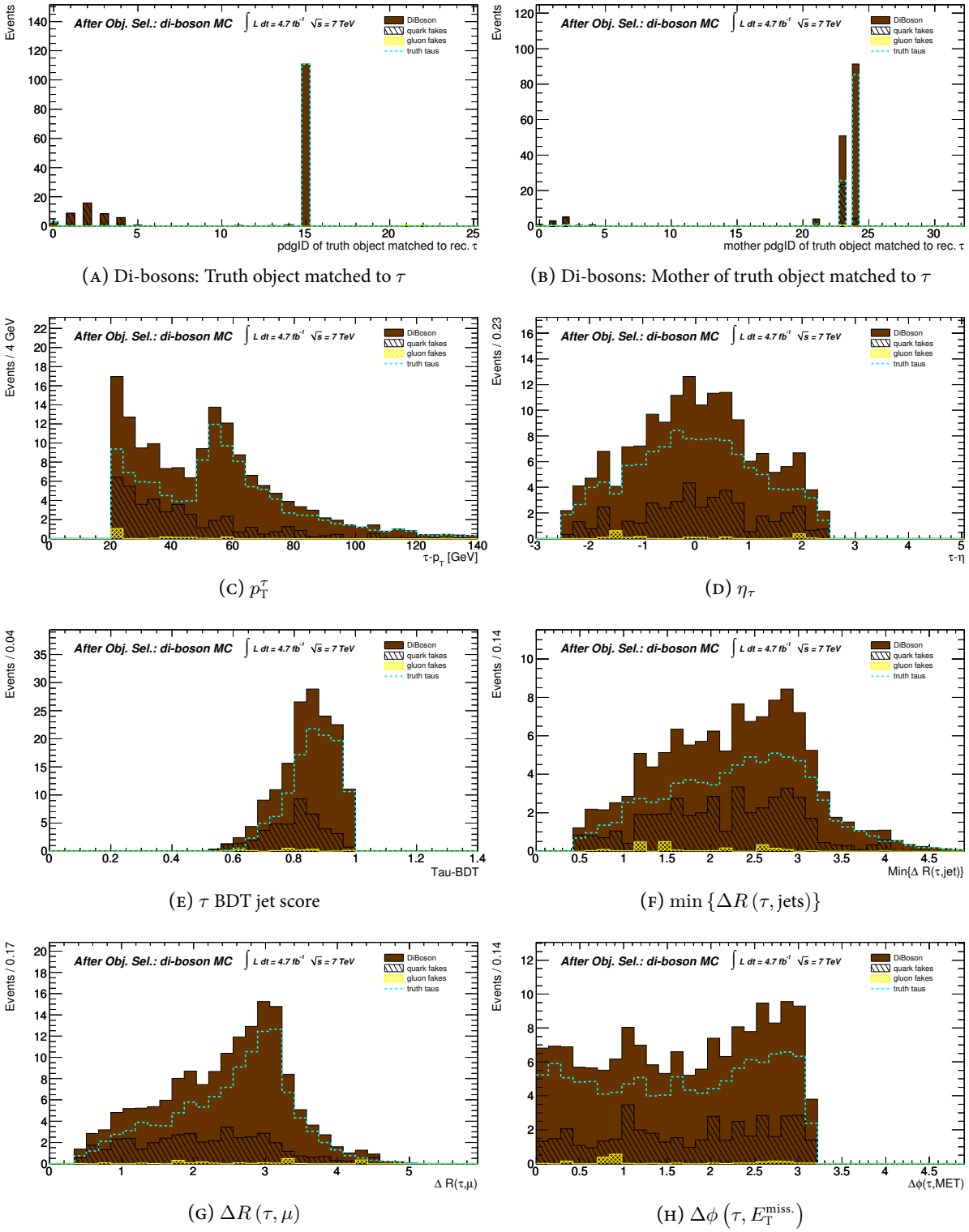

(A) Di-bosons: Truth object matched to τ

(B) Di-bosons: Mother of truth object matched to τ

(C) p_{T}^{τ}

(D) η_{τ}

(E) τ BDT jet score

(F) $\min\{\Delta R(\tau, \text{jets})\}$

(G) $\Delta R(\tau, \mu)$

(H) $\Delta\phi\left(\tau, E_{\mathrm{T}}^{\text{miss.}}\right)$

Figure 4.22 Control plots for di-bosons MC. (A): PDG ID of the truth object matched to the tau candidate and (B): The PDG ID of its mother. Most taus are truth taus from Z^0 or W decays, fakes are dominantly quark initiated. (C) to (H): Tau kinematics. Tau is BDT medium.

Summary

The SM backgrounds from Top and W+jets are corrected by data-driven scale factors. The scalings for Top are close to unity, whereas W+jets needs to be scaled down. The W+jets scaling can be shown to be caused by an overestimated fake rate in the MC due to less complex and hence more tau-like jets in the W+jets MC. Furthermore, the scalings can be shown to be robust and free of any bias to kinematics or the use of b-tagging. The obtained values and uncertainties for the scalings have been cross checked by the charge asymmetry method as well as by a different χ^2-method.

The background for QCD is estimated completely data-driven and can be confirmed in QCD enriched kinematic phase space. Z^0+jets contributions are controlled by the verification of its MC description in control regions. Drell-Yan and di-bosons cannot be investigated individually in CRs due to their small contributions. However, Drell-Yan can be estimated conservatively under the assumption of the same behaviour as Z^0+jets. The di-bosons estimate is obtained from pure MC prediction, which could be justified by the results of the other background studies.

In general, it could be consistently seen that events with truth taus are described properly, whereas fakes from W+jets are mismodelled. The correct description of truth taus will also apply for the signal samples and hence modelling of the tau efficiency in the signal selection can be assumed to be correct. Clearly, this only holds for truth tau dominated signal selections.

Chapter 5

Entering a New Regime

The Search for SUSY with Taus and a Muon

The contributions from the SM and their appearance in the analysis have been investigated in the previous chapter. With their knowledge, SUSY-like signatures can now be searched, as will be described in this chapter. The analysis parameters that quantify the SUSY-likeness of the event topologies are optimized for a maximal discrimination power between GMSB and the SM. Moreover, the systematic uncertainties on the final event selection are quantified. Finally, the data observation is compared to the SM expectation as well as to potential GMSB predictions.

5.1 Event Selection Optimization

For an optimal analysis sensitivity, the event selection must be optimized to suppress SM backgrounds and at the same time guarantee an efficient selection of SUSY events. Since the search aims at a whole set of possible SUSY realizations in the GMSB model, the analysis has to be simultaneously optimized for all grid points. They have been specified in Equations 2.89 to 2.91 (p. 33). Furthermore, the selection cuts have to be investigated with respect to the changing phenomenology in the parameter grid.

5.1.1 Object Selection in the GMSB Model

As a first characterization of the analysis, the performance of the object selection is studied in the GMSB grid. The origin of selected leptons is of special interest to confirm whether the analysis really probes the tau richness of GMSB. Figure 5.1(a) shows the purity of taus in the object selection, i.e. the fraction of events in which the selected tau candidate originates from a truth tau. The selected taus are truth tau dominated in the whole grid and hence the hadronic tau requirement is sensitive to the enhanced tau production in GMSB models. The studies from Chapter 4 also showed that truth taus are not affected by any issues in the tau identification. Hence, the signal efficiency can be assumed to be correctly modelled.

Figure 5.1(b) gives the fraction of events where the selected muon comes from a tau decay. The purity is lower due to the presence of prompt muons. These predominantly arise from either $\widetilde{\chi}_1^0$, $\widetilde{\chi}_2^0$ or $\widetilde{\mu}_{L,R}$ decays and have better reconstruction efficiency compared to muons from taus, since these loose energy from two neutrinos. However, in the high $\tan\beta$ space about $2/3$ of the muons come from tau decays and hence probe the tau richness as well. This can be attributed to the larger mass splitting in the stau sector as explained in Section 2.2.3, which leads to much more staus compared to smuons. In the low $\tan\beta$ region, the reconstructed muons are rather prompt muons since the stau mixing is small and the sleptons are nearly mass degenerated. Still, for high Λ nearly $50\,\%$ of the muons come from taus. Here, the tau transverse momenta are sufficiently high to compensate for the loss of the neutrino energies in $\tau \to \nu_\tau \nu_\mu \mu$. Faked muons can be shown to be negligible.

Figure 5.2(a) shows the acceptance, i.e. the fraction of MC signal events that pass the object selection. As expected, the sensitivity is better in the high $\tan\beta$ region where taus dominate. The phenomenology

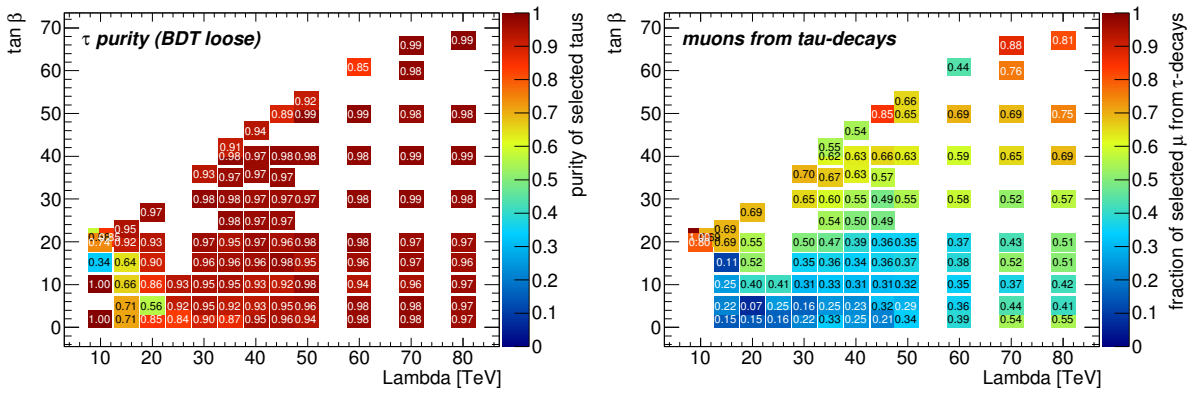

(A) Purity of taus

(B) Fraction of muons coming from τ-decays

Figure 5.1 (A): The purity of selected taus and (B): The fraction of muons coming from tau decays.

of the low $\tan\beta$ region is dominated by the first generation sleptons and for very low Λ objects are too soft to be reconstructed. Hence, these points have smaller acceptance.

The acceptance of the full object selection is also unfold into the efficiencies of the individual object requirements. Here, efficiency is defined by

$$\frac{N^{\mathrm{MC}}\,(\text{after cut})}{N^{\mathrm{MC}}\,(\text{before cut})}\,. \tag{5.1}$$

As shown in Figure 5.2(B), the muon trigger is more effective in the low $\tan\beta$ region, which has more high-p_{T} prompt muons. Since the muon is required in any case at a later stage, this does not reduce the analysis power. The trigger efficiency for the finally required high p_{T} muon is close to one. Figure 5.2(C) shows the signal efficiency for the jet trigger plateau cut and demonstrates high and constant performance. Obviously, the combination of a jet trigger with the muon trigger does not reduce SUSY signals from strong production and is an appropriate choice to construct unprescaled triggers. This will be even more true for the final event selection, which will explicitly require hadronic activity.

Figure 5.2(D) shows the efficiency of the muon requirement. The lower efficiency for small $\tan\beta$ is an interplay of the already applied muon trigger and the GMSB physics. Typically, leptons arise by decay chains like

$$\widetilde{\chi}_i^0 \to \widetilde{\ell}\ell \to \widetilde{G}\ell\ell\,, \tag{5.2}$$

where two same-flavour leptons are produced. In the case of taus, their decay to the searched final state of a muon and a hadronic tau decouples the flavour correlation. In the low $\tan\beta$ region, triggered prompt muons are accompanied by a second muon. This is vetoed at this stage to avoid overlap to the di-lepton search. This loss is no deficit since the analysis targets tau final states and not prompt muons. Finally, Figure 5.2(E) shows the fraction of selected events before and after the tau requirement, which his BDT medium. The tau-rich high $\tan\beta$ region has more taus and hence more events are selected.

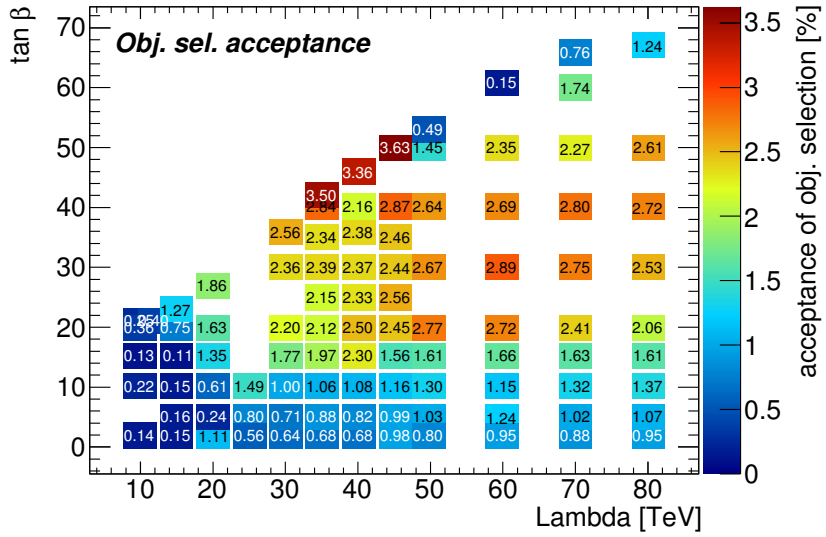

(A) Acceptance of object selection

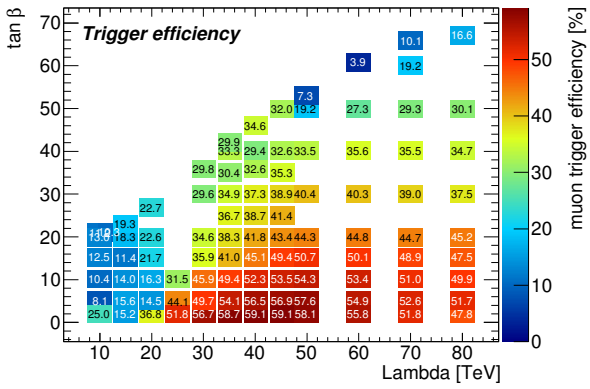

(B) Trigger efficiency

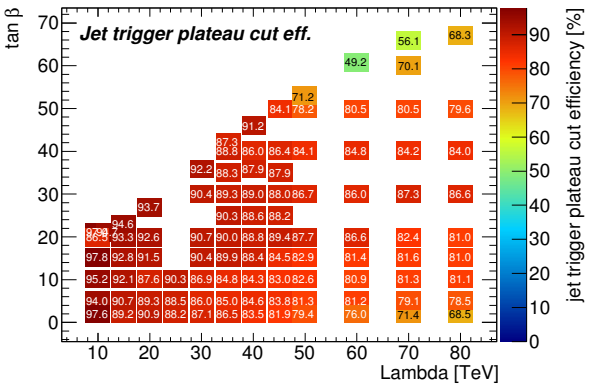

(C) Jet efficiency ($N_{\text{jet}}^{50\,\text{GeV}} \geq 1$)

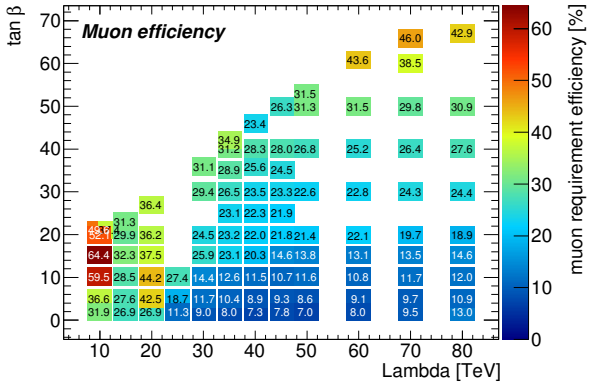

(D) Muon efficiency ($N_{\mu}^{20\,\text{GeV}} = 1$)

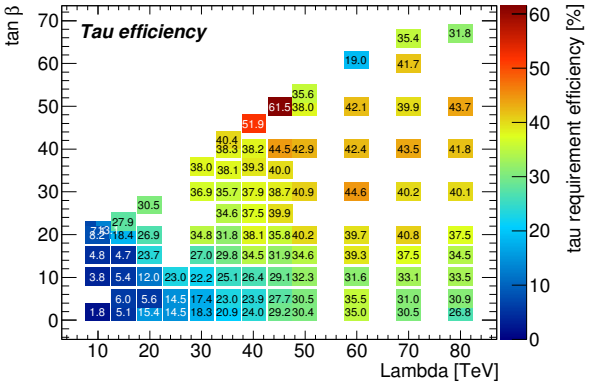

(E) Tau efficiency ($N_{\tau,\text{medium}}^{20\,\text{GeV}} \geq 1$)

FIGURE 5.2 (A): The acceptance of the object selection and (B) to (E) the efficiency of the individual selection cuts.

5.1.2 Optimization of Kinematic Cuts for GMSB

In addition to the object selection, further selection cuts are applied to select potential SUSY events and to suppress SM background. The search for jets and missing transverse energy has been motivated by the expected appearance of SUSY in Section 2.3 and the observables that quantify these topologies have been defined and discussed in Section 3.3.8. The considered quantities can be seen in Figure 5.3. They show the expected SM contributions and two SUSY benchmarks. The chosen benchmarks are

$$\Lambda = 50\,\text{GeV} \qquad \tan\beta = 20 \qquad \text{and} \qquad \Lambda = 50\,\text{GeV} \qquad \tan\beta = 40\,, \tag{5.3}$$

which are close to the final expected sensitivity limit. Figure 5.3(A) shows that most SM contributions accumulate below $m_{\text{T}}^{\mu} = 100\,\text{GeV}$, whereas Figure 5.3(B) shows flat behaviour for the signal samples. In W+jets and Top events with fake taus, this can be explained by the kinematic constraint of the transverse mass. If $E_{\text{T}}^{\text{miss.}}$ and the muon both arise from a leptonic $W \to \mu\nu_{\mu}$ decay, it has to be below the W mass. In the signal events, these quantities are less correlated and hence flatter around $m_{\text{T}}^{\mu} \approx 100\,\text{GeV}$. Since this cut is driven by the W mass in the background and m_{T}^{μ} is approximately flat in GMSB, no individual optimization is done and the cut is chosen to be

$$m_{\text{T}}^{\mu} > 100\,\text{GeV}\,. \tag{5.4}$$

The further discriminants can be seen in Figures 5.3(C) to (F). In all cases, small values of these variables are SM dominated, whereas the high tails are populated by SUSY. The optimal choice of the cuts should have stable performance throughout the whole parameter grid and should not be specific for the phenomenology of a certain grid point. To cover sufficient different possible phenomenologies, six benchmarks in the grid are considered that are paired to high and low $\tan\beta$ values for three different sets of mass scales Λ.

For these benchmarks, the performance of different cuts on the considered kinematic variables are tested. The different cuts are applied to the SM as well as the signal samples and the obtained significance is calculated. Significance is tested with the Asimov value [290]

$$Z_0 = \sqrt{2\left[(s+b)\ln\left(1+\frac{s}{b}\right) - s\right]}\,, \tag{5.5}$$

where s denotes expected signal events and b expected background events, respectively. In addition to pure sensitivity, also remaining MC background statistics has to be considered. This will finally contribute as systematic uncertainty and also the evaluation of all other systematic uncertainties are taken from MC. Therefore, upper limits on possible cut values are set by the technical requirement of non-vanishing MC statistics.

In addition to kinematic cuts, also the strictness of the required taus can be varied and used as a discriminator between SUSY and SM. In principle, all the discriminators could be correlated among each other, so that the optimal cut value depends on all already applied cuts. To first oder, the strictness of the tau identification should not be strongly correlated to the discrimination power of the kinematic variables. Therefore, the kinematic cuts are tuned by the use of BDT loose taus, which give comprehensive MC statistics, and finally the tau identification working point is optimized. The optimization is done with NLO reweighted signal samples and with rescaled Top and W+jets background samples. The cut on $m_{\text{T}}^{\mu} > 100\,\text{GeV}$ is also applied since it will be used for the final selection.

Figure 5.4 shows the obtained significances of the four discriminants. In each plot, only the m_{T}^{μ} cut and one given on the x-axis is applied. As a first result, it can be seen that $\tan\beta$ has only small impact

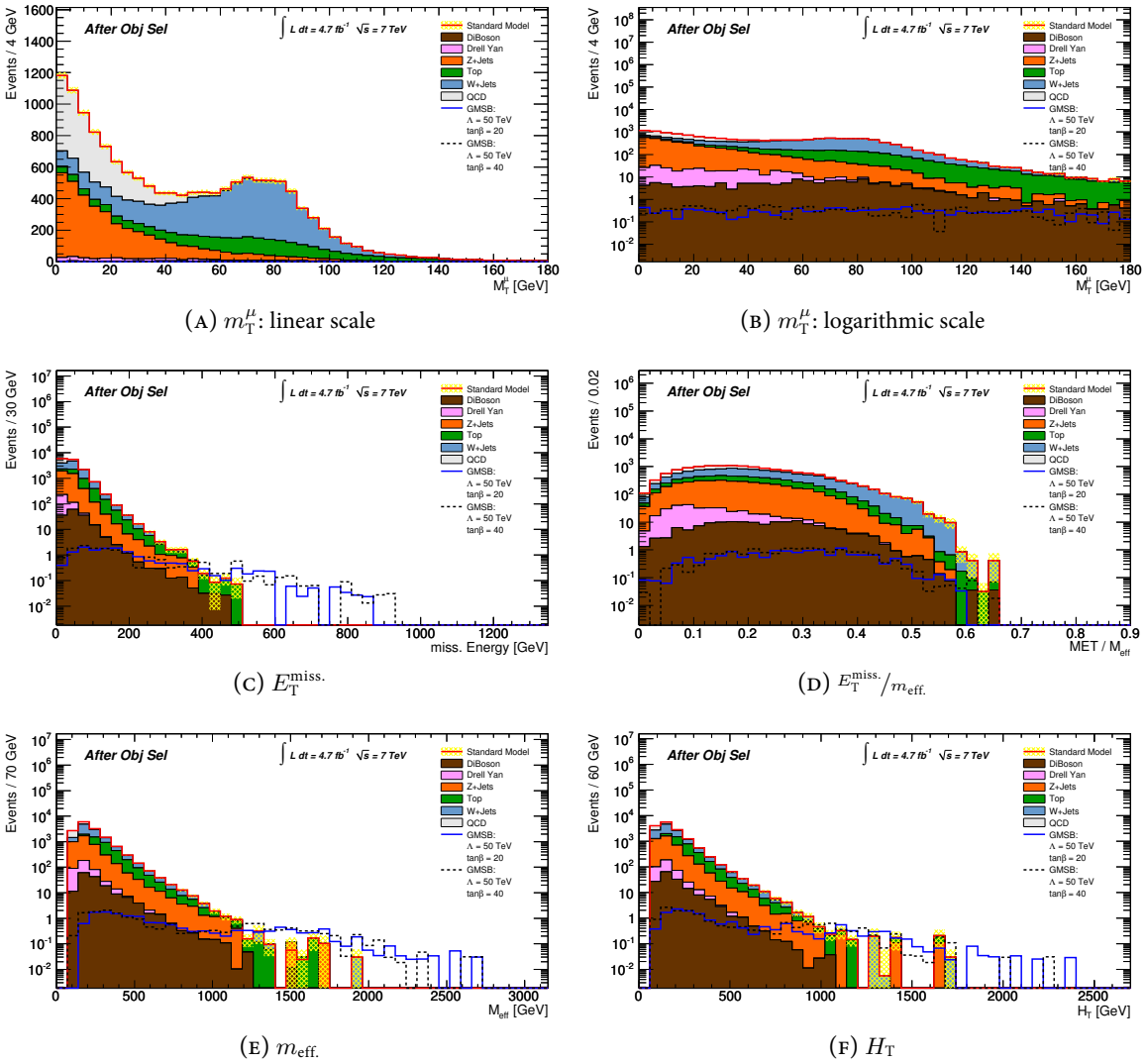

(A) m_{T}^{μ}: linear scale

(B) m_{T}^{μ}: logarithmic scale

(C) $E_{\mathrm{T}}^{\mathrm{miss.}}$

(D) $E_{\mathrm{T}}^{\mathrm{miss.}}/m_{\mathrm{eff.}}$

(E) $m_{\mathrm{eff.}}$

(F) H_{T}

Figure 5.3 Comparison of two GMSB benchmarks and the SM for the considered SUSY discriminants.

on the optimal cut choice compared to Λ, which governs the kinematic phenomenology. Since this parameter controls the sparticle mass scale, higher Λ prefers harder cuts due to higher transverse momenta. Concurrently, the models with higher SUSY masses have smaller cross sections and hence the obtained significances are lower. The curves are cutoff as soon as no SM background is left and hence Equation 5.5 gives infinity.

In addition to the sensitivity of different cuts, also the obtained relative background uncertainty due to limited MC statistics, $\Delta N/N$, is given. Its scale is given by the right axis. The values exceeding one are due to negative event weights from Top MC samples. They can reduce N, but increase ΔN and hence allowing for a ratio above one. For the same reason, the relative statistical MC uncertainty can decrease for harder cuts. This effect can be seen notably in the high SM tails, which are Top dominated.

The absolute scales of the obtained significances suggest that $m_{\mathrm{eff.}}$ has the best discovery potential, closely followed by $E_{\mathrm{T}}^{\mathrm{miss.}}$ and then H_{T}. $E_{\mathrm{T}}^{\mathrm{miss.}}/m_{\mathrm{eff.}}$ is not well suited to discriminate background and signal. This can be understood by the expected hadronic activity that comes from strongly produced

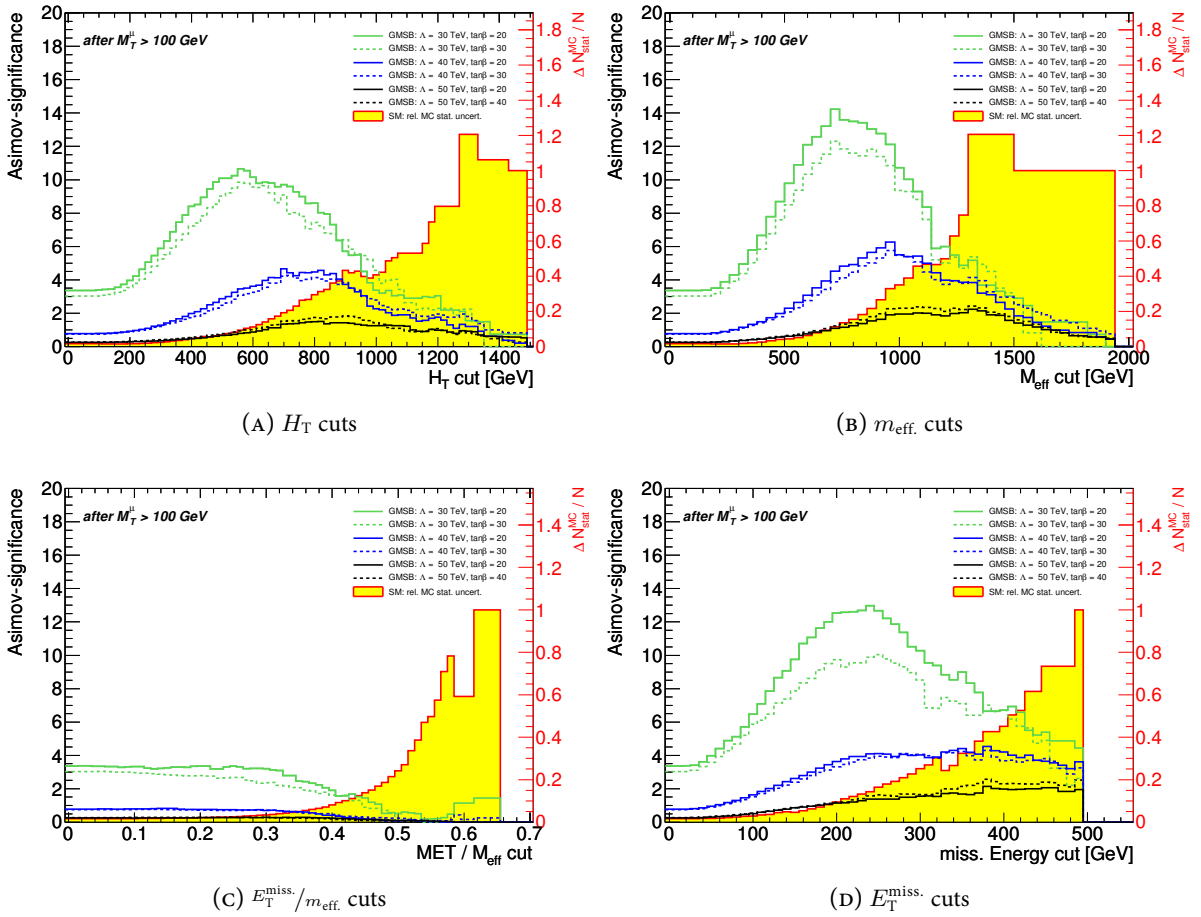

(A) H_{T} cuts (B) $m_{\text{eff.}}$ cuts

(C) $E_{\mathrm{T}}^{\text{miss.}}/m_{\text{eff.}}$ cuts (D) $E_{\mathrm{T}}^{\text{miss.}}$ cuts

Figure 5.4 Obtained significances for six GMSB benchmarks for different kinematic cuts. The $m_T^\mu > 100\,\text{GeV}$ is already applied, taus are BDT loose, backgrounds are rescaled by the data-driven scale factors and signal is NLO reweighted. MC statistical uncertainty scale is given by the right axis.

SUSY events. In these SUSY events, a substantial contribution to $m_{\text{eff.}}$ comes from H_{T} and hence $E_{\mathrm{T}}^{\text{miss.}}$ does not dominate $m_{\text{eff.}}$. Typically, the ratio of $E_{\mathrm{T}}^{\text{miss.}}$ to $m_{\text{eff.}}$ is an efficient discriminant for QCD, where only low real $E_{\mathrm{T}}^{\text{miss.}}$ is expected. In that sense, it serves as a missing energy significance, see Section 3.3.8. Due to the muon requirement, QCD is already sufficiently suppressed (see Section 4.4.2) and hence does not require a special rejection cut. The remaining backgrounds, especially Top and W+jets, also have high real $E_{\mathrm{T}}^{\text{miss.}}$ contributions to $m_{\text{eff.}}$ and hence appear SUSY-like, see Figure 5.3(D).

The discrimination power of H_{T} and $E_{\mathrm{T}}^{\text{miss.}}$ express the more pronounced appearance of hadronic transverse energy and missing transverse energy in SUSY events. Since $m_{\text{eff.}}$ is the sum of them, it shows the best performance for the signal selection and to some extend already includes potential correlation among the two. However, the two most promising variables, $m_{\text{eff.}}$ and $E_{\mathrm{T}}^{\text{miss.}}$, are investigated for more optimal combinations in Figure 5.5. Here, the significance scan for $m_{\text{eff.}}$ is redone after additional $E_{\mathrm{T}}^{\text{miss.}}$ cuts and indeed some combinations, e.g. high $m_{\text{eff.}}$ with $E_{\mathrm{T}}^{\text{miss.}} > 200\,\text{GeV}$ have slightly better sensitivity for the high mass points.

Nonetheless, this comes at the price of very low MC statistics, which would not allow for a reasonable estimate of systematic uncertainties. In addition, the kinematic vicinity of these cut combinations

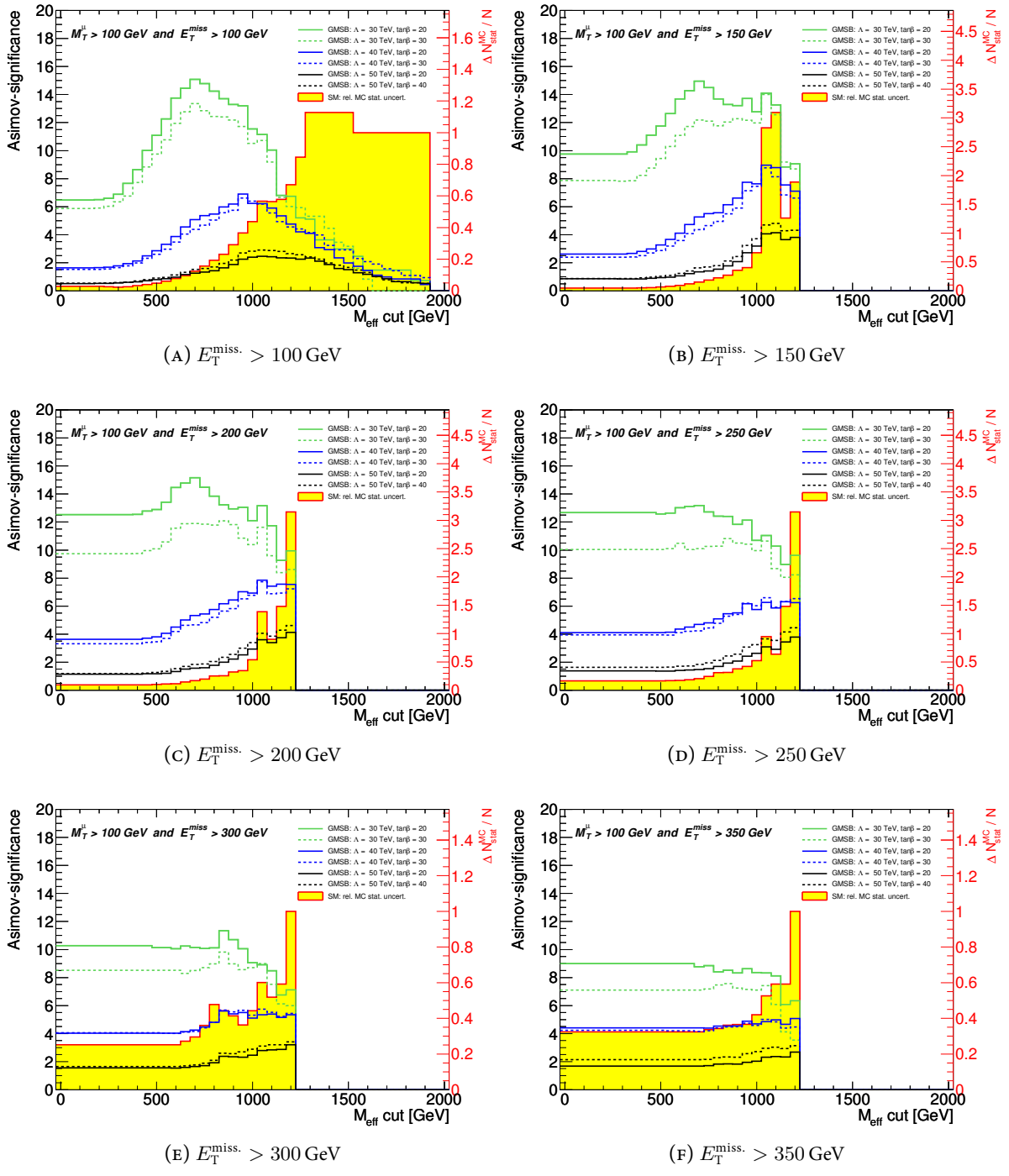

(A) $E_{\mathrm{T}}^{\mathrm{miss.}} > 100\,\mathrm{GeV}$

(B) $E_{\mathrm{T}}^{\mathrm{miss.}} > 150\,\mathrm{GeV}$

(C) $E_{\mathrm{T}}^{\mathrm{miss.}} > 200\,\mathrm{GeV}$

(D) $E_{\mathrm{T}}^{\mathrm{miss.}} > 250\,\mathrm{GeV}$

(E) $E_{\mathrm{T}}^{\mathrm{miss.}} > 300\,\mathrm{GeV}$

(F) $E_{\mathrm{T}}^{\mathrm{miss.}} > 350\,\mathrm{GeV}$

FIGURE 5.5 Obtained significances for six GMSB benchmarks for different combinations of $E_T^{miss.}$ and $m_{eff.}$ after $m_T^\mu >$ 100 GeV. Taus are BDT loose, backgrounds are rescaled by the data-driven scale factors and signal is NLO reweighted. MC statistical uncertainty scale is given by the right axis.

does not show flat sensitivity and hence could be susceptible to small mismodellings. In that case, the sensitivity could be overestimated and therefore the small gain in sensitivity is relinquished to sustain reliability.

In addition, different combinations of $m_{\text{eff.}}$ and H_{T}, as well as combinations of H_{T} and $E_{\text{T}}^{\text{miss.}}$ have been tested and can be seen in Appendix B in Figures B.6 (p. 164) and B.7 (p. 165). For all combinations, an individual cut on $m_{\text{eff.}}$ can be seen to be a preferable compromise between sensitivity, remaining MC statistics and stable performance. The final cut is obtained from Figure 5.4(b) and decided to be

$$m_{\text{eff.}} > 1000\,\text{GeV}\,. \tag{5.6}$$

It is well operating for all benchmarks and has smooth performance for small variations at the critical high mass points.

5.1.3 Optimization of Tau Lepton Identification for GMSB

With the fixed kinematic selection, the optimal tau identification working point can be chosen. Figure 5.6(a), (c) and (e) show the expected significance after the full kinematic selection, i.e. object selection with m_{T}^{μ} and $m_{\text{eff.}}$ cut applied, for loose, medium and tight tau identification. The differences are not very pronounced, but the best discovery potential is achieved with BDT medium taus.

The BDT loose requirement increases the fake tau dominated W+jets background and thereby suffers from larger backgrounds. The smaller sensitivity for the tight requirement comes from the signal taus characteristics. The correlation between p_{T}^{τ} and the BDT output implicitly increases the tau transverse momenta with tighter cuts on the BDT. In GMSB, the taus prefer to be rather soft and hence a tight identification reduces the signal. Table 5.1 shows the cutflows for all tau identification working points to the signal region. The final W+jets contribution increases by more than a factor of 3 for loose taus, whereas nearly half of the final signal is lost with tight taus. The optimal working point is medium strictness in the tau identification and hence will be used for the final selection.

The different background compositions of the different tau identifications points could have an interplay with the optimal choice of the kinematic cuts. E.g. the loose tau identification is dominated by W+jets and might have a different optimal $m_{\text{eff.}}$ cut than the Top dominated selection with medium taus, see Table5.1. This correlation has been neglected by the individual optimization of the kinematic cuts in Section 5.1.2 with the use of loose taus. To quantify this effect, the cut scan is redone with loose, medium and tight taus in the object selection, which can be seen in Figure 5.6(b), (d) and (f). By construction, Figure 5.6(b) and 5.4(b) are identical. No sizable change can be seen and the argumentation for cut choice of $m_{\text{eff.}} > 1000\,\text{GeV}$ remains unchanged.

With the settled tau identification, the final event selection for the signal region (SR) is fixed. The required objects are

$$N_{\text{jet}}^{50\,\text{GeV}} \geq 1 \qquad N_{\mu}^{20\,\text{GeV}} = 1 \qquad N_{\tau,\text{medium}}^{20\,\text{GeV}} \geq 1 \tag{5.7}$$

and the kinematic cuts are

$$m_{\text{T}}^{\mu} > 100\,\text{GeV} \qquad m_{\text{eff.}} > 1000\,\text{GeV}\,. \tag{5.8}$$

5.1.4 Final Background Estimates

The backgrounds from Top and W+jets have already been rescaled by the extensively checked data-driven scalings from Section 4.4.1. Therefore, their scaled MC predictions are already the final estimate. Also

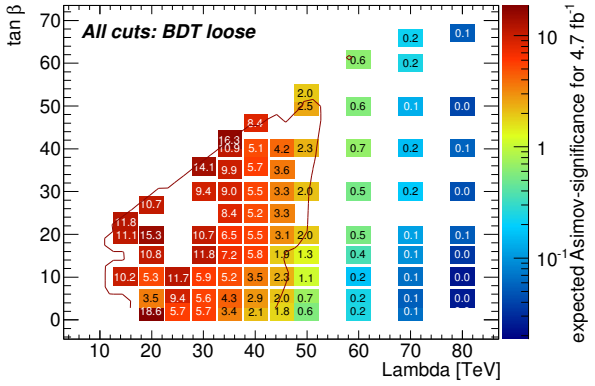

(A) BDT loose taus

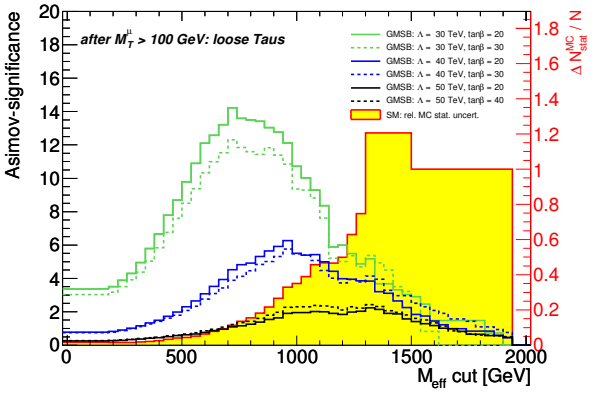

(B) BDT loose taus

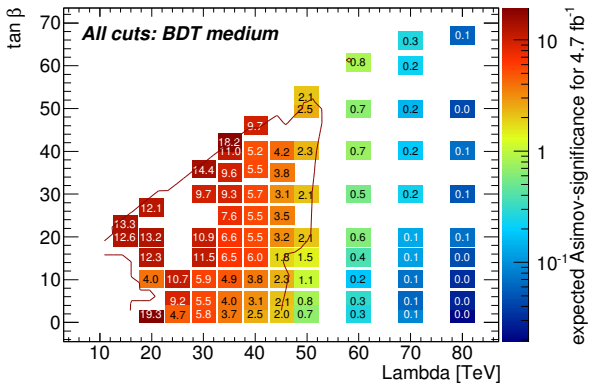

(C) BDT medium taus

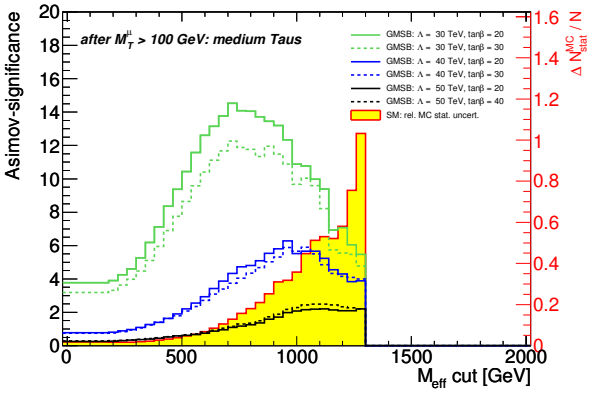

(D) BDT medium taus

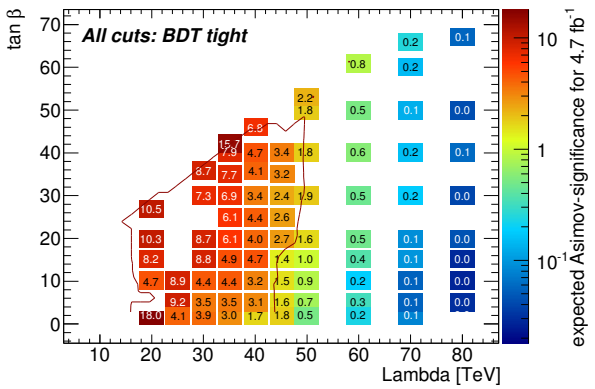

(E) BDT tight taus

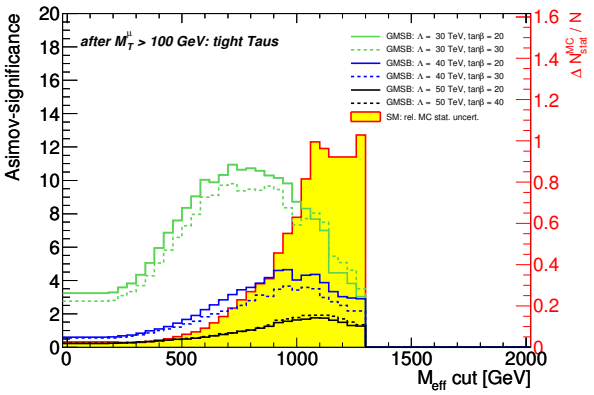

(F) BDT tight taus

Figure 5.6 (A), (C) and (E): The performance of the tau identification working points loose, medium and tight. The line gives the $Z_0 = 2$ contour. The performance is similar, but medium has best discovery potential. (B), (D) and (F): The $m_{eff.}$ significance scan for object selections with loose, medium and tight taus. No sizable difference can be seen.

	$\Lambda = 50$ TeV $\tan\beta = 40$	DiBoson	Drell Yan	Z+Jets	Top	W+Jets	QCD (DD)	SM	
GRL	638	44 253	55 194 030	19 350 596	950 153	145 489 056	–	221 028 089	± 48 080
Trigger	214	12 546	231 819	1 766 665	174 229	10 880 125	–	13 065 385	± 9616
cleaning cuts	210	12 298	228 107	1 694 491	173 287	10 300 801	–	12 408 984	± 9261
$N_{\text{jet}}^{50\text{ GeV}} \geq 1$	177	4997	41 470	248 992	153 694	1 377 472	–	1 826 625	± 1583
$N_{\mu}^{20\text{ GeV}} = 1$	47.4	2988	19 586	99 186	88 532	1 180 140	845 744	2 236 177	± 209 662
$N_{\mu}^{20\text{ GeV}} = 1$	47.4	2988	19 586	99 186	88 532	1 180 140	845 744	2 236 177	± 209 662
$N_{\tau} \geq 1$ (loose)	20.4	210	402	4741	3304	10 230	5076	23 962	± 1390
$m_{\text{T}}^{\mu} > 100$ GeV	9.89	35.1	3.20	85.3	528	630	4.23	1286	± 34
$m_{\text{eff.}} > 1000$ GeV	3.67	0.15	0.00	0.16	0.31	0.96	0.01	1.59	± 0.55
$N_{\mu}^{20\text{ GeV}} = 1$	47.4	2988	19 586	99 186	88 532	1 180 140	845 744	2 236 177	± 209 662
$N_{\tau} \geq 1$ (medium)	16.8	157	254	3637	2162	5716	2829	14 755	± 784
$m_{\text{T}}^{\mu} > 100$ GeV	8.24	28.4	1.49	48.6	410	357	1.91	847	± 22
$m_{\text{eff.}} > 1000$ GeV	2.78	0.11	0.00	0.05	0.36	0.27	0.01	0.80	± 0.28
$N_{\mu}^{20\text{ GeV}} = 1$	47.4	2988	19 586	99 186	88 532	1 180 140	845 744	2 236 177	± 209 662
$N_{\tau} \geq 1$ (tight)	10.4	82.6	98.0	1967	1022	2023	897	6090	± 263
$m_{\text{T}}^{\mu} > 100$ GeV	4.69	16.5	0.26	20.1	220	126	0.04	383	± 11
$m_{\text{eff.}} > 1000$ GeV	1.59	0.04	0.00	0.05	0.11	0.21	0	0.41	± 0.25

Table 5.1 Cutflow into the signal region for loose, medium and tight taus. The upper cutflow shows expected events up to the muon requirement. The three lower cutflows show the expected events for the final selection with the three different tau identification working points. The loose requirement increases the fake dominated W+jets background by a factor of 3.5, whereas the tight identification loses nearly half of the signal. The medium tau identification strictness is optimal and will be used.

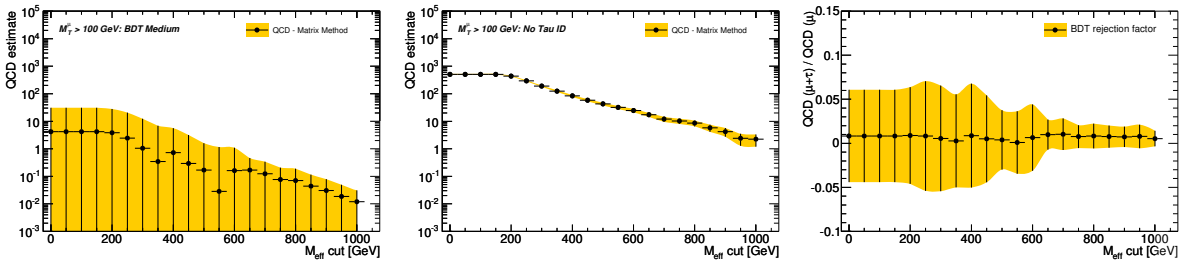

(A) QCD with medium taus (B) QCD with no tau ID (C) BDT rejection factor

FIGURE 5.7 Control tests of the data-driven QCD estimate. (A): The estimate for different $m_{eff.}$ cuts up to the final event selection. (B): The estimate for different $m_{eff.}$ up to the final kinematic selection but without tau ID. (C): The ratio of (A) and (B), i.e. the QCD rejection due to tau identification.

the Z^0+jets contributions could be shown to be correctly modelled in Section 4.4.3 and hence its MC prediction is considered as the final estimate.

The QCD estimate suffers from the small remaining available statistics in the extreme kinematic phase space above $m_{\text{eff.}} > 1000\,\text{GeV}$. Figure 5.7(A) shows the evolution of the QCD estimate from the matrix method for different cuts on $m_{\text{eff.}}$ up to the final SR. The cut on $m_{\text{T}}^{\mu} > 100\,\text{GeV}$ is also already applied. Since the contributions decrease smooth and continuously, the final upper limit on QCD at $m_{\text{eff.}} = 1000\,\text{GeV}$ of

$$N_{\text{QCD}} = 0.012 \pm 0.019 \tag{5.9}$$

would be sufficient.

As an additional control test, the QCD estimate is repeated with the object selection as described in Section 4.3.2 without any tau identification related cut. Due to much more available statistics, the uncertainties on the QCD estimate are much smaller, as can be seen in Figure 5.7(B). The estimates from Figures 5.7(A) and 5.7(B) only differ by the tau identification. Hence, their ratio can be considered as the QCD rejection due to the appliance of tau identification. The ratio can be seen in Figure 5.7(C). It displays the QCD rejection factor of medium taus as a function of applied $m_{\text{eff.}}$ cut.

Since both estimates, i.e. the one with and the one without tau identification, are completely data-driven, also the QCD rejection is completely data-driven. The rejection of fake taus from QCD can hence be studied without any bias to the MC tau selection. The muon itself allows for a completely independent data-driven QCD estimate, which can be compared with and without tau identification. The rather large uncertainties on the rejection are driven by the small remaining QCD contributions after the kinematic cuts on the selection that includes taus.

The obtained rejection shows no dependence on the $m_{\text{eff.}}$ cut and hence it can be determined without this cut. To obtain a CR with high and independent statistics, the $m_{\text{T}}^{\mu} > 100\,\text{GeV}$ cut is reverted. This cut has been used in all selections of Figure 5.7. The BDT rejection can be estimated from this events if the tau identification performance does not dependent on m_{T}^{μ}. The region below $m_{\text{T}}^{\mu} < 50\,\text{GeV}$ is still excluded to avoid QCD events with very low $E_{\text{T}}^{\text{miss.}}$, which are kinematically quite different to the finally selected events. $E_{\text{T}}^{\text{miss.}}$ in QCD predominantly comes from mismeasured objects and very low $E_{\text{T}}^{\text{miss.}}$ topologies might have a bias to the tau performance. Following this argumentation, low-$E_{\text{T}}^{\text{miss.}}$ QCD events are better reconstructed and hence tau fake rate can be expected to be smaller. These events are excluded in order to avoid an underestimate of the tau fake rate.

In the region of $50\,\text{GeV} < m_{\text{T}}^{\mu} < 100\,\text{GeV}$, the QCD estimate of the matrix method is compared with and without applied tau identification

$$N_{\text{QCD}}^{\text{no}\,\tau} = 20\,049 \pm 93 \qquad \text{and} \qquad N_{\text{QCD}}^{\text{with}\,\tau} = 92.1 \pm 6.8\,. \tag{5.10}$$

This gives a BDT rejection factor for QCD of

$$r_{\text{BDT}} = \frac{N_{\text{QCD}}^{\text{with}\,\tau}}{N_{\text{QCD}}^{\text{no}\,\tau}} = 0.004\,59 \pm 0.000\,34\,. \tag{5.11}$$

This can be applied to the QCD estimate after the $m_{\text{eff.}} > 1000\,\text{GeV}$ for events without the tau identification of Figure 5.7(b):

$$N'_{\text{QCD}} = (2.25 \pm 1.06) \times (0.004\,59 \pm 0.000\,34) = 0.0103 \pm 0.0049\,. \tag{5.12}$$

The prediction is very good agreement with Equation 5.9. Since the BDT rejection is estimated from a rather high statistics CR, still the uncertainty from the matrix method on the final selection without tau identification is dominating. For the final estimate, the more conservative result from Equation 5.9 is used, which has four times bigger uncertainty. However, due to the small QCD contribution, this has no impact on the final sensitivity of the analysis.

Moreover, the data-driven QCD rejection can also serve as an additional cross check for the fake tau scaling in W+jets. The W+jets event selection without tau identification could be shown to be very well described by the MC. The discrepancies in W+jets have been shown to be caused by the tau identification, see Section 4.3.2. The rescaling of the W+jets MC after the tau identification is a data-driven correction of the (quark) jet fake rate for taus in the W+jets MC. In that sense, it remodels the (QCD) jet rejection in W+jets.[1] The data-driven rejection in W+jets is calculated by

$$r_{\text{BDT}}^{W\text{+jets}} = \frac{\omega_W N_{W\text{+jets}}^{\text{with}\,\tau}}{N_{W\text{+jets}}^{\text{no}\,\tau}} = \frac{(0.58 \pm 0.02) \times (9757 \pm 108)}{1\,180\,140 \pm 1426} = 0.004\,80 \pm 0.000\,17\,, \tag{5.13}$$

which shows good agreement with the one from the matrix method of Equation 5.11. Hence, the data-driven fake rate for QCD jets in W+jets events and pure QCD events is consistent, as expected.

Though expected to be very small, the contribution of Drell-Yan also needs special attention since the available Drell-Yan MC runs out of statistics in the SR. Therefore, Drell-Yan is estimated by extrapolation under the assumption that Drell-Yan and Z^0+jets have the same behaviour. Using Equation 4.34 (p. 91) and the numbers for Z^0+jets from the BDT medium selection in Table 5.1 yields

$$N_{\text{Drell-Yan}}^{\text{est.}} = \frac{0.05}{48.6} 1.49 = 0.0015 \pm 0.0017\,. \tag{5.14}$$

The rather large uncertainty includes the MC statistical uncertainties from all three contributing estimates as quadratic sum, which is not correct in a strict sense. Since the nominator is included in the denominator, they are not fully uncorrelated. However, the events after the additional $m_{\text{eff.}}$ cut make up about

[1] In contrast to *fake rate*, which is defined per object, the *BDT rejection* is defined at event level. The rejection already includes the jet multiplicity, where each jet constitutes a trial for the fake probability.

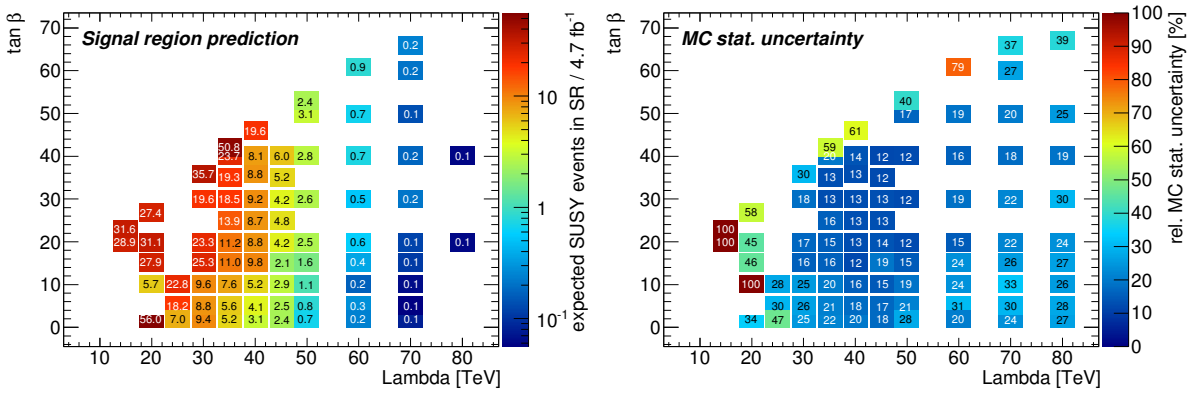

(A) Expected SUSY events in signal region

(B) MC statistical uncertainty

FIGURE 5.8 Signal expectation. (A): Expected SUSY events in the signal region and (B) relative uncertainty due to limited MC statistics in the signal samples.

one permille of the events before that cut. Therefore, the correlation is very small and has been neglected. The conservative Drell-Yan estimate is smaller than 0.0032 events at

$$\int_{-\infty}^{0.0032} G\left(\mu = 0.0015, \sigma = 0.0017\right) = \int_{-\infty}^{\mu+\sigma} G(\mu, \sigma) = 0.68 + \frac{1}{2}\left(1 - 0.68\right) = 0.84 = 84\,\% \quad (5.15)$$

confidence level. G is assumed to be a GAUSSian probability density with mean μ and standard deviation σ. Certainly, this cannot be strictly true since it would allow for negative Drell-Yan contributions. In any case, this shows that Drell-Yan is negligible, i.e. it is less than half a percent of the total expected background. However, Equation 5.14 will be used as final Drell-Yan expectation and the sum of backgrounds is

$$N^{\text{SM}} = 0.80 \pm 0.28^{\text{MC stat.}} \quad (5.16)$$

The expected GMSB contributions after the full event selection can be seen in Figure 5.8. The predicted events from the individual grid points are displayed in Figure 5.8(A) and Figure 5.8(B) shows the uncertainty due to limited MC statistics. The signal events can be compared to the expected background of 0.8 events. Up to $\Lambda = 50$ TeV, the signal expectation is larger than or equal to the background expectation and hence the analysis could have discovery potential. For the final sensitivity, all remaining systematic uncertainties have to be quantified.

5.2 Systematic Uncertainties

The analysis is subject to several systematic uncertainties that are evaluated in the following. Principally, only the uncertainty on the final number of selected background and signal events is needed. Nonetheless, the influence of the systematics are investigated at different cut stages, to study where they arise and which aspect in the analysis outline is affected mostly. In addition to the signal region expectation, also the backgrounds in the CRs are affected. Especially the CRs for Top and W+jets are important since they are used to derive the scalings. In that sense, they are part of the signal region prediction.

Since the change of the control and signal region predictions are correlated for each systematic, this has to be evaluated at once. In that sense, the correlated uncertainties on the matrix from Equation 4.20 (p. 75) are estimated here. For each systematic uncertainty, the scalings are rederived from the modified MC samples and the modified MC signal region prediction is corrected with these new scalings. This might have different impact on the final systematic. If signal and control region are affected correlated, i.e. both increase or decrease, the final systematic partially, or even totally, cancels out. For instance, this might be the case for uncertainties on object selection efficiencies. If efficiencies increase, the MC events in the control and signal regions will increase. Hence, the scalings decrease and absorb the increased events in the signal region.

The contrary is the case for anticorrelated response of signal and control region to a certain systematic. This might be the case for energy scale recalibrations. An increase of the energy scale of certain objects, e.g. jets, might increase the total $m_{\text{eff.}}$ in a way, such that a CR event now appears in the signal region. This decreases the MC prediction in the CR and hence increases the scalings. At the same time, this increases the MC signal region prediction and hence both effects enlarge the background prediction.

The influence of systematic uncertainties on the used objects, i.e. taus, jets, muons and $E_{\text{T}}^{\text{miss.}}$, are evaluated in the following and finally summarized in Table 5.3. For that, all MC samples are modified according to the expected changes and the whole analysis is rerun on these modified samples. The change of any quantity in the modified analysis with respect to the nominal value is considered as the one sigma uncertainty that comes from the tested systematic. Some of the systematic uncertainties are not related to any specific analysis object, but evaluated principally in the same way.

5.2.1 Tau Related Systematic Uncertainties

Tau jets are a specific combination of charged and neutral hadrons and hence their energy is calibrated separately to reconstruct the tau jet energy. Any imperfect knowledge on the correct energy scale will translate into a systematic shift of all tau energy measurements and hence has an impact on the event selection. The tau energy scale uncertainty has been measured by data-driven techniques as well as investigated in MC studies [237]. The resulting uncertainties are given in different ranges of η_τ and p_{T}^τ and range from 3 % to 6 %.

These uncertainties are used to once upscale and once downscale the energy of all tau candidates at object level and the analysis is redone. The resulting deviations in selected events after different cuts can be seen in Table 5.2, which gives the relative change with respect to the unmodified analysis. The first Table 5.2(A) shows the results with the use of the scaling factors from the unmodified selection for both modified selections. After the object selection, an uncertainty of 5 % can be seen, which roughly remains at the same throughout the kinematic cuts. The larger deviations after the final cuts are due to small remaining MC statistics.

As noted above, the CRs are also affected by the tau energy scale. Hence, the scalings have to be rederived from the modified MC samples. Table 5.2(B) shows the results with the use of individual scalings from the modified MC samples. This takes into account that also the CRs are affected by the systematic uncertainty. Here, the systematics partially cancel out due to the fact that CRs and SR are affected in the same manner and the uncertainties drop below percent level. In the following, only the final uncertainties with individual scalings are shown. Since the tau has only small impact on the total effective mass, the final uncertainty is taken after the 600 GeV cut to have more available MC statistics.

Uncertainties on the tau identification efficiencies and fake rates have been investigated with tag and probe methods in $Z^0 \to \tau\tau$ and $W \to \tau\nu_\tau$ events [234]. Since taus from W-decays dominate the event selection, these are used. The uncertainties are a combination of systematic and statistical sources on the estimated efficiency and fake rate. For the uncertainty on the event selection, the eventweights

% Deviation $^{\text{TES up}}_{\text{TES down}}$	DiBoson	Drell Yan	Z+Jets	Top	W+Jets	SM
Object selection	4.22 −5.31	5.9 −6.9	8.13 −8.01	3.84 −3.41	6.18 −6.63	6.31 −6.45
$m_{\text{T}}^{\mu} > 100$ GeV	4.62 −4.6	34.27 0	6.35 −3.08	3.44 −3.08	3.89 −6.58	3.9 −4.68
$m_{\text{eff.}} > 400$ GeV	2.9 −3.11	0 0	6.08 −1.23	4.01 −3.3	4.18 −6.89	4.09 −3.95
$m_{\text{eff.}} > 600$ GeV	1.72 −15.88	0 0	0 0	3.71 −3.24	9.61 −6.6	4.69 −4.38
$m_{\text{eff.}} > 800$ GeV	0 −3.78	0 0	0 0	3.57 −6.48	−0.02 −11.57	2.05 −7.64
$m_{\text{eff.}} > 1000$ GeV	0 −12.11	0 0	0 0	−0.05 −8.61	−0.02 −100	−0.03 −25.47

(A) No individual rescaling

% Deviation $^{\text{TES up}}_{\text{TES down}}$	DiBoson	Drell Yan	Z+Jets	Top	W+Jets	SM
Object selection	4.22 −5.31	5.9 −6.9	8.13 −8.01	−0.39 0.07	−1.4 0.62	1.85 −2.28
$m_{\text{T}}^{\mu} > 100$ GeV	4.62 −4.6	34.27 0	6.35 −3.08	−1.24 0.55	−3.53 0.67	−1.56 0.22
$m_{\text{eff.}} > 400$ GeV	2.9 −3.11	0 0	6.08 −1.23	−0.74 0.34	−3.26 0.34	−0.83 0.14
$m_{\text{eff.}} > 600$ GeV	1.72 −15.88	0 0	0 0	−1.02 0.39	1.78 0.65	−0.25 −0.32
$m_{\text{eff.}} > 800$ GeV	0 −3.78	0 0	0 0	−1.14 −2.96	−7.16 −4.71	−2.87 −3.49
$m_{\text{eff.}} > 1000$ GeV	0 −12.11	0 0	0 0	−4.59 −5.15	−7.16 −100	−4.32 −23.2

(B) Individual rescaling

TABLE 5.2 The systematic uncertainties due to different modelling of the tau energy scale uncertainties. (A): Usage of the same scalings and (B) with the use of individual scalings. Since signal and control regions are effected in the same manner, effects partially cancel.

are reweighted with the uncertainty of the selected tau candidate. Since each tau is either fake or truth, identification and fake rate uncertainties are considered uncorrelated and added quadratically. The final uncertainty of 3.64 % is rather small since it is reduced by the rescaling of the modified samples. The obtained systematic uncertainties can be seen in more detail in Table A.23 (p. 156).

5.2.2 Jet and B-tag Related Systematic Uncertainties

The search for SUSY from strong production made jets to one of the most important search patterns. The uncertainty on the scale that is used for the reconstruction of their energy (JES) is considered as an up- and downscaling of all jet energies. The rescaling of energy is performed as a function of the jet energy, the jet pseudorapidity, the ΔR to closest nearby jet and the pile-up conditions [291, 292] and ranges from 3 % to 15 %. The change in jet energies are then propagated to the $E_{\mathrm{T}}^{\mathrm{miss.}}$ by

$$E'^{\,\mathrm{miss}}_{x,y} = E^{\mathrm{miss}}_{x,y} + \sum_{\mathrm{jets}} p^{\mathrm{jet}}_{x,y} - \sum_{\mathrm{jets}} p'^{\,\mathrm{jet}}_{x,y} \,, \tag{5.17}$$

where the primed quantities denote the modified energies and momenta. The equation mixes energies and momenta. Strictly speaking, only the transverse momentum can be reconstructed since the mass of the missing particles are not known. Moreover, an energy is a scalar quantity. However, the jet masses are assumed to be small compared to their momentum and the equation follows common notations.

The difference in expected events are shown in Table A.16 (p. 153). As expected, the first sizable influence can be seen at the cut for the jet trigger plateau. The Top samples are less affected, since most events have at least one (b-)jet that passes the jet cut in any case. In Z^0+jets and W+jets, the 50 GeV cut is located in the trailing edge of the jet transverse momentum spectrum and hence translates into larger differences in selected events. Their changes are very similar since the additional jet activity is approximately blind to the electroweak gauge boson's quantum numbers. Parts of the uncertainties in the W+jets sample are compensated by the rescaling after the tau requirement.

The total uncertainty is only about 2.4 % after the object selection. The small fluctuations are caused by the fact that Top and W+jets dominate, where Top is barely affected and W+jets is rescaled. Nonetheless, the uncertainty rises for higher cuts on $m_{\mathrm{eff.}}$ since events are biased to higher hadronic activity. After the final cuts, the uncertainty seems to drop again, which could be an artifact of low MC statistics. Therefore, the uncertainty at $m_{\mathrm{eff.}} > 600$ GeV is taken as a conservative estimate.

In addition to the energy scale, the energy resolution of the jet reconstruction (JER) is subject to uncertainties [293]. They are estimated by data-driven techniques and agree within 10 % with the simulation. The remaining discrepancy is taken into account by resmearing of the jets after their reconstruction. This is done η and p_{T} dependent and the change in jet energies is propagated to the missing energy by Equation 5.17.

The resulting uncertainties can be seen in Table A.17 (p. 153). The total uncertainty is about a few percent, except the larger uncertainty at the next to last cut. It is caused by a single W+jets event with a high event weight. This event did not enter the nominal selection and is rejected again at the later cut. The final uncertainty is about 6 %. Since energies are smeared randomly with positive and negative sign, i.e. Gaussian around the nominal energy, the obtained deviations are interpreted as symmetric uncertainties around the nominal value with no specific tendency.

Though it is not used for the final event selection, b-tagging is used for the definition of the CRs and hence might influence the final result via the applied scalings. Therefore, also the b-tagging related uncertainties are considered. These are taken into account by the uncertainties on the scale factors that are applied whenever b-tagging is used. The scale factors for truth b-jets are up- and downscaled by their p_{T}

and η dependent uncertainty. The results can be seen in Table A.12 (p. 151). Since b-tagging is not used for the final event selection, di-bosons, Drell-Yan and Z^0+jets are not affected at all and only Top and W+jets are affected via the change of their scalings.

A rise of b-tagging efficiency increases the MC prediction in the Top CR. Thereby, its scaling decreases and hence the final Top contribution gets smaller, and vice versa for a lower b-tagging efficiency. Since b-tags are vetoed in the W+jets CR, an increased efficiency vetoes more Top events in the W+jets CR. Thereby, it increases the scale factors, which leads to higher final SR contribution and vise versa for lower b-tag efficiency. The constant change throughout the full selection for W+jets reflects the common scale factor for all W+jets events. In Top, the fake and truth contributions are slightly differently affected and hence Top uncertainties change with the purity of selected taus.

Table A.13 (p. 151) shows the uncertainties as derived by up- and downscaling events according to the b-mistag probability uncertainty. Since the Top CR is dominated by truth b-tags, the mistagging uncertainty has only subleading impact on the Top scalings compared to the efficiency uncertainties. For W+jets, an increased b fake rate vetoes more W+jets events and hence increases scale factors and final expected events.

5.2.3 Muon Related Uncertainties

The muon is an accurately measurable object and subject to smaller systematic uncertainties, as will be shown in the following. The biggest uncertainties come from the trigger efficiencies, which are remodelled in the MC by data-driven scale factors. These scale factors have uncertainties themselves that result in slight mismodelling of trigger efficiencies. This effect is quantified by modulation of the scale factors within their uncertainties (up and down) and evaluation of the difference in expected events.

The results can be seen in Table A.19 (p. 154), showing uncertainties of few percent. The last uncertainty is rather large and dominated by a single W+jets MC event. Although the two next to last cuts show stable uncertainties for W+jets, a more relaxed cut for the uncertainty estimate is not possible. Due to the more busy event topology, the remaining backgrounds show a distinct trend to larger uncertainties for harder $m_{\text{eff.}}$ cuts. Therefore, the more conservative final estimate of $12.5\,\%$ is taken.

Beyond the trigger efficiency, also the muon reconstruction efficiency is affected by systematic uncertainties. The applied identification scale factors try to adapt the MC efficiencies to the ones measured in data. The uncertainties on these scalings are taken into account by up- and downscaling the event weight with the estimated uncertainty. The change in selected events can be seen in Table A.18 (p. 154) and is well below one percent since muon identification is well understood. Top and W+jets are even less effected since they are rescaled and CRs and SR are affected in a very similar manner.

Finally, the finite momentum resolution is considered by up- and downscaling the muon momentum measurement. This is done separately for the measurement in the inner detector (ID) and in the muouon spectrometer (MS) and results can be seen in Table A.20 and A.21 (p. 155). The change in expected events is at the percent level and does not show sizable influence.

5.2.4 Event Modelling Related Uncertainties

Beyond the systematics associated to special objects, there are additional uncertainties from event related issues. These account for energies that are not associated to any object, pile-up conditions, modelling of events kinematics by the generators and uncertainties from the data-driven scale factors.

Soft Term Uncertainties

The $E_{\mathrm{T}}^{\mathrm{miss.}}$ in each event was changed in agreement with the modified jet energies.[2] In addition, there are also contributions from energy deposits that are not associated to any particular object, see Section 3.3.5. Since these *soft terms* cannot be identified as any physical particle, the correct calibration of their energy is not well known. This introduces rather large uncertainties on their total energies and their resolution.

The obtained differences in expected events can be seen in Table A.25 and A.24 (p. 157) for scale and resolution uncertainty, respectively. Whereas the resolution uncertainties have random orientation and hence no strong bias to $m_{\mathrm{eff.}}$, the scale uncertainties increase with higher $m_{\mathrm{eff.}}$. This can be explained by the more busy event activity for high $m_{\mathrm{eff.}}$ where larger *soft terms* might appear. However, the final uncertainties are about $4\,\%$.

Pile-Up Uncertainties

Another important source of systematic uncertainties is the pile-up remodelling. It was designed to adapt the pile-up conditions in MC to the one in data. The sensitivity of the analysis to a potential mismodelling is investigated by a deliberate false reweighting. The analysis can then be carried out on the mismodelled MC samples. The obtained change in expected events is displayed in Table A.22 (p. 156) and gives sizable deviations.

The impact on the analysis has a dependence on the $m_{\mathrm{eff.}}$ cut, but the estimate of uncertainties for the hard cuts suffer from low statistics. In addition, the misweighting is overdone as shown in Figure 5.9. It gives the vertex multiplicity of the nominal reweighted samples and the one from the modified samples after the object selection. It is obvious that the standard reweighting matches the data conditions rather accurately, whereas the modified one is way off. Therefore, the conditions are known to be better described as in the samples used for the uncertainties in Table A.22. In that sense, they can be considered to overestimate the uncertainty.

As final systematic uncertainty $17.83\,\%$ is used as a conservative upper bound on the uncertainty. It takes into account the rather large statistical contributions for the hard effective mass cuts and the results from the tau and electron channel. This channel has a pile-up uncertainty of only $3.5\,\%$ [156], which suggests an overestimate of this uncertainty in this analysis. This assumes that the pile-up uncertainty is independent of the lepton flavour. The value of $17.83\,\%$ is taken from the cut at $m_{\mathrm{eff.}} > 800\,\mathrm{GeV}$.

Uncertainties from Event Generators

Furthermore, uncertainties from the event modelling of the generators are considered. When possible, the results from different generators are compared and the difference is taken as the systematic uncertainty. Table A.14 (p. 152) shows the difference in selected events between `MC@NLO` and `Sherpa` generator for di-bosons, which is estimated purely MC based. The changes are evaluated by comparing `Sherpa` samples to the nominal `MC@NLO` samples. Though the final di-bosons estimate changes by $15.95\,\%$, the total uncertainty is only $1.61\,\%$ due to the small contributions from di-bosons. The small change in the W+jets prediction is due to different di-bosons contributions to the CRs and hence slightly different scalings. The corresponding changes for Top are present, but too small to be seen in the table.

The Top generator dependence of the scalings has already been tested (see Figure 4.12 (p. 78) or Figure B.3 (p. 161)) and scalings could be shown to be robust if `MC@NLO` is replaced by `Alpgen`. Nonetheless,

[2] Muon corrections are not propagated to $E_{\mathrm{T}}^{\mathrm{miss.}}$ since their impact is much smaller than the $E_{\mathrm{T}}^{\mathrm{miss.}}$ resolution, see Figures 3.3(b) (p. 45) and 3.5(a) (p. 49). The change in tau energy scale is also not considered for $E_{\mathrm{T}}^{\mathrm{miss.}}$ since taus are treated as jets in the $E_{\mathrm{T}}^{\mathrm{miss.}}$ and are taken into account with the jet energy scale. A separate treatment of the tau energy scale in $E_{\mathrm{T}}^{\mathrm{miss.}}$ would double count for these objects and use improper (tau) energy scaling.

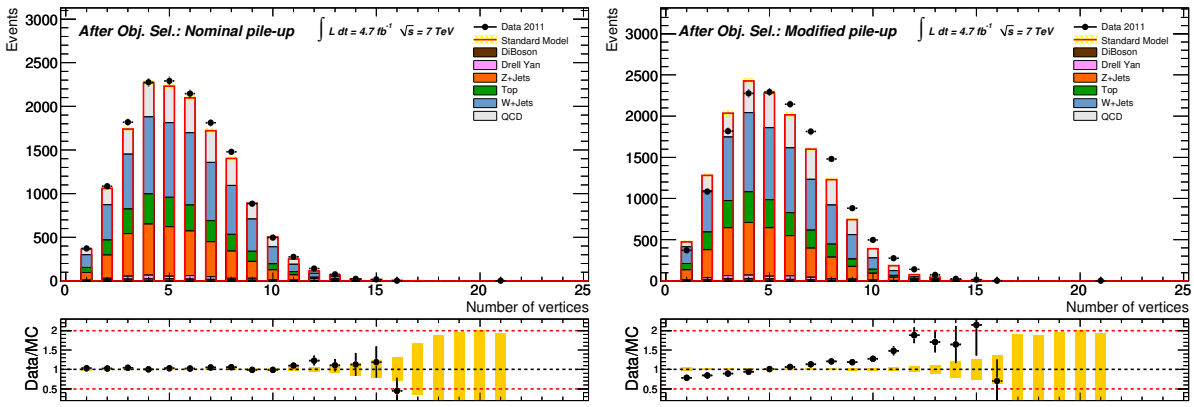

(A) Nominal pile-up reweighting

(B) Mismodelled pile-up reweighting

FIGURE 5.9 The multiplicity of vertices with at least four associated tracks after the object selection. (A): With the normal reweighting used for the analysis and (B) with purposely misweighted pile-up conditions.

Table A.15 (p. 152) shows sizable differences in the final estimate, where Top events are completely estimated by `Alpgen` instead of `MC@NLO`. Up to the muon requirement, the change in events is at percent level and after the tau requirement about 7 %. The latter might be explained by different performance of the tau identification in the different MC generators. With very high $m_{\text{eff.}}$ cuts, these uncertainties increase to rather large values, which are driven by very few events in the high $m_{\text{eff.}}$ tail of the `Alpgen` samples.

To get an estimate that is free of this overlaid statistical effect, a different approach, as explained in the following, is used to obtain the Top generator modelling uncertainties. The same technique is also used for the W+jets generator uncertainties, where additional samples turned out to have too low MC statistics.

The appliance of data-driven scale factors already removes some of the generator dependence of the background prediction. However, it relies on a correct shape modelling of the variables that separate the signal and the control regions. Hence, the remaining generator dependence of the SR prediction is caused by the shape modelling of the variables that define signal and control regions. It can be evaluated by modification of the generator settings and look for changes in the scaled signal region prediction.

Let A and B denote two sets of generator tunes that give two scalings, $\omega_{A,B}$, and two MC predictions for the signal and control region, $N_{\text{SR}}^{A,B}$ and $N_{\text{CR}}^{A,B}$. The two corresponding scaled SR predictions are then

$$\text{tune } A\text{:} \qquad \omega_A = \frac{N_{\text{data}}}{N_{\text{CR}}^A} \qquad N_{\text{SR}}^{\prime,A} = \omega_A N_{\text{SR}}^A \tag{5.18}$$

$$\text{tune } B\text{:} \qquad \omega_B = \frac{N_{\text{data}}}{N_{\text{CR}}^B} \qquad N_{\text{SR}}^{\prime,B} = \omega_B N_{\text{SR}}^B \,. \tag{5.19}$$

The change in the scaled signal region prediction can be expressed by the transfer factor

$$T_{A\to B} = \frac{N_{\text{SR}}^{\prime,A}}{N_{\text{SR}}^{\prime,B}} = \frac{\omega_A N_{\text{SR}}^A}{\omega_B N_{\text{SR}}^B} = \frac{N_{\text{SR}}^A N_{\text{CR}}^B}{N_{\text{CR}}^A N_{\text{SR}}^B} = \frac{\frac{N_{\text{SR}}^A}{N_{\text{CR}}^A}}{\frac{N_{\text{SR}}^B}{N_{\text{CR}}^B}} \,. \tag{5.20}$$

This ratio indicates the change of scaled signal region prediction and hence gives the uncertainty for different generator tunes. The signal and control region predictions for the different tunes are estimated at generator level from `Alpgen` samples for the processes

- $W \to \mu\nu_\mu$ + jets
- $t\bar{t}$ semileptonic
- $t\bar{t}$ dileptonic.

These samples didn't need to undergo the detector simulation since only the generator shape modelling of the kinematic variables are needed. Hence, they have very high available statistics. The event selection is mimicked at generator level in the following way: To very good approximation, muons are always truth muons in W+jets and Top and hence the presence of a truth muon with the same basic kinematic properties is required. In addition, truth taus, jets, $E_{\mathrm{T}}^{\mathrm{miss.}}$, $m_{\mathrm{eff.}}$ and m_{T}^{μ} are taken from truth objects.

In order to incorporate fake taus to the generator level object selection, the tau candidate is replaced by a jet with the same basic kinematic properties, i.e. p_{T}^{τ}, η_{τ}, etc. The overall decrease in events by a realistic tau (and other object) identification cancels out to first order since the transfer factor is a ratio of two ratios. This would not hold only if there is a direct interplay of the change in generator tune and the tau identification performance. In any case, the different performance of the tau identification in data and MC is already taken into account by the data-driven scalings, see Section 4.3. Only the shape modelling of kinematic variables is investigated here.

In the W+jets background, the replacement of the tau by a jet is already sufficient since purity of taus is well below permille level. The Top contributions are mixed with either real taus from dileptonic $t\bar{t}$ or events with an additional jet with the tau's kinematic properties from semileptonic $t\bar{t}$. The relative contributions are combined in compliance with the expected purity of taus.

With this procedure, the event selection for signal and control regions can be mimicked at generator level and the scaled signal region prediction of any generator tune can be compared to the nominal generator settings. The considered generator variations are:

1. The matching scheme for the removal of double counting of events in the same kinematic phase space. This might be caused by jets from the leading order matrix element and jets from parton shower algorithms. The latter are a phenomenological approximation of missing higher order matrix elements. If the parton shower algorithms duplicate an event with a kinematic configuration that has been already considered by the leading order matrix element, it is rejected.
2. The hard process scale dependence due to missing higher order matrix elements.
3. The parton emission scale dependence due to missing higher order matrix elements.
4. The functional form to describe the hard process scale dependence.

The matching scheme is mainly determined by a momentum threshold, which is varied once up and once down. Also the hard process and parton emission scale are varied up and down. The last tune is considered by an additional functional form. This gives $2 + 2 + 2 + 1 = 7$ variations in total. For the final uncertainty on the background prediction in the signal region, the scale variations of Top fake, Top truth and W+jets are added correlated and weighted by the expected relative contribution. The correlated treatment takes into account that the scales might vary up or down for all hard processes and hence correlated among W+jets, Top semileptonic and Top dileptonic. The only exception is the functional from of the hard process, which is different for Top and W+jets. Therefore, Top truth and Top fake are added

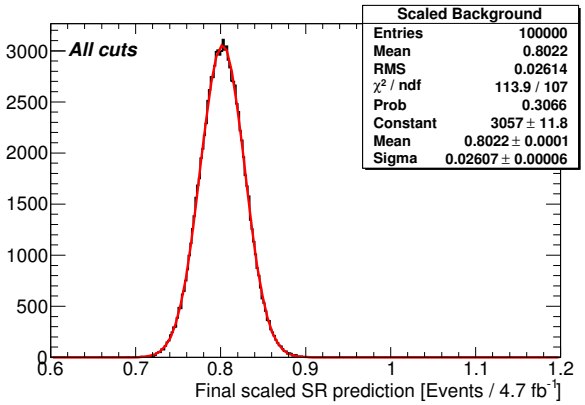

FIGURE 5.10 The systematic uncertainty on the final background estimate in the signal region from the statistical uncertainty on the background scalings. The width includes the full correlation among all three scalings.

correlated, but these are combined uncorrelated with W+jets. For the final combination with the other search channels, the uncertainties have to be split up again to take into account the correlations among the channels as well. Therefore, these seven uncertainties are given individually for the final results.

For this channel, they can be combined uncorrelated since no strong correlation among the individual generator tunes is expected. Potential correlations of the tunes (2) and (3) via the interplay with their removal from (1) have not been quantified and are neglected. The up/down averaged quadratic sum of the four variations is

$$\frac{\Delta N(\text{gen. tune})}{N_{\text{SR}}^{\text{tot.}}} = 25.6\,\% \,. \tag{5.21}$$

It is given as relative uncertainty from the Top and W+jets generator tunes on the total expected SM background in the signal region. This choice of variations, its realization in the generators and the procedure of their evaluation are based on the experience of the single lepton analysis. The samples are officially provided by the SUSY working group, further details can be found in [294].

Uncertainties from Data-Driven Scalings

The transfer factors account for systematic shifts of the scalings due to the settings of the MC generators. In addition, the statistical uncertainties on the used scalings, as derived in Equation 4.21 (p. 75), have to be translated into an uncertainty on the final background prediction. Special attention has to be paid to the full correlation among the three scalings, as already shown in Equation 4.22 (p. 75). Since the scalings cannot be changed independently, the full uncertainty on the final background estimate is evaluated in the following way: For each set of scalings that is derived from the fully smeared matrix of Equation 4.14 (p. 64), i.e. for each triple of scalings in Figure 4.11 (p. 75), the pure MC background prediction in the SR is scaled. This leads to 100 000 estimates for the SR expectation where the scalings are varied according to their uncertainties and correlation. The result can be seen in Figure 5.10. It contributes with a relative uncertainty of

$$\frac{\Delta N(\text{scale stat.})}{N_{\text{SR}}^{\text{tot.}}} = \frac{0.026}{0.80} = 3.25\,\% \,. \tag{5.22}$$

The uncertainties of the Top related scalings are about 16 % to 20 %, but the final estimate has a relative uncertainty of only three percent due to the anticorrelation among the Top scalings.

Combination of Systematic Uncertainties

The obtained uncertainties are summarized in Table 5.3. The vanishing uncertainties for Drell-Yan for many of the systematics are due to lacking MC statistics after the hard effective mass cuts. In any case, the final Drell-Yan contributions sum up to less than a half percent of the total background. Even if the same uncertainties as for Z^0+jets are assumed, this would not change the accuracy of the background prediction and hence no further attempts for a better estimate are needed. To some extent, this argument also holds for the Z^0+jets and di-bosons background since Top and W+jets make up 80 % of the expected background in the signal region and hence dominate the uncertainties.

For the combination of the uncertainties, possible correlations have to be considered. All energy scale related uncertainties could have non-trivial correlations due to common calibration procedures. Hence the jet, tau and soft term energy scale uncertainties are added 100 % correlated for up and down variations. The remaining uncertainties are either randomly directed smearings or related to distinct aspects in the analysis, e.g. tau identification and b-tagging. Hence, they are treated uncorrelated. The asymmetric uncertainties are averaged for up and down variations and are combined to the numbers in the row *sum*. Since the uncertainties in each row of Table 5.3 can be correlated among the backgrounds, e.g. for b-tagging as explained in Section 5.2.2, the total uncertainty in the column "SM" is not the weighted quadratic sum from the individual backgrounds.

The uncertainties from the generator modelling and the statistical uncertainties on the scalings are not given individually for Top and W+jets backgrounds as they are estimated combined due to correlations. The final systematic uncertainty on the total signal region prediction is 34.42 %. This is roughly of the same size as the uncertainties from the MC statistics (see Table 5.1 (p. 104)) and the final background prediction is

$$N^{\text{SM}} = 0.80 \pm 0.28^{\text{MC stat.}} \pm 0.275^{\text{syst.}} \,. \tag{5.23}$$

5.2.5 Systematic Signal Uncertainties

The predicted GMSB contributions in the signal region are also affected by the same systematic uncertainties. The only exceptions are the data-driven scaling and b-tagging related uncertainties since neither scalings nor b-tagging are used for any signal sample. In addition, there are generator uncertainties for the background. Since Top and W+jets are rescaled by data-driven scale factors, cross section uncertainties are compensated and only the shape modelling of kinematic variables had an impact. The cross section uncertainty for di-bosons is included in the shown generator uncertainties. They are obtained from different di-bosons samples with their individually calculated cross section. The signal prediction is also subject to theory uncertainties on the cross section calculation.

For all GMSB points, each event is luminosity weighted according to the NLO cross section of the initial SUSY production process and the total abundance of that process in the sample. This ensures the correct absolute luminosity normalization as well as the correct relative weight among the different SUSY production processes in each sample. The uncertainties on these NLO cross sections are included by variation of the event weight in agreement with the NLO uncertainty. These include variations of the PDFs, the renormalization and factorization scale as well as uncertainties on the strong coupling [295]. The resulting change in expected events in the signal region can be seen in Figure 5.11(a) and is of 10 % to 30 %.

Systematic [%]	DiBoson	Drell Yan	Z+Jets	Top	W+Jets	SM
jet energy scale	−0.54 −13.45	97.57 0	−27.98 −3.98	11.29 −13.04	14.05 −2.28	10.41 −10.31
jet energy resolution	0	0	0	±9.02	±2.38	±5.66
tau energy scale	1.72 −15.88	0 0	0 0	−1.02 0.39	1.78 0.65	−0.25 −0.32
tau identification and fake	±5.8	0	±4.65	±4.64	±2.29	±3.64
b-tag efficiency	0 0	0 0	0 0	−5.83 6.97	1.6 −1.91	−3.45 4.13
b-mistag probability	0 0	0 0	0 0	0.18 −0.17	0.16 −0.18	0.15 −0.14
di-bosons generator	±15.95	0	0	0	±0.85	±1.61
μ trigger efficiency	10.57 −9.91	0 0	34.23 −31.47	6.83 −6.58	29.94 −29.19	12.81 −12.31
μ identification efficiency	0.32 −0.32	0 0	0.4 −0.4	−0.01 0.02	0.06 −0.07	0.06 −0.06
p_{T}^{μ} smearing (ID)	0 0	0 0	0 0	0.41 −0.26	0.01 0.05	0.27 −0.16
p_{T}^{μ} smearing (MS)	0 0	0 0	0 0	5.05 0.36	−0.01 0.1	3.3 0.25
pile-up conditions	±7.93	0	±5.68	±12.35	±34.17	±17.83
soft term scale	0 0	0 0	0 0	−7.13 −5.53	−0.38 0.35	−4.74 −3.56
soft term resolution	0 0	0 0	0 0	0.72 −10.88	1.55 1.9	0.76 −6.77
sum	±25.55	±49.02	±16.16	±21.39	±37.09	±22.77
Top and W+jets generator modelling	–	–	–	–	–	±25.6
statistic uncertainties of scales	–	–	–	–	–	±3.25
final						±34.42

Table 5.3 Summary of the systematic uncertainties. All numbers are relative deviations in percent for the final background estimate in the signal region.

Among all systematics, the ones with the biggest impact on the analysis can be seen as well in Figure 5.11. They are given in percent relative to the total expected events. The muon trigger uncertainties are of 3 % to 12 % and give consistent results with the findings of the background uncertainty. The tau identification uncertainties reflect the tau efficiency uncertainties because the selection is completely true tau dominated. They are slightly bigger as the corresponding ones for the background since its rescaling reduces the impact.

The jet energy resolution in the signal results in compatible uncertainties to the ones in the background. Contrary, the jet energy scale uncertainties are somewhat smaller in the signal. The JES uncertainties had big impact from the jet trigger plateau and $m_{\text{eff.}}$ cuts, which are not so critical for the SUSY samples. These have sufficient hadronic activity to surpass the jet trigger plateau cut anyway, see Figure 5.2(c) (p. 97) and have flatter $m_{\text{eff.}}$ distributions, see Figure 5.3(e) (p. 99). In that sense, the findings for the rather SUSY-like Top contributions are consistent: They have also been less effected by JES, see Table A.16 (p. 153).

The remaining uncertainties can be seen in Figure B.8 (p. 166) in Appendix B. They contribute mostly with uncertainties below percent level. Together with the MC statistical uncertainty, see Figure 5.8(b), these are the final uncertainties on the expected SUSY contributions.

5.3 Data Observation

The expectation of the final event selection and its full uncertainty can now be compared to the data observation. Table 5.4 shows the cutflow for expected background and the data observation at all cut stages. QCD is estimated by the matrix method and Top and W+jets are scaled. One event can be seen in the signal region and data and expected background are found to be in good agreement at all cut stages starting at the muon requirement. The cuts before lack a proper QCD estimate.

5.3.1 Signal Region Data Characterization

Although only the integrated number of events above the final effective mass cut of 1 TeV is chosen as the final observable, the data in the signal region are investigated in more detail. This does not provide any additional information that could be used to either reject or confirm SUSY to be present in the data. The choice which information will be used for the final result has been settled beforehand and cannot be revised after it was uncovered. Any change after the final unblinding of the analysis might systematically bias the analysis towards deviations or in the direction of the expectation. Hence, it might either fake a signal or underestimate the analysis potential. Nonetheless, the single data event is studied in more detail for a purely academic purpose and to understand which data event composes the expected background.

The final $m_{\text{eff.}}$ distribution after the object selection and the cut on the transverse mass $m_{\text{T}}^{\mu} > 100\,\text{GeV}$ can be seen in Figure 5.12(a). Data and background expectation are in agreement up to the signal region and as expected one event is seen in the signal region. Nevertheless, the single data event is seen with an unexpectedly high effective mass, which suggests even more to scrutinize the event.

Figure 5.12(b) shows an event display of the observed data event in the signal region. In the upper left, the event can be seen as sectional image in beam pipe direction, which will be called *front view* in the following. The lower panel shows a side view where the beams come in from the left and the right. In the upper right, the η-ϕ plane is unfold. It shows the spacial separation of the objects. The total effective mass of the event of

$$m_{\text{eff.}} = 2417\,\text{GeV} \tag{5.24}$$

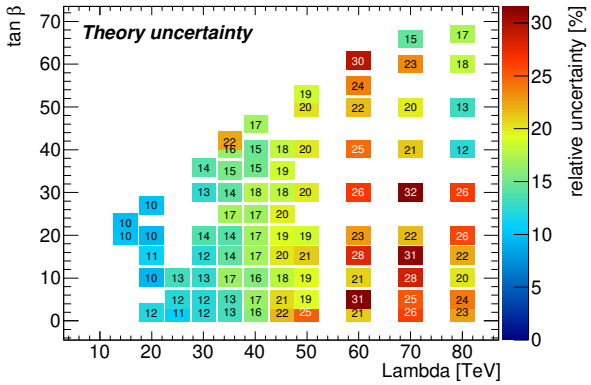

(A) Theory uncertainties

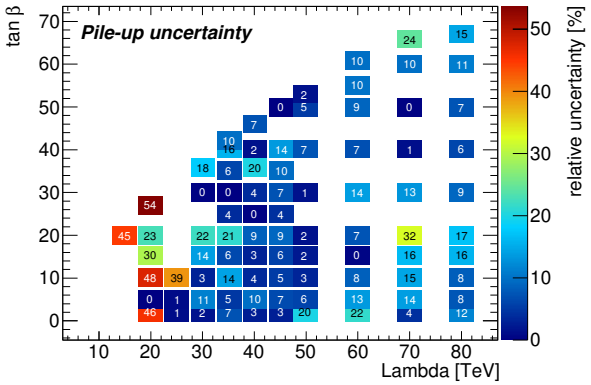

(B) Pile-up uncertainties

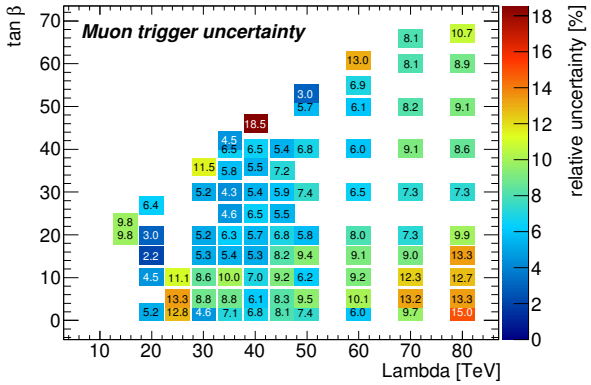

(C) Trigger uncertainties

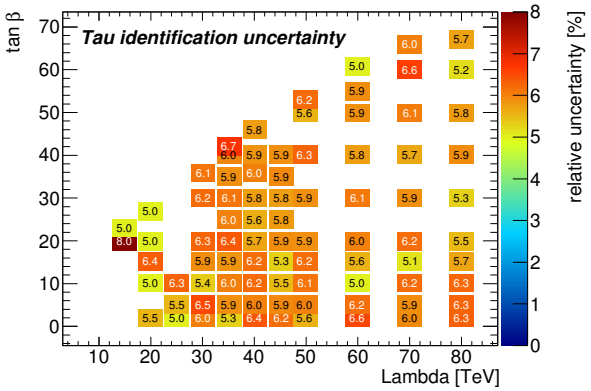

(D) Tau identification uncertainties

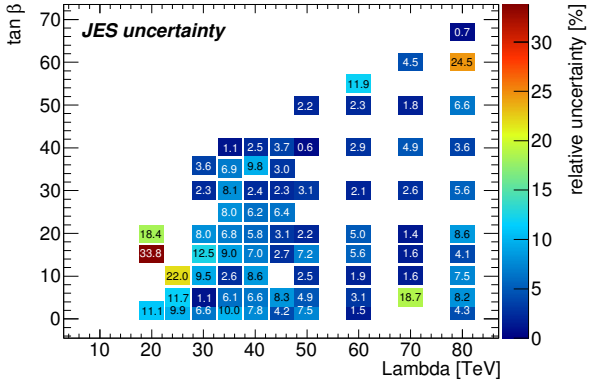

(E) JES uncertainties

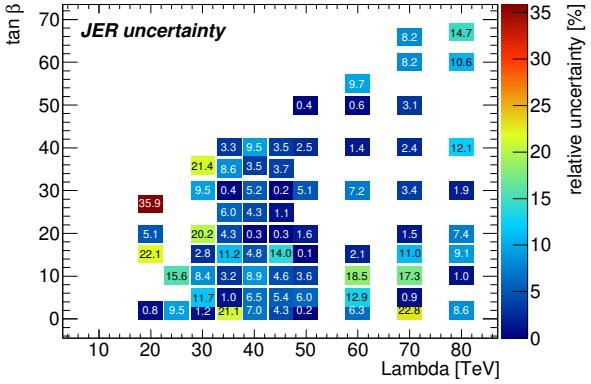

(F) JER uncertainties

FIGURE 5.11 Systematic uncertainties on the GMSB prediction in the signal region. All numbers are given in percent relative to the total prediction.

	2011 Data	DiBoson	Drell Yan	Z+Jets	Top	W+Jets	QCD (DD)	SM	
GRL	229 373 908	44 253	55 194 030	19 350 596	950 153	145 489 056	–	221 028 089	± 48 080
Trigger	137 185 828	12 546	231 819	1 766 665	174 229	10 880 125	–	13 065 385	± 9616
cleaning cuts	134 553 518	12 298	228 107	1 694 491	173 287	10 300 801	–	12 408 984	± 9261
$N_{\text{jet}}^{50\text{ GeV}} \geq 1$	50 374 151	4997	41 470	248 992	153 694	1 377 472	–	1 826 625	± 1583
$N_{\mu}^{20\text{ GeV}} = 1$	2 437 754	2988	19 586	99 186	88 532	1 180 140	845 744	2 236 177	± 209 662
$N_{\tau,\text{ medium}}^{20\text{ GeV}} \geq 1$	15 194	157	254	3637	2162	5716	2829	14 755	± 784
$m_{\text{T}}^{\mu} > 100$ GeV	844	28.4	1.49	48.6	410	357	1.91	847	± 22
$m_{\text{eff.}} > 600$ GeV	23	1.46	0.037	1.22	15.5	6.14	0.23	24.6	± 1.9
$m_{\text{eff.}} > 1000$ GeV	1	0.11	0.0015	0.05	0.36	0.27	0.01	0.80	± 0.28

Table 5.4 Data and expected background cutflow into the signal region. QCD is estimated by the matrix method and Top and W+jets are scaled. An additional intermediate effective mass cut at 600 GeV *is also shown, where more statistics in data and MC are available. The Drell-Yan contributions after the effective mass cuts are estimated via Equation 4.34 (p. 91). No deviation can be seen in the signal region and agreement is good at each cut stage.*

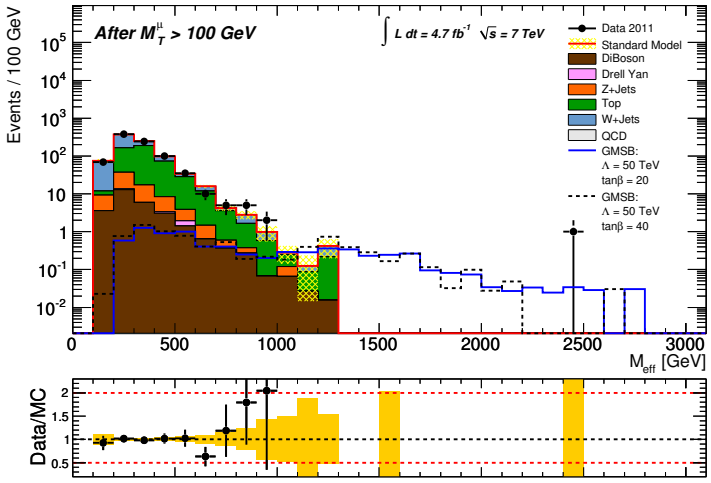

(A) Final effective mass distribution

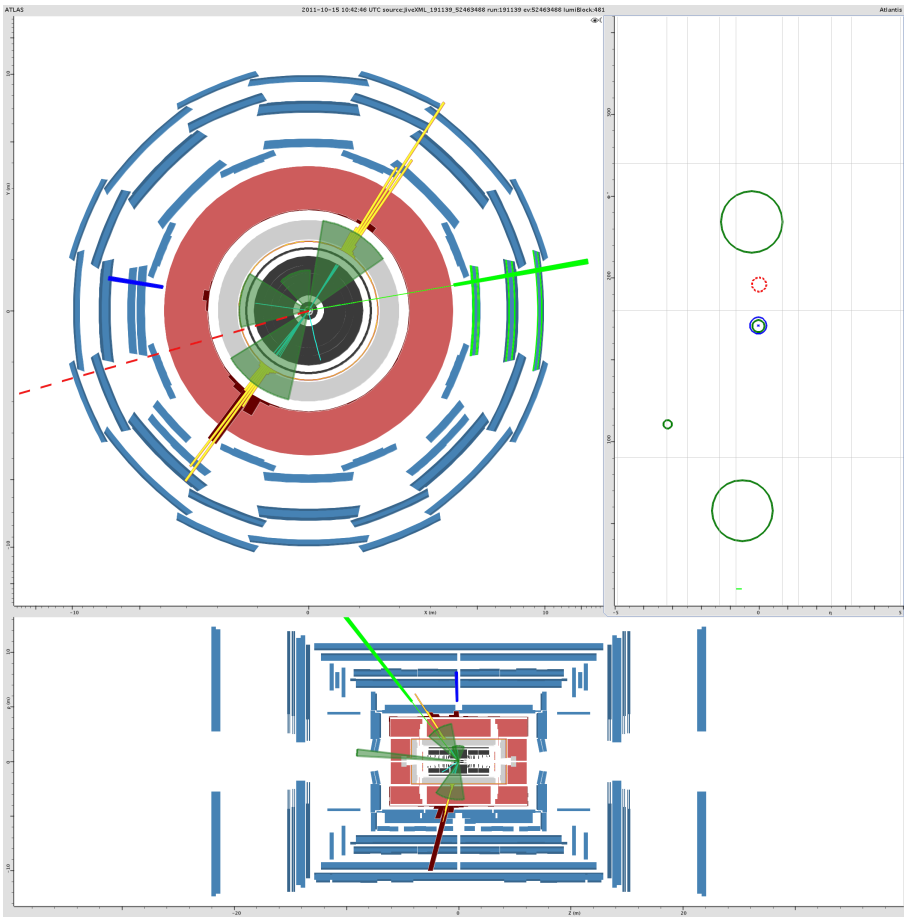

(B) Event display from data event in signal region

FIGURE 5.12 (A): The final effective mass distribution. The agreement up to the signal region is good, but the effective mass of the single data event is unexpectedly high. (B): Event display of the single data event in the signal region.

is largely dominated by two p_{T}-balanced back-to-back jets (indicated in dark green). They point to the upper right and lower left in the front view with the transverse momenta

$$p_{\mathrm{T}}^{1.\,\mathrm{jet}} = 1073.5\,\mathrm{GeV} \qquad \text{and} \qquad p_{\mathrm{T}}^{2.\,\mathrm{jet}} = 1043.8\,\mathrm{GeV}. \tag{5.25}$$

Both are associated to the primary vertex and have no b-tag, even if looser b-tag requirements are applied. In total, there are six reconstructed vertices with four or more associated tracks in the event, which is a rather low pile-up event. There have been 12.31 average interactions per bunch crossing at the data taking period where this event has been recorded.

A peculiar feature of the second leading jet (pointing upper right in the front view) is its small hadronic energy deposition (shown in dark red). About $98\,\%$ of its energy is deposited in the LAr calorimeter (shown in yellow, the leading jet has $81\,\%$ of its energy in the LAr calorimeter) and in that sense it can also be regarded as a photon. Nevertheless, this identification interpretation fails the normal tight photon requirements and is also in contradiction to the bundle of tracks laying in the jet. For visual clarity, tracks with transverse momenta below $4\,\mathrm{GeV}$ are not displayed. There is a single track above this threshold that is not associated to any object. It points to the lower right in the front view and has a transverse momentum of $7.3\,\mathrm{GeV}$.

There are two additional jets: One points upwards and one to the left in the front view, where the latter one is the tau. The other jet has $\eta < -3.2$ (the jet pointing to the left in the side view and the outer left small green circle in the η-ϕ plane). It is not considered in the analysis since it fails the η-cut. Nevertheless, the energy of this jet is $E^{3.\,\mathrm{jet}} = 260\,\mathrm{GeV}$. The tau points to the left in the front view and is indicated by the blue line. It has

$$p_{\mathrm{T}}^{\tau} = 37.04\,\mathrm{GeV}\,, \qquad \eta_{\tau} = -0.042 \qquad \text{and} \qquad \tau\text{-BDT jetscore} = 0.83, \tag{5.26}$$

and hence fulfills BDT medium, but not tight. The tau is well isolated to any jet by

$$\min\{\Delta R\,(\tau, \text{jets})\} = 1.12\,, \tag{5.27}$$

has one track (track $p_{\mathrm{T}} = 15.3\,\mathrm{GeV}$, track fit: $\chi^2/\mathrm{ndf} = 0.652$) and the jet assigned to the tau is also associated to the primary vertex. There is no other track above $p_{\mathrm{T}} > 1\,\mathrm{GeV}$ that points to the calorimeter cells of the tau. The fraction of electromagnetic to total energy of the tau is $39.5\,\%$.

The muon, colored in light green, is also well isolated by

$$\min\{\Delta R\,(\mu, \text{jets})\} = 0.845\,. \tag{5.28}$$

This is more than twice as big in separation as to be potentially considered to originate from a jet. Its basic kinematic properties are

$$p_{\mathrm{T}}^{\mu} = 164.3\,\mathrm{GeV}\,, \qquad \eta_{\mu} = -0.7 \qquad \text{and} \qquad d_0 = 1.66\,\mathrm{mm}\,, \tag{5.29}$$

where the latter is the impact parameter with respect to the beam pipe. The muon has a high track fit quality of $\chi^2/\mathrm{ndf} = 0.529$. Both, the tau and the muon, are positively charged.

The red dashed line shows the direction of the

$$E_{\mathrm{T}}^{\mathrm{miss.}} = 98.78\,\mathrm{GeV} \qquad \text{or} \qquad E_{\mathrm{T}}^{\mathrm{miss.}}/m_{\mathrm{eff.}} = 0.0409\,. \tag{5.30}$$

It lies right in between the tau and the leading jet. Given its rather small value compared to the jet (its less than 10 % of the leading jet transverse momentum), it might be composed of the ν_τ and mismeasured jet energy. The transverse masses with the leptons are

$$m_{\mathrm{T}}^{\mu} = 239.4\,\mathrm{GeV} \qquad \text{and} \qquad m_{\mathrm{T}}^{\tau} = 59.3\,\mathrm{GeV} \tag{5.31}$$

and the invariant mass of the two leptons is

$$m_{(\tau,\mu)} = 162.6\,\mathrm{GeV}\,. \tag{5.32}$$

5.3.2 Possible Event Interpretation in the Standard Model

The presence of two same-sign leptons already suspends many possible SM hypotheses about the event origin. A Top pair would result in an oppositely charged lepton pair and also produce two b-jets. The lacking b-tags for the two jets could be caused by the exceedingly high transverse jet momenta. The strongly collimated tracks might not allow for the reconstruction of a secondary vertex. On the other hand, highly boosted b-quarks would result in a very significant secondary vertex displacement. Furthermore, the sharing of the two Top quark's energies into two very hard jets and two leptons in the order of only 10 % of the jet energies appears unnatural.

Also the hypothesis of a Z^0+jets event seems unlikely since one of the lepton charges would have to be misidentified. The tau is a one-prong candidate with no other tracks in its surrounding and has a track momentum of about 15 GeV with high track fit quality. That makes a charge misidentification rather unlikely. The higher $p_{\mathrm{T}}^{\mu} \approx 165\,\mathrm{GeV}$ might be more susceptible to charge misidentification, but muons can be followed over a larger distance in the detector and the track has also a high fit quality. Muons from $W' \to \mu\nu_\mu$ decays can be shown to have charge mistag probabilities of below 0.5 % in the barrel for a 1 TeV W'-mass [296] and hence seems implausible as well. In addition, the invariant mass of the lepton pair is way above the Z^0 mass limit.

A pair of two same-sign leptons could be produced by di-bosons, e.g. $W^{\pm}Z^0$ or Z^0Z^0 where either one or two leptons are missing. Figure 5.13 shows potential Feynman diagrams for the production of di-bosons. For same-sign final states Figure 5.13(A) and (B) could contribute to either Z^0Z^0 or $W^{\pm}Z^0$ and Figure 5.13(C) to $W^{\pm}Z^0$. Figure 5.13(D) and (E) can give contributions to Z^0Z^0, whereas Figure 5.13(F) cannot contribute to same-sign leptons due to the missing tri-Z^0 coupling in the SM. In all cases, a production of a single same-sign lepton pair is not possible since none of the diagrams allows for $W^{\pm}W^{\pm}$. Figure 5.13(A) to (C) need quark-anti-quark initial states and Figure 5.13(D) to (F) have electrical neutral final states.

In addition, this would only explain the same-sign lepton pair of the event. The hard jets would need to be caused by additional QCD interaction in the hard event. The high-p_{T} and balanced di-jet topology of the event actually suggests that the two hard jets are initially produced. The leptons could then arise from additional processes. One possibility would be $W^{\pm}$ radiation as shown in Figure 5.13(G). Here, a same-sign W-pair is possible since the intermediate gluon decouples the initial quark flavour and charge correlation. This was needed for the diagrams from Figure 5.13(A) to (C).

In order to produce same-sign $\mathrm{SU}(2)_L$ gauge bosons, the primary produced quarks have to be (left-chiral) same-sign quarks. This could be realized by either an up-type or a down-type quark pair as well as by a quark-anti-quark pair of mixed up- and down-type. Therefore, s-channel diagrams via strong production are already excluded: At tree level, a quark-anti-quark pair would have same flavour and hence leads to oppositely charged W-bosons. t-channel diagrams with quarks as mediators are also not

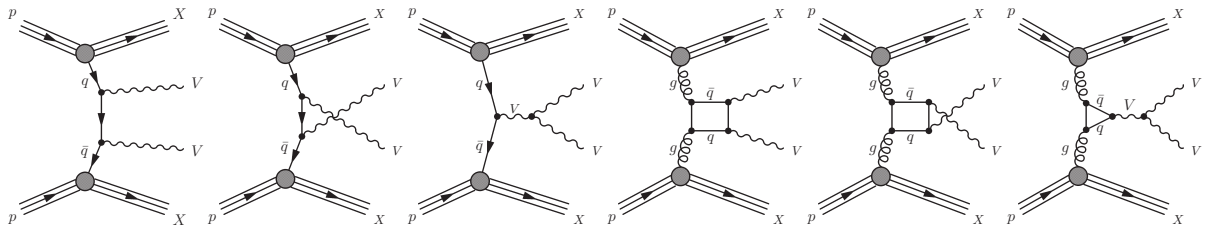

(A) t-channel (B) u-channel (C) s-channel (D) t-channel (E) u-channel (F) s-channel

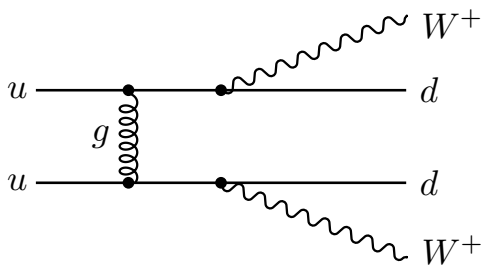

(G) Final state radiated W^+ bosons

Figure 5.13 Feynman diagrams for the di-bosons production at the LHC. (A) and (B): Z^0Z^0, $W^\pm Z^0$ and $W^\pm W^\mp$. (C): $W^\pm W^\mp$ and $Z^0 W^\pm$. (D) and (E): Z^0Z^0 and $W^\pm W^\mp$. (F): $W^\pm W^\mp$. (G): Production of a same-sign W^+W^+ pair via W^+ radiation.

possible. They would either result in at least one primary produced gluon or a same-flavour anti-quark pair.

More general, the only tree level QCD diagrams that allow for the needed primary produced state are the SM versions of Figures 2.7(P), (Q) and (S) (p. 24). The first one is a SUSY version of the hard process of Figure 5.13(G) and the latter the corresponding u-channel. The SM version of Figure 2.7(Q) would replace one of the incoming quarks in Figure 5.13(G) by a $\bar{d}$, which could also radiate a W^+.

The radiation of a W-boson from both quarks might seem unlikely at the first glance, but for jet energies at the TeV scale, the W becomes practically massless. In this limit, W radiation is kinematically similar to photon radiation. The observation of two positively charged leptons, as seen in the event, is also consistent with the larger up-type content of the proton. Nonetheless, the cross section for like-sign $W^\pm W^\pm$ production, e.g. as in Figure 5.13(G), is roughly two orders of magnitude smaller than for opposite-sign $W^\pm W^\mp$ production [297]. However, this only holds for the total cross section. The differential cross sections for these processes to appear in the signal region might be much closer. The high $m_{\text{eff.}}$ cut requires high-p_{T} jets, where processes like Figure 5.13(G) become more likely. In contrast, high-p_{T} jets need to be produced in association to the $W^\pm W^\mp$ pairs from Figure 5.13(A) to (F). Therefore, the expected abundance of the WW production from Figures 5.13(A) to (F) is suppressed in the signal region compared to the process of Figure 5.13(G). In any case, the origin of the selected event cannot be finally decided and the single event will be taken as the final data observation.

5.4 Limit Setting in GMSB and Interpretation

The agreement of SM expectation and observation supports the background-only hypothesis. This can be used to set limits on the possible existence of certain GMSB model points. Clearly, the high Λ points have too few expected contributions to be excluded, see Figure 5.8(A).

5.4.1 Limits in GMSB

The confidence level for the exclusion of a given signal point is quantified by the p-value of the signal and background hypothesis. It is the probability to find the observed or less data events in the signal region under the assumption that signal and background are present. A signal point is excluded if the one-sided hypothesis test gives $p < 0.05$. In that case, the probability that the observation is consistent with signal and background hypothesis is below 5 %. The p-value is calculated in a statistical model that uses a logarithmic likelihood ratio as test statistic. The considered likelihood is

$$\mathcal{L}\left(\mu, \vec{\lambda}\right) = \underbrace{\frac{\left[\mu s\left(\vec{\lambda}\right) + b\left(\vec{\lambda}\right)\right]^N}{N!} \exp\left\{-\left[\mu s\left(\vec{\lambda}\right) + b\left(\vec{\lambda}\right)\right]\right\}}_{\text{Poisson-distribution}} \underbrace{\prod_{k=1}^{M} \frac{1}{\sqrt{2\pi}} \exp\left(-\frac{\lambda_k^2}{2}\right)}_{\text{nuisance priors}} , \tag{5.33}$$

where the first part is a Poisson distribution. It gives the probability to observe N events for an expectation of $\mu s + b$, where μ is the signal strength. Signal and background are given by

$$s\left(\vec{\lambda}\right) = s \prod_{k=1}^{M} \left(1 + \lambda_k \sigma_{s,k}^{\text{syst.}}\right) \qquad \text{and} \qquad b\left(\vec{\lambda}\right) = b \prod_{k=1}^{M} \left(1 + \lambda_k \sigma_{b,k}^{\text{syst.}}\right) , \tag{5.34}$$

where s and b are signal and background predictions for the signal region. The M systematic uncertainties $\sigma_k^{\text{syst.}}$ are parameterized linearly with the nuisance parameters λ_k. Their prior probabilities are constrained by the Gauss distributions in the second part of Equation 5.33.

The used test statistic is then

$$T(N) = \log\left(\frac{\mathcal{L}\left(\mu = 1, \vec{\lambda}'\right)}{\mathcal{L}\left(\mu'', \vec{\lambda}''\right)}\right) , \tag{5.35}$$

where $\vec{\lambda}'$ is the set of nuisance parameters that maximize the nominator likelihood with nominal signal expectation ($\mu = 1$). $\vec{\lambda}''$ are the nuisance parameters that maximize the denominator likelihood with floating signal strength μ''. The ratio expresses the level of agreement that can be obtained with background plus signal hypothesis and free signal contribution. The probability density for $T(N')$, $f_T(N')$, is obtained from pseudo experiments with the hypothetical observation of N' events and a signal point is excluded if

$$\int_{-\infty}^{N^{\text{obs.}}} f_T(N')\mathrm{d}N' = p = \mathrm{CL}_{s+b} < 0.05 . \tag{5.36}$$

$N^{\text{obs.}}$ are the observed data events in the SR, i.e. $N^{\text{obs.}} = 1$ for this analysis, and the test is one-sided, i.e. tested against equal or lesser events. More details on the used logarithmic likelihood ratio are described in [290].

The nuisance parameters are treated correlated among signal and background. E.g. if the JES increases in the background, it does so in the signal. The only exception is the uncertainty from MC statistics, which is uncorrelated in signal and background. Furthermore, the b-tagging, scale factor and background event generator related uncertainties are fixed to $\sigma_{s,k}^{\text{syst.}} = 0$ in Equation 5.34. They do not affect the signal selection. For the theory uncertainties of the signal, the calculation of the p-values is repeated with decreased and increased SUSY expectations according to the theory uncertainties.

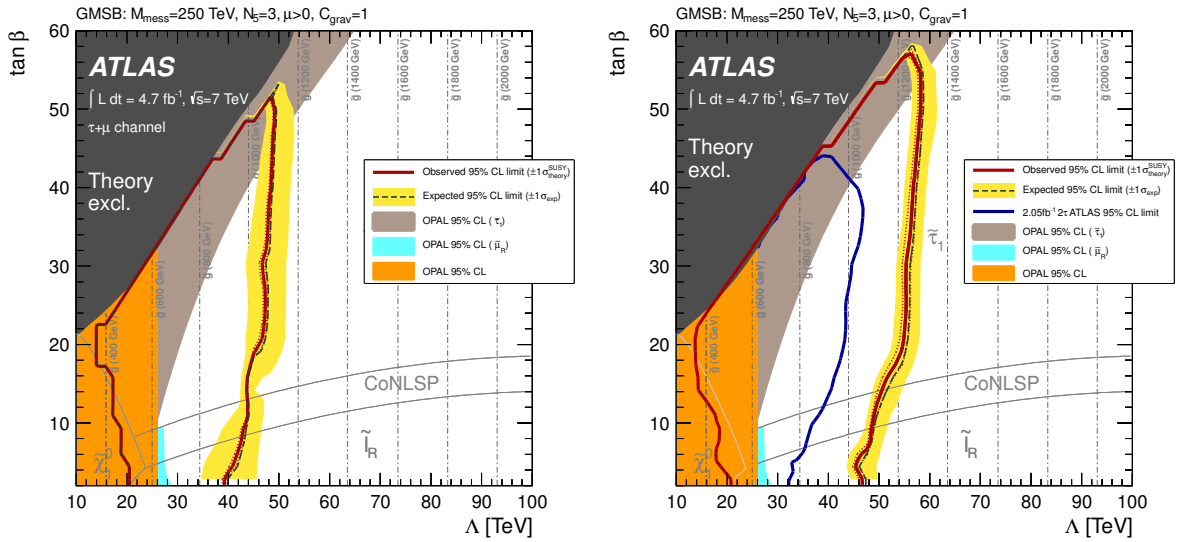

(A) τ and μ only

(B) Combined tau searches

Figure 5.14 The obtained exclusion limit in the GMSB grid for (A) the presented search with tau leptons and one muon and (B) the combined limit for the di-tau, one-tau, tau and electron and tau and muon analysis.

The calculations are performed by the ATLAS `HistFitter` package.[3] It samples $f_T(N')$ in Equation 5.36 with 10^4 pseudo experiments. The result can be seen in Figure 5.14(A). The red line gives the observed exclusion limit and the black dashed line the expected limit. The latter is derived from a pseudo experiment where the observation is set to the background expectation. The expected limit is slightly tighter since it assumes a slightly smaller observation (the 0.8 events from Equation 5.23 (p. 116), instead of the one observed data event). The marginal larger observation gives a larger p value in Equation 5.36 and hence looser exclusion limits.

The dark gray area is theoretically excluded since it leads to unphysical SUSY particle masses and the obtained limits from the opal experiment [298] are shown. Depending on $\tan\beta$, the analysis excludes Λ up to 40 TeV to 45 TeV. The SUSY expectation at $\Lambda \approx 50$ GeV could be seen to exceed the expected background of 0.8 events by up to 2 events, see Figure 5.8(A) (p. 107). Nonetheless, the combined uncertainties allow for sufficient background and signal fluctuations to hide potential signals.

The interpretation in GMSB can be repeated by the joint use of several tau searches, i.e. the di-tau, one-tau and tau with electron channel. They have been designed to be free of overlap after the object selection, see Section 4.1.2. Thereby, all signal and control regions are orthogonal and no statistical correlation among the channels is present. For the combination, the likelihood in Equation 5.33, is expanded by

$$\mathcal{L}_{\text{combined}}\left(\mu,\vec{\lambda}\right) = \mathcal{L}_{\text{one-tau}}\left(\mu,\vec{\lambda}\right) \times \mathcal{L}_{\text{di-tau}}\left(\mu,\vec{\lambda}\right) \times \mathcal{L}_{\tau+e}\left(\mu,\vec{\lambda}\right) \times \mathcal{L}_{\tau+\mu}\left(\mu,\vec{\lambda}\right) . \tag{5.37}$$

Some of the channels have different systematics, e.g. the muon related systematics are not present for the other channels. Therefore, some nuisance parameters are fitted to only certain channels. Still, systematics that are present for all channels, like JES or TES, are described by the same nuisance parameter

[3] https://twiki.cern.ch/twiki/bin/viewauth/AtlasProtected/SusyFitter
https://twiki.cern.ch/twiki/bin/viewauth/AtlasProtected/HistFitterReleaseNotes
https://svnweb.cern.ch/trac/atlasphys/browser/Physics/SUSY/Analyses/HistFitter

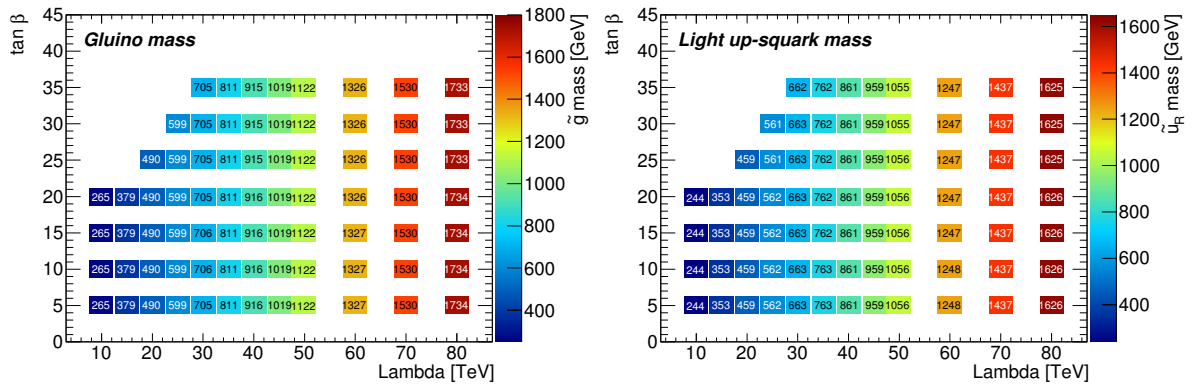

(A) $m_{\tilde{g}}$ (B) $m_{\tilde{u}_R}$

FIGURE 5.15 The masses of (A) the gluino and (B) the lighter up-squark in the GMSB grid. Masses below $\Lambda \approx 55$ TeV can be excluded.

and have the same GAUSSian prior to consider the correct correlation among the channels. The result can be seen in Figure 5.14(B) [156, 299]. The combination extends the exclusion up to $\Lambda = 50$ TeV to 55 TeV. The blue line gives the exclusion limit of the di-tau analysis with $2.05\,\text{fb}^{-1}$ [283], which has been the strongest published ATLAS limit before. This limit could be extended by 10 TeV to 15 TeV and also the regime of $45 < \tan\beta < 58$ could be reached in between $\Lambda = 40$ TeV to 52 TeV. At the time of publication, this has been the strongest limit on GMSB SUSY models in a large part of the considered parameter space.

5.4.2 Interpretation

The limits on the model parameters Λ and $\tan\beta$ can be transferred into limits on the SUSY particle masses. For instance, the predicted gluino mass in GMSB is also shown in Figure 5.14. Strictly speaking, all masses of SUSY particles can be excluded that are realized only in the excluded grid points. This is true as long as the considered GMSB model is assumed and a certain mass of a SUSY particle is not also realized by another, non-excluded point.

Figure 5.15 shows the gluino and lighter up-squark mass in the GMSB grid. The $\widetilde{u}_R$ and $\widetilde{d}_R$ are the lightest first generation squarks and their masses only differ by a few permille due to different hypercharge. For $\tan\beta$ above 20, all grid points below $\Lambda \lesssim 55$ TeV are excluded and hence the corresponding gluino and squark masses as well. This already sets limits on the gluino and squark masses of

$$m_{\tilde{g}} \gtrsim 1.2\,\text{TeV} \qquad \text{and} \qquad m_{\tilde{u}_R} \gtrsim 1.1\,\text{TeV}\,. \tag{5.38}$$

These are obtained from a global limit on $\Lambda > 55$ TeV and neglect the $\tan\beta$ dependence of the exclusion limit of Figure 5.14(B). However, this dependence has no strong impact on this conclusion. The symbol '$\gtrsim$' denotes that the mass limits are estimated roughly by visual judgement rather than by explicit calculations. The limit on the lighter stop mass is slightly looser

$$m_{\tilde{t}_1} \gtrsim 1\,\text{TeV}\,, \tag{5.39}$$

see Figure 6.1(b) (p. 133). The mixing in the stop sector leads to lighter stops compared to the other squarks. The corresponding mass limits for the lightest chargino, neutralino and stau are

$$m_{\tilde{\chi}_1^\pm} \gtrsim 380\,\text{GeV} \qquad \text{and} \qquad m_{\tilde{\chi}_1^0} \gtrsim 220\,\text{GeV} \qquad \text{and} \qquad m_{\tilde{\tau}_1} \gtrsim 140\,\text{GeV} \tag{5.40}$$

and can be seen from Figures 6.2(c), (d) and (e) (p. 136), respectively. The obtained mass limits on the colored SUSY particles are much higher than the corresponding for the electroweak gauge bosons and the stau. This is a feature of GMSB, where a common Λ translates into much higher masses for strongly interacting SUSY particles, see Equations 2.84 and 2.85 (p. 32).

In principle, the non-observation of any excess above the SM shifts the possible masses of SUSY particles to higher energy scales, which are experimentally not (yet) accessible. Although SUSY could still be realized at this high energy scales, this might already question the naturalness of SUSY. One of its most compelling features is the solution of many SM shortcomings by the introduction of the symmetry of Equation 2.22 (p. 12). However, the solution of the hierarchy problem, the unification of the SM gauge couplings and the correct prediction of the electroweak mixing angle all require

$$M_{\text{susy}} \not\gtrsim 1\,\text{TeV}\,, \tag{5.41}$$

see Chapter 2. Exact SUSY even postulates equal masses of particles and their superpartners, see Equation 2.28 (p. 14). The introduction of SUSY breaking is an exigency due to the non-observation of SUSY particles. Although the limit from Equation 5.41 has not yet been significantly surpassed, the naturalness of SUSY suffers from the ongoing raise of the possible SUSY mass scale. In that sense, the combined result of the SUSY searches with taus cast the considered GMSB model into doubt to be a natural extension of the SM.

Clearly, this argumentation only holds for the considered GMSB model, which is one possible realization of SUSY. In less constrained models, like the MSSM, the mapping of observations to limits on SUSY masses is more involved. Hence, the results from this analysis can not be easily transferred to other SUSY models. However, the mass hierarchy of GMSB is also predicted by the RGEs, see Equation 2.47 (p. 20), if the unification at the GUT scale is assumed, see Equation 2.40 (p. 19). In that sense, the analysis has also sensitivity to more generic tau-rich SUSY models.

This might be suppressed in specific SUSY models, e.g. if the mass difference of two subsequent SUSY particles in a decay chain is very small. In that case, the visible SM particle could be too soft to be reconstructed. Especially taus from SUSY decay chains, see Equations 2.74 (p. 29) or 2.92 (p. 34), would suffer from this because their reconstruction efficiency drops with smaller transverse momenta. Nevertheless, this would be a specific feature of a certain model and the analysis still has sensitivity to a wide region of tau-rich SUSY parameter space. Unfortunately, this region is hard to quantify.

In order to set limits in different models, the contribution of the SUSY model to the analysis needs to be quantified. Hence, each model has to be tested explicitly as a function of its free parameters. Then, all SUSY particle masses can be excluded that are only realized by excluded parameters. A convenient way to parameterize a model would be by the masses of its SUSY particles. Unfortunately, this is not feasible or even impossible in many SUSY models. Either the SUSY particle masses cannot be individually chosen, e.g. in GMSB, or there are too many parameters that need to be considered simultaneously, e.g. in the MSSM.

The latter case can be tackled by the construction of simplified models. These try to parameterize a SUSY model's contribution to a certain final state by as few as possible parameters. Thereby, they concentrate on a single SUSY decay chain that is expected to dominate the contribution to the searched final state. A single decay chain can then be parameterized by the involved SUSY particle's masses and

their couplings. Unfortunately, the latter includes the full mixing among the charginos, neutralinos and sleptons if they occur in the decay chain. E.g. the MSSM decay chain

$$\widetilde{g} \to \widetilde{q}q \to \widetilde{\chi}_i^0 qq \to \widetilde{\tau}\tau qq \to \widetilde{\chi}_1^0 \tau\tau qq \tag{5.42}$$

is parameterized by the eight parameters

$$m_{\tilde{g}}, \qquad m_{\tilde{q}}, \qquad M_1, \qquad M_2, \qquad \mu, \qquad \tan\beta, \qquad m_{\tilde{\tau}} \qquad \text{and} \qquad \vartheta_{\tilde{\tau}}\,,$$

see Equations 2.49 (p. 20) and 2.59 (p. 22). Still, this is a significant reduction compared to the more than 100 parameters of the MSSM. In future analyses, these simplified models might give less model dependent mass constraints on SUSY particles.

Chapter 6

Revisiting the Analysis

Critical Review and Possible Refinement

This chapter reviews the analysis from theoretical and experimental point of views. In the first instance, the impact of the discovery of a Higgs-like particle, which was detected during the analysis development, is sketched. In addition, possible progress in the analysis is proposed that might improve the sensitivity, but could not be realized in the first analysis cycle.

6.1 Implications of a Possible Higgs Signal at $m_H = 125\,\text{GeV}$

The discovery of a Higgs-like particle with a mass of about $m_H = 125\,\text{GeV}$ by ATLAS [12] and CMS [13] might have already implications for SUSY. Though not finally confirmed, a Higgs mass at 125 GeV is rather heavy for SUSY, where the lightest neutral Higgs is bound to

$$m_{h_0} \leq m_{Z^0} \tag{6.1}$$

at tree level, see Equation 2.26 (p. 13). The mass can be raised only by higher order loop corrections, which might already constrain individual SUSY models. The mass of the lightest neutral Higgs boson, h_0, in the used GMSB grid can be seen in Figure 6.1(a). Obviously, none of the considered grid points has a sufficiently high h_0 mass. Hence, the model would be excluded already if the discovered Higgs-like particle would be assumed to be the h_0. The heavier H_0 has a mass of 100 GeV to 1200 GeV in the parameter grid.

However, GMSB is chosen as a guideline for general SUSY with taus, missing transverse momentum and hadronic activity. Although its special realization might not be consistent with the mass of the newly detected particle, it could still be adequate as a generic reference model. In this respect, the more interesting question is the dependence of the SUSY phenomenology on the mass of the lightest neutral Higgs.

The signatures used in this analysis are summarized in Table 6.1, together with the theoretical assumptions that allow for their realization. In the following, the occurrence of these signatures shall be reviewed in the light of a h_0 with a mass of 125 GeV. If SUSY models with sufficiently high h_0 mass and these signatures exist, the search is still well motivated. E.g. in the MSSM, numerous parameters can be chosen independently and hence the Higgs mass might be looser coupled to the SUSY collider appearance. Certainly, in a more constrained model that reduces parameters by more specific assumptions about the breaking mechanism, there might be stronger correlations between the model appearance and the Higgs mass.

signature	realization	theoretical assumption	motivation
jets	colored sparticle decays	$\{m_{\tilde{g}}\ ,\ m_{\tilde{q}}\} \not\gg 1\,\text{TeV}$	hierarchy problem
$E_{\text{T}}^{\text{miss.}}$	stable weakly interacting sparticle	R-parity conservation	dark matter, proton stability
taus	electroweak sparticle decays	large stau mixing	large τ Yukawa couplings

Table 6.1 The searched signatures of the analysis together with their realization, theoretical assumptions and an example motivation.

Indeed, there are connections of the collider phenomenology to the Higgs mass in GMSB. Due to their enhanced Yukawa coupling, stops have the largest loop contributions to the Higgs mass from Equation 2.26. At one loop level it can be shown to be approximately [300]

$$m_{h_0}^2 = m_{Z^0}^2 \cos^2 2\beta \tag{6.2}$$

$$+ \frac{3m_t^4}{4\pi^2 v^2}\left(\underbrace{\ln\left(\frac{m_{\widetilde{t}_1} m_{\widetilde{t}_2}}{m_t^2}\right)}_{\text{(I)}} + \underbrace{\frac{\left(A_t - \mu\cot\beta\right)^2}{m_{\widetilde{t}_1} m_{\widetilde{t}_2}}\left(1 - \frac{\left(A_t - \mu\cot\beta\right)^2}{12 m_{\widetilde{t}_1} m_{\widetilde{t}_2}}\right)}_{\text{(II)}} \right)\ , \tag{6.3}$$

where the term (I) typically dominates in GMSB [301]. The mixing term (II) is reduced by the fact that A_t vanishes at messenger scale in GMSB. It gets non-vanishing contributions only by the RGEs. Moreover, the targeted high $\tan\beta$ parameter space diminishes the $\cot\beta$ contribution.

The increase of the Higgs mass with Λ, see Figure 6.1(a), can be explained by the increasing $\widetilde{t}$ mass. This can be seen in Figure 6.1(b) and therefore heavy stops are preferred to generate a rather high Higgs mass. Since SUSY breaking is mediated by the gauge interactions, the squark masses depend only their gauge quantum numbers. These are strongly dominated by their $\text{SU}(3)_C$ coupling in Equation 2.85 (p. 32) and hence all squarks have approximately equal masses. The degenerated squark mass spectrum can be split up only by the (smaller) $\text{SU}(2)_L$ coupling in Equation 2.85 or by mixings like from Equation 2.61 (p. 22). Hence, the tightly coupled squark masses already shift their mass spectrum to hardly accessible scales if a very high $\widetilde{t}$ mass required.

A Higgs mass of (125 ± 1) GeV in GMSB can be shown to result in multi-TeV squarks and gluinos and thereby violates the assumptions for strong SUSY production. Nonetheless, the targeted high $\tan\beta$ parameter space is still consistent with smaller possible Λ and hence smaller sparticle masses [301]. In mSUGRA models, high mass SUSY particle spectra can also result from the $m_{h_0} = 125$ GeV constraint [302].

The term (II) in Equation 6.3 is proportional to the mixing in the stop sector and prefers large mixing. Since top quarks are up-type and tau leptons are down-type fermions, the $\tan\beta$ dependence is reverted for $\widetilde{t}$ mixing. Hence, large mixing in the $\widetilde{\tau}$ sector is biased towards smaller mixing in the $\widetilde{t}$ sector and vice versa, see Equations 2.57 and 2.61 (p. 22). Obviously, this can be partly decoupled by non-universal trilinear couplings $A_\tau \neq A_t$ in Equation 2.55 (p. 21).

The different mixing in the $\widetilde{t}$ and $\widetilde{\tau}$ sector of GMSB can be seen in Figures 6.1(c) and (d). They show the mass difference of the lighter and heavier stau and stop. In both cases, the mass splitting increases with Λ due to rising sfermion masses. However, the mass splitting increases with $\tan\beta$ in the $\widetilde{\tau}$ sector, whereas it drops in the $\widetilde{t}$ sector.

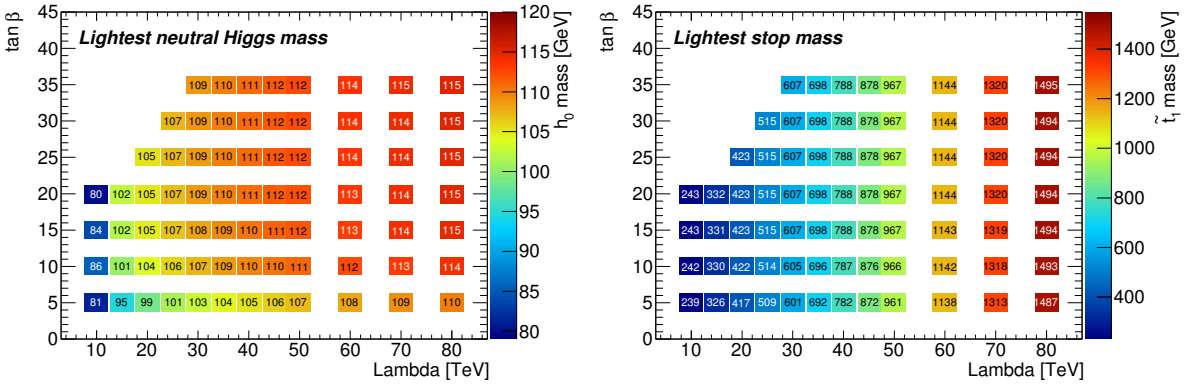

(A) m_{h_0}

(B) $m_{\tilde{t}_1}$

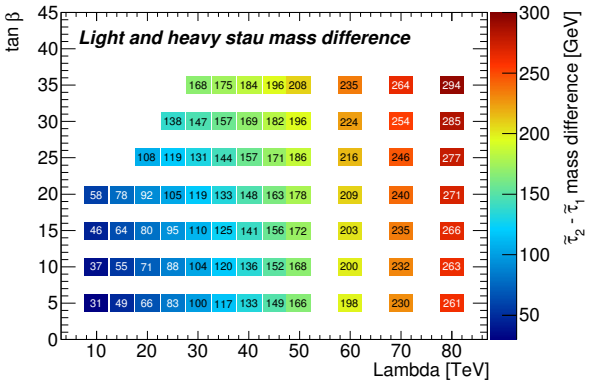

(C) $m_{\tilde{\tau}_2} - m_{\tilde{\tau}_1}$

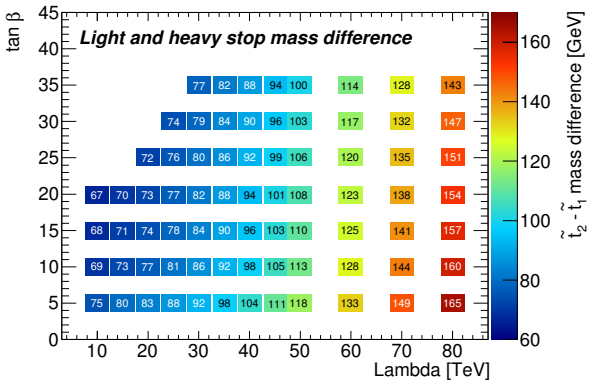

(D) $m_{\tilde{t}_2} - m_{\tilde{t}_1}$

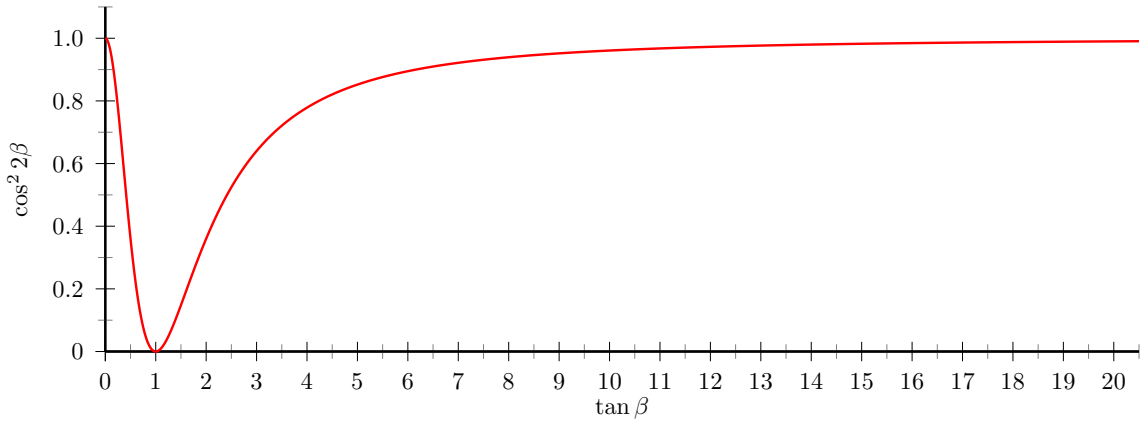

(E) The $\tan\beta$ dependence of the m_{Z^0} contribution to m_{h_0}

Figure 6.1 (A) The lightest neutral Higgs mass, (B) the lighter $\widetilde{t}$ mass and the sfermion mass difference in (C) the $\widetilde{\tau}$ sector and (D) the $\widetilde{t}$ sector. (E): The $\tan\beta$ dependence of the m_{Z^0} contribution to m_{h_0}.

In addition, a slight dependence of the Higgs mass on $\tan\beta$ can be seen in Figure 6.1(a). The mass of the h_0 increases for higher $\tan\beta$. In that regions, the Z^0 mass contribution in Equation 6.2 is even reduced by

$$\cos^2 2\beta = \left(\frac{1-\tan^2\beta}{1+\tan^2\beta}\right)^2 , \tag{6.4}$$

which is shown in Figure 6.1(e). Above $\tan\beta > 1$, it enlarges m_{h_0} and makes large $\tan\beta$ more compatible with heavy SUSY Higgs bosons. This is only true in the sense that the tree level upper bound is not even significantly below the Z^0 mass. This $\tan\beta$ dependence cannot generate Higgs masses above m_{Z^0}. Therefore, high stop masses, and hence high squark masses, would be the most effective and natural way to explain a heavy Higgs in GMSB. The tight constraints on the squark masses can be relaxed in more general GMSB models that allow for heavier Higgs bosons [303, 304] with lighter squarks.

The second signature in Table 6.1, the $E_{\mathrm{T}}^{\mathrm{miss.}}$, is less critical with respect to the Higgs mass. If SUSY particles can be produced at the LHC, the existence of $E_{\mathrm{T}}^{\mathrm{miss.}}$ above the SM expectation is predicted by pure R-parity conservation. This is true as long as sufficient energy is carried by the final LSP in the decay chains.

The most interesting possible implication from the Higgs mass affects the tau richness of the SUSY scenario. Taus are predicted by the lighter $\widetilde{\tau}$ mass, which is driven by larger L-R mixing in the $\widetilde{\tau}$ sector, see Section 2.3.3. In GMSB (and also other models), this can be controlled by $\tan\beta$. Equation 6.2 slightly favors high values of $\tan\beta$ for high m_{h_0}, as explained above. Nonetheless, if the large Higgs mass shall be generated by large mixings in the $\widetilde{t}$ sector, this could be controlled only by A_τ and A_t. The $\tan\beta$ dependence of the mixing is reverted in the two sectors and hence cannot generate large mixing in both of them.

Also the number of messenger fields, N_5, has an interplay with the Higgs mass. The mixing corrections in term (II) of Equation 6.3 depend on the ratio $A_t/m_{\widetilde{t}}$. In GMSB, A_t vanishes at messenger scale and has non-zero contributions only be the RGEs. They are dominated by the coupling to the gluino mass parameter M_3 [17]. Since M_3 scales linearly with N_5 and $m_{\widetilde{t}}$ only with $\sqrt{N_5}$ (see Equations 2.84 and 2.85 (p. 32)), a larger N_5 increases the ratio $A_t/m_{\widetilde{t}}$. This enforces the impact of the $\widetilde{t}$ mixing contributions in Equation 6.3 and hence loosens the constraints on the $\widetilde{t}$ masses [301]. By the same argument, more messenger multiplets N_5 enlarge the gaugino masses relative to the scalar masses and replace the $\widetilde{\chi}_1^0$ NLSP by a $\widetilde{\ell}$ NLSP models. This is needed for the abundant appearance of leptons, i.e. taus for high $\tan\beta$.

In less constrained models, e.g. the MSSM, the interplay of the Higgs mass and the SUSY phenomenology can be much looser coupled but also more complicated. These considerations are beyond the scope of this section. Nevertheless, a review of the GMSB in the light of a potential 125 GeV Higgs might be reasonable for future analyses.

6.2 Potential Refinements and Extensions of the Analysis

The analysis sensitivity could be improved by either more accurate background and signal estimates or by a more effective separation of signal and background. These two options are not uncorrelated. Tighter cuts for background suppression come at the prize of small MC statistics, and hence larger uncertainties. The cut optimization was performed under consideration of available MC statistics. In the end, the uncertainty from MC statistics turned out to be as large as the remaining systematic uncertainties, see Equation 5.23 (p. 116). Obviously, higher MC statistic would be of help, but the gain is limited by the remaining systematic uncertainties. They account for half of the total uncertainties.

The analysis would also profit from a reduction of the systematic uncertainties as well. Table 5.3 (p. 117) shows that the most influential systematics are JES, trigger efficiency, pile-up conditions and generator modelling. To a large extend, the sizable pile-up contributions are driven by the conservative way to estimate them, see Section 5.2.4. The analysis would notably profit from a more event generator setting independent modelling of the event kinematics. This constitutes the biggest uncertainty. Certainly, this is a highly non-trivial task due to missing higher order calculations for the hard process and the phenomenological approach to hadronization. The trigger related uncertainties might get smaller with higher available data statistics and hence better understanding of the trigger efficiencies.

The influence of many systematic uncertainties could also be minimized by use of completely data-driven estimates for the dominant backgrounds, i.e. Top and W+jets. For W+jets, the charge asymmetry method, see Section 4.2.2, might be suited for that. Though the ratio of positively to negatively charged leptons is obtained from MC, the charge independent systematics cancel out in the ratio. However, the method assumes a sufficiently significant W+jets contribution on top of charge symmetric backgrounds for the estimate. This is not the case for the low statistics signal region and hence the method has been used only as cross check in high statistics control regions. In addition, this method might be biased by potential overlaid charge asymmetric signal contributions in the signal region. The large Top contributions to the final selection also suggest to develop completely data-driven Top estimates. This could not been realized within this work.

A more effective choice in cuts could also extend the sensitivity. For that, either more SUSY sensitive variables could be considered or more sophisticated techniques could be used to derive the optimal cuts on them. The inclusion of all correlations among the variables and the systematic uncertainties for each set of cuts might lead to a better sensitivity. The latter would demand for a full set of systematic uncertainties for all cut combinations. Since systematics are estimated from modified MC samples, this was technically unfeasible.

In addition, this optimization might tend to peculiar cuts, where certain systematics vanish due to insufficient MC statistics in the kinematic vicinity of the cuts. If the available MC events are too sparsely populated to resolve the expected deviations from the uncertainty, no change in selected events would be seen. These cuts would be preferred since background uncertainties are considered as very small and hence sensitivity is overestimated. In this respect, preference is given to reliability rather than to sensitivity. Similar techniques have been tried, but are not used for the final result.

Possible refinements in the choice of cuts could be done with respect to signal phenomenology. So far, a single set of cuts has been tuned to have good performance in the whole grid. Since SUSY appearance might change with the parameters Λ and $\tan\beta$, different regions might have different topologies and hence favor different cuts. This could be considered by different signal regions for different parameter regions.

An obvious division would be the separation in different Λ regions. This parameter governs the mass scale of the SUSY model and hence the kinematic distributions, i.e. higher mass points prefer harder cuts, see Figure 5.4 (p. 100). Unfortunately, the chosen cut of $m_{\text{eff.}} > 1000\,\text{GeV}$ is already at the upper limit with respect to sufficient background MC. Hence, no further increase without additional background information is possible. However, the lower Λ regions might be excluded with higher confidence level (i.e. even more below $p < 0.05$) for looser effective mass cuts.

Another interesting feature of the high Λ region is the change in the SUSY production processes. The cross section for any primary SUSY process depends on the coupling strength and the masses of the produced SUSY particles. At a proton collider, strong interactions dominate, but gluino and squark masses increase with Λ. Figure 6.2(A) and (B) give the gluino and light up squark mass in the used GMSB grid, respectively. The masses enter the TeV range above $\Lambda > 50\,\text{TeV}$ and hence production is kinematically suppressed by the required energy threshold to produce SUSY particles.

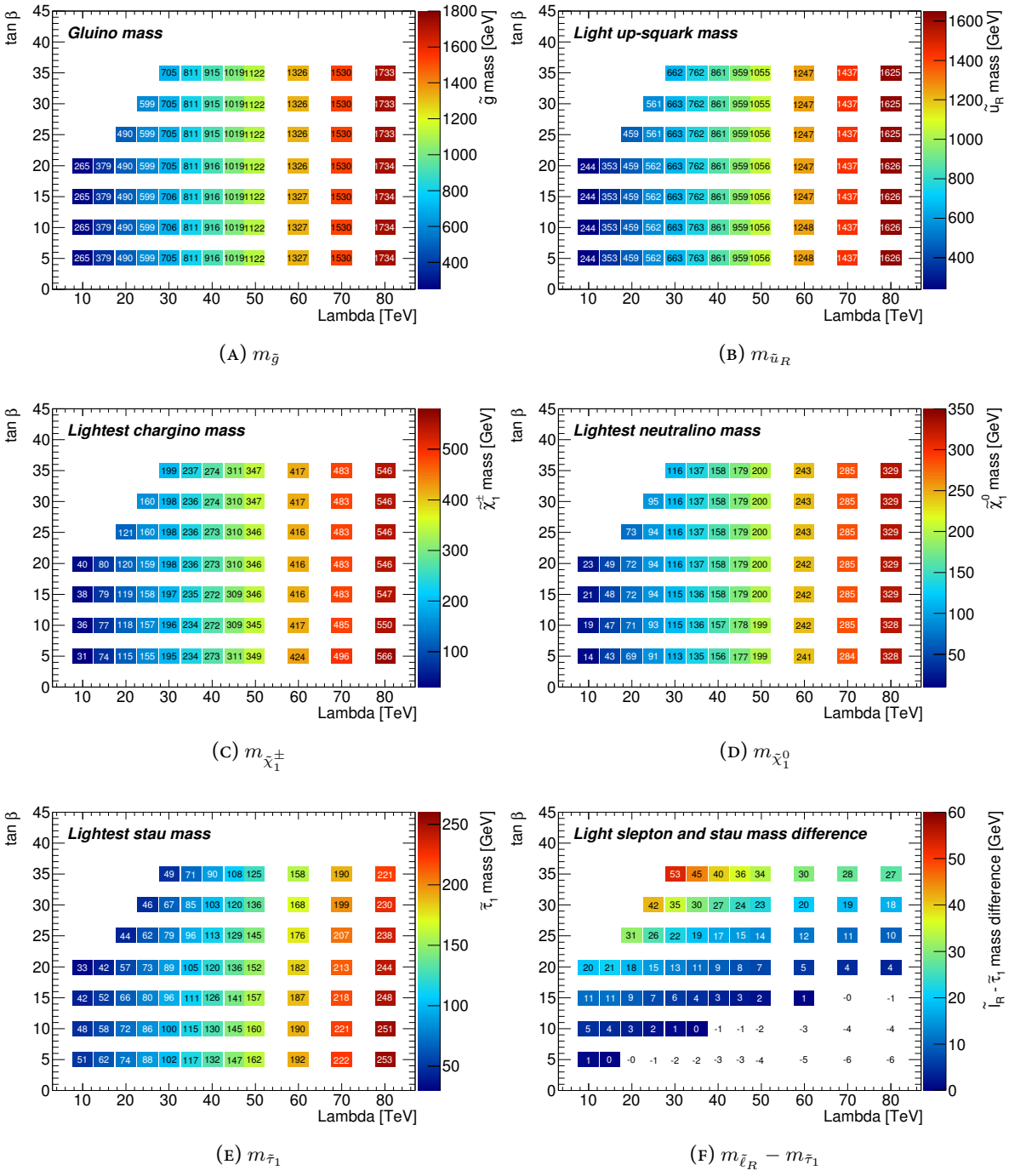

(A) $m_{\tilde{g}}$ (B) $m_{\tilde{u}_R}$

(C) $m_{\tilde{\chi}_1^\pm}$ (D) $m_{\tilde{\chi}_1^0}$

(E) $m_{\tilde{\tau}_1}$ (F) $m_{\tilde{\ell}_R} - m_{\tilde{\tau}_1}$

Figure 6.2 The masses of (A) the gluino, (B) the lighter up-squark, (C) the lightest chargino, (D) the lightest neutralino and (E) the lighter stau. (F): the mass difference of the lighter stau and slepton.

The electroweak gauginos still have masses sufficiently below the TeV range, see Figure 6.2(c) and (d). This can be explained by Equations 2.43 or 2.44 (p. 19). The expected mass ratio for gluino, wino and bino mass is clearly visible in the figures. Since the gluino and squark masses exceed the other SUSY masses considerably, electroweak production might account for a bigger relative contribution to the total SUSY production at very high Λ.

However, the detection of electroweak SUSY production demands for different search strategies. Especially the pattern of hadronic activity, i.e. hard jets, cannot be expected to appear any longer and other selection cuts have to be considered. For electroweak production, Top events could now be suppressed by a veto on (b-)jets. A preliminary study showed that W+jets is the most challenging background. Here, the muon comes from the W decay and the tau is faked. For strong production, these events could be sufficiently suppressed by the high effective mass requirements. This is not any longer possible for electroweak production.

In any case, an extension of the analysis towards direct electroweak gaugino production might increase the sensitivity, especially for the high Λ region. In these events, taus will also play an important role since the stau is kinematically accessible in $\widetilde{\chi}_1^\pm$ and $\widetilde{\chi}_1^0$ decays. The mass of the lighter stau can be seen in Figure 6.2(e). The larger $\widetilde{\tau}_L$ component in $\widetilde{\tau}_1$ would also lead to preferred decays of a wino-like $\widetilde{\chi}_1^\pm$ or $\widetilde{\chi}_2^0$ into staus. Nevertheless, for small $\tan\beta$ at high Λ, the selectron and smuon masses are smaller, see Figure 6.2(f). Hence, final states with only light leptons might be more sensitive. However, this final state is covered by the di-lepton search and hence not targeted within this analysis.

6.3 Prospects with 8 TeV Data

After the shutdown period of the LHC, its center-of-mass energy is increased from 7 TeV to 8 TeV with restarting operation. The new recorded data with higher energy and higher integrated luminosity of $20.7\,\text{fb}^{-1}$ are not included in this analysis, but some prospects on expected improvement can be made. In principle, there are two changes in the experimental conditions of the LHC with respect to the presented analysis: A higher integrated luminosity that gives more available data and a higher energy in the collisions. The increase in center-of-mass energy leads to higher cross sections for signal and background.

The expected events are given by

$$N = \sigma(E) \int \mathcal{L}\, \mathrm{d}t = \sigma(E) L\,. \tag{6.5}$$

If the analysis sensitivity is quantified by the significance

$$s = \frac{N_\text{SUSY}}{\sqrt{N_\text{SM}}}\,, \tag{6.6}$$

the proportionality of event yield to integrated luminosity and cross section of Equation 6.5 leads to an expected improvement of

$$s' = \frac{\frac{\sigma^{8\,\text{TeV}}_\text{SUSY} L'}{\sigma^{7\,\text{TeV}}_\text{SUSY} L}}{\sqrt{\frac{\sigma^{8\,\text{TeV}}_\text{SM} L'}{\sigma^{7\,\text{TeV}}_\text{SM} L}}} s = \sqrt{\frac{L'}{L}} \frac{\frac{\sigma^{8\,\text{TeV}}_\text{SUSY}}{\sigma^{7\,\text{TeV}}_\text{SUSY}}}{\sqrt{\frac{\sigma^{8\,\text{TeV}}_\text{SM}}{\sigma^{7\,\text{TeV}}_\text{SM}}}} s\,. \tag{6.7}$$

Process	σ at 7 TeV [pb]	σ at 8 TeV [pb]	ratio
$t\bar{t}$	166.8	238.06	1.43
$W \to \mu\nu_\mu + 0$ jets	8287	9535	1.15
$W \to \mu\nu_\mu + 1$ jets	1560	1874	1.2
$W \to \mu\nu_\mu + 2$ jets	452	567	1.25
$W \to \mu\nu_\mu + 3$ jets	122	159	1.3
$W \to \mu\nu_\mu + 4$ jets	31	42	1.35
$W \to \mu\nu_\mu + 5$ jets	8.4	12.6	1.5
$Z \to \tau\tau + 0$ jets	829	876	1.06
$Z \to \tau\tau + 1$ jets	167	190	1.14
$Z \to \tau\tau + 2$ jets	51	60	1.18
$Z \to \tau\tau + 3$ jets	14	17	1.21
$Z \to \tau\tau + 4$ jets	3.5	4.6	1.31
$Z \to \tau\tau + 5$ jets	0.95	1.37	1.44
$W^\pm W^\mp \to \ell\nu_\ell \ell'\nu_{\ell'}$	4.59	5.8	1.26

Table 6.2 Comparison of 7 TeV and 8 TeV SM cross sections.

The gain from higher luminosity and cross section can hence be factorized and will be considered independently. For the integrated luminosity, the profit in sensitivity is simply

$$\sqrt{\frac{20.7\,\text{fb}^{-1}}{4.7\,\text{fb}^{-1}}} \approx 2.1\,. \tag{6.8}$$

The influence from the changing cross sections is more involved. The differential SM cross section for events that appear in the kinematic phase space of the signal region is hard to evaluate. Assuming the same relative abundance in the signal region for 7 TeV and 8 TeV cross sections, the total cross sections can be compared.

Table 6.2 gives 7 TeV and 8 TeV cross sections for the most important SM backgrounds. The W+jets and Z^0+jets backgrounds increase more for higher jet multiplicities. The high jet multiplicities will also dominate in the final event selection due to the hard effective mass cut. As a rough estimate, a background composition of 50 %, 35 % and 15 % for Top, W+jets and di-bosons is assumed. This roughly reflects the background composition of the SR, see Table 5.4 (p. 120). The average increase of the SM cross section is then

$$\frac{\sigma_{\text{SM}}^{8\text{ TeV}}}{\sigma_{\text{SM}}^{7\text{ TeV}}} = 0.5 \cdot 1.43 + 0.35 \cdot 1.35 + 0.15 \cdot 1.26 = 1.377\,. \tag{6.9}$$

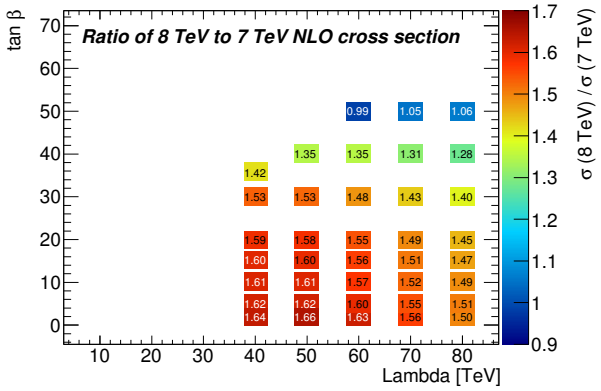

Figure 6.3 The ratio of 8 TeV *to* 7 TeV *cross sections in the GMSB parameter plane.*

The di-bosons background is assumed to be completely WW dominated and for W+jets the ratio from four additional jets is taken. Using Equations 6.8 and 6.9 in Equation 6.7 gives

$$s' = 1.79 \frac{\sigma^{8\,\text{TeV}}_{\text{SUSY}}}{\sigma^{7\,\text{TeV}}_{\text{SUSY}}} s \,, \tag{6.10}$$

and hence the increased available luminosity already compensates for the increased background cross sections. The final gain also depends on the increase of signal cross section. Figure 6.3 shows the ratio of 8 TeV to 7 TeV cross section. The plot shows the ratio of the summed NLO cross sections for the different initially produced SUSY particles, e.g. gluino-gluino, squark-gluino, squark-squark, etc. The nominator and denominator both include production of gluinos, first to third generation squark pairs, electroweak and mixed strong and electroweak production. There are only limited grid points with available NLO cross sections for 7 and 8 TeV: The 8 TeV grid is designed to reach higher SUSY masses that are beyond the 7 TeV grid. Moreover, the lower Λ are already excluded and hence not realized in the 8 TeV grid.

Likewise for the background cross sections, these are the ratios of total cross sections. They do not show the differential change of the cross section for the appearance of events in the signal region. E.g. the analysis aims at strong SUSY production, but the ratio also includes electroweak production. If electroweak production should increase less than strong production for the higher center-of-mass energy, still the enhancement in the signal region, dominated by strong production, could be larger.

Assuming an average increase of signal cross section of 1.5, Equation 6.10 leads to

$$s \approx 2.69 s \,. \tag{6.11}$$

The dominant contribution comes from the increased luminosity, see Equation 6.8, whereas the rising signal cross section play only a smaller role. Since SM cross section ratios enter only via the square root, they attenuate the sensitivity only moderately by $\sqrt{1.377} \approx 1.17$, see Equations 6.9 and 6.7.

The simple argumentation is based on the significance from Equation 6.6, which ignores systematic uncertainties. Furthermore, it assumes the same signal regions for 7 TeV and 8 TeV analyses. For higher energies and available statistics, there might be more suitable harder cuts and the gain in sensitivity might be even better. In that sense, Equation 6.11 is a conservative estimate and the sensitivity with 8 TeV data will be investigated in the corresponding analyses.

Chapter 7

Summary

SUSY is an interesting and well motivated extension of the SM that explains a wide range of phenomena that are inexplicable within the SM. Thus, the search for any evidence of its existence in Nature is one of the foremost ventures in the scientific program of the LHC experiments. The unprecedented center-of-mass energy of 7 TeV and high luminosity make the LHC to the leading experimental environment to produce potentially existing SUSY particles.

A promising approach to discover SUSY particles is the direct detection of their visible decay products with the ATLAS experiment. At the LHC, the search for missing transverse momentum, jets and leptons can be shown to be a well detectable signature with high sensitivity to SUSY. In many SUSY models, tau leptons occur preferably and hence this thesis presented a search for SUSY with multiple tau leptons, jets and missing transverse energy. This final state is realized in GMSB that is specified by the parameters

$$N_5 = 3 \qquad \operatorname{sgn}\mu = +1 \qquad C_{\tilde{G}} = 1 \qquad \langle S \rangle = 250\,\text{TeV}\,. \tag{7.1}$$

The remaining parameters Λ and $\tan\beta$ have been varied in nearly 100 combinations in the range of

$$\tan\beta = 2 \ldots 70 \tag{7.2}$$

$$\Lambda = 10\,\text{TeV} \ldots 80\,\text{TeV}\,. \tag{7.3}$$

Final states with tau leptons come along with the complicated experimental task of tau lepton reconstruction, which tries to identify hadronically decaying tau leptons. The performance of this tau lepton reconstruction could be shown to be among the leading challenges in searches for SUSY with taus. Especially, the sizable misidentification rate for objects of non-tau origin in the involved experimental environment of the ATLAS experiment complicates a precise and reliable background prediction.

This problem was tackled by the extension of the analysis to taus where one of them decays into a muon. Muons can be shown to have marginal misidentification rates and high identification efficiency. In this context, the muon could be shown to be a beneficial object for tau identification performance studies and for the suppression and accurate estimation of backgrounds. Furthermore, this final state bridged the gap between the pure hadronic di-tau analysis and the pure light lepton final states of the di-lepton analysis. It also allowed for a statistical combination with the other SUSY tau searches that veto on muons.

The SM backgrounds are divided into W+jets, Z^0+jets, Top, di-bosons, QCD and Drell-Yan. Their contributions to the SUSY search are estimated by Monte-Carlo (MC) simulation techniques. Whenever necessary, these estimates are replaced, corrected or confirmed by data-driven approaches. W+jets and Top could be shown to have the largest impact on the final event selection. Their contributions are predicted from corrected Monte-Carlo simulations that are rescaled by data-driven scalings. QCD is estimated completely data-driven. The modelling of the Z^0+jets MC could be confirmed in dedicated control regions and Drell-Yan has been conservatively estimated by the assumption of identical behaviour to Z^0+jets. Based on the obtained information from all other backgrounds, no feature of the di-bosons MC could be seen that could give doubt about its correct modelling.

The background studies consistently demonstrated the correct description of truth tau leptons in the MC simulation. The contributions from misidentified taus, which are non-tau jets, could be shown to require correction. The beneficial reconstruction characteristics of the muon could be used to isolate the tau identification performance as the origin of the mismodelling.

The final search patterns have been optimized for maximal discrimination between expected SM and GMSB contributions. For that, the signal has been represented by six benchmarks from the grid given above. The considered analysis parameters that have been optimized are the strictness of the tau identification and additional cuts on SUSY sensitive variables, i.e. $E_{\mathrm{T}}^{\mathrm{miss.}}$, $m_{\mathrm{eff.}}$, H_{T} and $E_{\mathrm{T}}^{\mathrm{miss.}}/m_{\mathrm{eff.}}$. The performance of different cut combinations has been tested with the Asimov value, where special attention was paid to remaining background statistics for a reliable estimate. The optimal sensitivity for GMSB was obtained with BDT medium taus in the object selection

$$N_{\mathrm{jet}}^{50\,\mathrm{GeV}} \geq 1 \qquad N_{\mu}^{20\,\mathrm{GeV}} = 1 \qquad N_{\tau,\,\mathrm{medium}}^{20\,\mathrm{GeV}} \geq 1\,. \tag{7.4}$$

The final kinematic cuts are

$$m_{\mathrm{T}}^{\mu} > 100\,\mathrm{GeV} \qquad \text{and} \qquad m_{\mathrm{eff.}} > 1000\,\mathrm{GeV}\,, \tag{7.5}$$

which leave an expected SM background of

$$N^{\mathrm{SM}} = 0.80 \pm 0.28^{\mathrm{MC\ stat.}} \pm 0.275^{\mathrm{syst.}}\,. \tag{7.6}$$

The systematic uncertainty includes object related contributions, i.e. from the trigger, taus, the muon, jets, b-tags and $E_{\mathrm{T}}^{\mathrm{miss.}}$. Furthermore, it contains event based uncertainties that come from pile-up conditions, generator modelling and the used data-driven techniques. The final observation of a single data event is consistent with the SM expectation, although it could be seen to have a unexpectedly high effective mass. The event has been scrutinized in detail and no suspicious patterns could be seen.

The agreement of observation and expectation was used to set limits on the considered GMSB signal grid. A grid point has been considered as excluded if the probability to observe one or less events is below 0.05 under the assumption of the background and signal hypothesis. For that, the p-value was quantified in a statistical model that uses a logarithmic likelihood ratio as test statistic. The exclusion limit of the presented analysis covered a $\tan\beta$ dependent region up to approximately 45 TeV for Λ. The combination with the di-tau, one-tau and tau and electron analysis extended the limit up to 50 TeV to 55 TeV. At the time of publication, this has been the most stringent test of a large part of the considered GMSB SUSY parameter space.

The limit on Λ could be translated into limits on the gluino and the squark masses of

$$m_{\tilde{g}} \gtrsim 1.2\,\mathrm{TeV}\,, \qquad m_{(\tilde{u},\tilde{d})_R} \gtrsim 1.1\,\mathrm{TeV} \qquad \text{and} \qquad m_{\tilde{t}_1} \gtrsim 1\,\mathrm{TeV}\,. \tag{7.7}$$

They are at the boundary to SUSY models that do not longer inherently solve the hierarchy problem or give the correct prediction for the electroweak mixing angle. In that sense, the considered GMSB model could not be seen to match the requirements of a candidate for a natural extension of the SM. This is also supported by the discovery of a Higgs-like particle with a mass of about 125 GeV.

Appendix A

Auxiliary Tables

This appendix gives all auxiliary tables and summarizes the Monte-Carlo data sets used for the analysis. For some samples, two sets from different generators have been used in order to perform cross checks and systematic studies. The explanation of the other tables' contents are given where they are referenced in the text.

ID No.	Name	Generator	LO [pb]	k-factor	NLO [pb]	events
107680	WenuNp0	AlpgenJimmy	6930.5	1.196	8288.88	3 458 883
107681	WenuNp1	AlpgenJimmy	1305.3	1.196	1561.14	2 499 645
107682	WenuNp2	AlpgenJimmy	378.13	1.196	452.24	3 768 632
107683	WenuNp3	AlpgenJimmy	101.86	1.196	121.82	1 008 947
107684	WenuNp4	AlpgenJimmy	25.68	1.196	30.71	250 000
107685	WenuNp5	AlpgenJimmy	6.99	1.196	8.36	69 999
144022	WenuNp6_pt20	AlpgenJimmy	1.55	1.196	1.85	145 000
107690	WmunuNp0	AlpgenJimmy	6932.4	1.195	8284.22	3 462 942
107691	WmunuNp1	AlpgenJimmy	1305.9	1.195	1560.55	2 498 593
107692	WmunuNp2	AlpgenJimmy	378.07	1.195	451.79	3 768 737
107693	WmunuNp3	AlpgenJimmy	101.85	1.195	121.71	1 008 446
107694	WmunuNp4	AlpgenJimmy	25.72	1.195	30.74	254 950
107695	WmunuNp5	AlpgenJimmy	7	1.195	8.37	70 000
144023	WmunuNp6_pt20	AlpgenJimmy	1.55	1.195	1.85	145 000
107700	WtaunuNp0	AlpgenJimmy	6931.8	1.195	8283.50	3 418 296
107701	WtaunuNp1	AlpgenJimmy	1304.9	1.195	1559.36	2 499 194
107702	WtaunuNp2	AlpgenJimmy	377.93	1.195	451.63	3 750 986
107703	WtaunuNp3	AlpgenJimmy	101.96	1.195	121.84	1 009 946
107704	WtaunuNp4	AlpgenJimmy	25.71	1.195	30.72	249 998
107705	WtaunuNp5	AlpgenJimmy	7	1.195	8.37	65 000
144024	WtaunuNp6_pt20	AlpgenJimmy	1.55	1.195	1.85	150 000

Table A.1 Used W+jets Monte-Carlo samples with their ID number, used event generator, LO cross section, k-factor, NLO cross section and number of generated events. Applying the k-factor yields the NLO cross sections.

ID No.	Name	Generator	LO [pb]	k-factor	NLO [pb]	events
116250	ZeeNp0Mll10to40	AlpgenJimmy	3054.7	1.243	3798.37	994 949
116251	ZeeNp1Mll10to40	AlpgenJimmy	84.91	1.243	105.58	299 998
116252	ZeeNp2Mll10to40	AlpgenJimmy	41.19	1.243	51.22	999 946
116253	ZeeNp3Mll10to40	AlpgenJimmy	8.35	1.243	10.38	149 998
116254	ZeeNp4Mll10to40	AlpgenJimmy	1.85	1.243	2.30	40 000
116255	ZeeNp5Mll10to40	AlpgenJimmy	0.46	1.243	0.57	10 000
116260	ZmumuNp0Mll10to40	AlpgenJimmy	3054.9	1.243	3798.62	999 849
116261	ZmumuNp1Mll10to40	AlpgenJimmy	84.78	1.243	105.42	300 000
116262	ZmumuNp2Mll10to40	AlpgenJimmy	41.13	1.243	51.14	999 995
116263	ZmumuNp3Mll10to40	AlpgenJimmy	8.34	1.243	10.37	150 000
116264	ZmumuNp4Mll10to40	AlpgenJimmy	1.87	1.243	2.33	39 999
116265	ZmumuNp5Mll10to40	AlpgenJimmy	0.46	1.243	0.57	10 000
116270	ZtautauNp0Mll10to40	AlpgenJimmy	3054.8	1.243	3798.49	999 649
116271	ZtautauNp1Mll10to40	AlpgenJimmy	84.88	1.243	105.54	299 999
116272	ZtautauNp2Mll10to40	AlpgenJimmy	41.28	1.243	51.33	498 899
116273	ZtautauNp3Mll10to40	AlpgenJimmy	8.35	1.243	10.38	150 000
116274	ZtautauNp4Mll10to40	AlpgenJimmy	1.83	1.243	2.28	39 999
116275	ZtautauNp5Mll10to40	AlpgenJimmy	0.46	1.243	0.57	10 000

Table A.2 Used Drell-Yan Monte-Carlo samples with their corresponding ID number, used event generator, LO cross section, k-factor, NLO cross section and number of generated events. Applying the k-factor yields the NLO cross sections.

ID No.	Name	Generator	NLO [pb]	k-factor	NNLO [pb]	events
105200	$t\bar{t}$ semileptonic (T1)	MCAtNLOJimmy	79.01	1.146	90.57	14 983 835
105204	$t\bar{t}$ full hadronic	MCAtNLOJimmy	66.48	1.146	76.23	1 199 034
117360	t-channel $t \to e\nu$	AcerMCPythia	8.06	0.865	6.97	999 295
117361	t-channel $t \to \mu\nu$	AcerMCPythia	8.06	0.865	6.97	999 948
117362	t-channel $t \to \tau\nu$	AcerMCPythia	8.05	0.855	6.97	998 995
108343	s-channel $t \to e\nu$	MCAtNLOJimmy	0.47	1.064	0.50	299 948
108344	s-channel $t \to \mu\nu$	MCAtNLOJimmy	0.47	1.064	0.50	299 998
108345	s-channel $t \to \tau\nu$	MCAtNLOJimmy	0.47	1.064	0.50	299 899
108346	single top Wt	MCAtNLOJimmy	14.79	1.064	15.74	899 694

Table A.3 Used Top ($t\bar{t}$ and single top) Monte-Carlo samples with their ID number, used event generator, NLO cross section and number of generated events. Applying the k-factor yields the NNLO cross sections.

ID No.	Name	Generator	LO [pb]	k-factor	NLO [pb]	events
105890	ttbarlnlnNp0	AlpgenJimmy	3.466	1.69	5.86	194 499
105891	ttbarlnlnNp1	AlpgenJimmy	3.3987	1.69	5.74	159 999
105892	ttbarlnlnNp2	AlpgenJimmy	2.1238	1.69	3.59	336 897
117897	ttbarlnlnNp3	AlpgenJimmy	0.946 98	1.69	1.60	148 000
117898	ttbarlnlnNp4	AlpgenJimmy	0.334 09	1.69	0.56	60 000
117899	ttbarlnlnNp5	AlpgenJimmy	0.127 53	1.69	0.22	25 000
105894	ttbarlnqqNp0	AlpgenJimmy	13.764	1.77	24.36	647 396
105895	ttbarlnqqNp1	AlpgenJimmy	13.608	1.77	24.09	652 997
105896	ttbarlnqqNp2	AlpgenJimmy	8.4181	1.77	14.90	1 145 892
117887	ttbarlnqqNp3	AlpgenJimmy	3.7759	1.77	6.68	652 495
117888	ttbarlnqqNp4	AlpgenJimmy	1.3361	1.77	2.36	118 999
117889	ttbarlnqqNp5	AlpgenJimmy	0.503 99	1.77	0.89	79 997

Table A.4 Additional $t\bar{t}$ samples with their ID number, used event generator, LO cross section and number of generated events. Applying the k-factor yields the NLO cross sections. These samples are used for systematic studies only.

ID No.	Generator	Process	NLO [pb]	events
125950	Sherpa	Ztoee2JetsEW2JetsQCD15GeVM40	0.447 02	199 999
125951	Sherpa	Ztomm2JetsEW2JetsQCD15GeVM40	0.445 85	181 200
125952	Sherpa	Ztott2JetsEW2JetsQCD15GeVM40	0.444 45	199 899
125956	Sherpa	Ztoee2JetsEW2JetsQCD15GeVM07to40	0.477 27	100 000
125957	Sherpa	Ztomm2JetsEW2JetsQCD15GeVM07to40	0.477 12	100 000
125958	Sherpa	Ztott2JetsEW2JetsQCD15GeVM07to40	0.469 24	99 900
128810	Sherpa	WWlnulnu	2.9832	1 999 697
128811	Sherpa	WZlllnu	0.361 64	299 950
128812	Sherpa	WZlllnuLowMass	1.0209	299 949
128813	Sherpa	ZZllll	0.266 22	100 000
128814	Sherpa	ZZllnn	0.238 38	349 900
143062	Sherpa	WZlnnn	0.718 68	100 000
143063	Sherpa	WZqqnn	1.4249	99 900
143064	Sherpa	Wtolnu2JetsEW1JetQCD	24.537	99 900
143065	Sherpa	Ztonunu2JetsEW1JetQCD	1.3368	99 999

Table A.5 Used alternative di-bosons MC samples for validation and systematics studies with their corresponding ID number, used event generator, NLO cross section and number of generated events.

ID No.	Generator	Process	NLO [pb]	events
105921	McAtNlo_JIMMY	$W^+W^- \to e\nu e\nu$	0.51	199 949
105922	McAtNlo_JIMMY	$W^+W^- \to e\nu\mu\nu$	0.51	200 000
105923	McAtNlo_JIMMY	$W^+W^- \to e\nu\tau\nu$	0.51	200 000
105924	McAtNlo_JIMMY	$W^+W^- \to \mu\nu\mu\nu$	0.51	199 000
105925	McAtNlo_JIMMY	$W^+W^- \to \mu\nu e\nu$	0.51	199 949
105926	McAtNlo_JIMMY	$W^+W^- \to \mu\nu\tau\nu$	0.51	200 000
105927	McAtNlo_JIMMY	$W^+W^- \to \tau\nu\tau\nu$	0.51	499 676
105928	McAtNlo_JIMMY	$W^+W^- \to \tau\nu e\nu$	0.51	199 950
105929	McAtNlo_JIMMY	$W^+W^- \to \tau\nu\mu\nu$	0.51	200 000
105930	McAtNlo_JIMMY	$Z^0Z^0 \to \ell\ell q\bar{q}$	0.270	25 000
105931	McAtNlo_JIMMY	$Z^0Z^0 \to \ell\ell\ell\ell$	0.026	99 999
105932	McAtNlo_JIMMY	$Z^0Z^0 \to \ell\ell\nu\nu$	0.077	99 999
106036	McAtNlo_JIMMY	$Z^0Z^0 \to 2\ell 2\tau$	1.695	25 000
106037	McAtNlo_JIMMY	$Z^0Z^0 \to 4\tau$	0.164	25 000
113192	McAtNlo_JIMMY	$Z^0Z^0 \to \tau\tau\nu\nu$	0.514	24 950
113193	McAtNlo_JIMMY	$Z^0Z^0 \to \tau\tau q\bar{q}$	0.928	25 000
105940	McAtNlo_JIMMY	$W^+Z^0 \to \ell\nu q\bar{q}$	0.090	100 000
105941	McAtNlo_JIMMY	$W^+Z^0 \to \ell\nu\ell\ell$	0.28	100 000
105942	McAtNlo_JIMMY	$W^+Z^0 \to q\bar{q}'\ell\ell$	0.086	25 000
106024	McAtNlo_JIMMY	$W^+Z^0 \to \tau\nu\ell\ell$	0.082	25 000
106025	McAtNlo_JIMMY	$W^+Z^0 \to \ell\nu\tau\tau$	0.043	199 950
106026	McAtNlo_JIMMY	$W^+Z^0 \to \tau\nu\tau\tau$	0.047	25 000
113190	McAtNlo_JIMMY	$W^+Z^0 \to q\bar{q}'\tau\tau$	0.045	25 000
105970	McAtNlo_JIMMY	$W^-Z^0 \to \ell\nu q\bar{q}$	0.0234	200 000
105971	McAtNlo_JIMMY	$W^-Z^0 \to \ell\nu\ell\ell$	0.0129	25 000
105972	McAtNlo_JIMMY	$W^-Z^0 \to q\bar{q}'\ell\ell$	0.0065	25 000
106027	McAtNlo_JIMMY	$W^-Z^0 \to \tau\nu\ell\ell$	0.2568	199 949
106028	McAtNlo_JIMMY	$W^-Z^0 \to \ell\nu\tau\tau$	0.1397	200 000
106029	McAtNlo_JIMMY	$W^-Z^0 \to \tau\nu\tau\tau$	0.0386	200 000
113191	McAtNlo_JIMMY	$W^-Z^0 \to q\bar{q}'\tau\tau$	0.1348	199 950

Table A.6 Used di-bosons Monte-Carlo samples with their corresponding ID number, used event generator, NLO cross section and number of generated events.

ID No.	Name	Generator	LO [pb]	k-factor	NLO [pb]	events
107650	ZeeNp0	AlpgenJimmy	669.6	1.243	832.61	6 618 284
107651	ZeeNp1	AlpgenJimmy	134.55	1.243	167.31	1 334 897
107652	ZeeNp2	AlpgenJimmy	40.65	1.243	50.55	2 004 195
107653	ZeeNp3	AlpgenJimmy	11.26	1.243	14.00	549 949
107654	ZeeNp4	AlpgenJimmy	2.84	1.243	3.53	149 948
107655	ZeeNp5	AlpgenJimmy	0.76	1.243	0.95	50 000
107660	ZmumuNp0	AlpgenJimmy	669.6	1.243	832.61	6 615 230
107661	ZmumuNp1	AlpgenJimmy	134.55	1.243	167.31	1 334 296
107662	ZmumuNp2	AlpgenJimmy	40.65	1.243	50.55	1 999 941
107663	ZmumuNp3	AlpgenJimmy	11.26	1.243	14.00	549 896
107664	ZmumuNp4	AlpgenJimmy	2.84	1.243	3.53	150 000
107665	ZmumuNp5	AlpgenJimmy	0.76	1.243	0.95	50 000
107670	ZtautauNp0	AlpgenJimmy	669.6	1.243	832.61	10 613 179
107671	ZtautauNp1	AlpgenJimmy	134.55	1.243	167.31	3 334 137
107672	ZtautauNp2	AlpgenJimmy	40.65	1.243	50.55	1 004 847
107673	ZtautauNp3	AlpgenJimmy	11.26	1.243	14.00	509 847
107674	ZtautauNp4	AlpgenJimmy	2.84	1.243	3.53	144 999
107675	ZtautauNp5	AlpgenJimmy	0.76	1.243	0.95	45 000
107710	ZnunuNp0	AlpgenJimmy	3572	1.26	49.93	54 949
107711	ZnunuNp1	AlpgenJimmy	738.73	1.26	569.09	909 848
107712	ZnunuNp2	AlpgenJimmy	222.91	1.26	247.68	169 899
107713	ZnunuNp3	AlpgenJimmy	61.874	1.26	75.45	144 999
107714	ZnunuNp4	AlpgenJimmy	15.635	1.26	19.55	309 899
107715	ZnunuNp5	AlpgenJimmy	4.3094	1.26	5.42	189 998

Table A.7 Used Z^0+jets Monte-Carlo samples with their corresponding ID number, used event generator, LO cross section, k-factor, NLO cross section and number of generated events. Applying the k-factor yields the NLO cross sections.

ID No.	Name	Generator	LO [pb]	events
105009	J0	Pythia	12 030 000 000	999 997
105010	J1	Pythia	807 266 000	999 993
105011	J2	Pythia	48 048 000	999 999
105012	J3	Pythia	2 192 900	999 992
105013	J4	Pythia	87 701	989 992
105014	J5	Pythia	2350.1	999 987
105015	J6	Pythia	33.61	999 974
105016	J7	Pythia	0.137 44	998 955
105017	J8	Pythia	0.000 006	998 948

Table A.8 Used QCD Monte-Carlo samples with their corresponding ID number, used event generator, cross section and number of generated events.

Particle Identification Number Scheme for Monte-Carlo		
Particle	Symbol	Identification Number
down quark	d	1
up quark	u	2
strange quark	s	3
charm quark	c	4
bottom quark	b	5
top quark	t	6
electron	e^-	11
electron neutrino	ν_e	12
muon	μ^-	13
muon neutrino	ν_μ	14
tau	τ^-	15
tau neutrino	ν_τ	16
gluon	g	21
photon	γ	22
Z^0-boson	Z^0	23
W-boson	W	24

Table A.9 The numbering scheme of particles in the Monte-Carlo. The antiparticles have the corresponding negative number.

	2011 Data	DiBoson	Drell Yan	Z+Jets	Top	W+Jets	QCD (DD)	SM
GRL	229 373 908	44 253	55 194 030	19 350 596	950 153	145 489 056	–	221 028 089 ± 48 080
Trigger	137 185 828	12 546	231 819	1 766 665	174 229	10 880 125	–	13 065 385 ± 9616
cleaning cuts	134 553 518	12 298	228 107	1 694 491	173 287	10 300 801	–	12 408 984 ± 9261
$N_{\text{jet}}^{50\ \text{GeV}} \geq 1$	50 374 151	4997	41 470	248 992	153 694	1 377 472	–	1 826 625 ± 1583
$N_{\mu}^{20\ \text{GeV}} = 1$	2 437 754	2988	19 586	99 186	88 532	1 180 140	845 744	2 236 177 ± 209 662
$N_{\tau} \geq 1$	15 194	157	254	3637	2162	5716	2829	14 755 ± 784
$E_{\text{T}}^{\text{miss}} > 70$ GeV	2308	44.2	4.03	339	808	1161	21.7	2378 ± 44
$E_{\text{T}}^{\text{miss}} < 150$ GeV	2147	39.0	4.03	311	738	1106	21.7	2220 ± 42

Table A.10 The cutflow into the test control region. The Top and W+jets scalings are applied starting from the tau requirement. The good agreement shows that scalings have no bias to the b-tagging. QCD is estimated by the matrix method and hence can be evaluated only after the muon requirement. Taus are BDT medium.

	2011 Data	DiBoson	Drell Yan	Z+Jets	Top	W+Jets	QCD (DD)	SM
GRL	229 373 908	44 253	55 194 030	19 350 596	950 153	145 489 056	–	221 028 089 ± 48 080
Trigger	137 185 828	12 546	231 819	1 766 665	174 229	10 880 125	–	13 065 385 ± 9616
cleaning cuts	134 553 518	12 298	228 107	1 694 491	173 287	10 300 801	–	12 408 984 ± 9261
$N_{\text{jet}}^{50\text{ GeV}} \geq 1$	50 374 151	4997	41 470	248 992	153 694	1 377 472	–	1 826 625 ± 1583
$N_{\mu}^{20\text{ GeV}} = 1$	2 437 754	2988	19 586	99 186	88 532	1 180 140	845 744	2 236 177 ± 209 662
$N_{\tau} \geq 1$	24 705	210	402	4741	3304	10 230	5076	23 962 ± 1390
μ, τ opposite sign	17 596	165	230	4090	2706	7706	2736	17 633 ± 810
$m_{\text{T}}^{\mu} < 40$ GeV	8735	45.8	165	3334	606	1705	2505	8361 ± 618
$p_{\text{T}}^{\mu} > 30$ GeV	3909	32.2	82.0	1691	449	1274	375	3903 ± 202
$m_{(\tau,\mu)}^{\text{CL}} > 60$ GeV	2763	23.7	38.2	1311	312	868	240	2792 ± 139
$m_{(\tau,\mu)} < 90$ GeV	1277	8.61	11.5	926	114	187	86.2	1333 ± 51

Table A.11 The cutflow into the Z^0+jets control region. The Top and W+jets scalings are applied starting from the tau requirement. QCD is estimated by the matrix method and hence can be evaluated only after the muon requirement. Taus are BDT loose to ensure sufficient statistics in the control region.

% Deviation $^{b\text{ eff. up}}_{b\text{ eff. down}}$	DiBoson	Drell Yan	Z+Jets	Top	W+Jets	SM
$N_\tau \geq 1$	0 0	0 0	0 0	−5.18 6.15	1.6 −1.91	−0.15 0.17
$m_{\mathrm{T}}^{\mu} > 100$ GeV	0 0	0 0	0 0	−5.84 7	1.6 −1.91	−2.01 2.41
$m_{\mathrm{eff.}} > 400$ GeV	0 0	0 0	0 0	−5.85 7.02	1.6 −1.91	−3.75 4.5
$m_{\mathrm{eff.}} > 600$ GeV	0 0	0 0	0 0	−5.85 7.01	1.6 −1.91	−3.71 4.45
$m_{\mathrm{eff.}} > 800$ GeV	0 0	0 0	0 0	−5.84 6.99	1.6 −1.91	−2.86 3.43
$m_{\mathrm{eff.}} > 1000$ GeV	0 0	0 0	0 0	−5.83 6.97	1.6 −1.91	−3.45 4.13

Table A.12 The relative uncertainties on selected events due to uncertainties of the b-tagging efficiency at different cut stages.

% Deviation $^{b\text{ fake up}}_{b\text{ fake down}}$	DiBoson	Drell Yan	Z+Jets	Top	W+Jets	SM
$N_\tau \geq 1$	0 0	0 0	0 0	−0.46 0.46	0.17 −0.18	0 −0.01
$m_{\mathrm{T}}^{\mu} > 100$ GeV	0 0	0 0	0 0	0.26 −0.24	0.16 −0.18	0.19 −0.19
$m_{\mathrm{eff.}} > 400$ GeV	0 0	0 0	0 0	0.32 −0.3	0.16 −0.18	0.26 −0.25
$m_{\mathrm{eff.}} > 600$ GeV	0 0	0 0	0 0	0.29 −0.27	0.16 −0.18	0.24 −0.23
$m_{\mathrm{eff.}} > 800$ GeV	0 0	0 0	0 0	0.25 −0.23	0.16 −0.18	0.2 −0.19
$m_{\mathrm{eff.}} > 1000$ GeV	0 0	0 0	0 0	0.18 −0.17	0.16 −0.18	0.15 −0.14

Table A.13 The relative uncertainties on selected events due to uncertainties of the b-mistagging modelling at different cut stages.

% DiBoson generator	DiBoson	Drell Yan	Z+Jets	Top	W+Jets	SM
GRL	±273.46	0	0	0	0	±0.05
Trigger	±138.53	0	0	0	0	±0.13
cleaning cuts	±140.91	0	0	0	0	±0.14
$N_{\text{jet}}^{50\text{ GeV}} \geq 1$	±219.29	0	0	0	0	±0.57
$N_{\mu}^{20\text{ GeV}} = 1$	±313.68	0	0	0	0	±0.68
$N_{\tau} \geq 1$	±26.93	0	0	0	0	±0.26
$m_{\text{T}}^{\mu} > 100$ GeV	±11.68	0	0	0	±0.85	±0.04
$m_{\text{eff.}} > 400$ GeV	±5.94	0	0	0	±0.85	±0.03
$m_{\text{eff.}} > 600$ GeV	±19.52	0	0	0	±0.85	±1.03
$m_{\text{eff.}} > 800$ GeV	±15.38	0	0	0	±0.85	±1.56
$m_{\text{eff.}} > 1000$ GeV	±15.95	0	0	0	±0.85	±1.61

Table A.14 The relative uncertainties on selected events at different cut stages for the use of different di-bosons generators.

% Top generator	DiBoson	Drell Yan	Z+Jets	Top	W+Jets	SM
GRL	0	0	0	±0.14	0	0
Trigger	0	0	0	±1.54	0	±0.02
cleaning cuts	0	0	0	±1.51	0	±0.02
$N_{\text{jet}}^{50\text{ GeV}} \geq 1$	0	0	0	±2.72	0	±0.22
$N_{\mu}^{20\text{ GeV}} = 1$	0	0	0	±1.84	0	±0.12
$N_{\tau} \geq 1$	0	0	0	±7.21	0	±1.08
$m_{\text{T}}^{\mu} > 100$ GeV	0	0	0	±5.31	±0.96	±2.99
$m_{\text{eff.}} > 400$ GeV	0	0	0	±19.17	±0.96	±13.95
$m_{\text{eff.}} > 600$ GeV	0	0	0	±18.43	±0.96	±13.31
$m_{\text{eff.}} > 800$ GeV	0	0	0	±70.02	±0.96	±42.06
$m_{\text{eff.}} > 1000$ GeV	0	0	0	±81.84	±0.96	±55.22

Table A.15 The relative uncertainties on selected events at different cut stages due to the use of different Top generators.

% Deviation $^{\text{JES up}}_{\text{JES down}}$	DiBoson	Drell Yan	Z+Jets	Top	W+Jets	SM
cleaning cuts	0 0.02	0 0.03	0 0.03	−0.01 0.03	0 0.02	0 −0.07
$N_{\text{jet}}^{50\text{ GeV}} \geq 1$	5.79 −6.15	10.88 −10.32	9.07 −8.58	1.47 −1.67	8.69 −8.38	1.78 −3.21
$N_{\mu}^{20\text{ GeV}} = 1$	5.92 −6.14	12.13 −11.29	10.21 −10.44	1.56 −1.28	8.65 −7.93	14.47 −11.28
$N_{\tau} \geq 1$	2.74 −2.62	6.46 −5.49	4.32 −3.91	3.1 −3.85	0.73 −0.76	2.37 −2.38
$m_{\text{T}}^{\mu} > 100$ GeV	−0.04 3.02	−19.29 17.31	−1.33 8.1	5.11 −7.41	−6.87 12.94	−0.78 2.89
$m_{\text{eff.}} > 400$ GeV	4.13 −5.06	−36.21 0.04	−4.95 1.55	12.02 −11.76	−0.24 −1.77	8.1 −8.7
$m_{\text{eff.}} > 600$ GeV	−0.54 −13.45	97.57 0	−27.98 −3.98	11.29 −13.04	14.05 −2.28	10.41 −10.31
$m_{\text{eff.}} > 800$ GeV	0.6 −3.42	0 0	0 −33.24	12.94 −18.19	12.2 33.19	11.28 −1.39
$m_{\text{eff.}} > 1000$ GeV	0 −12.11	0 0	0 −100	−1.47 −38.84	−3.47 153.48	−1.6 −3.21

Table A.16 The relative uncertainties on selected events due to jet energy scale uncertainties at different cut stages.

% JER	DiBoson	Drell Yan	Z+Jets	Top	W+Jets	SM
cleaning cuts	±0.01	0	±0.01	±0.01	±1.26	±1.04
$N_{\text{jet}}^{50\text{ GeV}} \geq 1$	±0.4	±2.13	±1.34	±0.05	±5.25	±3.96
$N_{\mu}^{20\text{ GeV}} = 1$	±0.31	±2.71	±2.18	±0.59	±4.85	±4.28
$N_{\tau} \geq 1$	±1.22	±1.63	±0.31	±0.5	±0.05	±0.02
$m_{\text{T}}^{\mu} > 100$ GeV	±3.59	±33.72	±15.96	±1.89	±10.04	±4.28
$m_{\text{eff.}} > 400$ GeV	±12.22	±67.71	±8	±0.06	±7.22	±1.97
$m_{\text{eff.}} > 600$ GeV	±15.07	0	±23.49	±1.3	±3.17	±1.29
$m_{\text{eff.}} > 800$ GeV	±7.23	0	±81.33	±2.17	±31.48	±12.03
$m_{\text{eff.}} > 1000$ GeV	0	0	0	±9.02	±2.38	±5.66

Table A.17 The relative uncertainties on selected events at different cut stages due to jet energy resolution uncertainties.

% Deviation $^{\mu\text{ ID eff. up}}_{\mu\text{ ID eff. down}}$	DiBoson	Drell Yan	Z+Jets	Top	W+Jets	SM
$N_\tau \geq 1$	0.27 −0.27	0.26 −0.26	0.25 −0.25	−0.01 −0.01	−0.04 0.02	0.06 −0.07
$m_{\mathrm{T}}^{\mu} > 100$ GeV	0.3 −0.3	0.35 −0.35	0.32 −0.32	−0.02 0.04	−0.01 0	0.01 −0.01
$m_{\text{eff.}} > 400$ GeV	0.31 −0.31	0.32 −0.32	0.35 −0.35	−0.02 0.03	0.02 −0.03	0.02 −0.01
$m_{\text{eff.}} > 600$ GeV	0.35 −0.35	0.24 −0.24	0.34 −0.34	−0.01 0.02	0.03 −0.05	0.03 −0.03
$m_{\text{eff.}} > 800$ GeV	0.33 −0.33	0 0	0.34 −0.34	0.01 0.01	0.02 −0.04	0.05 −0.05
$m_{\text{eff.}} > 1000$ GeV	0.32 −0.32	0 0	0.4 −0.4	−0.01 0.02	0.06 −0.07	0.06 −0.06

Table A.18 The relative uncertainties on selected events at different cut stages due to potential mismodelling of the muon reconstruction efficiency.

% Deviation $^{\mu\text{ trigger eff. up}}_{\mu\text{ trigger eff. down}}$	DiBoson	Drell Yan	Z+Jets	Top	W+Jets	SM
$N_\tau \geq 1$	3.58 −3.49	2.77 −2.73	2.84 −2.8	−0.12 0.11	−0.22 0.2	0.82 −0.82
$m_{\mathrm{T}}^{\mu} > 100$ GeV	5.64 −5.41	7.28 −7	5.97 −5.71	−0.16 0.18	1.05 −1.09	0.94 −0.92
$m_{\text{eff.}} > 400$ GeV	8.38 −7.9	7.97 −7.57	10.86 −10.17	1.02 −1	5.72 −5.63	2.78 −2.7
$m_{\text{eff.}} > 600$ GeV	9.91 −9.29	4.8 −4.72	8.2 −7.68	2.87 −2.83	10.93 −10.73	5.13 −5.01
$m_{\text{eff.}} > 800$ GeV	9.81 −9.2	0 0	13.56 −12.62	4.24 −4.11	10.36 −10.1	6.88 −6.65
$m_{\text{eff.}} > 1000$ GeV	10.57 −9.91	0 0	34.23 −31.47	6.83 −6.58	29.94 −29.19	12.81 −12.31

Table A.19 The relative uncertainties on selected events at different cut stages due to uncertainties in the trigger efficiency modelling.

% Deviation p_{T}^{μ} ID up / p_{T}^{μ} ID down	DiBoson	Drell Yan	Z+Jets	Top	W+Jets	SM
$N_\tau \geq 1$	0.04 0.01	0 0	0 0.01	0.11 −0.1	−0.01 0.05	0.01 0.01
$m_{\mathrm{T}}^{\mu} > 100$ GeV	−0.02 0.04	0 0	1.81 0	0.46 −0.28	−0.25 0.26	0.21 −0.02
$m_{\mathrm{eff.}} > 400$ GeV	−0.27 0.08	0 0	1.12 0	0.48 −0.23	0.01 0.45	0.38 −0.06
$m_{\mathrm{eff.}} > 600$ GeV	−11.4 0	0 0	0 0	0.6 −0.18	0.01 0.05	−0.1 −0.12
$m_{\mathrm{eff.}} > 800$ GeV	0 0	0 0	0 0	0.41 0.7	0.01 0.05	0.24 0.42
$m_{\mathrm{eff.}} > 1000$ GeV	0 0	0 0	0 0	0.41 −0.26	0.01 0.05	0.27 −0.16

Table A.20 The relative uncertainties on selected events at different cut stages due to muon momentum smearing in the inner detector.

% Deviation p_{T}^{μ} MS up / p_{T}^{μ} MS down	DiBoson	Drell Yan	Z+Jets	Top	W+Jets	SM
$N_\tau \geq 1$	0.01 0	0.1 −0.11	0 0	−0.05 0.12	−0.01 0.08	−0.01 0.06
$m_{\mathrm{T}}^{\mu} > 100$ GeV	−0.14 0.07	0 −19.29	2.11 1.09	0.06 0.35	0.56 −0.11	0.39 0.15
$m_{\mathrm{eff.}} > 400$ GeV	0 0.33	0 −36.21	1.12 −1.44	0.28 0.41	0.93 −0.7	0.45 −0.08
$m_{\mathrm{eff.}} > 600$ GeV	−2.11 0	0 0	0 −9.36	0.04 0.4	−0.01 4.92	−0.07 0.94
$m_{\mathrm{eff.}} > 800$ GeV	0 0	0 0	0 0	−0.09 −0.77	−0.01 0.1	−0.06 −0.41
$m_{\mathrm{eff.}} > 1000$ GeV	0 0	0 0	0 0	5.05 0.36	−0.01 0.1	3.3 0.25

Table A.21 The relative uncertainties on selected events at different cut stages due to muon momentum smearing in the muon spectrometer.

% pile-up	DiBoson	Drell Yan	Z+Jets	Top	W+Jets	SM
GRL	0	0	0	0	0	0
Trigger	±0.38	±0.08	±0.6	±0.24	±0.65	±0.62
cleaning cuts	±0.36	±0.06	±0.57	±0.24	±0.6	±0.58
$N_{\text{jet}}^{50\text{ GeV}} \geq 1$	±0.04	±0.55	±0.19	±0.19	±0.17	±0.2
$N_{\mu}^{20\text{ GeV}} = 1$	±0.52	±0.37	±0.16	±0.09	±0.06	±0.07
$N_{\tau} \geq 1$	±0.18	±1.55	±1.11	±0.53	±0.01	±0.15
$m_{\text{T}}^{\mu} > 100$ GeV	±0.36	±7.86	±5.63	±0.42	±5.15	±2.69
$m_{\text{eff.}} > 300$ GeV	±1.57	±10.93	±6.16	±0.81	±4.99	±1.98
$m_{\text{eff.}} > 400$ GeV	±1.6	±7.01	±4.49	±1	±9.23	±2.78
$m_{\text{eff.}} > 500$ GeV	±8	±7.01	±5.52	±0.52	±13.41	±3.21
$m_{\text{eff.}} > 600$ GeV	±3.03	±6.75	±13.08	±1.57	±6.12	±3.02
$m_{\text{eff.}} > 700$ GeV	±4.52	0	±34.25	±3.07	±35.63	±10.9
$m_{\text{eff.}} > 800$ GeV	±7.93	0	±5.68	±12.35	±34.17	±17.83
$m_{\text{eff.}} > 900$ GeV	±1.69	0	±9.71	±36.23	±36.19	±32.42
$m_{\text{eff.}} > 1000$ GeV	±4.93	0	±9.71	±43.08	±10.02	±27.36

Table A.22 The relative uncertainties on selected events at different cut stages due to pile-up mismodelling.

% TID	DiBoson	Drell Yan	Z+Jets	Top	W+Jets	SM
$N_{\tau} \geq 1$	±6.01	±6.16	±6	±0.63	±0.73	±1.52
$m_{\text{T}}^{\mu} > 100$ GeV	±5.83	±5.78	±6.03	±0.63	±0.77	±0.08
$m_{\text{eff.}} > 400$ GeV	±5.3	±5.76	±5.97	±0.83	±1.08	±0.33
$m_{\text{eff.}} > 500$ GeV	±4.91	±5.76	±5.65	±1.11	±1.89	±0.6
$m_{\text{eff.}} > 600$ GeV	±3.42	±7.82	±5.74	±1.1	±2.29	±0.8
$m_{\text{eff.}} > 1000$ GeV	±5.8	0	±4.65	±4.64	±2.29	±3.64

Table A.23 The relative uncertainties on selected events at different cut stages for the tau identification efficiency uncertainties.

% Deviation $\frac{\text{ST reso. up}}{\text{ST reso. down}}$	DiBoson	Drell Yan	Z+Jets	Top	W+Jets	SM
$N_\tau \geq 1$	−0.04 −0.04	−0.09 −0.09	−0.03 −0.04	0.96 0.79	1.54 1.88	0.91 1.05
$m_{\mathrm{T}}^{\mu} > 100$ GeV	−0.05 −2.12	0 0	2.74 −0.3	−0.27 −0.07	1.47 0.66	0.68 0.17
$m_{\text{eff.}} > 400$ GeV	−1.97 −3.22	0 0	−0.03 −0.04	0.17 0.39	3.79 3.97	0.86 1.01
$m_{\text{eff.}} > 600$ GeV	−1.3 −12.71	0 0	−8.89 0	−0.51 −0.7	1.55 6.66	−0.44 0.34
$m_{\text{eff.}} > 800$ GeV	0 0	0 0	0 0	0.94 0.47	1.55 1.9	1.02 0.86
$m_{\text{eff.}} > 1000$ GeV	0 0	0 0	0 0	0.72 −10.88	1.55 1.9	0.76 −6.77

Table A.24 The relative uncertainties on selected events at different cut stages due to energy resolution uncertainties on the soft terms in $E_T^{miss.}$.

% Deviation $\frac{\text{ST scale up}}{\text{ST scale down}}$	DiBoson	Drell Yan	Z+Jets	Top	W+Jets	SM
$N_\tau \geq 1$	0 0	0 0	0 0	−0.29 0	−0.38 0.35	−0.24 0.17
$m_{\mathrm{T}}^{\mu} > 100$ GeV	0.17 −0.38	0 0	1.18 0.16	−0.89 −0.16	1.27 −1.2	0.22 −0.61
$m_{\text{eff.}} > 400$ GeV	−0.58 −0.27	0 0	0 −1.44	−1.06 −0.5	2.14 −0.39	−0.3 −0.51
$m_{\text{eff.}} > 600$ GeV	0 0	0 0	0 0	−1.96 0.05	−0.38 0.35	−1.44 0.11
$m_{\text{eff.}} > 800$ GeV	0 0	0 0	0 0	−4.28 1.15	−0.38 0.35	−2.58 0.77
$m_{\text{eff.}} > 1000$ GeV	0 0	0 0	0 0	−7.13 −5.53	−0.38 0.35	−4.74 −3.56

Table A.25 The relative uncertainties on selected events at different cut stages due to energy scale uncertainties on the soft terms in $E_T^{miss.}$.

Appendix B

Auxiliary Figures

This appendix gives all auxiliary plots that have not been shown in the corresponding sections. The explanations of the figure's content are given where they are referenced in the text.

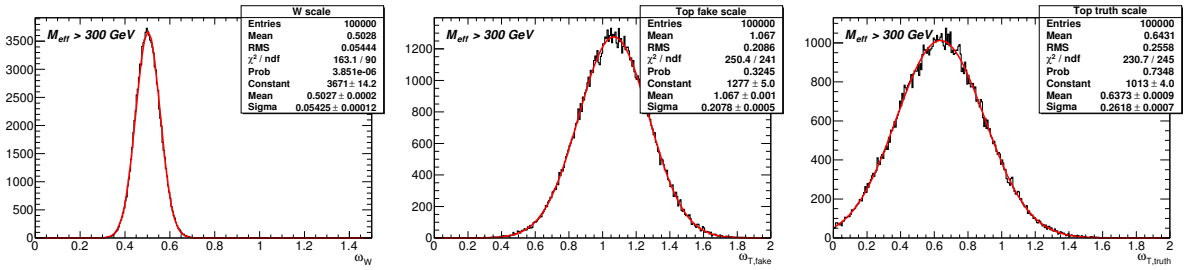

(A) W+jets scaling (B) Top with fake tau scaling (C) Top with truth tau scaling

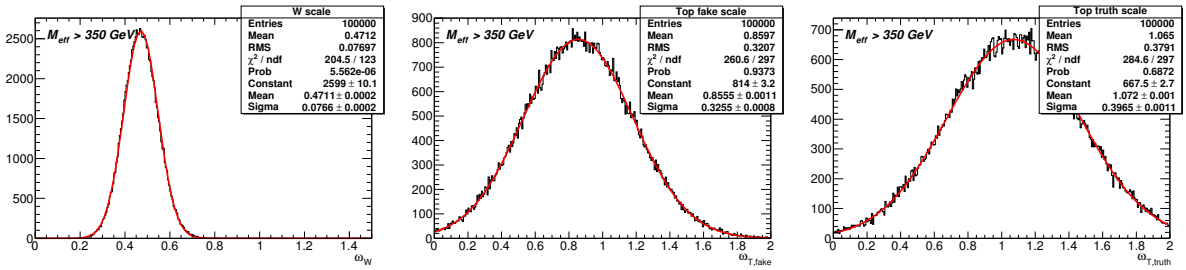

(D) W+jets scaling (E) Top with fake tau scaling (F) Top with truth tau scaling

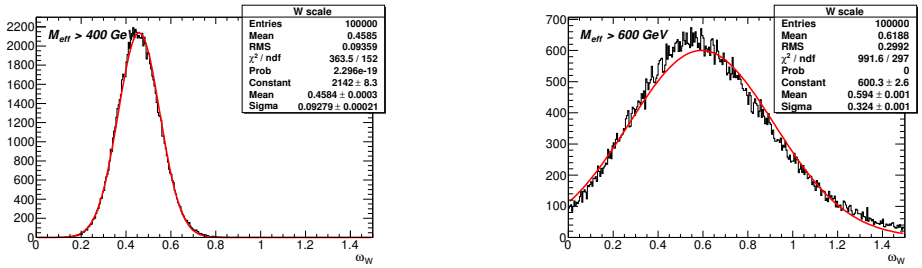

(G) W+jets scaling (H) W+jets scaling

Figure B.1 The obtained scalings for W+jets, Top with fake taus and Top with truth taus for different variations of kinematic selections. Scalings can be seen to be robust.

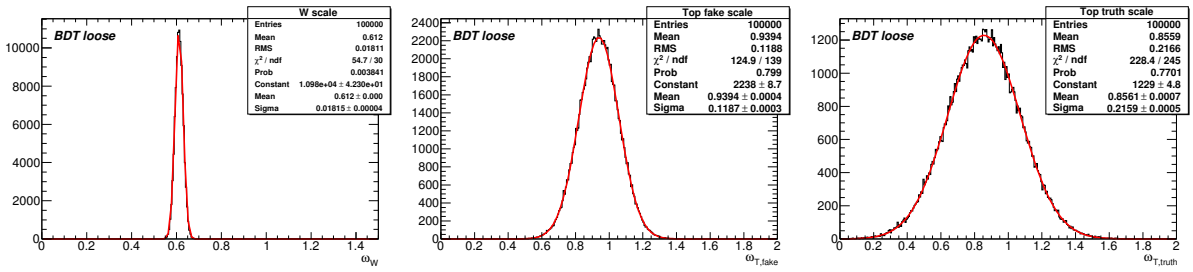

(A) W+jets scaling (B) Top with fake tau scaling (C) Top with truth tau scaling

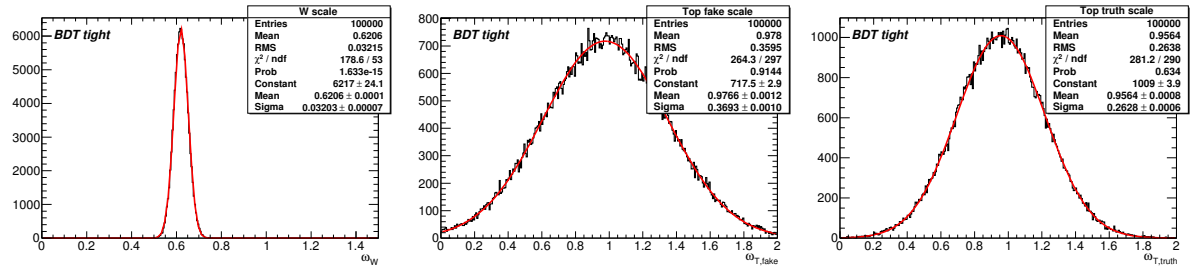

(D) W+jets scaling (E) Top with fake tau scaling (F) Top with truth tau scaling

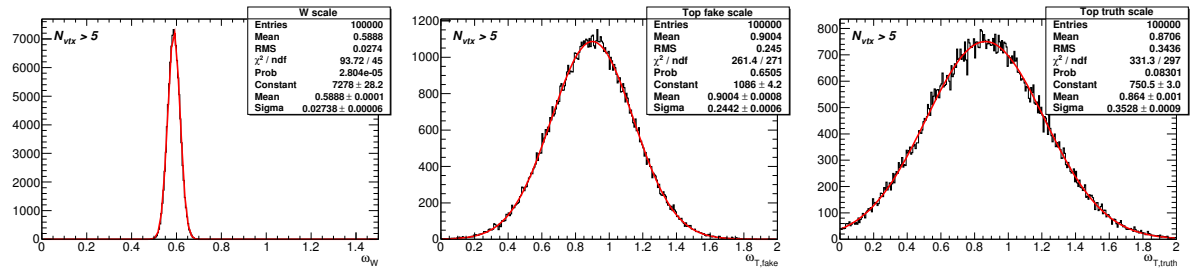

(G) W+jets scaling (H) Top with fake tau scaling (I) Top with truth tau scaling

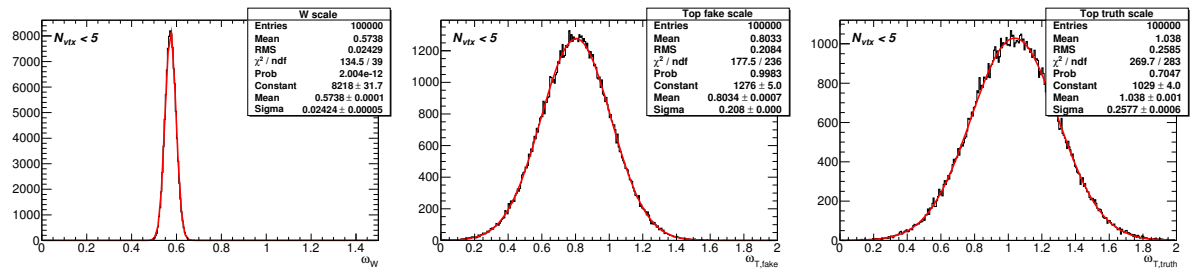

(J) W+jets scaling (K) Top with fake tau scaling (L) Top with truth tau scaling

Figure B.2 The obtained scalings for W+jets, Top with fake taus and Top with truth taus for different variations in tau BDT and pile-up conditions. Scalings can be seen to be robust.

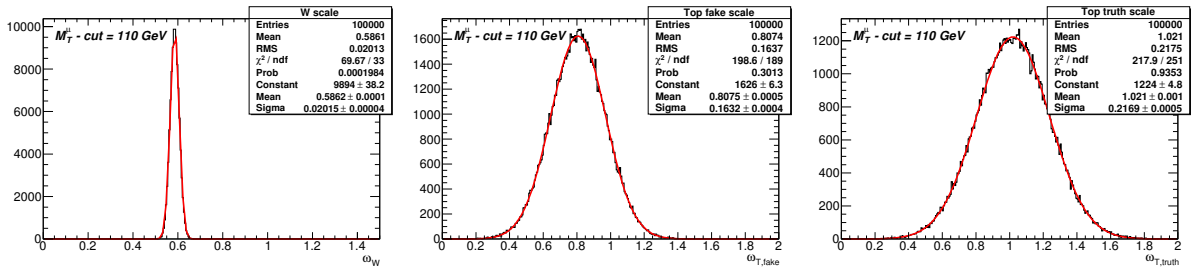

(A) W+jets scaling (B) Top with fake tau scaling (C) Top with truth tau scaling

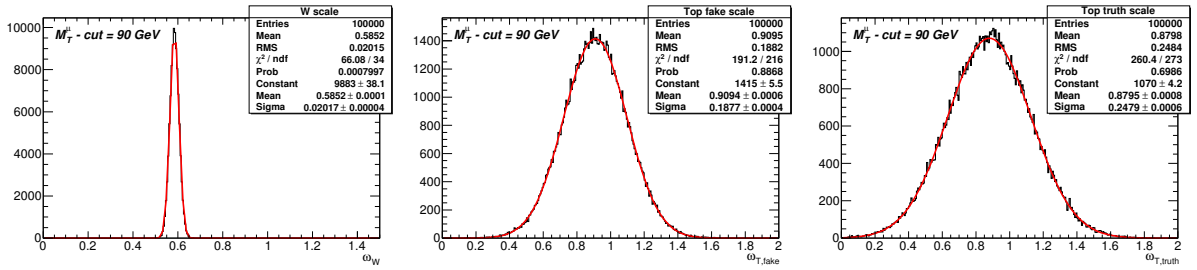

(D) W+jets scaling (E) Top with fake tau scaling (F) Top with truth tau scaling

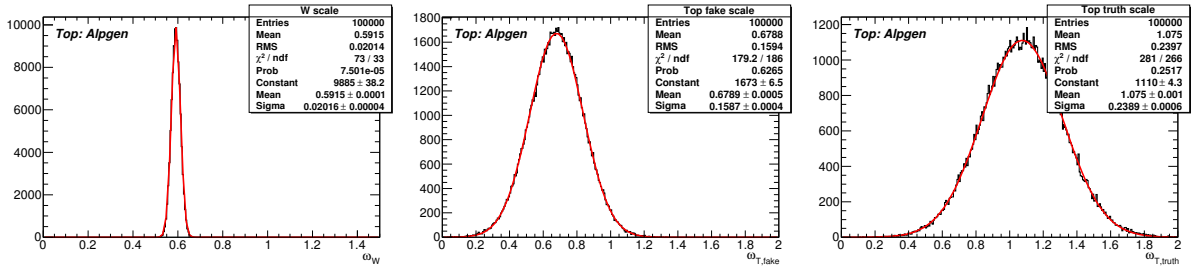

(G) W+jets scaling (H) Top with fake tau scaling (I) Top with truth tau scaling

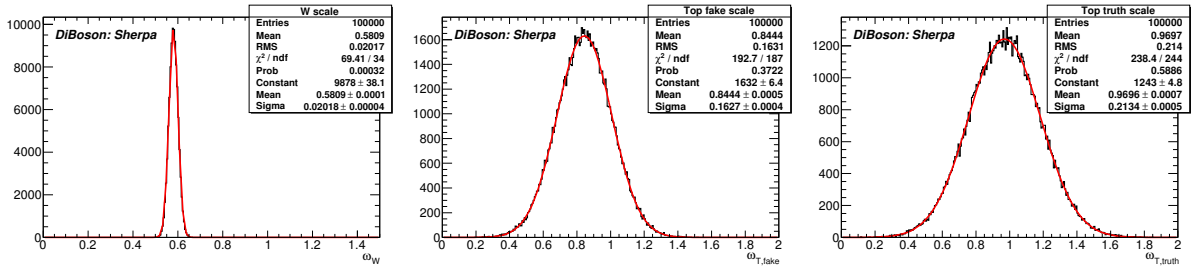

(J) W+jets scaling (K) Top with fake tau scaling (L) Top with truth tau scaling

FIGURE B.3 The obtained scalings for W+jets, Top with fake taus and Top with truth taus for different variations of kinematic selections and generators. Scalings can be seen to be robust.

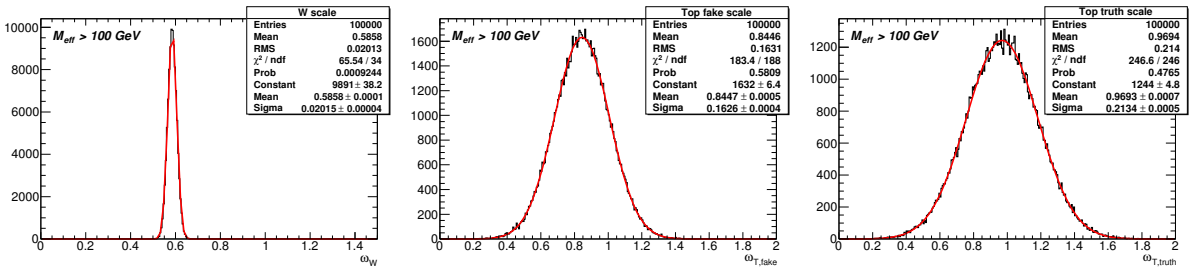

(A) W+jets scaling (B) Top with fake tau scaling (C) Top with truth tau scaling

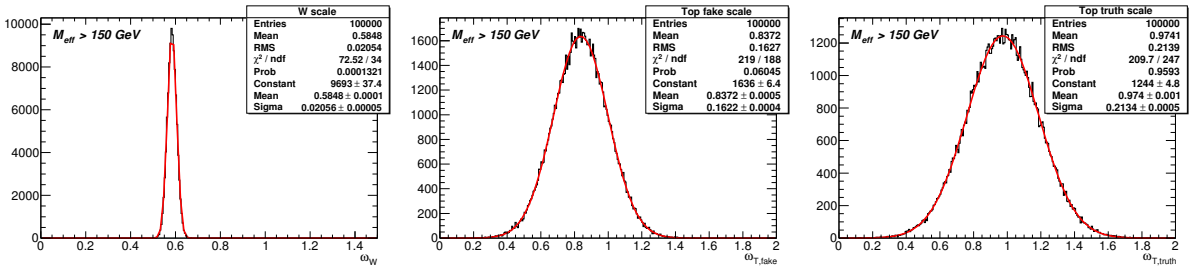

(D) W+jets scaling (E) Top with fake tau scaling (F) Top with truth tau scaling

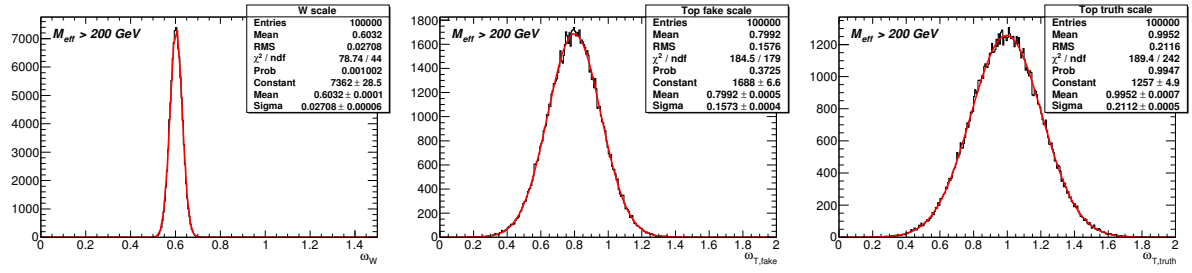

(G) W+jets scaling (H) Top with fake tau scaling (I) Top with truth tau scaling

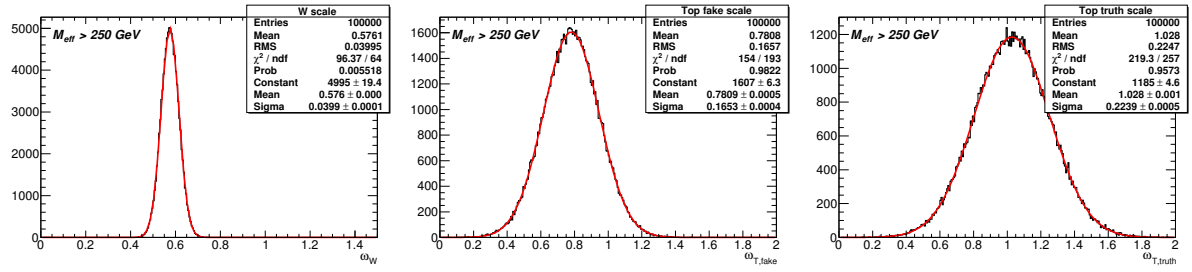

(J) W+jets scaling (K) Top with fake tau scaling (L) Top with truth tau scaling

Figure B.4 The obtained scalings for W+jets, Top with fake taus and Top with truth taus for different variations of kinematic selections. Scalings can be seen to be robust.

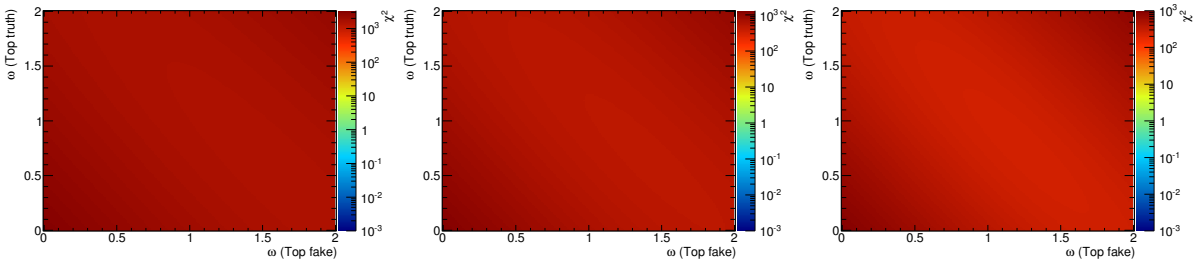

(A) χ^2: $\omega_{\mathrm{T,f}}$ vs. $\omega_{\mathrm{T,t}}$, $\omega_W = 0.1$ (B) χ^2: $\omega_{\mathrm{T,f}}$ vs. $\omega_{\mathrm{T,t}}$, $\omega_W = 0.2$ (C) χ^2: $\omega_{\mathrm{T,f}}$ vs. $\omega_{\mathrm{T,t}}$, $\omega_W = 0.3$

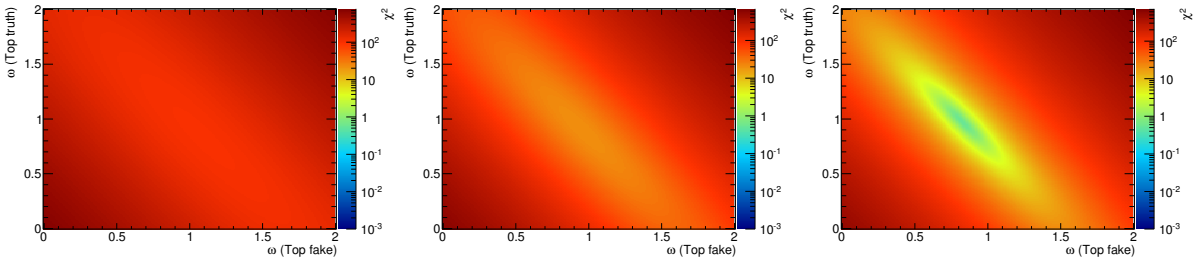

(D) χ^2: $\omega_{\mathrm{T,f}}$ vs. $\omega_{\mathrm{T,t}}$, $\omega_W = 0.4$ (E) χ^2: $\omega_{\mathrm{T,f}}$ vs. $\omega_{\mathrm{T,t}}$, $\omega_W = 0.5$ (F) χ^2: $\omega_{\mathrm{T,f}}$ vs. $\omega_{\mathrm{T,t}}$, $\omega_W = 0.6$

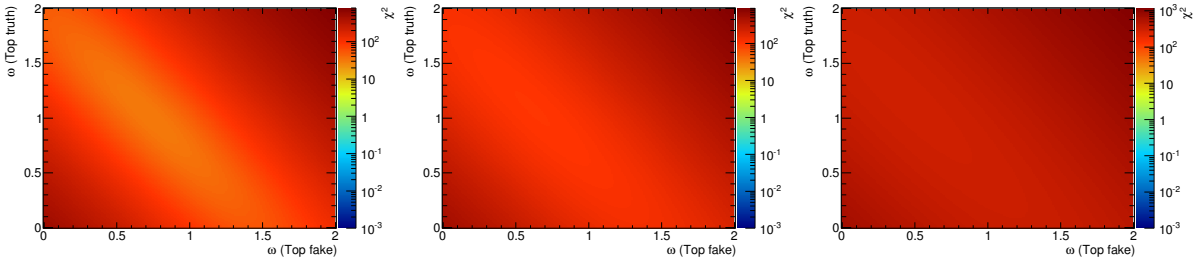

(G) χ^2: $\omega_{\mathrm{T,f}}$ vs. $\omega_{\mathrm{T,t}}$, $\omega_W = 0.7$ (H) χ^2: $\omega_{\mathrm{T,f}}$ vs. $\omega_{\mathrm{T,t}}$, $\omega_W = 0.8$ (I) χ^2: $\omega_{\mathrm{T,f}}$ vs. $\omega_{\mathrm{T,t}}$, $\omega_W = 1$

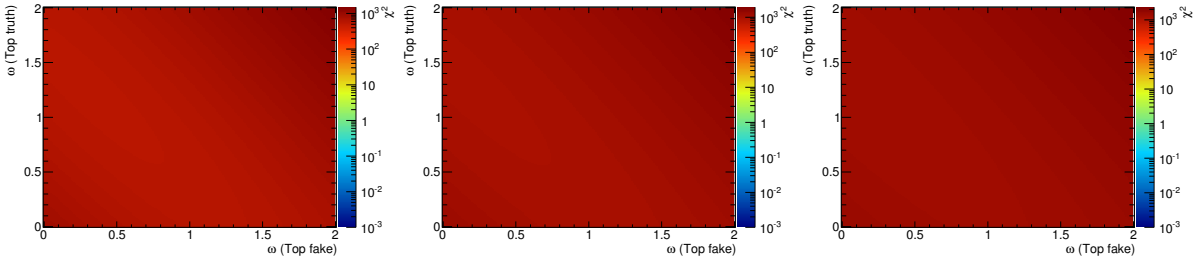

(J) χ^2: $\omega_{\mathrm{T,f}}$ vs. $\omega_{\mathrm{T,t}}$, $\omega_W = 1.2$ (K) χ^2: $\omega_{\mathrm{T,f}}$ vs. $\omega_{\mathrm{T,t}}$, $\omega_W = 1.5$ (L) χ^2: $\omega_{\mathrm{T,f}}$ vs. $\omega_{\mathrm{T,t}}$, $\omega_W = 1.8$

FIGURE B.5 The obtained χ^2-distribution in different slices of ω_W. No secondary local minima can be seen.

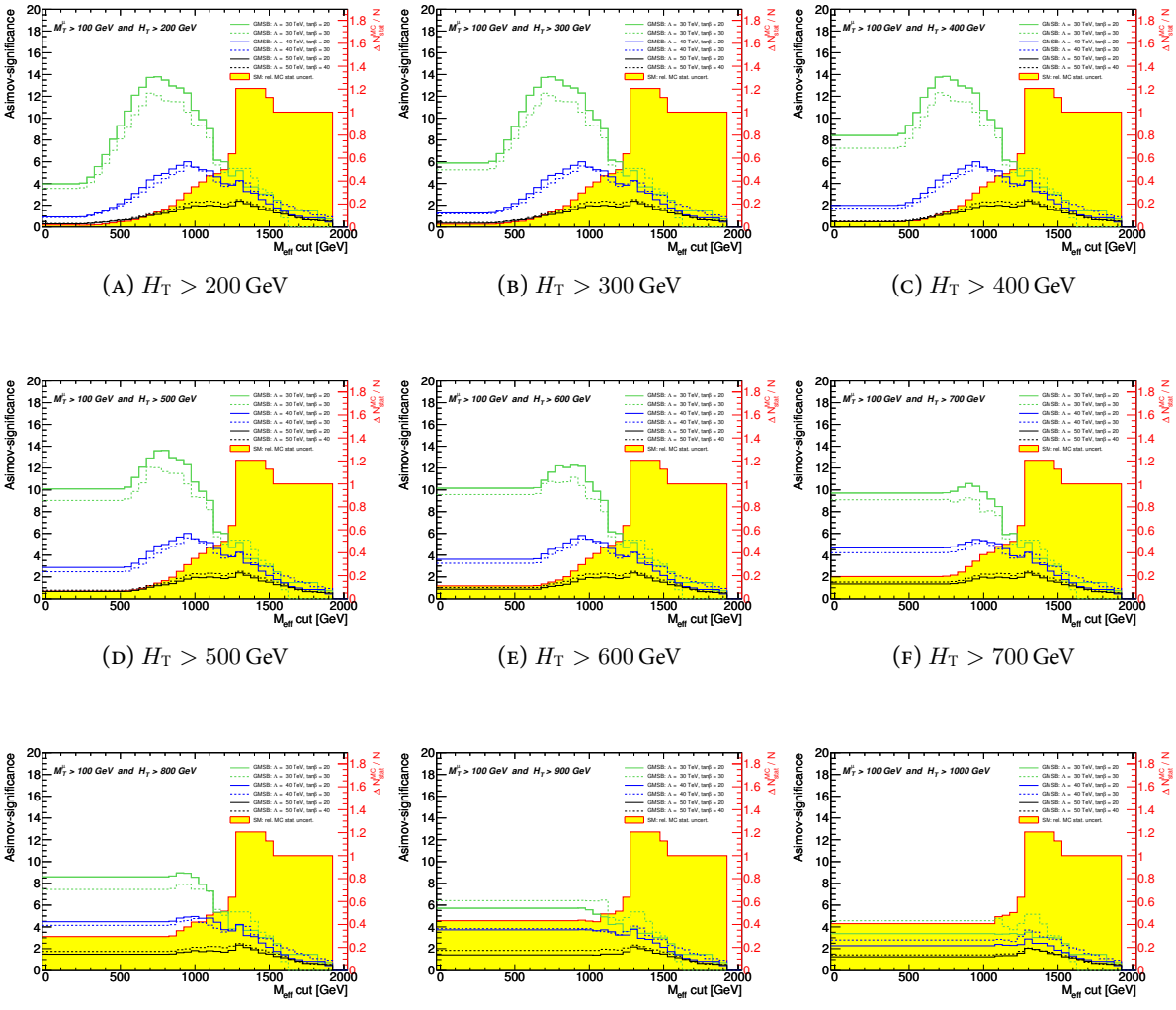

(A) $H_T > 200\,\text{GeV}$ (B) $H_T > 300\,\text{GeV}$ (C) $H_T > 400\,\text{GeV}$

(D) $H_T > 500\,\text{GeV}$ (E) $H_T > 600\,\text{GeV}$ (F) $H_T > 700\,\text{GeV}$

(G) $H_T > 800\,\text{GeV}$ (H) $H_T > 900\,\text{GeV}$ (I) $H_T > 1000\,\text{GeV}$

Figure B.6 Obtained significances for six GMSB benchmarks for different combinations of H_T and $m_{eff.}$ after $m_T^\mu > 100\,\text{GeV}$. Taus are BDT loose, backgrounds are rescaled with the data-driven scale factors and signal is NLO reweighted. MC statistical uncertainty scale is given by the right axis.
The plots show that no combination shows better performance than the individual cut on $m_{eff.}$. The relative statistical Monte-Carlo uncertainties above one are due to negative event weights. They can reduce the sum of weights, i.e. the expected background, considerably. However, they increase the statistical uncertainty, which leads to the ratios above one.

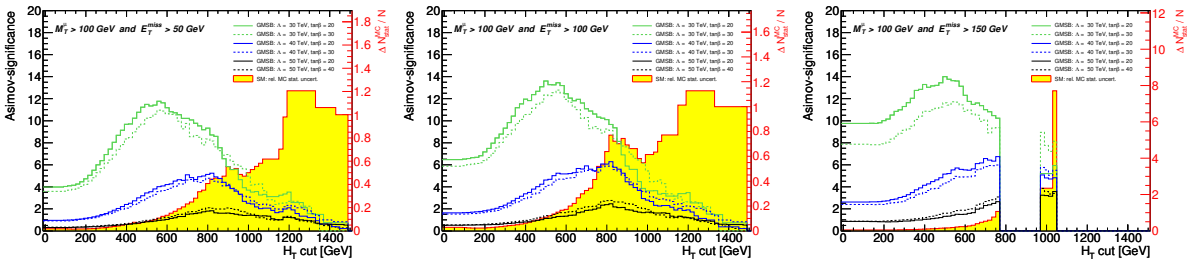

(A) $E_{\mathrm{T}}^{\mathrm{miss.}} > 50\,\mathrm{GeV}$ (B) $E_{\mathrm{T}}^{\mathrm{miss.}} > 100\,\mathrm{GeV}$ (C) $E_{\mathrm{T}}^{\mathrm{miss.}} > 150\,\mathrm{GeV}$

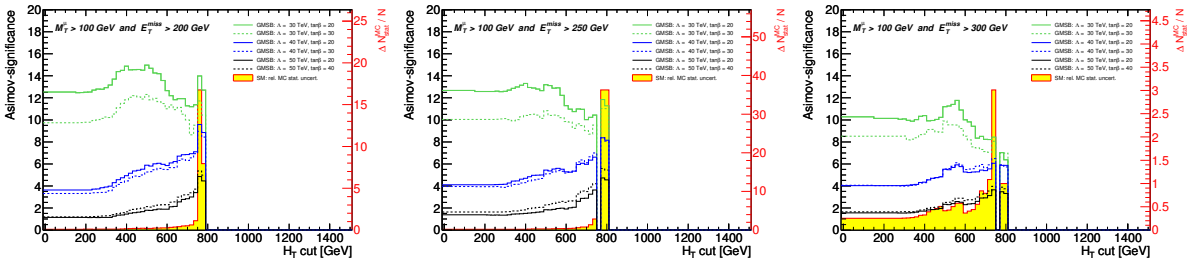

(D) $E_{\mathrm{T}}^{\mathrm{miss.}} > 200\,\mathrm{GeV}$ (E) $E_{\mathrm{T}}^{\mathrm{miss.}} > 250\,\mathrm{GeV}$ (F) $E_{\mathrm{T}}^{\mathrm{miss.}} > 300\,\mathrm{GeV}$

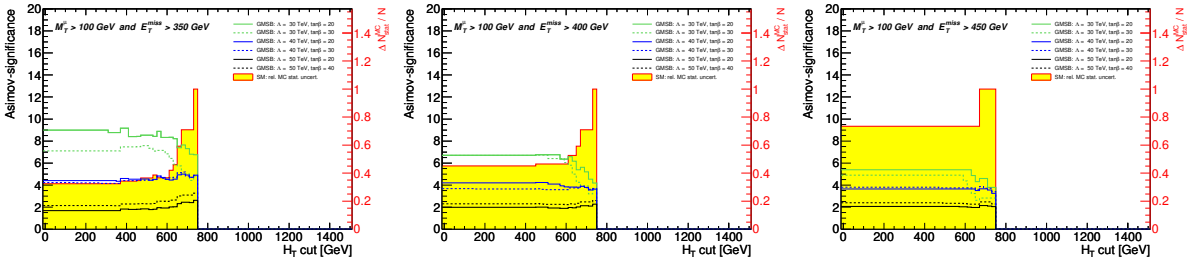

(G) $E_{\mathrm{T}}^{\mathrm{miss.}} > 350\,\mathrm{GeV}$ (H) $E_{\mathrm{T}}^{\mathrm{miss.}} > 400\,\mathrm{GeV}$ (I) $E_{\mathrm{T}}^{\mathrm{miss.}} > 450\,\mathrm{GeV}$

FIGURE B.7 Obtained significances for six GMSB benchmarks for different combinations of $E_T^{miss.}$ and H_T after $m_T^\mu > 100\,\mathrm{GeV}$. Taus are BDT loose, backgrounds are rescaled with the data-driven scale factors and signal is NLO reweighted. MC statistical uncertainty scale is given by the right axis. The gaps in significances as well as the high peaks in the relative uncertainties of the Monte-Carlo statistics are both due to cancellations of positive and negative Monte-Carlo event weights in the sparely populated high mass tails.
In the significance gaps, the sum of event weights is slightly negative. Hence, no background is expected and significance is infinity, which is not displayed. The high peaks in the relative uncertainties of Monte-Carlo statistics are due to weights that cancel out up to a slightly positive sum. This positive sum is then much smaller than the quadratic sum of the weights, i.e. the uncertainty. In both cases, the Monte-Carlo prediction is close to zero but the Monte-Carlo statistic is too low for a proper estimate. However, there is no combination that shows better performance compared to the individual $m_{eff.}$ cut.

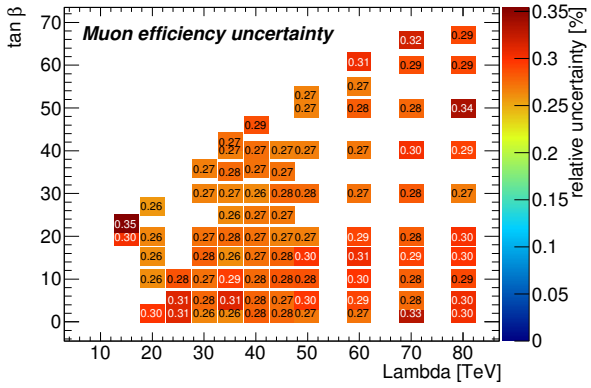

(A) Muon efficiency uncertainties

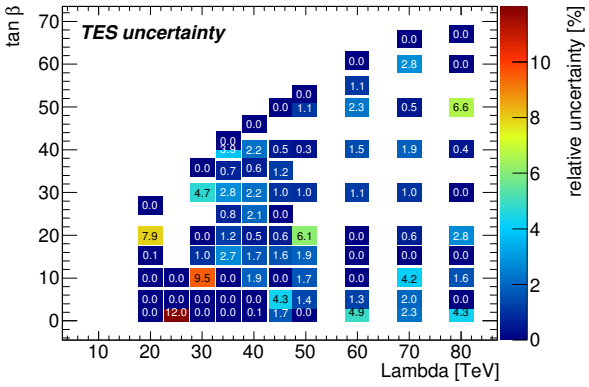

(B) TES uncertainties

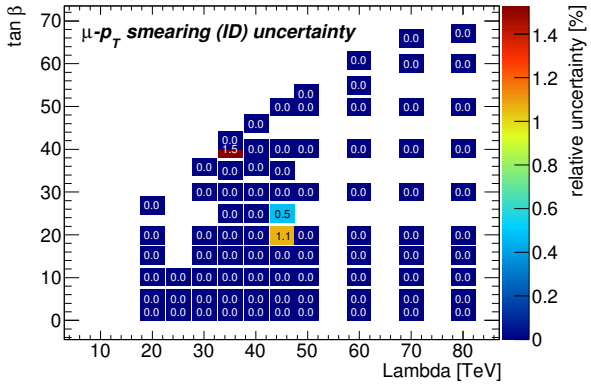

(C) Muon smearing (inner detector)

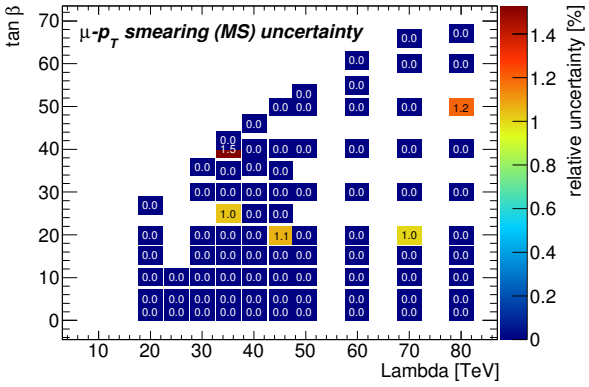

(D) Muon smearing (muon spectrometer)

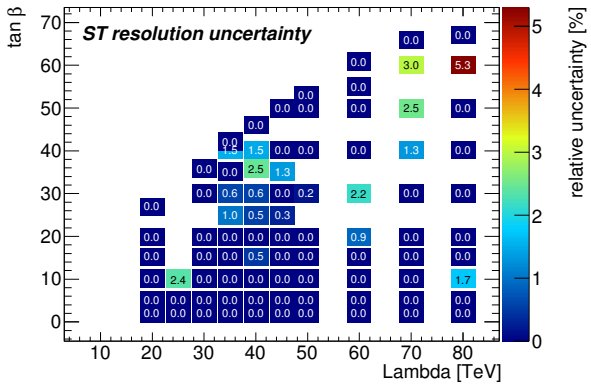

(E) Soft term resolution uncertainties

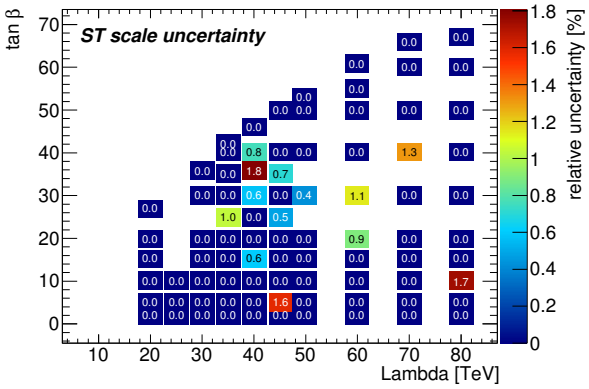

(F) Soft term scale uncertainties

Figure B.8 Systematic uncertainties on the signal prediction in the signal region. All numbers are given in percent relative to the total prediction.

Bibliography

[1] Halzen, F. · Martin, A.: *Quarks & Leptons: An introductory course in modern particle physics*. New York, USA: John Wiley & Sons, 1984 (cit. on p. 5).

[2] Cottingham, W. · Greenwood, D.: *An Introduction to the Standard Model of Particle Physics*. Cambridge University Press, 2007. ISBN: 9780521852494 (cit. on p. 5).

[3] Beringer, J. et al.: *Review of Particle Physics (RPP)*. Phys. Rev. D86 (2012) page 010001. DOI: 10.1103/PhysRevD.86.010001 (cit. on pp. 6, 7, 9, 16).

[4] Higgs, P. W.: *Broken symmetries, massless particles and gauge fields*. Phys. Lett. 12 (1964) pages 132–133. DOI: 10.1016/0031-9163(64)91136-9 (cit. on p. 7).

[5] Higgs, P. W.: *Broken Symmetries and the Masses of Gauge Bosons*. Phys. Rev. Lett. 13 (1964) pages 508–509. DOI: 10.1103/PhysRevLett.13.508 (cit. on p. 7).

[6] Higgs, P. W.: *Spontaneous Symmetry Breakdown without Massless Bosons*. Phys. Rev. 145 (1966) pages 1156–1163. DOI: 10.1103/PhysRev.145.1156 (cit. on p. 7).

[7] Smith, C. L.: *High energy behaviour and gauge symmetry*. Physics Letters B 46.2 (1973) pages 233–236. DOI: 10.1016/0370-2693(73)90692-8 (cit. on p. 8).

[8] Cornwall, J. M. · Levin, D. N. · Tiktopoulos, G.: *Uniqueness of Spontaneously Broken Gauge Theories*. Phys. Rev. Lett. 30 (1973) pages 1268–1270. DOI: 10.1103/PhysRevLett.30.1268 (cit. on p. 8).

[9] Cornwall, J. M. · Levin, D. N. · Tiktopoulos, G.: *Derivation of gauge invariance from high-energy unitarity bounds on the S matrix*. Phys. Rev. D 10 (1974) pages 1145–1167. DOI: 10.1103/PhysRevD.10.1145 (cit. on p. 8).

[10] D'Agostini, G. · Degrassi, G.: *Constraints on the Higgs boson mass from direct searches and precision measurements*. Eur. Phys. J. C10 (1999) pages 663–675. DOI: 10.1007/s100520050604. arXiv: hep-ph/9902226 (cit. on p. 8).

[11] Renton, P. B.: *Electroweak fits and constraints on the Higgs mass* (2004). arXiv: hep-ph/0410177 (cit. on p. 8).

[12] Aad, G. et al.: *Observation of a new particle in the search for the Standard Model Higgs boson with the ATLAS detector at the LHC*. Phys. Lett. B716 (2012) pages 1–29. DOI: 10.1016/j.physletb.2012.08.020. arXiv: 1207.7214 (cit. on pp. 8, 131).

[13] Chatrchyan, S. et al.: *Observation of a new boson at a mass of 125 GeV with the CMS experiment at the LHC*. Phys. Lett. B716 (2012) pages 30–61. DOI: 10.1016/j.physletb.2012.08.021. arXiv: 1207.7235 (cit. on pp. 8, 131).

[14] Weinberg, S.: *Implications of Dynamical Symmetry Breaking*. Phys. Rev. D13 (1976) pages 974–996. doi: 10.1103/PhysRevD.13.974 (cit. on p. 8).

[15] Gildener, E.: *Gauge Symmetry Hierarchies*. Phys. Rev. D14 (1976) page 1667. doi: 10.1103/PhysRevD.14.1667 (cit. on p. 8).

[16] Susskind, L.: *Dynamics of Spontaneous Symmetry Breaking in the Weinberg- Salam Theory*. Phys. Rev. D20 (1979) pages 2619–2625. doi: 10.1103/PhysRevD.20.2619 (cit. on p. 8).

[17] Martin, S. P.: *A supersymmetry primer* (1997). arXiv: hep-ph/9709356 (cit. on pp. 8, 11, 12, 16–19, 30, 134).

[18] Kaul, R. K. · Majumdar, P.: *Cancellation of Quadratically Divergent Mass Corrections in Globally Supersymmetric Spontaneously Broken Gauge Theories*. Nucl. Phys. B199 (1982) page 36. doi: 10.1016/0550-3213(82)90565-X (cit. on p. 9).

[19] Dimopoulos, S. · Raby, S.: *Supercolor*. Nucl. Phys. B192 (1981) page 353. doi: 10.1016/0550-3213(81)90430-2 (cit. on p. 9).

[20] Dimopoulos, S. · Georgi, H.: *Softly Broken Supersymmetry and SU(5)*. Nucl. Phys. B193 (1981) page 150. doi: 10.1016/0550-3213(81)90522-8 (cit. on p. 9).

[21] Feynman, R. P.: *Quantum Electrodynamics*. Reading · Massachusetts: Addison-Wesley, 1998 (cit. on p. 9).

[22] Wilson, F. L.: *Fermi's Theory of Beta Decay*. American Journal of Physics 36 (1968) (cit. on p. 9).

[23] Weinberg, S.: *A Model of Leptons*. Phys. Rev. Lett. 19 (1967) pages 1264–1266. doi: 10.1103/PhysRevLett.19.1264 (cit. on p. 9).

[24] Glashow, S.: *Partial Symmetries of Weak Interactions*. Nucl. Phys. 22 (1961) pages 579–588. doi: 10.1016/0029-5582(61)90469-2 (cit. on p. 9).

[25] Salam, A. · Ward, J. C.: *Electromagnetic and weak interactions*. Phys. Lett. 13 (1964) pages 168–171. doi: 10.1016/0031-9163(64)90711-5 (cit. on p. 9).

[26] Weinberg, S.: *Conceptual Foundations of the Unified Theory of Weak and Electromagnetic Interactions*. Rev. Mod. Phys. 52 (1980) pages 515–523. doi: 10.1103/RevModPhys.52.515 (cit. on p. 9).

[27] Hasert, F. et al.: *Observation of Neutrino Like Interactions without Muon or Electron in the Gargamelle Neutrino Experiment*. Nucl. Phys. B73 (1974) pages 1–22. doi: 10.1016/0550-3213(74)90038-8 (cit. on p. 9).

[28] Hasert, F. · Faissner, H. · Krenz, W. · Von Krogh, J. · Lanske, D. et al.: *SEARCH FOR ELASTIC MUON-NEUTRINO ELECTRON SCATTERING*. Phys. Lett. B46 (1973) pages 121–124. doi: 10.1016/0370-2693(73)90494-2 (cit. on p. 9).

[29] Arnison, G. et al.: *Experimental Observation of Isolated Large Transverse Energy Electrons with Associated Missing Energy at s**(1/2) = 540-GeV*. Phys. Lett. B122 (1983) pages 103–116. doi: 10.1016/0370-2693(83)91177-2 (cit. on p. 9).

[30] Banner, M. et al.: *Observation of Single Isolated Electrons of High Transverse Momentum in Events with Missing Transverse Energy at the CERN anti-p p Collider*. Phys. Lett. B122 (1983) pages 476–485. doi: 10.1016/0370-2693(83)91605-2 (cit. on p. 9).

[31] Arnison, G. et al.: *Experimental Observation of Lepton Pairs of Invariant Mass Around 95-GeV/c^2 at the CERN SPS Collider*. Phys. Lett. B126 (1983) pages 398–410. doi: 10.1016/0370-2693(83)90188-0 (cit. on p. 9).

[32] Bagnaia, P. et al.: *Evidence for $Z^0 \to e^+e^-$ at the CERN anti-p p Collider*. Phys. Lett. B129 (1983) pages 130–140. doi: 10.1016/0370-2693(83)90744-X (cit. on p. 9).

[33] Langacker, P. · Luo, M.: *Implications of precision electroweak experiments for m_t, ρ_0, $\sin^2\theta_W$, and grand unification*. Phys. Rev. D 44 (1991) pages 817–822. doi: 10.1103/PhysRevD.44.817 (cit. on pp. 9, 10, 18).

[34] Georgi, H. · Glashow, S.: *Unity of All Elementary Particle Forces*. Phys. Rev. Lett. 32 (1974) pages 438–441. doi: 10.1103/PhysRevLett.32.438 (cit. on p. 10).

[35] Pati, J. C. · Salam, A.: *Lepton Number as the Fourth Color*. Phys. Rev. D10 (1974) pages 275–289. doi: 10.1103/PhysRevD.10.275 (cit. on p. 10).

[36] Buras, A. · Ellis, J. R. · Gaillard, M. · Nanopoulos, D. V.: *Aspects of the Grand Unification of Strong, Weak and Electromagnetic Interactions*. Nucl. Phys. B135 (1978) pages 66–92. doi: 10.1016/0550-3213(78)90214-6 (cit. on p. 10).

[37] Raby, S.: *SUSY GUT Model Building*. Eur. Phys. J. C59 (2009) pages 223–247. doi: 10.1140/epjc/s10052-008-0736-x. arXiv: 0807.4921 (cit. on p. 10).

[38] Bajc, B.: *SUSY breaking in GUTs*. Int. J. Mod. Phys. A22 (2007) pages 5831–5840. doi: 10.1142/S0217751X07039055 (cit. on p. 10).

[39] Dimopoulos, S. · Raby, S. · Wilczek, F.: *Supersymmetry and the Scale of Unification*. Phys. Rev. D24 (1981) pages 1681–1683. doi: 10.1103/PhysRevD.24.1681 (cit. on pp. 10, 18).

[40] Ellis, J. R. · Kelley, S. · Nanopoulos, D. V.: *Probing the desert using gauge coupling unification*. Phys. Lett. B260 (1991) pages 131–137. doi: 10.1016/0370-2693(91)90980-5 (cit. on pp. 10, 18).

[41] Amaldi, U. · Boer, W. · Furstenau, H.: *Comparison of grand unified theories with electroweak and strong coupling constants measured at LEP*. Phys. Lett. B260 (1991) pages 447–455. doi: 10.1016/0370-2693(91)91641-8 (cit. on pp. 10, 18).

[42] Freedman, D. Z. · Nieuwenhuizen, P. · Ferrara, S.: *Progress Toward a Theory of Supergravity*. Phys. Rev. D13 (1976) pages 3214–3218. doi: 10.1103/PhysRevD.13.3214 (cit. on p. 10).

[43] Van Nieuwenhuizen, P.: *Supergravity*. Phys. Rept. 68 (1981) pages 189–398. doi: 10.1016/0370-1573(81)90157-5 (cit. on p. 10).

[44] Shima, K.: *PROGRESS TOWARD A THEORY OF GENERAL SUPERGRAVITY*. Prog. Theor. Phys. 84 (1990) pages 381–385. doi: 10.1143/PTP.84.381 (cit. on p. 10).

[45] Persic, M. · Salucci, P. · Stel, F.: *The Universal rotation curve of spiral galaxies: 1. The Dark matter connection*. Mon. Not. Roy. Astron. Soc. 281 (1996) page 27. arXiv: astro-ph/9506004 (cit. on p. 10).

[46] Persic, M. · Salucci, P. · Stel, F.: *Rotation curves of 967 spiral galaxies: Implications for dark matter* (1995). arXiv: astro-ph/9503051 (cit. on p. 10).

[47] Bahcall, N. A. · Fan, X.-h.: *The Most massive distant clusters: Determining omega and sigma_8*. Astrophys. J. 504 (1998) page 1. doi: 10.1086/306088. arXiv: astro-ph/9803277 (cit. on p. 10).

[48] Kashlinsky, A.: *Determining Omega from cluster correlation function*. Phys. Rept. 307 (1998) pages 67–73. doi: 10.1016/S0370-1573(98)00050-7. arXiv: astro-ph/9806236 (cit. on p. 10).

[49] Koopmans, L. · Treu, T.: *The structure and dynamics of luminous and dark matter in the early-type lens galaxy of 0047-281 at $z = 0.485$*. Astrophys. J. 583 (2003) pages 606–615. doi: 10.1086/345423. arXiv: astro-ph/0205281 (cit. on p. 10).

[50] Moustakas, L. A. · Metcalf, R. B.: *Detecting dark matter substructure spectroscopically in strong gravitational lenses*. Mon. Not. Roy. Astron. Soc. 339 (2003) page 607. doi: 10.1046/j.1365-8711.2003.06055.x. arXiv: astro-ph/0206176 (cit. on p. 10).

[51] Hu, W. · Dodelson, S.: *Cosmic microwave background anisotropies*. Ann. Rev. Astron. Astrophys. 40 (2002) pages 171–216. doi: 10.1146/annurev.astro.40.060401.093926. arXiv: astro-ph/0110414 (cit. on p. 10).

[52] Hu, W. · Sugiyama, N. · Silk, J.: *The Physics of microwave background anisotropies*. Nature 386 (1997) pages 37–43. doi: 10.1038/386037a0. arXiv: astro-ph/9604166 (cit. on p. 10).

[53] Navarro, J. F. · Hayashi, E. · Power, C. · Jenkins, A. · Frenk, C. S. et al.: *The Inner structure of Lambda-CDM halos 3: Universality and asymptotic slopes*. Mon. Not. Roy. Astron. Soc. 349 (2004) page 1039. doi: 10.1111/j.1365-2966.2004.07586.x. arXiv: astro-ph/0311231 (cit. on p. 10).

[54] Fukushige, T. · Kawai, A. · Makino, J.: *Structure of dark matter halos from hierarchical clustering. 3. Shallowing of the Inner cusp*. Astrophys. J. 606 (2004) pages 625–634. doi: 10.1086/383192. arXiv: astro-ph/0306203 (cit. on p. 10).

[55] Reed, D. · Governato, F. · Verde, L. · Gardner, J. · Quinn, T. R. et al.: *Evolution of the density profiles of dark matter halos*. Mon. Not. Roy. Astron. Soc. 357 (2005) pages 82–96. doi: 10.1111/j.1365-2966.2005.08612.x. arXiv: astro-ph/0312544 (cit. on p. 10).

[56] Bertone, G. · Hooper, D. · Silk, J.: *Particle dark matter: Evidence, candidates and constraints*. Phys. Rept. 405 (2005) pages 279–390. arXiv: hep-ph/0404175 (cit. on p. 11).

[57] Bergstrom, L.: *Dark Matter Evidence, Particle Physics Candidates and Detection Methods* (2012). arXiv: 1205.4882 (cit. on p. 11).

[58] Fayet, P.: *Supersymmetry, dark matter and new particles*. AIP Conf. Proc. 1446 (2010) pages 55–72. doi: 10.1063/1.4727989 (cit. on p. 11).

[59] Lahanas, A.: *LSP as a Candidate for Dark Matter*. Lect. Notes Phys. 720 (2007) pages 35–68. doi: 10.1007/978-3-540-71013-4_2. arXiv: hep-ph/0607301 (cit. on p. 11).

[60] Gondolo, P. · Gelmini, G. · Roulet, E.: *Cornering the supersymmetry preferred dark matter candidate: The Neutralino*. Nucl. Phys. Proc.Suppl. 14B (1990) pages 251–258 (cit. on p. 11).

[61] Perlmutter, S. et al.: *Measurements of Omega and Lambda from 42 high redshift supernovae*. Astrophys. J. 517 (1999) pages 565–586. doi: 10.1086/307221. arXiv: astro-ph/9812133 (cit. on p. 11).

[62] Riess, A. G. et al.: *Observational evidence from supernovae for an accelerating universe and a cosmological constant*. Astron. J. 116 (1998) pages 1009–1038. doi: 10.1086/300499. arXiv: astro-ph/9805201 (cit. on p. 11).

[63] Hamilton, A.: *Formulae for growth factors in expanding universes containing matter and a cosmological constant*. Mon. Not. Roy. Astron. Soc. 322 (2001) page 419. doi: 10.1046/j.1365-8711.2001.04137.x. arXiv: astro-ph/0006089 (cit. on p. 11).

[64] Rugh, S. E. · Zinkernagel, H.: *The Quantum vacuum and the cosmological constant problem*. Stud. Hist. Philos. Mod. Phys. (2000). arXiv: hep-th/0012253 (cit. on p. 11).

[65] Nobbenhuis, S.: *The Cosmological Constant Problem, an Inspiration for New Physics* (2006). arXiv: gr-qc/0609011 (cit. on p. 11).

[66] Coleman, S. R. · Wess, J. · Zumino, B.: *Structure of phenomenological Lagrangians. 1.* Phys. Rev. 177 (1969) pages 2239–2247. doi: 10.1103/PhysRev.177.2239 (cit. on p. 11).

[67] Callan, J. · Coleman, S. R. · Wess, J. · Zumino, B.: *Structure of phenomenological Lagrangians. 2.* Phys. Rev. 177 (1969) pages 2247–2250. doi: 10.1103/PhysRev.177.2247 (cit. on p. 11).

[68] Wess, J. · Zumino, B.: *Supergauge Transformations in Four-Dimensions*. Nucl. Phys. B70 (1974) pages 39–50. doi: 10.1016/0550-3213(74)90355-1 (cit. on p. 11).

[69] Wess, J. · Zumino, B.: *A Lagrangian Model Invariant Under Supergauge Transformations*. Phys. Lett. B49 (1974) page 52. doi: 10.1016/0370-2693(74)90578-4 (cit. on p. 11).

[70] Wess, J. · Zumino, B.: *Supergauge Transformations in Four-Dimensions*. Nucl. Phys. B70 (1974) pages 39–50. doi: 10.1016/0550-3213(74)90355-1 (cit. on p. 11).

[71] Aitchison, I. J.: *Supersymmetry and the MSSM: An Elementary introduction* (2005). arXiv: hep-ph/0505105 (cit. on pp. 11, 15, 18, 22).

[72] Bilal, A.: *Introduction to supersymmetry* (2001). arXiv: hep-th/0101055 (cit. on p. 11).

[73] Lykken, J. D.: *Introduction to supersymmetry* (1996) pages 85–153. arXiv: hep-th/9612114 (cit. on p. 11).

[74] Nilles, H. P.: *Supersymmetry, Supergravity and Particle Physics*. Phys. Rept. 110 (1984) pages 1–162. doi: 10.1016/0370-1573(84)90008-5 (cit. on p. 11).

[75] Coleman, S. R. · Mandula, J.: *ALL POSSIBLE SYMMETRIES OF THE S MATRIX*. Phys. Rev. 159 (1967) pages 1251–1256. doi: 10.1103/PhysRev.159.1251 (cit. on p. 12).

[76] Haag, R. · Lopuszanski, J. T. · Sohnius, M.: *All Possible Generators of Supersymmetries of the s Matrix*. Nucl. Phys. B88 (1975) page 257. doi: 10.1016/0550-3213(75)90279-5 (cit. on p. 12).

[77] Preskill, J.: *Gauge anomalies in an effective field theory*. Annals Phys. 210 (1991) pages 323–379. doi: 10.1016/0003-4916(91)90046-B (cit. on p. 12).

[78] Gunion, J. F. · Haber, H. E. · Kane, G. L. · Dawson, S.: *THE HIGGS HUNTER'S GUIDE*. Front. Phys. 80 (2000) pages 1–448 (cit. on p. 13).

[79] Ellis, J. R. · Ridolfi, G. · Zwirner, F.: *Radiative corrections to the masses of supersymmetric Higgs bosons*. Phys. Lett. B257 (1991) pages 83–91. doi: 10.1016/0370-2693(91)90863-L (cit. on p. 13).

[80] Carena, M. S. · Espinosa, J. · Quiros, M. · Wagner, C.: *Analytical expressions for radiatively corrected Higgs masses and couplings in the MSSM*. Phys. Lett. B355 (1995) pages 209–221. doi: 10.1016/0370-2693(95)00694-G. arXiv: hep-ph/9504316 (cit. on p. 14).

[81] Carena, M. S. · Quiros, M. · Wagner, C.: *Effective potential methods and the Higgs mass spectrum in the MSSM*. Nucl. Phys. B461 (1996) pages 407–436. doi: 10.1016/0550-3213(95)00665-6. arXiv: hep-ph/9508343 (cit. on p. 14).

[82] Roy, P.: *Mechanisms of supersymmetry breaking in the MSSM*. Pramana 60 (2003) pages 169–182. doi: 10.1007/BF02706401. arXiv: hep-ph/0207293 (cit. on p. 14).

[83] Cabibbo, N.: *Unitary Symmetry and Leptonic Decays*. Phys. Rev. Lett. 10 (1963) pages 531–533. doi: 10.1103/PhysRevLett.10.531 (cit. on p. 14).

[84] Kobayashi, M. · Maskawa, T.: *CP Violation in the Renormalizable Theory of Weak Interaction*. Prog. Theor. Phys. 49 (1973) pages 652–657. doi: 10.1143/PTP.49.652 (cit. on p. 14).

[85] Stocchi, A.: *Current status of the CKM matrix and the CP violation* (2004) pages 31–82. arXiv: hep-ph/0405038 (cit. on p. 14).

[86] Bilenky, S. M. · Bottino, A. · Giunti, C. · Kim, C. W.: *Neutrino oscillations in the framework of three generation mixings with mass hierarchy*. Phys. Lett. B356 (1995) pages 273–281. arXiv: hep-ph/9504405 (cit. on p. 14).

[87] Gonzalez-Garcia, M. · Maltoni, M. · Salvado, J. · Schwetz, T.: *Global fit to three neutrino mixing: critical look at present precision* (2012). arXiv: 1209.3023 (cit. on p. 14).

[88] Morisi, S. · Valle, J.: *Neutrino masses and mixing: a flavour symmetry roadmap* (2012). arXiv: 1206.6678 (cit. on p. 14).

[89] Dimopoulos, S. · Sutter, D. W.: *The Supersymmetric flavor problem*. Nucl. Phys. B452 (1995) pages 496–512. doi: 10.1016/0550-3213(95)00421-N. arXiv: hep-ph/9504415 (cit. on p. 15).

[90] Barbieri, R. · Hall, L. J. · Strumia, A.: *Violations of lepton flavor and CP in supersymmetric unified theories*. Nucl. Phys. B445 (1995) pages 219–251. doi: 10.1016/0550-3213(95)00208-A. arXiv: hep-ph/9501334 (cit. on p. 15).

[91] Barbieri, R. · Giudice, G.: *$b \to s\gamma$ decay and Supersymmetry*. Phys. Lett. B309 (1993) pages 86–90. doi: 10.1016/0370-2693(93)91508-K. arXiv: hep-ph/9303270 (cit. on p. 15).

[92] Hisano, J. · Moroi, T. · Tobe, K. · Yamaguchi, M. · Yanagida, T.: *Lepton flavor violation in the supersymmetric standard model with seesaw induced neutrino masses*. Phys. Lett. B357 (1995) pages 579–587. doi: 10.1016/0370-2693(95)00954-J. arXiv: hep-ph/9501407 (cit. on p. 15).

[93] Gabbiani, F. · Gabrielli, E. · Masiero, A. · Silvestrini, L.: *A Complete analysis of FCNC and CP constraints in general SUSY extensions of the standard model*. Nucl. Phys. B477 (1996) pages 321–352. doi: 10.1016/0550-3213(96)00390-2. arXiv: hep-ph/9604387 (cit. on p. 15).

[94] Chankowski, P. H. · Slawianowska, L.: *$B_0(d,s) \to \mu^-\mu^+$ decay in the MSSM*. Phys. Rev. D63 (2001) page 054012. doi: 10.1103/PhysRevD.63.054012. arXiv: hep-ph/0008046 (cit. on p. 15).

[95] Barbier, R. · Berat, C. · Besancon, M. · Chemtob, M. · Deandrea, A. et al.: *R-parity violating supersymmetry*. Phys. Rept. 420 (2005) pages 1–202. doi: 10.1016/j.physrep.2005.08.006. arXiv: hep-ph/0406039 (cit. on pp. 16, 17).

[96] Sakai, N. · Yanagida, T.: *Proton Decay in a Class of Supersymmetric Grand Unified Models*. Nucl. Phys. B197 (1982) page 533. doi: 10.1016/0550-3213(82)90457-6 (cit. on p. 16).

[97] Dimopoulos, S. · Raby, S. · Wilczek, F.: *Proton Decay in Supersymmetric Models*. Phys. Lett. B112 (1982) page 133. doi: 10.1016/0370-2693(82)90313-6 (cit. on p. 16).

[98] Barbieri, R. · Masiero, A.: *Supersymmetric Models with Low-Energy Baryon Number Violation*. Nucl. Phys. B267 (1986) page 679. doi: 10.1016/0550-3213(86)90136-7 (cit. on p. 16).

[99] Barger, V. D. · Giudice, G. · Han, T.: *Some New Aspects of Supersymmetry R-Parity Violating Interactions*. Phys. Rev. D40 (1989) page 2987. doi: 10.1103/PhysRevD.40.2987 (cit. on p. 16).

[100] Bhattacharyya, G. · Choudhury, D.: *D and tau decays: Placing new bounds on R-parity violating supersymmetric coupling*. Mod. Phys. Lett. A10 (1995) pages 1699–1704. doi: 10.1142/S0217732395001812. arXiv: hep-ph/9503263 (cit. on p. 16).

[101] Bhattacharyya, G.: *R-parity violating supersymmetric Yukawa couplings: A Minireview*. Nucl. Phys. Proc. Suppl. 52A (1997) pages 83–88. arXiv: hep-ph/9608415 (cit. on p. 16).

[102] Farrar, G. R. · Fayet, P.: *Phenomenology of the production, decay, and detection of new hadronic states associated with supersymmetry*. Physics Letters B 76.5 (1978) pages 575–579. doi: 10.1016/0370-2693(78)90858-4 (cit. on p. 16).

[103] Fayet, P.: *Supersymmetry and Weak, Electromagnetic and Strong Interactions*. Phys. Lett. B64 (1976) page 159. doi: 10.1016/0370-2693(76)90319-1 (cit. on p. 16).

[104] Tatar, R. · Watari, T.: *A Stable Proton without R-Parity: Implications for the LSP*. Phys. Lett. B646 (2007) pages 258–264. doi: 10.1016/j.physletb.2007.01.020. arXiv: hep-ph/0605315 (cit. on p. 17).

[105] Dreiner, H. K. · Luhn, C. · Thormeier, M.: *What is the discrete gauge symmetry of the MSSM?* Phys. Rev. D73 (2006) page 075007. doi: 10.1103/PhysRevD.73.075007. arXiv: hep-ph/0512163 (cit. on p. 17).

[106] Ibanez, L. E. · Ross, G. G.: *Discrete gauge symmetries and the origin of baryon and lepton number conservation in supersymmetric versions of the standard model.* Nucl. Phys. B368 (1992) pages 3–37. doi: 10.1016/0550-3213(92)90195-H (cit. on p. 17).

[107] Hempfling, R.: *SUSY without R-parity: Symmetry breaking and LSP phenomenology* (1997) pages 255–266. arXiv: hep-ph/9702412 (cit. on p. 17).

[108] Siegel, W.: *Supersymmetric Dimensional Regularization via Dimensional Reduction.* Phys. Lett. B84 (1979) page 193. doi: 10.1016/0370-2693(79)90282-X (cit. on p. 17).

[109] Capper, D. · Jones, D. · Nieuwenhuizen, P.: *Regularization by Dimensional Reduction of Supersymmetric and Nonsupersymmetric Gauge Theories.* Nucl. Phys. B167 (1980) page 479. doi: 10.1016/0550-3213(80)90244-8 (cit. on p. 17).

[110] Georgi, H. · Quinn, H. R. · Weinberg, S.: *Hierarchy of Interactions in Unified Gauge Theories.* Phys. Rev. Lett. 33 (1974) pages 451–454. doi: 10.1103/PhysRevLett.33.451 (cit. on p. 18).

[111] Georgi, H. · Glashow, S.: *Unity of All Elementary Particle Forces.* Phys. Rev. Lett. 32 (1974) pages 438–441. doi: 10.1103/PhysRevLett.32.438 (cit. on p. 18).

[112] Martin, S. P. · Vaughn, M. T.: *Regularization dependence of running couplings in softly broken supersymmetry.* Phys. Lett. B318 (1993) pages 331–337. doi: 10.1016/0370-2693(93)90136-6. arXiv: hep-ph/9308222 (cit. on p. 19).

[113] Barbieri, R. · Ferrara, S. · Savoy, C. A.: *Gauge Models with Spontaneously Broken Local Supersymmetry.* Phys. Lett. B119 (1982) page 343. doi: 10.1016/0370-2693(82)90685-2 (cit. on p. 20).

[114] Hall, L. J. · Lykken, J. D. · Weinberg, S.: *Supergravity as the Messenger of Supersymmetry Breaking.* Phys. Rev. D27 (1983) pages 2359–2378. doi: 10.1103/PhysRevD.27.2359 (cit. on p. 20).

[115] Ellis, J. R. · Nanopoulos, D. V. · Tamvakis, K.: *Grand Unification in Simple Supergravity.* Phys. Lett. B121 (1983) page 123. doi: 10.1016/0370-2693(83)90900-0 (cit. on p. 20).

[116] Choi, S. Y. · Kalinowski, J. · Moortgat-Pick, G. A. · Zerwas, P. M.: *Analysis of the neutralino system in supersymmetric theories.* Eur. Phys. J. C22 (2001) pages 563–579. doi: 10.1007/s100520100808. arXiv: hep-ph/0108117 (cit. on p. 20).

[117] Kalinowski, J. · Moortgat-Pick, G. A.: *SUSY parameters from charginos.* eConf C010630 (2001) pages P352. arXiv: hep-ph/0202084 (cit. on p. 21).

[118] Choi, S. · Djouadi, A. · Guchait, M. · Kalinowski, J. · Song, H. et al.: *Reconstructing the chargino system at e+ e- linear colliders.* Eur. Phys. J. C14 (2000) pages 535–546. doi: 10.1007/s100520000365. arXiv: hep-ph/0002033 (cit. on p. 21).

[119] Choi, S. · Djouadi, A. · Dreiner, H. K. · Kalinowski, J. · Zerwas, P.: *Chargino pair production in e+ e- collisions*. Eur. Phys. J. C7 (1999) pages 123–134. doi: 10.1007/s100529800957. arXiv: hep-ph/9806279 (cit. on p. 21).

[120] Haber, H. E. · Kane, G. L.: *The Search for Supersymmetry: Probing Physics Beyond the Standard Model*. Phys. Rept. 117 (1985) pages 75–263. doi: 10.1016/0370-1573(85)90051-1 (cit. on p. 21).

[121] Kraml, S.: *Stop and sbottom phenomenology in the MSSM* (1999). arXiv: hep-ph/9903257 (cit. on p. 22).

[122] Bjorken, J. · Paschos, E. A.: *Inelastic Electron Proton and gamma Proton Scattering, and the Structure of the Nucleon*. Phys. Rev. 185 (1969) pages 1975–1982. doi: 10.1103/PhysRev.185.1975 (cit. on p. 23).

[123] Pumplin, J. · Stump, D. · Huston, J. · Lai, H. · Nadolsky, P. M. et al.: *New generation of parton distributions with uncertainties from global QCD analysis*. JHEP 0207 (2002) page 012. arXiv: hep-ph/0201195 (cit. on pp. 23, 52).

[124] Nadolsky, P. M. · Lai, H.-L. · Cao, Q.-H. · Huston, J. · Pumplin, J. et al.: *Implications of CTEQ global analysis for collider observables*. Phys. Rev. D78 (2008) page 013004. doi: 10.1103/PhysRevD.78.013004. arXiv: 0802.0007 (cit. on p. 23).

[125] Martin, A. · Stirling, W. · Thorne, R. · Watt, G.: *Update of parton distributions at NNLO*. Phys. Lett. B652 (2007) pages 292–299. doi: 10.1016/j.physletb.2007.07.040. arXiv: 0706.0459 (cit. on p. 23).

[126] Thorne, R.: *A Variable-flavor number scheme for NNLO*. Phys. Rev. D73 (2006) page 054019. doi: 10.1103/PhysRevD.73.054019. arXiv: hep-ph/0601245 (cit. on p. 23).

[127] Ball, R. D. et al.: *Unbiased global determination of parton distributions and their uncertainties at NNLO and at LO*. Nucl. Phys. B855 (2012) pages 153–221. doi: 10.1016/j.nuclphysb.2011.09.024. arXiv: 1107.2652 (cit. on p. 23).

[128] Ball, R. D. et al.: *Fitting Parton Distribution Data with Multiplicative Normalization Uncertainties*. JHEP 1005 (2010) page 075. doi: 10.1007/JHEP05(2010)075. arXiv: 0912.2276 (cit. on p. 23).

[129] Cooper-Sarkar, A.: *PDF Fits at HERA*. PoS EPS-HEP2011 (2011) page 320. arXiv: 1112.2107 (cit. on p. 23).

[130] Grindhammer, G.: *Determination of PDFs and $\alpha_S(M_Z)$ from Inclusive and Jet Measurements in DIS @ HERA*. AIP Conf. Proc. 1441 (2012) pages 225–228. doi: 10.1063/1.3700518. arXiv: 1112.0224 (cit. on p. 23).

[131] Spira, M.: *Higgs and SUSY particle production at hadron colliders* (2002) pages 217–226. arXiv: hep-ph/0211145 (cit. on p. 23).

[132] Harrison, P. · Llewellyn Smith, C.: *Hadroproduction of Supersymmetric Particles*. Nucl. Phys. B213 (1983) page 223. doi: 10.1016/0550-3213(83)90510-2 (cit. on p. 23).

[133] Dawson, S. · Eichten, E. · Quigg, C.: *Search for Supersymmetric Particles in Hadron - Hadron Collisions*. Phys. Rev. D31 (1985) page 1581. doi: 10.1103/PhysRevD.31.1581 (cit. on p. 23).

[134] Baer, H. · Tata, X.: *Component formulae for hadroproduction of left-and right-handed squarks*. Phys. Lett. B160 (1985) page 159. doi: 10.1016/0370-2693(85)91484-4 (cit. on p. 23).

[135] Beenakker, W. · Hopker, R. · Spira, M. · Zerwas, P.: *Squark and gluino production at hadron colliders*. Nucl. Phys. B492 (1997) pages 51–103. doi: 10.1016/S0550-3213(97)00084-9. arXiv: hep-ph/9610490 (cit. on p. 23).

[136] Beenakker, W. · Klasen, M. · Kramer, M. · Plehn, T. · Spira, M. et al.: *The Production of charginos / neutralinos and sleptons at hadron colliders*. Phys. Rev. Lett. 83 (1999) pages 3780–3783. doi: 10.1103/PhysRevLett.100.029901,10.1103/PhysRevLett.83.3780. arXiv: hep-ph/9906298 (cit. on p. 25).

[137] Katz, A. · Tweedie, B.: *Signals of a Sneutrino (N)LSP at the LHC*. Phys. Rev. D81 (2010) page 035012. doi: 10.1103/PhysRevD.81.035012. arXiv: 0911.4132 (cit. on p. 27).

[138] Gupta, S. K. · Mukhopadhyaya, B. · Rai, S. K.: *Right-Chiral Sneutrino LSP in mSUGRA: Event characteristics of NLSP at the LHC* (2007). arXiv: 0710.2508 (cit. on p. 27).

[139] Alan, A. · Sultansoy, S.: *The 'Right' sneutrino as the LSP*. J. Phys. G30 (2004) pages 937–944. doi: 10.1088/0954-3899/30/7/009. arXiv: hep-ph/0307143 (cit. on p. 27).

[140] Isidori, G. · Mescia, F. · Paradisi, P. · Temes, D.: *Flavour physics at large tan(beta) with a Bino-like LSP*. Phys. Rev. D75 (2007) page 115019. doi: 10.1103/PhysRevD.75.115019. arXiv: hep-ph/0703035 (cit. on p. 27).

[141] Hall, L. J. · Nomura, Y. · Shirai, S.: *Spread Supersymmetry with Wino LSP: Gluino and Dark Matter Signals* (2012). arXiv: 1210.2395 (cit. on p. 27).

[142] Ibe, M. · Moroi, T. · Yanagida, T.: *Possible Signals of Wino LSP at the Large Hadron Collider*. Phys. Lett. B644 (2007) pages 355–360. doi: 10.1016/j.physletb.2006.11.061. arXiv: hep-ph/0610277 (cit. on p. 27).

[143] Kane, G. L.: *Sphenomenology: An Overview, with a focus on a Higgsino LSP world, and on eventual tests of string theory*. Nucl. Phys. Proc. Suppl. 62 (1998) pages 144–151. doi: 10.1016/S0920-5632(97)00651-8. arXiv: hep-ph/9709318 (cit. on p. 27).

[144] Konar, P.: *Higgsino LSP in colliders and dark matter experiments*. AIP Conf. Proc. 805 (2006) pages 435–438. doi: 10.1063/1.2149749 (cit. on p. 27).

[145] Bae, K. J. · Dermisek, R. · Kim, H. D. · Kim, I.-W.: *Mixed bino-wino-higgsino dark matter in gauge messenger models*. JCAP 0708 (2007) page 014. doi: 10.1088/1475-7516/2007/08/014. arXiv: hep-ph/0702041 (cit. on p. 27).

[146] Schael, S. et al.: *Branching ratios and spectral functions of tau decays: Final ALEPH measurements and physics implications*. Phys. Rept. 421 (2005) pages 191–284. arXiv: hep-ex/0506072 (cit. on pp. 29, 30).

[147] Bullock, B. · Hagiwara, K. · Martin, A. D.: *Tau polarization and its correlations as a probe of new physics*. Nucl. Phys. B395 (1993) pages 499–533. doi: 10.1016/0550-3213(93)90045-Q (cit. on p. 30).

[148] Choi, S. Y. · Hagiwara, K. · Kim, Y. G. · Mawatari, K. · Zerwas, P. M.: *tau polarization in SUSY cascade decays*. Phys. Lett. B648 (2007) pages 207–212. arXiv: hep-ph/0612237 (cit. on p. 30).

[149] Nojiri, M. M.: *Polarization of tau lepton from scalar tau decay as a probe of neutralino mixing*. Phys. Rev. D51 (1995) pages 6281–6291. arXiv: hep-ph/9412374 (cit. on p. 30).

[150] Nattermann, T. · Desch, K. · Wienemann, P. · Zendler, C.: *Measuring tau-polarisation in chio(2) decays at the LHC*. JHEP 0904 (2009) page 057. doi: 10.1088/1126-6708/2009/04/057. arXiv: 0903.0714 (cit. on p. 30).

[151] Dine, M. · Nelson, A. E.: *Dynamical supersymmetry breaking at low-energies*. Phys. Rev. D48 (1993) pages 1277–1287. doi: 10.1103/PhysRevD.48.1277. arXiv: hep-ph/9303230 (cit. on p. 30).

[152] Dine, M. · Nelson, A. E. · Shirman, Y.: *Low-energy dynamical supersymmetry breaking simplified*. Phys. Rev. D51 (1995) pages 1362–1370. doi: 10.1103/PhysRevD.51.1362. arXiv: hep-ph/9408384 (cit. on p. 30).

[153] Dine, M. · Nelson, A. E. · Nir, Y. · Shirman, Y.: *New tools for low-energy dynamical supersymmetry breaking*. Phys. Rev. D53 (1996) pages 2658–2669. doi: 10.1103/PhysRevD.53.2658. arXiv: hep-ph/9507378 (cit. on p. 30).

[154] Kolda, C. F.: *Gauge mediated supersymmetry breaking: Introduction, review and update*. Nucl. Phys. Proc. Suppl. 62 (1998) pages 266–275. doi: 10.1016/S0920-5632(97)00667-1. arXiv: hep-ph/9707450 (cit. on pp. 30, 32).

[155] Giudice, G. · Rattazzi, R.: *Theories with gauge mediated supersymmetry breaking*. Phys. Rept. 322 (1999) pages 419–499. doi: 10.1016/S0370-1573(99)00042-3. arXiv: hep-ph/9801271 (cit. on p. 30).

[156] Salvatore, F et al.: *Search for Events with Large Missing Transverse Momentum, Jets, and Leptons (e/mu/tau) in 7 TeV Proton-Proton Collision Data with the ATLAS Detector*. Tech. rep. ATL-COM-PHYS-2012-567. CERN, (2012). [CDS rec.: 1449784] (cit. on pp. 33, 112, 127).

[157] Bruning, E. · Collier, E. · Lebrun, E. · Myers, E. · Ostojic, E. et al.: *LHC Design Report. 1. The LHC Main Ring*. Tech. rep. CERN-2004-003-V-1, CERN-2004-003. (2004). [CDS rec.: 782076] (cit. on p. 35).

[158] Buning, E. · Collier, E. · Lebrun, E. · Myers, E. · Ostojic, E. et al.: *LHC Design Report. 2. The LHC infrastructure and general services*. Tech. rep. CERN-2004-003-V-2, CERN-2004-003. (2004). [CDS rec.: 815187] (cit. on p. 35).

[159] Benedikt, E. · Collier, E. · Mertens, E. · Poole, E. · Schindl, E.: *LHC Design Report. 3. The LHC injector chain*. Tech. rep. CERN-2004-003-V-3, CERN-2004-003. (2004). [CDS rec.: 823808] (cit. on p. 35).

[160] Group, L. S.: *The Large Hadron Collider: Conceptual design*. Tech. rep. CERN-AC-95-05-LHC, CM-P00047618. (1995). [CDS rec.: 291782] (cit. on p. 35).

[161] Evans, e. · Bryant, e.: *LHC Machine*. JINST 3 (2008) pages S08001. doi: 10.1088/1748-0221/3/08/S08001 (cit. on pp. 35, 37).

[162] Borghini, N. · Wiedemann, U. A.: *Predictions for the LHC heavy ion programme*. J. Phys. G35 (2008) page 023001. doi: 10.1088/0954-3899/35/2/023001. arXiv: 0707.0564 (cit. on p. 35).

[163] Schukraft, J.: *Heavy ions at the LHC: Physics perspectives and experimental program*. Pramana 57 (2001) pages 345–354. doi: 10.1016/S0375-9474(01)01375-6 (cit. on p. 35).

[164] Schindl, K.: *The PS booster as preinjector for LHC*. Part. Accel. 58 (1997) pages 63–78. [CDS rec.: 1120300] (cit. on p. 35).

[165] Cappi, R.: *The PS in the LHC injector chain*. Part. Accel. 58 (1997) pages 79–89. [CDS rec.: 323933] (cit. on p. 35).

[166] Collier, P. · Goddard, B.: *The SPS as LHC Injector*. Conf. Proc. C0106181 (2001) pages 3150–3152. [CDS rec.: 556356] (cit. on p. 35).

[167] Collier, P. · Goddard, B. · Jung, R. · Kissler, K. · Linnecar, T. et al.: *The SPS as injector for LHC: Conceptual design*. Tech. rep. CERN-SL-97-007-DI, CERN-SL-97-07-DI, CERN-SL-97-7-DI. (1997). [CDS rec.: 322782] (cit. on p. 35).

[168] Wangler, T. P.: *RF Linear Accelerators*. Wiley-VCH, 2008 (cit. on p. 35).

[169] Cappi, R. · Garoby, R. · Hancock, S. · Martini, M. · Rasmussen, N. et al.: *The PS complex as part of the LHC injector chain*. Tech. rep. CERN-PS-91-07, CERN-LHC-NOTE-144. (1991). [CDS rec.: 234720] (cit. on p. 36).

[170] Bottura, L · Pugnat, P · Siemko, A · Vlogaert, J · Wyss, C: *Performance of the LHC Final Design, Full-Scale Superconducting Dipole Prototypes*. IEEE Trans. Appl. Supercond. 11.LHC-Project-Report-452. CERN-LHC-Project-Report-452. 1/2 (2000) page 1554 (cit. on p. 36).

[171] Bajko, M. · Bertinelli, F. · Bellesia, B. · Fessia, P. · Hagen, P. et al.: *Status report on the superconducting dipole magnet production for the LHC*. IEEE Trans. Appl. Supercond. 17 (2007) pages 1097–1100. doi: 10.1109/TASC.2007.899697 (cit. on p. 36).

[172] Tuckmantel, J.: *Synchrotron radiation damping in LHC and longitudinal bunch shape*. Tech. rep. CERN-LHC-PROJECT-REPORT-819. (2005). [CDS rec.: 858155] (cit. on p. 37).

[173] Bruning, O. S.: *LHC challenges and upgrade options*. J. Phys. Conf. Ser. 110 (2008) page 112002. doi: 10.1088/1742-6596/110/11/112002 (cit. on p. 37).

[174] Chatrchyan, S. et al.: *The CMS experiment at the CERN LHC*. JINST 3 (2008) pages S08004. doi: 10.1088/1748-0221/3/08/S08004 (cit. on p. 38).

[175] Aamodt, K. et al.: *The ALICE experiment at the CERN LHC*. JINST 3 (2008) pages S08002. doi: 10.1088/1748-0221/3/08/S08002 (cit. on p. 38).

[176] Alves, J. et al.: *The LHCb Detector at the LHC*. JINST 3 (2008) pages S08005. doi: 10.1088/1748-0221/3/08/S08005 (cit. on p. 38).

[177] Antchev, G. · Aspell, P. · Atanassov, I. · Avati, V. · Berardi, V. et al.: *The TOTEM detector at LHC*. Nucl. Instrum. Meth. A617 (2010) pages 62–66. doi: 10.1016/j.nima.2009.08.083 (cit. on p. 38).

[178] Adriani, O. et al.: *Technical design report of the LHCf experiment: Measurement of photons and neutral pions in the very forward region of LHC*. Tech. rep. CERN-LHCC-2006-004. (2006). [CDS rec.: 926196] (cit. on p. 38).

[179] Aad, G. et al.: *The ATLAS Experiment at the CERN Large Hadron Collider*. JINST 3 (2008) pages S08003. doi: 10.1088/1748-0221/3/08/S08003 (cit. on p. 38).

[180] Armstrong, W. et al.: *ATLAS: Technical proposal for a general-purpose p p experiment at the Large Hadron Collider at CERN*. Tech. rep. CERN-LHCC-94-43. (1994). [CDS rec.: 290968] (cit. on p. 38).

[181] Haywood, S · Rossi, L · Nickerson, R · Romaniouk, A: *ATLAS inner detector: Technical Design Report, 1*. Tech. rep. ATLAS-TDR-004. (1997). [CDS rec.: 331063] (cit. on p. 39).

[182] Haywood, S · Rossi, L · Nickerson, R · Romaniouk, A: *ATLAS inner detector: Technical Design Report, 2*. Tech. rep. ATLAS-TDR-005. (1997). [CDS rec.: 331064] (cit. on p. 39).

[183] Yamamoto, A. · Makida, Y. · Ruber, R. · Doi, Y. · Haruyama, T. et al.: *The ATLAS central solenoid*. Nucl. Instrum. Meth. A584 (2008) pages 53–74. doi: 10.1016/j.nima.2007.09.047 (cit. on p. 39).

[184] ATLAS Collaboration: *ATLAS central solenoid: Technical design report*. Tech. rep. ATLAS-TDR-009, CERN-LHCC-97-21. (1997). [CDS rec.: 331067] (cit. on p. 39).

[185] Aad, G. · Ackers, M. · Alberti, F. · Aleppo, M. · Alimonti, G. et al.: *ATLAS pixel detector electronics and sensors*. JINST 3 (2008) pages P07007. doi: 10.1088/1748-0221/3/07/P07007 (cit. on p. 39).

[186] Alam, M. et al.: *ATLAS pixel detector: Technical design report*. Tech. rep. ATLAS-TDR-011, CERN-LHCC-98-13. (1998). [CDS rec.: 381263] (cit. on p. 39).

[187] Abdesselam, A. · Akimoto, T. · Allport, P. · Alonso, J. · Anderson, B. et al.: *The barrel modules of the ATLAS semiconductor tracker*. Nucl. Instrum. Meth. A568 (2006) pages 642–671. doi: 10.1016/j.nima.2006.08.036 (cit. on p. 39).

[188] Abdesselam, A. et al.: *The ATLAS semiconductor tracker end-cap module*. Nucl. Instrum. Meth. A575 (2007) pages 353–389. doi: 10.1016/j.nima.2007.02.019 (cit. on p. 39).

[189] Abat, E. et al.: *The ATLAS Transition Radiation Tracker (TRT) proportional drift tube: Design and performance*. JINST 3 (2008) pages P02013. doi: 10.1088/1748-0221/3/02/P02013 (cit. on p. 39).

[190] Akesson, T. et al.: *Status of design and construction of the Transition Radiation Tracker (TRT) for the ATLAS experiment at the LHC*. Nucl. Instrum. Meth. A522 (2004) pages 131–145. doi: 10.1016/j.nima.2004.01.033 (cit. on p. 39).

[191] Klinkby, E.: *Simulation of Transition Radiation and Electron Identification Ability of the ATLAS TRT*. Tech. rep. ATL-INDET-PROC-2011-043, ATL-COM-INDET-2011-138. (2011). [CDS rec.: 1405697] (cit. on p. 41).

[192] Akesson, T. · Arik, E. · Assamagan, K. · Baker, O. K. · Barberio, E. et al.: *Particle identification using the time-over-threshold method in the ATLAS Transition Radiation Tracker*. Nucl. Instrum. Meth. A474 (2001) pages 172–187. doi: 10.1016/S0168-9002(01)00878-6 (cit. on p. 41).

[193] ATLAS Collaboration: *ATLAS liquid argon calorimeter: Technical design report*. Tech. rep. ATLAS-TDR-002, CERN-LHCC-96-41. (1996). [CDS rec.: 331061] (cit. on p. 41).

[194] Aad, G. et al.: *Readiness of the ATLAS Liquid Argon Calorimeter for LHC Collisions*. Eur. Phys. J. C70 (2010) pages 723–753. doi: 10.1140/epjc/s10052-010-1354-y. arXiv: 0912.2642 (cit. on p. 41).

[195] Aubert, B. et al.: *Construction, assembly and tests of the ATLAS electromagnetic barrel calorimeter*. Nucl. Instrum. Meth. A558 (2006) pages 388–418. doi: 10.1016/j.nima.2005.11.212 (cit. on p. 41).

[196] Aleksa, M. et al.: *Construction, assembly and tests of the ATLAS electromagnetic end-cap calorimeters*. JINST 3 (2008) pages P06002. doi: 10.1088/1748-0221/3/06/P06002 (cit. on p. 41).

[197] Artamonov, A. · Bailey, D. · Belanger, G. · Cadabeschi, M. · Chen, T. et al.: *The ATLAS forward calorimeters*. JINST 3 (2008) pages P02010. doi: 10.1088/1748-0221/3/02/P02010 (cit. on p. 41).

[198] Gingrich, D. · Lachat, G. · Pinfold, J. · Soukoup, J. · Axen, D. et al.: *Construction, assembly and testing of the ATLAS hadronic end-cap calorimeter*. JINST 2 (2007) pages P05005. doi: 10.1088/1748-0221/2/05/P05005 (cit. on p. 41).

[199] ATLAS Collaboration: *ATLAS tile calorimeter: Technical design report*. Tech. rep. ATLAS-TDR-003, CERN-LHCC-96-42. (1996). [CDS rec.: 331062] (cit. on p. 41).

[200] Aad, G. et al.: *Readiness of the ATLAS Tile Calorimeter for LHC collisions*. Eur. Phys. J. C70 (2010) pages 1193–1236. doi: 10.1140/epjc/s10052-010-1508-y. arXiv: 1007.5423 (cit. on p. 41).

[201] ATLAS Collaboration: *ATLAS muon spectrometer: Technical design report*. Tech. rep. CERN-LHCC-97-22, ATLAS-TDR-10. (1997). [CDS rec.: 331068] (cit. on p. 41).

[202] Palestini, S.: *The muon spectrometer of the ATLAS experiment*. Nucl. Phys. Proc. Suppl. 125 (2003) pages 337–345. doi: 10.1016/S0920-5632(03)91013-9 (cit. on p. 41).

[203] Mikenberg, G.: *The ATLAS muon spectrometer*. Mod. Phys. Lett. A25 (2010) pages 649–667. doi: 10.1142/S0217732310032974 (cit. on p. 41).

[204] ATLAS Collaboration: *ATLAS magnet system: Technical design report*. Tech. rep. ATLAS-TDR-006, CERN-LHCC-97-18. (1997). [CDS rec.: 338080] (cit. on p. 41).

[205] Chevalier, L. · Guyot, C. · Kozanecki, W. · Virchaux, M. · Wotschack, J.: *Physics- and Detector-related Design Requirements for the ATLAS Toroid Magnet System*. Tech. rep. ATL-MUON-96-159, ATL-M-PN-159. (1996). [CDS rec.: 684192] (cit. on p. 41).

[206] Ventura, S.: *The monitored drift tube chambers of ATLAS*. AIP Conf. Proc. 794 (2005) pages 287–290. doi: 10.1063/1.2125672 (cit. on p. 42).

[207] Curatolo, M.: *The Monitored Drift Tube (MDT) chambers for the muon precision tracking in the ATLAS spectrometer*. Nucl. Phys. Proc. Suppl. 78 (1999) pages 422–425. doi: 10.1016/S0920-5632(99)00580-0 (cit. on p. 42).

[208] Di Ciaccio, A.: *The ATLAS RPC trigger chamber system*. Nucl. Instrum. Meth. A572 (2007) pages 48–49. doi: 10.1016/j.nima.2006.10.346 (cit. on p. 42).

[209] Di Ciaccio, A.: *Resistive plate chambers in ATLAS*. Nucl. Instrum. Meth. A384 (1996) pages 222–224. doi: 10.1016/S0168-9002(96)00891-1 (cit. on p. 42).

[210] Argyropoulos, T. · Assamagan, K. A. · Benedict, B. H. · Chernyatin, V. · Cheu, E. et al.: *Cathode strip chambers in ATLAS: Installation, commissioning and in situ performance*. IEEE Trans. Nucl. Sci. 56 (2009) pages 1568–1574. doi: 10.1109/TNS.2009.2020861 (cit. on p. 42).

[211] Nagai, K.: *Thin gap chambers in ATLAS*. Nucl. Instrum. Meth. A384 (1996) pages 219–221. doi: 10.1016/S0168-9002(96)01065-0 (cit. on p. 42).

[212] ATLAS Collaboration: *ATLAS detector and physics performance: Technical Design Report, 1*. Tech. rep. ATLAS-TDR-014, CERN-LHCC-99-014. (1999). [CDS rec.: 391176] (cit. on pp. 42, 44).

[213] ATLAS Collaboration: *ATLAS detector and physics performance: Technical Design Report, 2*. Tech. rep. ATLAS-TDR-015, CERN-LHCC-99-015. (1999). [CDS rec.: 391177] (cit. on p. 42).

[214] Asquith, L et al.: *Performance of Jet Algorithms in the ATLAS Detector*. Tech. rep. ATL-PHYS-INT-2010-129. CERN, (2010). [CDS rec.: 1311867] (cit. on p. 43).

[215] Cacciari, M. · Salam, G. P.: *Dispelling the N^3 myth for the k_t jet-finder*. Phys. Lett. B641 (2006) pages 57–61. doi: 10.1016/j.physletb.2006.08.037. arXiv: hep-ph/0512210 (cit. on p. 43).

[216] Cacciari, M. · Salam, G. P. · Soyez, G.: *The Anti-k(t) jet clustering algorithm*. JHEP 0804 (2008) page 063. doi: 10.1088/1126-6708/2008/04/063. arXiv: 0802.1189 (cit. on p. 43).

[217] ATLAS Collaboration: *Expected electron performance in the ATLAS experiment*. Tech. rep. ATL-PHYS-PUB-2011-006. CERN, (2011). [CDS rec.: 1345327] (cit. on p. 43).

[218] Aad, G. et al.: *Electron performance measurements with the ATLAS detector using the 2010 LHC proton-proton collision data*. Eur. Phys. J. C72 (2012) page 1909. doi: 10.1140/epjc/s10052-012-1909-1. arXiv: 1110.3174 (cit. on p. 43).

[219] Lampl, W et al.: *Calorimeter Clustering Algorithms: Description and Performance*. Tech. rep. ATL-LARG-PUB-2008-002, ATL-COM-LARG-2008-003. CERN, (2008). [CDS rec.: 1099735] (cit. on pp. 44, 46).

[220] ATLAS Collaboration: *Expected photon performance in the ATLAS experiment*. Tech. rep. ATL-PHYS-PUB-2011-007, ATL-COM-PHYS-2010-1051. CERN, (2011). [CDS rec.: 1345329] (cit. on p. 44).

[221] ATLAS Collaboration: *Measurements of the photon identification efficiency with the ATLAS detector using 4.9 fb^{-1} of pp collision data collected in 2011*. Tech. rep. ATLAS-CONF-2012-123. CERN, (2012). [CDS rec.: 1473426] (cit. on p. 44).

[222] Lagouri, T. · Adams, D. · Assamagan, K. · Biglietti, M. · Carlino, G. et al.: *A Muon Identification and Combined Reconstruction Procedure for the ATLAS Detector at the LHC at CERN*. IEEE Trans. Nucl. Sci. 51 (2004) pages 3030–3033. doi: 10.1109/TNS.2004.839102 (cit. on p. 44).

[223] Hassani, S. · Chevalier, L. · Lancon, E. · Laporte, J. · Nicolaidou, R. et al.: *A muon identification and combined reconstruction procedure for the ATLAS detector at the LHC using the (MUONBOY, STACO, MuTag) reconstruction packages*. Nucl. Instrum. Meth. A572 (2007) pages 77–79. doi: 10.1016/j.nima.2006.10.340 (cit. on p. 44).

[224] Gavrilenko, I: *Description of Global Pattern Recognition Program (XKalman)*. Tech. rep. ATL-INDET-97-165, ATL-I-PN-165. CERN, (1997). [CDS rec.: 686017] (cit. on p. 44).

[225] Virchaux, M: *Muonbox: a full 3D tracking programme for Muon reconstruction in the ATLAS Spectrometer*. Tech. rep. ATL-MUON-97-198, ATL-M-PN-198. CERN, (1997). [CDS rec.: 685575] (cit. on p. 44).

[226] Kortner, O · Moyse, E: *Pile-up Depedence of the ATLAS Muon Performance*. https://atlas.web.cern.ch/Atlas/GROUPS/PHYSICS/MUON/PublicPlots/2011/Dec/index.html. ATL-COM-PHYS-2011-1640. CERN, (2011). [CDS rec.: 1403080] (cit. on p. 45).

[227] ATLAS Collaboration: *Muon Momentum Resolution in First Pass Reconstruction of pp Collision Data Recorded by ATLAS in 2010*. Tech. rep. ATLAS-CONF-2011-046. CERN, (2011). [CDS rec.: 1338575] (cit. on pp. 44, 45).

[228] ATLAS Collaboration: *A measurement of the ATLAS muon reconstruction and trigger efficiency using J/psi decays*. Tech. rep. ATLAS-CONF-2011-021. CERN, (2011). [CDS rec.: 1336750] (cit. on pp. 44, 57).

[229] Aad, G. et al.: *Studies of the performance of the ATLAS detector using cosmic-ray muons*. Eur. Phys. J. C71 (2011) page 1593. doi: 10.1140/epjc/s10052-011-1593-6. arXiv: 1011.6665 (cit. on p. 44).

[230] Tarrade, F.: *Reconstruction and identification of hadronic tau decays in ATLAS*. Nucl. Phys. Proc. Suppl. 169 (2007) pages 357–362. doi: 10.1016/j.nuclphysbps.2007.03.028 (cit. on p. 45).

[231] ATLAS Collaboration: *Performance of the Reconstruction and Identification of Hadronic Tau Decays in ATLAS with 2011 Data*. Tech. rep. ATLAS-CONF-2012-142. CERN, (2012). [CDS rec.: 1485531] (cit. on pp. 45, 48).

[232] Jennens, D: *Reconstruction and Identification of Hadronically Decaying Tau Leptons at ATLAS*. Tech. rep. ATL-PHYS-PROC-2012-119. CERN, (2012). [CDS rec.: 1463234] (cit. on p. 45).

[233] Roe, B. P. · Yang, H.-J. · Zhu, J. · Liu, Y. · Stancu, I. et al.: *Boosted decision trees, an alternative to artificial neural networks*. Nucl. Instrum. Meth. A543 (2005) pages 577–584. doi: 10.1016/j.nima.2004.12.018. arXiv: physics/0408124 (cit. on p. 46).

[234] ATLAS Collaboration: *Performance of the Reconstruction and Identification of Hadronic Tau Decays with ATLAS*. Tech. rep. ATLAS-CONF-2011-152. CERN, (2011). [CDS rec.: 1398195] (cit. on pp. 46, 48, 108).

[235] Speckmayer, P. · Hocker, A. · Stelzer, J. · Voss, H.: *The toolkit for multivariate data analysis, TMVA 4*. J. Phys. Conf. Ser. 219 (2010) page 032057. doi: 10.1088/1742-6596/219/3/032057 (cit. on p. 47).

[236] Hocker, A. · Stelzer, J. · Tegenfeldt, F. · Voss, H. · Voss, K. et al.: *TMVA - Toolkit for Multivariate Data Analysis*. PoS ACAT (2007) page 040. arXiv: physics/0703039 (cit. on p. 47).

[237] ATLAS Collaboration: *Determination of the tau energy scale and the associated systematic uncertainty in proton-proton collisions at sqrts = 7 TeV with the ATLAS detector at the LHC in 2011*. Tech. rep. ATLAS-CONF-2012-054. CERN, (2012). [CDS rec.: 1453781] (cit. on pp. 48, 108).

[238] Aad, G. et al.: *Performance of Missing Transverse Momentum Reconstruction in Proton-Proton Collisions at 7 TeV with ATLAS*. Eur. Phys. J. C72 (2012) page 1844. doi: 10.1140/epjc/s10052-011-1844-6. arXiv: 1108.5602 (cit. on p. 48).

[239] ATLAS Collaboration: *Performance of Missing Transverse Momentum Reconstruction in ATLAS with 2011 Proton-Proton Collisions at sqrts = 7 TeV*. Tech. rep. ATLAS-CONF-2012-101. CERN, (2012). [CDS rec.: 1463915] (cit. on pp. 48, 49).

[240] Piacquadio, G. · Weiser, C.: *A new inclusive secondary vertex algorithm for b-jet tagging in ATLAS*. J. Phys. Conf. Ser. 119 (2008) page 032032. doi: 10.1088/1742-6596/119/3/032032 (cit. on p. 49).

[241] ATLAS Collaboration: *Impact parameter-based b-tagging algorithms in the 7 TeV collision data with the ATLAS detector: the TrackCounting and JetProb algorithms*. Tech. rep. ATLAS-CONF-2010-041. CERN, (2010). [CDS rec.: 1277681] (cit. on p. 49).

[242] ATLAS Collaboration: *Commissioning of the ATLAS high-performance b-tagging algorithms in the 7 TeV collision data*. Tech. rep. ATLAS-CONF-2011-102. CERN, (2011). [CDS rec.: 1369219] (cit. on p. 49).

[243] ATLAS Collaboration: *Measuring the b-tag efficiency in a top-pair sample with 4.7 fb^{-1} of data from the ATLAS detector*. Tech. rep. ATLAS-CONF-2012-097. CERN, (2012). [CDS rec.: 1460443] (cit. on p. 49).

[244] ATLAS Collaboration: *Measurement of the Mistag Rate with 5 fb^{-1} of Data Collected by the ATLAS Detector*. Tech. rep. ATLAS-CONF-2012-040. CERN, (2012). [CDS rec.: 1435194] (cit. on p. 49).

[245] Aad, G. et al.: *Expected Performance of the ATLAS Experiment - Detector, Trigger and Physics* (2009). arXiv: 0901.0512 (cit. on p. 50).

[246] Kordas, K. · Abolins, M. · Alexandrov, I. · Amorim, A. · Aracena, I. et al.: *The ATLAS Data Acquisition and Trigger: Concept, design and status*. Nucl. Phys. Proc. Suppl. 172 (2007) pages 178–182. doi: 10.1016/j.nuclphysbps.2007.08.004 (cit. on p. 50).

[247] Cranmer, K.: *The ATLAS analysis architecture*. Nucl. Phys. Proc. Suppl. 177-178 (2008) pages 126–130. doi: 10.1016/j.nuclphysbps.2007.11.096 (cit. on p. 51).

[248] Rimoldi, A.: *The ATLAS detector simulation application*. Nucl. Phys. Proc. Suppl. 172 (2007) pages 49–52. doi: 10.1016/j.nuclphysbps.2007.07.005 (cit. on p. 51).

[249] Buckley, A. · Butterworth, J. · Gieseke, S. · Grellscheid, D. · Hoche, S. et al.: *General-purpose event generators for LHC physics*. Phys. Rept. 504 (2011) pages 145–233. doi: 10.1016/j.physrep.2011.03.005. arXiv: 1101.2599 (cit. on p. 51).

[250] Corcella, G. · Knowles, I. · Marchesini, G. · Moretti, S. · Odagiri, K. et al.: *HERWIG 6: An Event generator for hadron emission reactions with interfering gluons (including supersymmetric processes)*. JHEP 0101 (2001) page 010. arXiv: hep-ph/0011363 (cit. on p. 51).

[251] Marchesini, G. · Webber, B. · Abbiendi, G. · Knowles, I. · Seymour, M. et al.: *HERWIG: A Monte Carlo event generator for simulating hadron emission reactions with interfering gluons. Version 5.1 - April 1991*. Comput. Phys. Commun. 67 (1992) pages 465–508. doi: 10.1016/0010-4655(92)90055-4 (cit. on p. 51).

[252] Butterworth, J. · Forshaw, J. R. · Seymour, M.: *Multiparton interactions in photoproduction at HERA*. Z. Phys. C72 (1996) pages 637–646. doi: 10.1007/s002880050286. arXiv: hep-ph/9601371 (cit. on p. 52).

[253] Jadach, S. · Was, Z. · Decker, R. · Kuhn, J. H.: *The tau decay library TAUOLA: Version 2.4*. Comput. Phys. Commun. 76 (1993) pages 361–380. doi: 10.1016/0010-4655(93)90061-G (cit. on p. 52).

[254] Golonka, P. · Kersevan, B. · Pierzchala, T. · Richter-Was, E. · Was, Z. et al.: *The Tauola photos F environment for the TAUOLA and PHOTOS packages: Release. 2.* Comput. Phys. Commun. 174 (2006) pages 818–835. doi: 10.1016/j.cpc.2005.12.018. arXiv: hep-ph/0312240 (cit. on p. 52).

[255] Barberio, E. · Was, Z.: *PHOTOS: A Universal Monte Carlo for QED radiative corrections. Version 2.0*. Comput. Phys. Commun. 79 (1994) pages 291–308. doi: 10.1016/0010-4655(94)90074-4 (cit. on p. 52).

[256] Sherstnev, A. · Thorne, R.: *Parton Distributions for LO Generators*. Eur. Phys. J. C55 (2008) pages 553–575. doi: 10.1140/epjc/s10052-008-0610-x. arXiv: 0711.2473 (cit. on p. 52).

[257] Sjostrand, T.: *High-energy physics event generation with PYTHIA 5.7 and JETSET 7.4*. Comput. Phys. Commun. 82 (1994) pages 74–90. doi: 10.1016/0010-4655(94)90132-5 (cit. on p. 52).

[258] Sjostrand, T. · Eden, P. · Friberg, C. · Lonnblad, L. · Miu, G. et al.: *High-energy physics event generation with PYTHIA 6.1*. Comput. Phys. Commun. 135 (2001) pages 238–259. doi: 10.1016/S0010-4655(00)00236-8. arXiv: hep-ph/0010017 (cit. on p. 52).

[259] Andersson, B. · Gustafson, G. · Ingelman, G. · Sjostrand, T.: *Parton Fragmentation and String Dynamics*. Phys. Rept. 97 (1983) pages 31–145. doi: 10.1016/0370-1573(83)90080-7 (cit. on p. 52).

[260] Azarkin, M. Y. · Dremin, I. · Leonidov, A.: *Soft ridge in proton-proton collisions*. Mod. Phys. Lett. A26 (2011) pages 963–966. doi: 10.1142/S0217732311035468. arXiv: 1102.3258 (cit. on p. 52).

[261] Mangano, M. L. · Moretti, M. · Piccinini, F. · Pittau, R. · Polosa, A. D.: *ALPGEN, a generator for hard multiparton processes in hadronic collisions*. JHEP 0307 (2003) page 001. arXiv: hep-ph/0206293 (cit. on p. 52).

[262] Frixione, S. · Webber, B. R.: *The MC@NLO 3.3 Event Generator* (2006). arXiv: hep-ph/0612272 (cit. on p. 52).

[263] Frixione, S. · Webber, B. R.: *Matching NLO QCD computations and parton shower simulations*. JHEP 06 (2002) page 029. arXiv: hep-ph/0204244 (cit. on p. 52).

[264] Frixione, S. · Nason, P. · Webber, B. R.: *Matching NLO QCD and parton showers in heavy flavour production*. JHEP 08 (2003) page 007. arXiv: hep-ph/0305252 (cit. on p. 52).

[265] Frixione, S. · Laenen, E. · Motylinski, P. · Webber, B. R.: *Single-top production in MC@NLO*. JHEP 03 (2006) page 092. doi: 10.1088/1126-6708/2006/03/092. arXiv: hep-ph/0512250 (cit. on p. 52).

[266] Lai, H.-L. · Guzzi, M. · Huston, J. · Li, Z. · Nadolsky, P. M. et al.: *New parton distributions for collider physics*. Phys. Rev. D82 (2010) page 074024. doi: 10.1103/PhysRevD.82.074024. arXiv: 1007.2241 (cit. on p. 52).

[267] Kersevan, B. P. · Richter-Was, E.: *The Monte Carlo event generator AcerMC version 2.0 with interfaces to PYTHIA 6.2 and HERWIG 6.5* (2004). arXiv: hep-ph/0405247 (cit. on p. 52).

[268] Alwall, J. · Demin, P. · Visscher, S. · Frederix, R. · Herquet, M. et al.: *MadGraph/MadEvent v4: The New Web Generation*. JHEP 0709 (2007) page 028. doi: 10.1088/1126-6708/2007/09/028. arXiv: 0706.2334 (cit. on p. 52).

[269] Alwall, J. · Herquet, M. · Maltoni, F. · Mattelaer, O. · Stelzer, T.: *MadGraph 5 : Going Beyond*. JHEP 1106 (2011) page 128. doi: 10.1007/JHEP06(2011)128. arXiv: 1106.0522 (cit. on p. 52).

[270] Murayama, H. · Watanabe, I. · Hagiwara, K.: *HELAS: HELicity amplitude subroutines for Feynman diagram evaluations*. KEK-91-11 (1992) (cit. on p. 52).

[271] Hagiwara, K. · Kanzaki, J. · Okamura, N. · Rainwater, D. · Stelzer, T.: *Fast calculation of HELAS amplitudes using graphics processing unit (GPU)*. Eur. Phys. J. C66 (2010) pages 477–492. doi: 10.1140/epjc/s10052-010-1276-8. arXiv: 0908.4403 (cit. on p. 52).

[272] Byckling, E. · Kajantie, K.: *N-particle phase space in terms of invariant momentum transfers*. Nucl. Phys. B9 (1969) pages 568–576. doi: 10.1016/0550-3213(69)90271-5 (cit. on p. 52).

[273] Agostinelli, S. et al.: *GEANT4: A Simulation toolkit*. Nucl. Instrum. Meth. A506 (2003) pages 250–303. doi: 10.1016/S0168-9002(03)01368-8 (cit. on p. 53).

[274] Allison, J. · Amako, K. · Apostolakis, J. · Araujo, H. · Dubois, P. et al.: *Geant4 developments and applications*. IEEE Trans. Nucl. Sci. 53 (2006) page 270. doi: 10.1109/TNS.2006.869826 (cit. on p. 53).

[275] Aad, G. et al.: *The ATLAS Simulation Infrastructure*. Eur. Phys. J. C70 (2010) pages 823–874. doi: 10.1140/epjc/s10052-010-1429-9. arXiv: 1005.4568 (cit. on p. 53).

[276] Adragna, P. · Alexa, C. · Anderson, K. · Antonaki, A. · Arabidze, A. et al.: *Measurement of pion and proton response and longitudinal shower profiles up to 20 nuclear interaction lengths with the ATLAS tile calorimeter*. Nucl. Instrum. Meth. A615 (2010) pages 158–181. doi: 10.1016/j.nima.2010.01.037 (cit. on p. 53).

[277] Cooke, M et al.: *In situ commissioning of the ATLAS electromagnetic calorimeter with cosmic muons*. Tech. rep. ATL-LARG-PUB-2007-013. ATL-COM-LARG-2007-012. CERN, (2007). [CDS rec.: 1071187] (cit. on p. 53).

[278] Aad, G. et al.: *Luminosity Determination in pp Collisions at $\sqrt{s} = 7$ TeV Using the ATLAS Detector at the LHC*. Eur. Phys. J. C71 (2011) page 1630. doi: 10.1140/epjc/s10052-011-1630-5. arXiv: 1101.2185 (cit. on pp. 53, 55).

[279] Brun, R. · Rademakers, F.: *ROOT: An object oriented data analysis framework*. Nucl. Instrum. Meth. A389 (1997) pages 81–86. doi: 10.1016/S0168-9002(97)00048-X (cit. on p. 54).

[280] Antcheva, I. · Ballintijn, M. · Bellenot, B. · Biskup, M. · Brun, R. et al.: *ROOT: A C++ framework for petabyte data storage, statistical analysis and visualization*. Comput. Phys. Commun. 180 (2009) pages 2499–2512. doi: 10.1016/j.cpc.2009.08.005 (cit. on p. 54).

[281] ATLAS Collaboration: *Improved Luminosity Determination in $\mathbf{pp}$ Collisions at $\sqrt{\mathbf{s}} = \mathbf{7}$ TeV using the ATLAS Detector at the LHC*. Tech. rep. ATLAS-CONF-2012-080. CERN, (2012). [CDS rec.: 1460392] (cit. on p. 55).

[282] ATLAS Collaboration: *Data-Quality Requirements and Event Cleaning for Jets and Missing Transverse Energy Reconstruction with the ATLAS Detector in Proton-Proton Collisions at a Center-of-Mass Energy of $sqrts = 7$ TeV*. Tech. rep. ATLAS-CONF-2010-038. CERN, (2010). [CDS rec.: 1277678] (cit. on p. 55).

[283] Aad, G. et al.: *Search for events with large missing transverse momentum, jets, and at least two tau leptons in 7 TeV proton-proton collision data with the ATLAS detector*. Phys. Lett. B714 (2012) pages 180–196. doi: 10.1016/j.physletb.2012.06.055. arXiv: 1203.6580 (cit. on pp. 56, 127).

[284] Aad, G. et al.: *Searches for supersymmetry with the ATLAS detector using final states with two leptons and missing transverse momentum in $\sqrt{s} = 7$ TeV proton-proton collisions*. Phys. Lett. B709 (2012) pages 137–157. doi: 10.1016/j.physletb.2012.01.076. arXiv: 1110.6189 (cit. on p. 56).

[285] ATLAS Collaboration: *Performance of the ATLAS muon trigger in 2011*. Tech. rep. ATLAS-CONF-2012-099. CERN, (2012). [CDS rec.: 1462601] (cit. on p. 57).

[286] Aad, G. et al.: *Measurement of the top quark-pair production cross section with ATLAS in pp collisions at $\sqrt{s} = 7$ TeV*. Eur. Phys. J. C71 (2011) page 1577. doi: 10.1140/epjc/s10052-011-1577-6. arXiv: 1012.1792 (cit. on p. 61).

[287] Aad, G. et al.: *Measurement of the Muon Charge Asymmetry from W Bosons Produced in pp Collisions at $\sqrt{s} = 7$ TeV with the ATLAS detector*. Phys. Lett. B701 (2011) pages 31–49. DOI: 10.1016/j.physletb.2011.05.024. arXiv: 1103.2929 (cit. on p. 62).

[288] Aad, G. et al.: *Measurement of the inclusive $W^{\pm}$ and Z/gamma cross sections in the electron and muon decay channels in pp collisions at $\sqrt{s} = 7$ TeV with the ATLAS detector*. Phys. Rev. D85 (2012) page 072004. DOI: 10.1103/PhysRevD.85.072004. arXiv: 1109.5141 (cit. on p. 63).

[289] Desch, K · Nattermann, T · Wienemann, P: *Prospects on measuring WZ and ZZ with tau final states*. Tech. rep. ATL-COM-PHYS-2009-611. CERN, (2009). [CDS rec.: 1222122] (cit. on p. 91).

[290] Cowan, G. · Cranmer, K. · Gross, E. · Vitells, O.: *Asymptotic formulae for likelihood-based tests of new physics*. Eur. Phys. J. C71 (2011) page 1554. DOI: 10.1140/epjc/s10052-011-1554-0. arXiv: 1007.1727 (cit. on pp. 98, 125).

[291] Aad, G. et al.: *Jet energy measurement with the ATLAS detector in proton-proton collisions at $\sqrt{s} = 7$ TeV* (2011). arXiv: 1112.6426 (cit. on p. 110).

[292] ATLAS Collaboration: *Light-quark and Gluon Jets: Calorimeter Response, Jet Energy Scale Systematics and Properties*. Tech. rep. ATLAS-CONF-2012-138. CERN, (2012). [CDS rec.: 1480629] (cit. on p. 110).

[293] Aad, G. et al.: *Jet energy resolution in proton-proton collisions at $\sqrt{s} = 7$ TeV recorded in 2010 with the ATLAS detector* (2012). arXiv: 1210.6210 (cit. on p. 110).

[294] Hohlfeld, M · Lungwitz, M · Meyer, C · Mueller, T: *Estimating theory uncertainties in W/Z+jets and ttbar+jets events using the Alpgen generator*. Tech. rep. ATL-COM-PHYS-2012-070. CERN, (2012). [CDS rec.: 1419198] (cit. on p. 115).

[295] Kramer, M. · Kulesza, A. · Leeuw, R. · Mangano, M. · Padhi, S. et al.: *Supersymmetry production cross sections in pp collisions at $\sqrt{s} = 7$ TeV* (2012). arXiv: 1206.2892 (cit. on p. 116).

[296] Shank, J. T. · Sliwa, K · Taylor, F · Willis, S · Zhou, B: *Studies on A0, Z' and W' with ATLAS Muon Detector*. Tech. rep. ATL-MUON-97-161. ATL-M-PN-161. CERN, (1997). [CDS rec.: 684215] (cit. on p. 123).

[297] Kulesza, A. · Stirling, W. J.: *Like sign W boson production at the LHC as a probe of double parton scattering*. Phys. Lett. B475 (2000) pages 168–175. DOI: 10.1016/S0370-2693(99)01512-9. arXiv: hep-ph/9912232 (cit. on p. 124).

[298] Abbiendi, G. et al.: *Searches for gauge-mediated supersymmetry breaking topologies in e+ e- collisions at LEP2*. Eur. Phys. J. C46 (2006) pages 307–341. DOI: 10.1140/epjc/s2006-02524-8. arXiv: hep-ex/0507048 (cit. on p. 126).

[299] Aad, G. et al.: *Search for Supersymmetry in Events with Large Missing Transverse Momentum, Jets, and at Least One Tau Lepton in 7 TeV Proton-Proton Collision Data with the ATLAS Detector*. Eur. Phys. J. C72 (2012) page 2215. DOI: 10.1140/epjc/s10052-012-2215-7. arXiv: 1210.1314 (cit. on p. 127).

[300] Draper, P. · Meade, P. · Reece, M. · Shih, D.: *Implications of a 125 GeV Higgs for the MSSM and Low-Scale SUSY Breaking*. Phys. Rev. D85 (2012) page 095007. doi: 10.1103/PhysRevD.85.095007. arXiv: 1112.3068 (cit. on p. 132).

[301] Ajaib, M. A. · Gogoladze, I. · Nasir, F. · Shafi, Q.: *Revisiting mGMSB in Light of a 125 GeV Higgs*. Phys. Lett. B713 (2012) pages 462–468. doi: 10.1016/j.physletb.2012.06.036. arXiv: 1204.2856 (cit. on pp. 132, 134).

[302] Baer, H. · Barger, V. · Mustafayev, A.: *Implications of a 125 GeV Higgs scalar for LHC SUSY and neutralino dark matter searches*. Phys. Rev. D85 (2012) page 075010. doi: 10.1103/PhysRevD.85.075010. arXiv: 1112.3017 (cit. on p. 132).

[303] Evans, J. L. · Ibe, M. · Shirai, S. · Yanagida, T. T.: *A 125GeV Higgs Boson and Muon g-2 in More Generic Gauge Mediation*. Phys. Rev. D85 (2012) page 095004. doi: 10.1103/PhysRevD.85.095004. arXiv: 1201.2611 (cit. on p. 134).

[304] Evans, J. L. · Ibe, M. · Yanagida, T. T.: *Relatively Heavy Higgs Boson in More Generic Gauge Mediation*. Phys. Lett. B705 (2011) pages 342–348. doi: 10.1016/j.physletb.2011.10.031. arXiv: 1107.3006 (cit. on p. 134).

List of Figures

List of Tables